STRUCTURAL CHARACTERISTICS OF AMINO ACID DERIVED METAL ORGANIC FRAMEWORKS (MOFS) FOR WATER ADSORPTION AND PROTON TRANSPORT

Thesis Submitted to

Academy of Scientific and
Innovative Research (AcSIR)
for the Degree of Doctor of
Philosophy in Chemical
Sciences

By

TANAY KUNDU

Registration Number: 10CC11J26028

Under the guidance of
Dr. Rahul Banerjee

Physical and Material Chemistry Division
CSIR National Chemical Laboratory
Pune-411008,
India

November
2014

Dedicated to

My Parents

CERTIFICATE

Certified that the work **"Structural Characteristics of Amino Acid Derived Metal Organic Frameworks (MOFs) for Water Adsorption and Proton Transport"** submitted to Academy of Scientific & Innovative Research (AcSIR) was carried out by **Tanay Kundu**, at the CSIR-National Chemical Laboratory Pune, under my supervision. Such material has not been submitted elsewhere for a degree.

Rahul Banerjee

Dr. Rahul Banerjee, **Date: 07.11.14**

(Thesis Supervisor),
Physical and Materials Chemistry Division,
CSIR-National Chemical Laboratory,
Pune-411008.
India

STATEMENT

I hereby declare that the matter embodied in this thesis entitled **“Structural Characteristics of Amino Acid Derived Metal Organic Frameworks (MOFs) for Water Adsorption and Proton Transport”** is the result of investigations carried out by me in Physical and Materials chemistry Division, CSIR-National Chemical Laboratory, Pune under the supervision of Dr. Rahul Banerjee.

In keeping with the general practice of reporting scientific observations due acknowledgements have been made wherever the work described is based on the findings of other investigators.

Tanay Kundu

Pune **Tanay Kundu**

November 2014

ACKNOWLEDGEMENT

I am sincerely grateful to my supervisor Dr. **Rahul Banerjee** for his steady guidance, support and encouragement throughout my PhD tenure. I am thankful to him for introducing me to the attractive field of MOF research. I warmly thank him for his precious advice, analysis, criticism and discussions on my work. I would like to thank my DAC committee members Dr. Prakash Wadgaonkar, Dr. T. G. Ajithkumar and Dr. Benudhar Punji for their research assistance, beneficial suggestions and innovative ideas throughout my PhD tenure.

Most of the experiments and their outcome described in this thesis have been obtained via close collaborations with National and International laboratories. Dr. Vedavati G Puranik provided us the opportunity to use single crystal instrument at the early stage of our research. I am thankful to Dr. Vijayamohanan K. Pillai and Dr. Sreekumar Kurungot for proton conductivity measurements. Finally, I thank Dr. David Diaz Diaz and Dr. Kumar Vanka for carefully checking the draft for publication and providing thoughtful insights.

I am grateful to CSIR, New Delhi for fellowship support. I thank all the non-teaching staff of CSIR-NCL for their assistance on various occasions. I wish to thank all my friendly and cooperative labmates *Pradip, Chandan, Arijit, Subhadeep, Tamas, Sharath, Bishnu, Suman, Bikash, Harshitha, Mohitosh, Saibal, Arjun, Jayshri, Gobinda and Digambar* for creating a cheerful environment in the lab. They were very supportive, collaborative and helpful during my entire stay at CSIR-NCL. I particularly thank *Subash* for guiding me at the initial stage. I am also grateful to *Shouvik* for providing friendly advice and research assistance. I thank project students particularly Souda, Vivek, Vikas who helped me in many projects.

My stay at CSIR-NCL has been pleasant with the relationship of all the research scholars. I am thankful to Joyasishda, Krisanuda, Patida, Shyamda, Debasisda, Parthada, Sumantrada, Garaida, Sujitda, Animeshda, Binoyda, Basabda, Analda, Anupamda, Saikatda, Kaushalendra, Chinmoy, Mangesh, Sekhar, Chandan (Chaudhry), Chakadola, Rajashri, Sushma, Vishal, Kuttan, Bihag, Abhik, Kamalika, Agni, Achintya, Arpan, Kanak, Susanta, Anjan, Pravat, Aryya, Munmun, Subha, Tanaya, Souvik, Subhadip, Prithvi, Prathit, Swagata, Jitu, Jhumur, Bala, Pushpanjali, Divya, Tanpreet, Prabhu, Pandi, Soumyojyoti, Prasenjit, Biplab.

I offer my sincere gratitude to all the people, teachers who have inspired me directly or indirectly in my research career.

I am grateful to CSIR, New Delhi, for awarding the research fellowship and Dr. Pal, Director, and Dr. Sivaram, former director, CSIR-National Chemical Laboratory to carry out my research works, utilizing the infrastructural facilities and to submit this work in the form of a thesis for the award of PhD degree. I am also thankful to Academy of Scientific & Innovative Research (AcSIR) for giving me a chance to complete one the dream in my life.

I thank my wife for her constant care, support and encouragement. I thank the entire members in my family for their invariable care and wishes. Last but not the least; I would like to pay deep regards to my parents for their sincere encouragement and inspiration throughout my research work. I owe everything to them. Dedicating this thesis to them is a minor recognition for their invaluable support and encouragement.

Tanay Kundu

PREFACE

Metal-organic frameworks (MOFs) are a novel class of organic-inorganic hybrid crystalline network which can be synthesized by the coordination bond formation between multitopic organic linkers with metal cations or clusters. MOFs have been used for promising new applications like gas storage, gas/vapor separation, chemical sensing, enantio-selective catalysis, drug delivery and conductivity. Owing to MOFs high surface area with tunable pore size and functionality, it can be hosted for a variety of guest molecules. Since its discovery, enormous efforts have been driven in last two decades on MOFs to improve their property and applicability. Bottom up construction of MOF architecture rely on the judicious choice of organic spacers and metal modes. Hence, various organic linkers of diverse length, shape, size and functionality have been reported for the fine tuning of overall MOF architecture. The most fascinating aspect in the MOF research is the direct structure-property relationship for challenging applications. Till now the main focus on MOFs are for adsorption and separation of industrially relevant gases viz. N_2, CO_2, H_2, CH_4, thanks to its framework void or porous backbone. However, recently many other interesting applications e.g. water adsorption, proton transport, electron mobility and light harvesting property has been investigated in MOF. In future, MOFs will definitely pioneer synthesis of functional solids with tailor made properties embedded within for future challenges.

Chapter 2 will address six new homochiral Metal-Organic Framework isomers that have been synthesized using pyridine derivatives of L-leucine, L-serine and L-threonine, respectively as organic link and $Cd(CH_3COO)_2{\cdot}2H_2O$ as metal precursor under hydrothermal condition. These MOFs show interesting water adsorption profile depending on the structure, hydrophobicity and hydrophilicity of the MOF interiors (*Cryst. Growth Des.* 2012, **12**, 4633–4640 and *CrystEngComm*, 2013, **15**, 9634-9640).

In Chapter 3, synthesis and characterization of four chiral MOFs were reported with an unprecedented zeolitic *unh*-topology and helical continuous water chain inside the pores. These MOFs exhibit single crystal to single crystal reversibility and different proton conductivity of almost zero to ~ 4.45×10^{-5} Scm^{-1} at ambient temperature although the MOFs adopt similar architecture. (*J. Am. Chem. Soc.,* 2011, **133**, 17950)

In Chapter 4, we observed unprecedented hydrolytic regenerability in all these homochiral MOFs i.e. they intent to dissolve in water at elevated temperature (>90 °C), forming a clear solution. Nevertheless, it again tends to recrystallize and regenerate evaporated to regain the original structure and the recrystallization complete whilst all water molecules departed. The ligand backbone and coordinated anions greatly modulate the framework recrystallization time. Furthermore, we have performed salt metathesis reaction on these 3D MOFs the hydrolytic regenerable nature with different Ag precursors which resulted in different Zn based 2D coordination polymers. These MOFs exhibit moderate to low water sorption based on framework constituents. (*Chem. Commun.* 2013, **49**, 5262)

In Chapter 5, we present a systematic analysis of diverse ZnO morphologies derived from calcination of porous 3D MOFs with different halogen anions, and their solar cell activities. Herein, two chiral 3D MOF isomers have been synthesized in micro form and systematically calcined both under air and nitrogen environment to get three different ZnO architectures. Both MOFs possesses similar architecture and only difference lies in halogen substitution (-Cl, -Br) in the crystal structure. (*Cryst. Growth & Des.* 2012*,* **12**, 2572)

In chapter 6, three two dimensional MOFs are presented namely Ca-SBBA, Sr-SBBA and Ba-SBBA, constructed from alkaline earth metals and 4,4′-sulphobisbenzoic acid (SBBA) as organic linker. Interestingly, the structures are completely different from each other although they bear same ligand and same group of metal atoms. All these three MOFs have thermal stability up to 500 °C, with a crystalline phase change above 100 °C. Most interestingly, they exhibit difference in proton conductivity under hydrous condition. (*Chem. Commun.* 2012, **48**, 4998)

Finally chapter 7 will describe the conclusion of the overall work presented and the future direction of this thesis.

An extended Appendix describes crystallographic information of all the MOF crystals reported in this thesis.

Tanay Kundu

CONTENTS

CHAPTER 1

CHAPTER 2

CHAPTER 5

ANION INDUCED MORPHOLOGICAL IMPACT ON ZINC OXIDE BY THERMOLYSIS OF AMINO ACID DERIVED MOFS 112-128

CHAPTER 6

ALKALI EARTH METAL DERIVED MOFS FOR PROTON CONDUCTION 128-147

CHAPTER 7

List of Figures, Tables and Schemes

Figures

Table

CHAPTER 1

INTRODUCTION TO METAL ORGANIC FRAMEWORKS (MOFS)

1.1 Emergence of MOFs:

Porous materials have undergone a huge revolution in the last century. Before that, it is limited to amorphous carbon based adsorbants, which have been synthesized mostly by the pyrolysis of carbon-rich materials [1.1]. Later, Zeolites have emerged as porous crystalline materials with a variety of pore size [1.2]. They have been widely used for their usefulness in day to day chemical processes as well as industrial applications. However, limited pore size span encouraged researchers in the search of advanced materials with high degree of pore size tunability and crystallinity. Surfactant templating and coupling with organic moieties to form periodic mesoporous organosilicas (PMOs) solved the problem to some extent [1.3]. However, the realization of these structures requires high temperature processing route which is disadvantageous as discussed later in this chapter. Researchers attempted to combine the advantages of organic porous materials (lightweight, functional tunabilty etc.) with the virtues of the inorganic solids (thermal stability). At the end of the century, metal-organic frameworks (MOFs) emerged as a material which bridges these two aspects [1.4]. MOFs are hybrid porous crystalline materials, principally comprised of coordination bonds between metal nodes (individual ion or in a cluster form) and organic connectors (pyridyl, carboxylates, sulfonates, phosphonates etc.) possessing permanent pores or voids that are accessible for gases, solvents and any type of guest molecules [1.5].

Soon after its discovery, MOFs became the most promising candidate for adsorbent applications [1.6]. MOFs have much higher surface areas than the traditional porous materials such as Zeolites, porous carbon [1.7]. In addition, the advantages of crystallinity in MOF materials provide an unique opportunity to determine the high resolution crystal structure and accurate pore size/dimension of the MOF channel via X-ray crystallography. This advantage provides better insight into the structural parameters that facilitates the rational design of MOF based porous solids. Moreover, various functionalities of the organic linkers inside the MOF facilitate post-synthetic modifications. The porosity of the

MOFs has been utilized for traditional applications including gas adsorption and storage, gas separation etc. [1.8]. However, in recent years, focus has been broadened to other relevant applications such as solvent adsorption, proton conduction, redox catalysis, light harvesting etc. [1.9]. These applications are particularly appealing in terms of renewable energy research, which have drawn attention worldwide. In the following parts of this chapter, we will depict a brief section of synthesis, structural aspects, particularly that of the chiral MOFs, and a bit of their applications.

1.2. Synthesis of MOFs:

The synthesis of metal-organic frameworks (MOFs) has been of prime interest due to the possibility of obtaining unprecedented structures with novel topologies. Before the discovery of MOFs, researchers explored various topologies from new inorganic and organic extended structures like Zeolites and Periodic Mesoporous Organosilicas (PMOs). After the initial evolution of MOFs, researchers understood the innumerable possibilities of combining organic and inorganic entities in a reaction vessel and generating a myriad of structural libraries where the MOFs are screened for predicted and non-predicted topologies (Figure 1.1). In general, MOFs are synthesized via liquid phase combination method where the metal salt solution and the ligand solutions are mixed homogenously in a culture tube (made of hard glass or pyrex) or in a hydrothermal bomb (made of Teflon with stainless steel lining) and heated the assembly at higher temperatures (100-180 °C) for an extended period of time (48-72 h). The solvent is one of the most important factors of MOF formation reactions which determine the solubility criteria of the constituents and the thermodynamic control over the system [1.10]. This aspect is critical to assay the

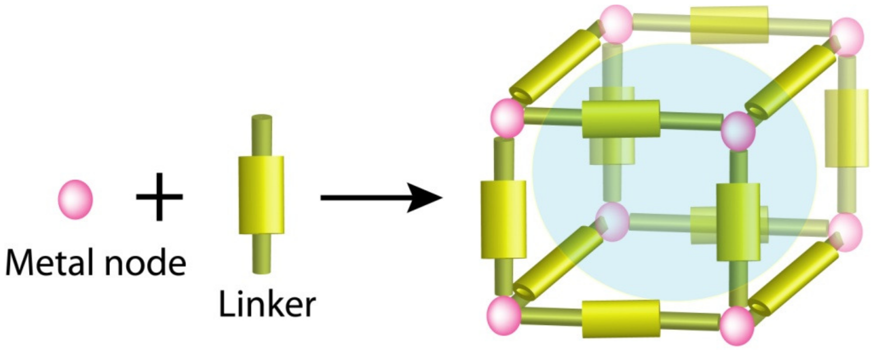

Figure 1.1: General scheme of synthesis for the preparation of MOFs.

crystallinity as well as the phase purity of the resulting MOF. High temperature solvothermal reactions mainly prefer high boiling solvents like DMF, DEF and NMP as it effectively solubilizes the ligand entity. Apart from that, aqueous medium in combination with suitable bases are also used for the abovementioned purpose. Temperature is another tipping point for MOF synthesis, which controls the thermodynamics to selectively crystallize one particular phase if other factors remain constant [1.11]. Time allowed for the reaction also allows kinetic control over the MOF formation [1.12]. A recent review highlights the different synthetic approaches to obtain the MOF structure [1.13]. The form of energy that is provided for the MOF formation mainly devide the various synthetic routes along with time, temperature and solvent which ultimately decide the preferable pathway to realize MOF architectures (Figure 1.4). For example, solvothermal processes rely on the thermal energy. In combination with the classical room temperature crystallization techniques (where dissolved metal salt and ligand solution are left to evaporate at ambient condition), microwave, electrochemical and sonochemical reactions have been used for production of MOFs. To enhance the screening rate and the scale up synthesis in solvothermal process, researchers have developed high-throughput methods for the production of MOF. Solid state reactions were also attempted for the synthesis of MOFs due to its simplicity, time efficiency and solvent free conditions. One of such example of solid phase reaction is the mechano-chemical aided synthesis where MOFs have been generated by mechanochemical force [1.14]. However, we must acknowledge that solvothermal process have been the primary source for the synthesis of three dimensional (3D) metal-organic frameworks (MOFs). This may be due to the opportunity of growing single crystals which is a necessary step for the structure determination of the MOFs.

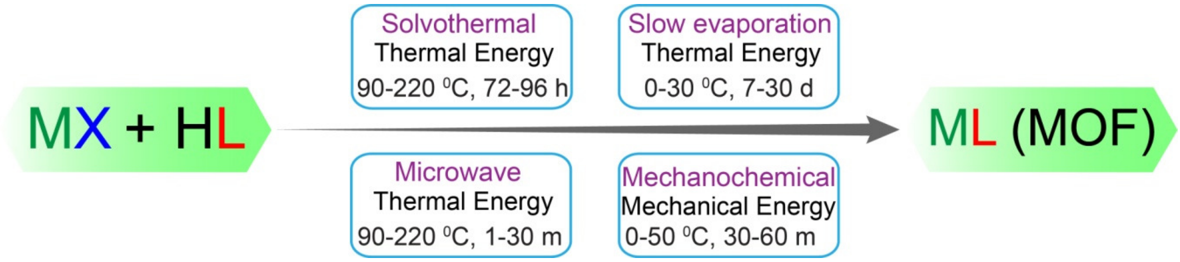

Figure 1.2: Scheme of various synthetic approaches and the conditions used for the preparation of MOFs.

1.3 Structure of MOFs:

Classical porous materials like activated carbons and porous polymers have no control over the structural integrity because the starting materials do not maintain their periodic arrangement in the long range [1.15]. On the other hand, Zeolites and PMOs have long range ordering but limited porosity [1.16]. However, MOF maintain periodic structural integrity in bulk phase owing to the rigid molecular joints made up from the ligand entity and metal ions or clusters. Thus, successful identification of the assembly between primary building blocks and secondary building units (SBUs) dictate the final topology of a framework (Figure 1.3). As a result, while considering the structure of MOFs, it is often necessary to be familiar with the the process of bringing two or more distinct SBUs together and recognize their underlying symmetry after MOF formation. In General, MOF

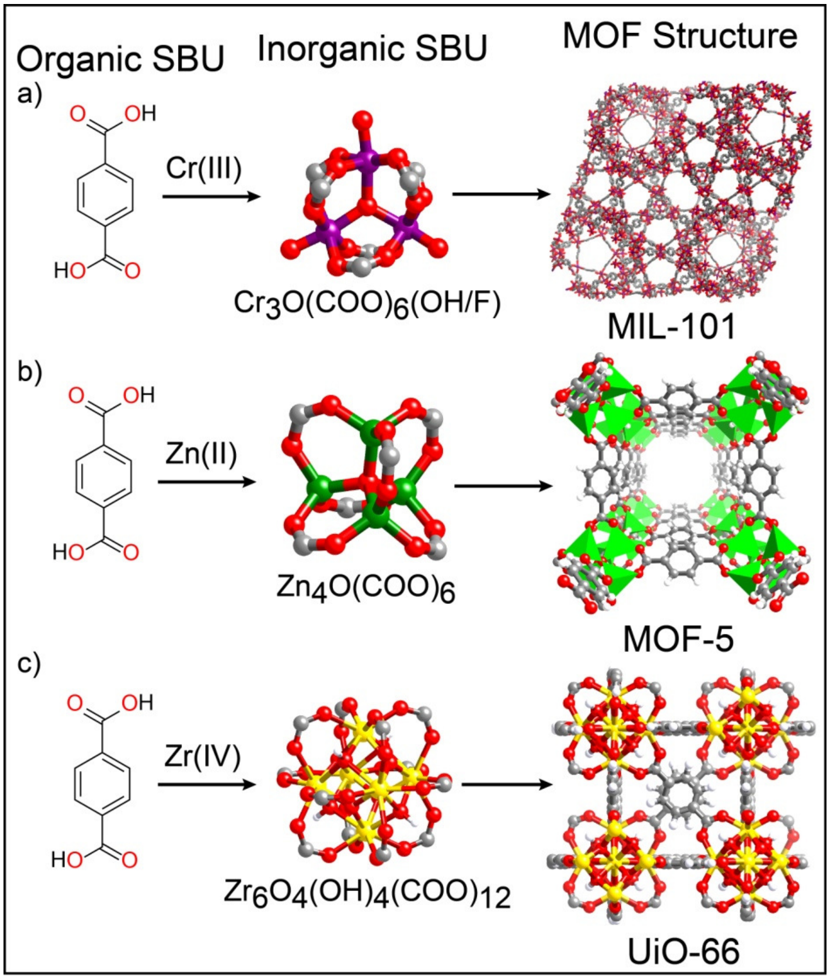

Figure 1.3: Assembly of various SBUs to form the MOF architecture.

synthesis involve reacting two types of primary building units. The first one is the multitopic organic spacer and the other one is polytopic metal centre or metal cluster. During the synthesis, two primary building units connects with each other to form secondary building units (SBUs) which finally results in higher dimension complex (1D, 2D and 3D) MOF architectures. All types of network structures of higher dimensions (i.e. organic, inorganic or organic-inorganic hybrid materials) possess inherent nets, and the interest of researchers lies in the successful understanding of the topological construction of MOF networks based on rational assembly of building units in different magnitude [1.17].

To simplify the aforementioned rationale we will discuss the structural aspects of one of the primitive MOF architectures i.e. MOF 5. The detailed investigation of the MOF 5 structure reveals tetrahedral Zn_4O SBU connected with organic linker terepthalic acid and extends over three dimensional cubic networks with interconnected pores of 8 Å apertures and 12 Å pore diameter [1.4]. In contrast, by changing the metal building block from Zn_4O to Cr_3O keeping terepthalic acid constant generate a totally different structure called MIL-101 which have different pore aperture and diameter (~3 nm) compared to MOF 5 [1.18]. A Further complicated building block made of Zr (Zr_6O_4) which combines with the same linker to yield UiO-66 MOF, with different architecture and pore size and shape than both MOF 5 and MIL-101 [1.19].

1.4 Chiral MOFs:

1.4.1 Introduction to chiral MOFs:

Chirality is inherent in living beings in the form of amino acids, peptides, proteins, hormones and DNAs [1.20]. Even different ion channels prefer chiral architecture [1.21]. Although natural chiral molecules are abundant, synthetic or artificial chirality has its own importance from industrial perspectives. Chirality has become an intriguing part in many fields such as agriculture, pharmaceutical industry, chemical plants and clinical analysis [1.22]. In many cases, enantiomers of the same substance have been proved to behave differently in the physiology (being markers of different diseases and inactive substrate) or the environment. For example, if one enantiomer of a drug is therapeutic, the other may be toxic [1.23]. Therefore, enantiomerically pure drugs are a mandatory for their use in the body. As a result, the production and availability of enantiomerically pure drugs are one of the great significance in the chemical and pharmaceutical industries. Currently available methods to provide enantiopure chemical products are the following: a) resolution of racemic mixtures, b) isolation from natural resources and c) asymmetric catalysis with resolution. In particular, chirality has a very crucial role in determining enantioselectivity in chiral recognition or separation and catalysis.

In past decades, huge research efforts have been devoted to the development of chiral Zeolites. On this line, there has been success in the synthesis of Zeolites with pores larger than 13 Å. However, researchers frequently failed to obtain chiral Zeolites in enantiopure form till date. No wonder, Zeolite β and titanosilicate ETS-10 are the only two types of Zeolitic structures that have chiral forms [1.24]. Zeolite β possess a three-dimensional architecture which crystallizes in chiral polymorph, in either a left or right handed form. However, it is extremely difficult to obtain Zeolite β and ETS-10 in enantiopure form. The Zeolite VFI is a typical example of chiral Zeolite, which has cylindrical pore structure and a helical water channel along crystallographic *c* axis [1.25]. The water chains form a complex triple helicate structure inside the pore via hydrogen bonding with the neighbouring water molecules (Figure 1.4). The realization of enantiopure Zeolites is difficult in the sense that they are typically synthesized in presence of chiral surfactant templates, which are removed

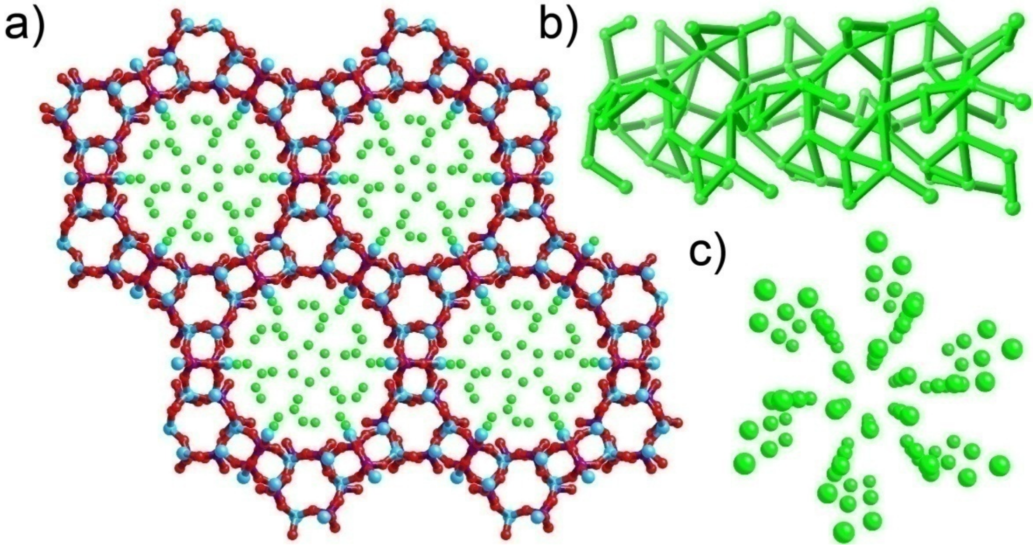

Figure 1.4: a) Example of a chiral Zeolite, VFI having cylindrical channel filled with water molecules. b) Complex helical hydrogen bonding between the water molecules within the channel. c) Perspective view of the water molecules viewed from crystallographic *c* axis. Color code: Silicon sky blue, coordinated Oxygen red, solvent Oxygen green.

after formation via calcinations at 400-550 °C [1.26]. Thus, synthesis of chiral Zeolites is totally depending on the ability of the chiral surfactants to assemble the Zeolite precursors into its chiral forms. However, calcinations at high temperatures disrupt the chiral arrangements which most of the cases result in either achiral or racemic mixtures of the Zeotypes. As a result, completely new strategies are required to synthesize chiral Zeolitic materials for industrially relevant applications.

The abovementioned rationale explains that although Zeolites have been widely used for the production of many industrial chemicals and domestic products, its applications in enantioselective separations and catalysis have been rarely observed. In comparison, MOFs are mostly synthesized under mild conditions (100-180 °C), which allow simplistic assembly in homochiral MOFs by judicious choice of the chiral ligands. In practical, these homochiral MOFs possess chiral functionalities that should be accessible through the pore cavity. Such ordered chiral functionalities can be a boon towards realizing heterogeneous asymmetric catalysts, which can combine both the advantages of homogeneous catalysts (homogeneity of active sites, high solubility and effectiveness, reproducibility, controllability and mild reaction conditions) and heterogeneous catalysts (easy catalyst separation and recovery via filtration, size selectivity and high thermal stability). Thus, homochiral MOFs with chiral open channels can be envisaged for applications in enantioselective uptake and separations. In this way, rational design of homochiral MOFs can overcome the limitations of Zeolitic materials into the chiroselective processes.

1.4.2 Literature examples of chiral MOFs:

Till date three distinct strategies have been used for designing and synthesizing homochiral MOFs for enantioselective reactions;

a) Chiral MOF from achiral building blocks

b) Chiral MOF from ancillary chiral building blocks

c) Chiral MOF from totally chiral building blocks

As a special class and relevant to this thesis, we will also focus on d) amino acid derived MOFs, which comprises both the second and third strategy. Another strategy involving e) post synthetic modification of an achiral MOF with chiral substrate is out of scope of the current discussion.

1.4.2.1 Chiral MOF from achiral building blocks:

In the first strategy, homochiral MOFs are synthesized from entirely achiral constituents. In this process, resolution of chirality has been evolved during crystal growth phenomena. The greatest advantage of this approach lies in absence of initial chiral components, which is often expensive. However, almost all of these MOFs are racemic as the bulk MOFs comprises both enantiomorphs. The first example of such homochiral MOF is the Cd(apd)$(NO_3)_2H_2O$.EtOH which is synthesized by combining achiral Cd(II) centers and 5-(9-anthracenyl)pyrimidine (apd) bridging ligand [1.27]. The MOF crystallizes in the chiral space group $P2_1$. The chirality is generated from the pyrimidine-Cd(II) helical arrangements (Figure 1.5). The MOF crystals were observed to grow from the first nucleus, which suggests the case of seed mediated growth of the homochiral MOF in the bulk phase. Solid-state circular dichroism spectroscopy confirms the seed-mediated synthesis of the homochiral MOF from totally achiral components. It is to be noted that the handedness of the MOF crystals cannot be predicted a priori. As a result, although simple and cost effective, this method has major drawbacks in practical purposes from enantiomeric purity point of view.

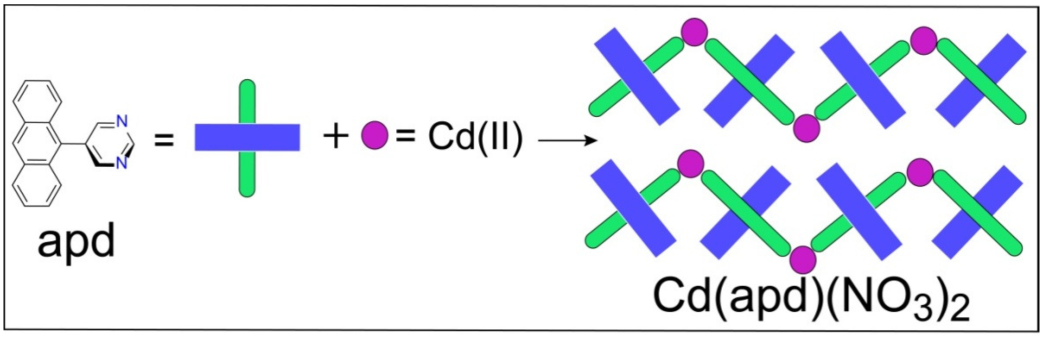

Figure 1.5: Example of a chiral MOF synthesis from achiral linker.

1.4.2.2 Chiral MOF from ancillary chiral building blocks:

In the following approach, homochiral MOFs are synthesized from an achiral linker, in combination of an ancillary chiral building block. In this method, most of the cases the chiral building block bridges metal nodes in a neutral manner where the achiral component balances the charge and add to the dimensionality of the frameworks. One of the representative examples of this kind is a salen based homochiral MOF, which has been synthesized using the following strategy [1.28]. The chiral MOF was constructed using metallosalen ligand (L_1), biphenyl-4,4'-dicarboxylic acid (H_2bpdc), and Zn(II) as metal node (Figure 1.6a). The bpdc linker form a paddlewheel building block with Zn(II) whereas the metallosalen acts as struts. The framework $[Zn_2(bpdc)_2L_1](10DMF)(8H_2O)$ was synthesized by solvothermal method, and shows a twofold interpenetrating structure with 3D network (Figure 1.6b). The channel dimensions along the crystallographic *a* and *c* axis are 6.2 × 6.2 Å and 6.2 × 15.7 Å, respectively. All the Mn(III) active sites are directed towards the channels and thus accessible to the guest molecules. The framework was investigated for asymmetric olefin epoxidation reactions, which efficiently catalyzed 2,2-dimethyl-2H-chromene to the desired epoxidated product in 71% yield and excellent chiral selectivity of 82% ee (Figure 1.6c). Interestingly, the MOF has a higher activity than its homogeneous analogue, with slightly lower enantioselectivity. Moreover, it maintained the activity throughout a three hour reaction time where related homogeneous epoxidation catalysts are highly active only for few minutes. In Addition, it was recycled and reused upto three times, with a slight decrease in activity and no further loss in enantioselectivity.

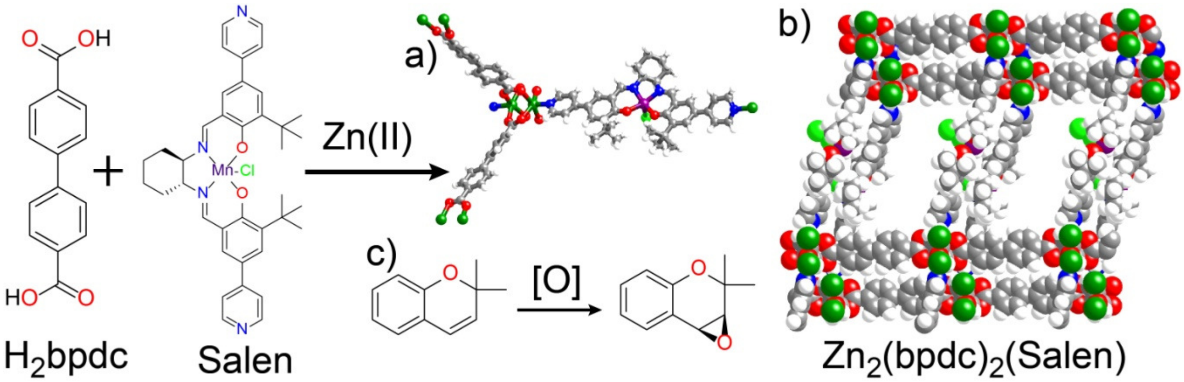

Figure 1.6: Example of a chiral MOF synthesized from achiral biphenyldicarboxylate and ancillary metallosalen linker. a) Asymmetric unit of the MOF structure. b) 3D interpenetrated spacefill model of the structure that exhibit porosity along *c* axis. c) Asymmetric olefin epoxidation reactions using the MOF.

In 2006, the catalytic separation applications of a homochiral porous MOF for enantioselective adsorption and oxidation of thioethers have been explored [1.29]. The homochiral porous material [Zn_2(bdc)(L-lac)(DMF)]·(DMF) was prepared by heating a mixture of $Zn(NO_3)_2$, Terephthalic acid (H_2bdc) as primary linker and L-lactic acid (lac) as an auxiliary building block in DMF at 110 °C for 2 days. The zinc ions bridged by lactate anions form parallel chiral 1D chains along the crystallographic *a* axis. These chains are interconnected by terephthalate spacers to give a 3D porous structure, with pore dimensions of 5 × 5 Å (Figure 1.7a). The chiral centers of the L-lactate functionalities are poked towards the channels. The evacuated MOF was stirred in a CH_2Cl_2 solution containing a racemic mixture of small sulfoxides with smaller substituents for ~ 16 h, which showed excellent sorption ability. The ee values for the occluded sulfoxides were ~ 27%, with the S enantiomer in preference in both cases. However, inclusion of sulfoxides with larger substituents could not be achieved in significant amount due to pore size constraints. Such size and enantioselectivity in guest uptake indicates that the MOF has a robust structure with uniform chiral pore size, which could be readily regenerated and reused in the successive cycles without considerable loss of sorption capacity. In addition, the MOF can also used for high size and chemoselective catalytic oxidation of thioethers to sulfoxides by either urea hydroperoxide (UHP) or H_2O_2, signifying that the reaction primarily occurs inside the pores within the MOFs (Figure 1.7b). Although chemoselectivity toward the sulfoxides was good to end of the column, both (R)- and (S)-sulfoxides could be isolated with relatively high yields because the sulfide (PhSMe) comes out from the column before PhSOMe. This work firstly recognized the use of MOFs as chiral stationary phases for preparative liquid phase chromatography.

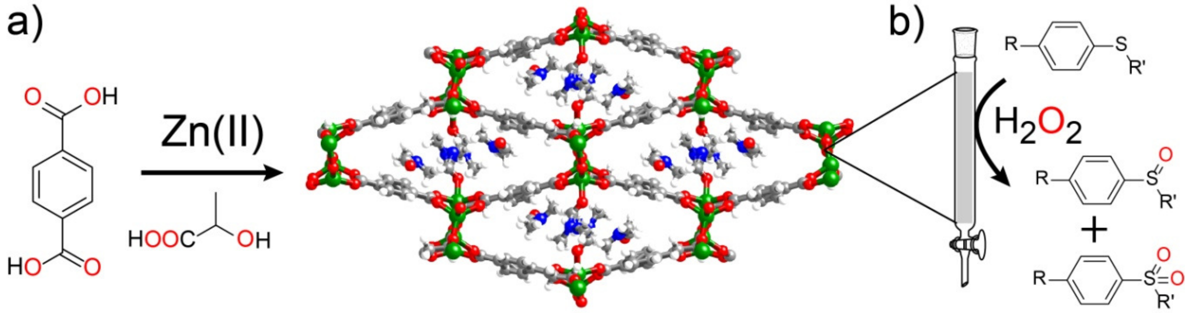

Figure 1.7: a) Example of a chiral MOF synthesized from achiral terephthalate and chiral lactate ancillary ligand. b) Thioether oxidation reaction using MOF column.

The advantage of this method is that it combines both the chiral and achiral building blocks, which effectively minimizes the cost of using pure enantiomeric spacer. However, one major drawback is that the position and the exposure of the active sites cannot be predicted in all cases and thus sans warranty for their activity in catalytic and enantioselective recognition processes.

1.4.2.3 Chiral MOF from totally chiral building blocks:

This strategy involves synthesis of homochiral MOFs from entirely enantiopure chiral linkers. The spacers self organize surrounding the metal centre to build the homochiral framework. One of the primitive example of such case is the homochiral MOF reported in 2000, where the first example of asymmetric catalysis has been documented [1.30]. In this account, a chiral porous MOF $[Zn_3O(L_1)](2H_3O)(12H_2O)$(D-POST-1) was synthesized by a solvothermal reaction between $Zn(NO_3)_2$ and chiral ligand L_1 which is readily derived from the enantiopure D-tartaric acid (Figure 1.8). The oxo-bridged trinuclear zinc unit is connected by six carboxylate groups to form a SBU, which is further extended through coordination via zinc ions and pyridyl functionalities to result in large chiral 1D channels of the dimension of c.a. 13 Å through the crystallographic *c* axis. Interestingly, each trinuclear zinc cluster surrounds six pyridyl groups, three of which are coordinated, and two are

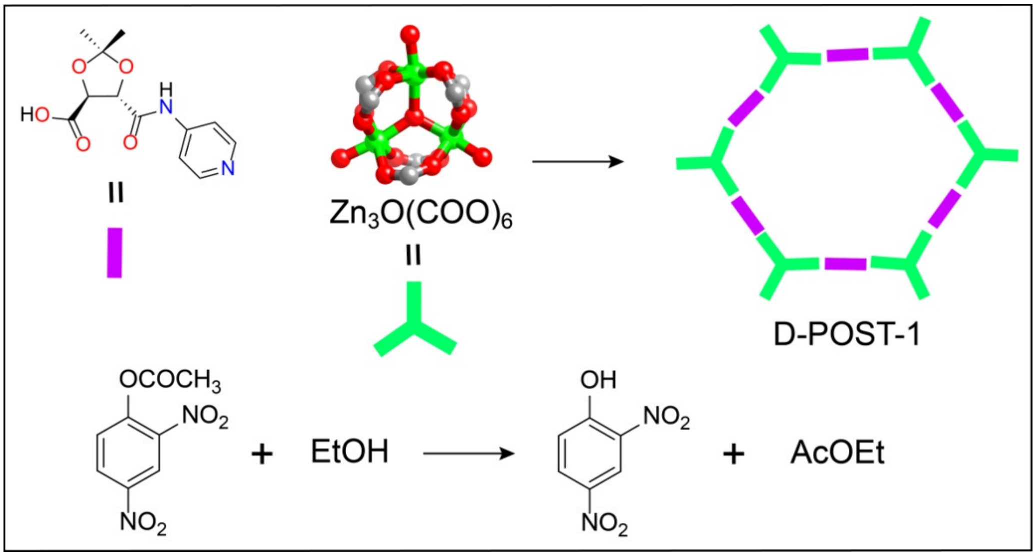

Figure 1.8: Example of a chiral MOF consisting entirely chiral linker and trinuclear Zn node. It exhibit moderate enantioselectivity towards transesterification reaction.

protonated. These remaining exposed pyridine groups showed moderate catalytic activity in the transesterification reaction of esters. For example, when a racemic alcohol 1-phenyl-2-propanol was used, the ester shows a modest enantiomeric excess (ee ~ 8%) in favor of the S-enantiomer. Although the figure is not prominent, this example opens up the possibilities of using MOFs as a catalyst for enantioselective reactions.

Later in 2004, a series of chiral BINOL based tetracarboxylic acid ligands (Figure 1.9a) have been synthesized with orthogonal dihydroxy functional groups [1.31]. Combining the tetracarboxylate groups of the linkers with carboxylate-bridged di-copper paddlewheel SBUs resulted in a series of 4,4-connected isoreticular CMOFs (Figure 1.9b). All the above

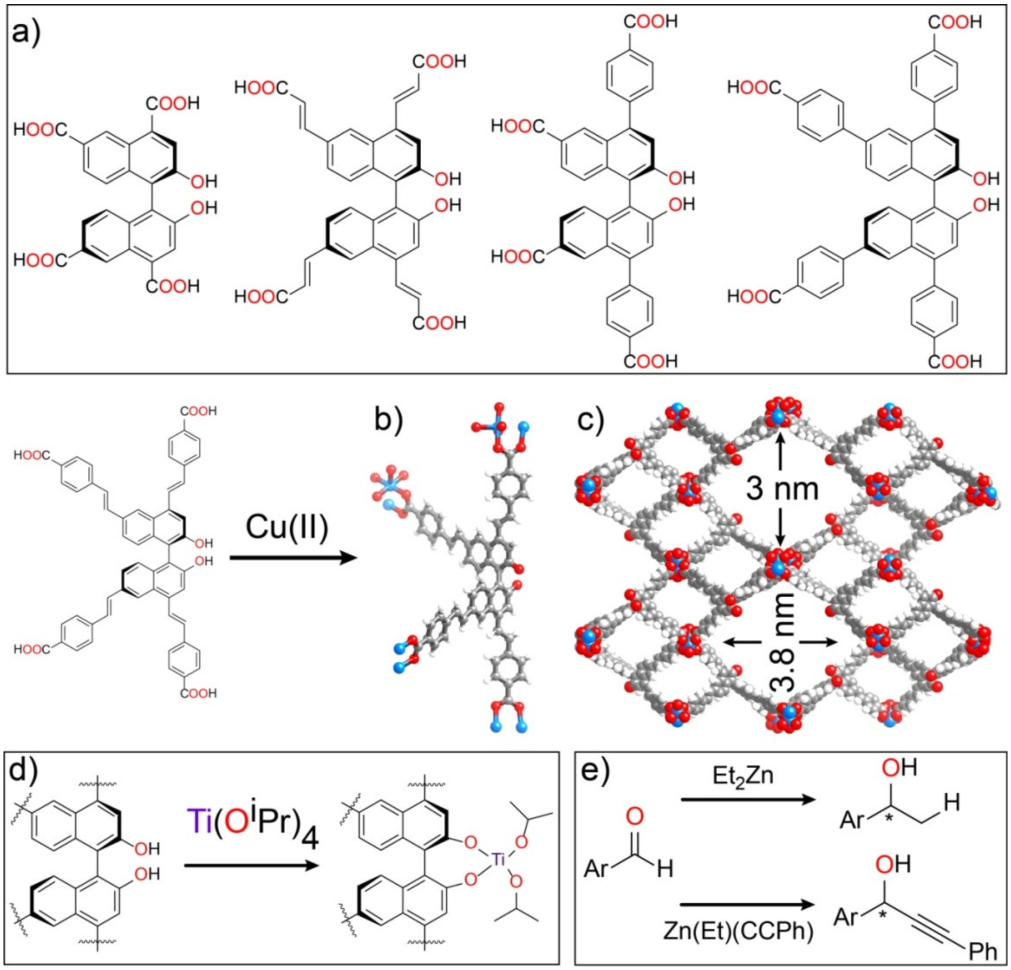

Figure 1.9: a) Some instances of chiral BINOL linkers used for preparing chiral MOFs (CMOFs). b) Asymmetric unit of one of the CMOFs. c) 3D packing spacefill model of the CMOF along *a* axis. d) Post-synthetic modification of the catalytic sites by Ti(O^{i}Pr)$_4$. e) Asymmetric reduction of substituted benzaldehydes by the CMOF catalyst.

CMOFs are isostructural and have a 3D non-interpenetrating crystal structure of the same chiral space group $I4_122$. Due to the elongated nature of the tetracarboxylate linkers, the resulting non-interpenetrating frameworks have large open channels which prevail in all the three axes of the crystals (Figure 1.9c). The homochiral MOFs acts as a tunable platform to produce heterogeneous asymmetric catalysts through post-synthetic modification with excess $Ti(O^iPr)_4$ (Figure 1.9d). This led to the formation of an active catalysts for the addition of diethylzinc to a variety of aromatic aldehydes with near quantitative conversions (~ 99%), high selectivity for secondary alcohols (~ 92%), and high ee (~ 91%) (Figure 1.9e). The tunable structures of the MOFs allow differential substrate and product diffusion and thus the dependence of the ee's on the pore sizes.

In 2008, semiflexible pyridyl-functionalized salen-based ligand that forms cyclic clusters with enzyme-like chiral pores was introduced as a promising candidate for applications in enantioselective separation of chemicals [1.32]. When a mixture of the L_1 [6,6'-cyclohexane-1,2-diylbis(azanylylidene))bis(methanylylidene))bis(2-(tert-butyl)-4-(pyridin-4-yl)phenol] and $Zn(NO_3)_2{\cdot}6H_2O$ was heated in a solvent mixture of DMF-CH_3CN or DMF-THF it led to the formation of two crystalline materials $[Zn_4(L_1)_4]{\cdot}4CH_3CN$ and $[Zn_6(L_1)_6]{\cdot}6THF$, respectively. Both compounds have an unsaturated zinc site and two semiflexible pyridyl groups extend the framework to form a cyclic ring. Each of these rings contains six such units of metallosalen linkers. The rings form a chiral cavity with CH_3CN

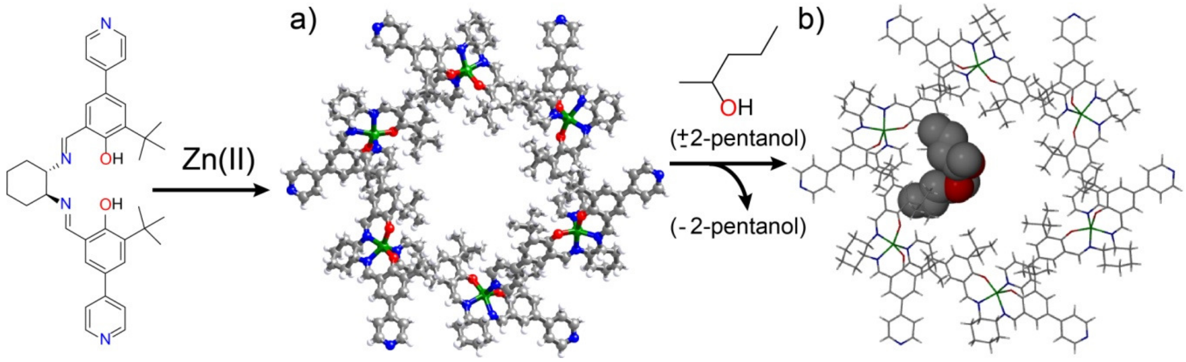

Figure 1.10: Example of pyridyl-functionalized salen linker for chiral MOF synthesis. a) Packing view of the MOF along crystallographic *c* axis. b) Chiral separation reaction performed with racemic alcohol affords single crystal evidence of the occluded R isomer.

or THF molecules as solvents. The six pairs of the tert-butyl groups of the metallosalen units are oriented towards the pore to generate six hydrophobic cavities. Noncovalent interactions (mainly intermolecular $\pi\ldots\pi$ and CH…π interactions) led to a porous 3D nanotubular structure with a pore opening of 1.4 × 1.0 nm (Figure 1.10a). Single-crystal XRD and PXRD confirms that both the materials undergo reversible single-crystal to single-crystal structural transformations upon guest reversible removal (Figure 1.10b). The permanent porosity was measured by its N_2 adsorption isotherm (Langmuir surface area of 504 m^2g^{-1} and a pore volume of 0.48 mLg^{-1}). The chiral resolution of 2-butanol was achieved by immersing the evacuated material in racemic alcohols in a vial at 40 °C for 2-3 days. Chiral GC analysis proved ee value of 99.8% in preference of the (R) isomer. Similar enantioselective inclusion was observed for racemic 3-methyl-2-butanol. However, longer alcohols e.g. 2-pentanol cannot be resolved as the pore cavity is smaller than the guest dimensions.

The advantage of this strategy is the uniform distribution of the homochiral sites, which increases both the catalytic and separation processes many fold than any of the previous approaches. However, high cost of the building blocks is one typical barrier for this process.

1.4.2.4 Amino acid derived MOFs:

Amino acids are one of the first molecules that appear on earth even before the evolution of first life. Its chiral environment translated into various forms of building blocks like peptides, proteins, and hormones which control the basic processes of our body. Undoubtedly, amino acids are one of the most abundant and the cheapest chiral source in Nature. Hence, several attempts have been driven to design amino acid based materials for synthetic polymers and biomaterials [1.33]. In this regard, synthesis of amino acid based MOFs should be one fascinating structure having low synthetic cost with diverse functionalities comprising chirality and porosity. These aspects will have definite impact on chiral recognition and enantioselective catalysis applications. However, in practical most of the amino acid based MOF structures are either 0D complexes or 1D chains due to the high chelating ability of the amino acids (as found in metalloenzymes) [1.34]. In this section, we will give a brief overview on some of the structures and the strategies applied to increase the dimensionality of the MOF architectures.

In 2006, a series of porous homochiral MOFs have been reported based on amino acid backbone for the separation of racemic alcohols [1.35]. The MOF $[Ni_2(L\text{-}asp)_2(bipy)]\cdot xCH_3OH\cdot yH_2O$ was synthesized by solvothermal reaction between $Ni(asp)\cdot 3H_2O$ (a 1D coordination chain) and 4,4'-bipyridine (bipy) in a water/methanol mixture at 150 °C. The neutral chiral Ni(L-asp) layers are connected via 4,4'-bipyridine linkers to form a pillared framework with 1D channels having dimension of ~ 3.8 × 4.7 Å, with ~ 23% solvent-accessible space. This approach could be a modified version of the second strategy, where the bipy act as a primary building block and framework extender and the asp behave as an ancillary linker and balances the charge. Moreover, the replacement of 4,4'-bipyridine with longer bridging ligands afford analogous MOFs with larger channel dimensions. The permanent porosity is verified by CO_2 adsorption isotherm (BET surface area of 247(3) m^2g^{-1}). The enantioselective adsorption of guests was investigated by a library of chiral

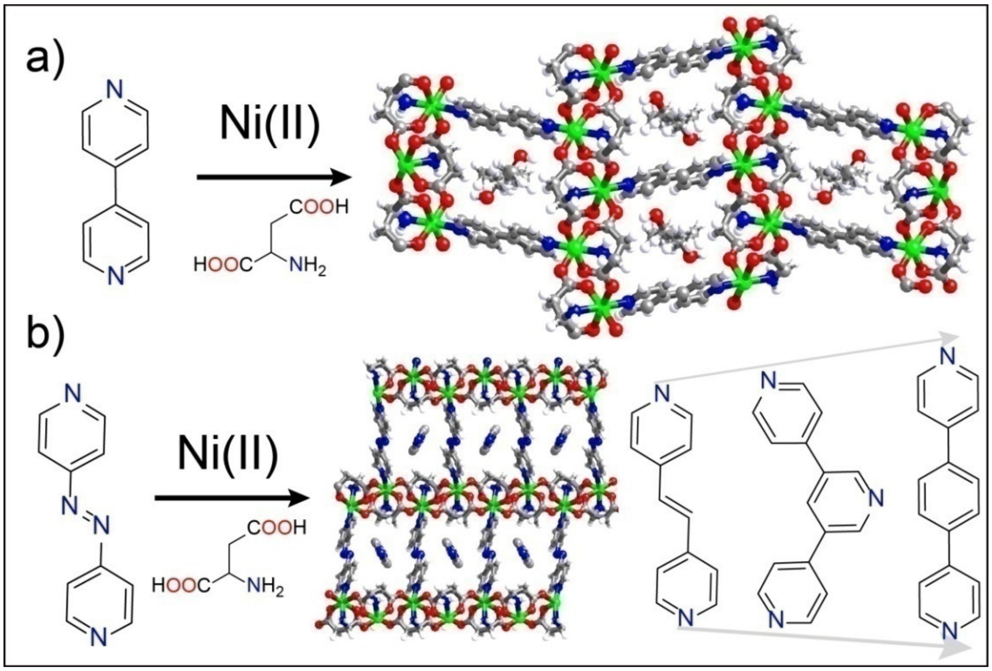

Figure 1.11: a) Chiral MOF synthesis scheme using bipy as struts and aspertate as ancillary linker. The 1,2-propanediol occupy the pore cavity. b) The higher bipy analogues resulted in pore space occlusion by uncoordinated spacers.

small molecules. For a preset chain length of four carbon atoms, 1,3-butanediol showed significantly greater enantioselective uptake compared to 1,2-butanediol and 2,3-butanediol. The preferential uptake of the 1,3-substituted diol units was further corroborated by the high ee value of 2,4-pentanediol, with reference to the 1,2-pentanediol and 2,5-hexanediol. The highest ee value observed for the diol guests was 53.7% for 2-methyl-2,4-pentanediol. The details of the interactions between a diol guest and the internal porous surface are disclosed by the crystal structure of $[Ni_2(asp)_2(bipy)]\cdot$1,2-propanediol (Figure 1.11a), where the diol is located within the pocket made by two neighboring 4,4'-bipyridine molecules and the diol groups are hydrogen bonded with the oxygen atoms of the carboxylate moieties of the Ni(asp) layers. As a result, it is evident that besides good match between the size and shape of the MOF pores and the guest molecules, the channel surface also plays a significant role in chiral recognition and separation processes. However, further attempt to increase the pore size by increasing the length of the bipy spacer (Figure 1.11b) was mostly unsuccessful as the noncoordinated spacers occupy the pore spaces of the resulting MOFs [1.36].

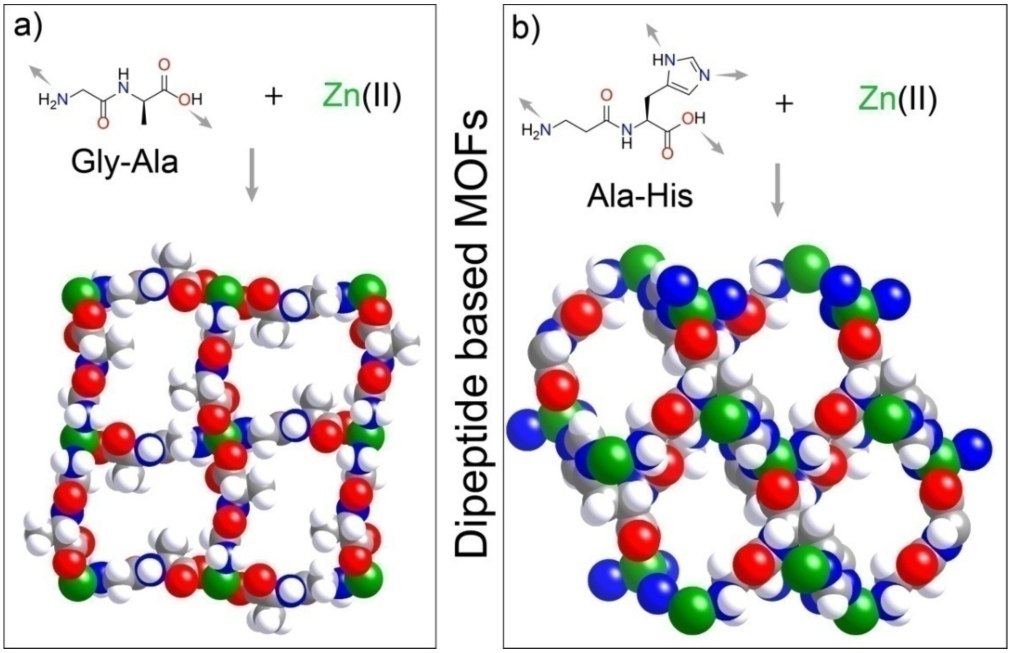

Figure 1.12: Example of chiral MOF synthesis by dipeptide spacers. a) Gly-Ala peptide resulted in MOF with square-grid pore. b) Ala-His peptide have higher connectivity and form elliptical pore.

Further, dipeptide based linkers are also utilized to achieve chiral MOFs. They are endowed with porosity as well as flexibility by the help of rotatable peptide bonds. In this regard, Gly-Ala peptide was reacted with Zn(II) ion in slightly basic methanol-water mixture to afford the Zn(Gly-Ala)$_2$ MOF with 2D layered structure [1.37]. Similar kind of structure with greater connectivity has been achieved for Zn(Ala-His)$_2$ MOF by incorporating histidinyl moieties within the backbone [1.38]. The interesting aspect for the MOFs are their CO_2 adsorption isotherms, which exhibited gate-opening behavior at a pressure above 2 bar, and additional step adsorption at higher pressure which also prevail in the desorption hysteresis. Combined experiments and simulations signified that the torsion and displacement of the peptide linkers, in addition to the change in pore alignment is responsible for these uncommon phenomena.

In 2009, the naturally available chiral amino acid L-serine was functionalized with methylpyridine substituent (by reductive Schiff-Base addition with pyridine 4-carboxaldehyde) to afford the chiral linker (S)-3-hydroxy-2-(pyridin-4-ylmethylamino)-propanoic acid (HL$_2$). The reaction of HL$_2$ with $CuCl_2$ in a water and ethanol mixture forms the homochiral solid Cu(L$_2$)Cl (Figure 1.13), which is 1D in nature and it is better to term it as coordination polymer than MOF [1.39]. There are two distinct Cu(II) atoms present in the framework. Each Copper atom is coordinated by a carboxylate group of the linker, an amino group and a hydroxy group of the serine moiety and by one pyridyl group from

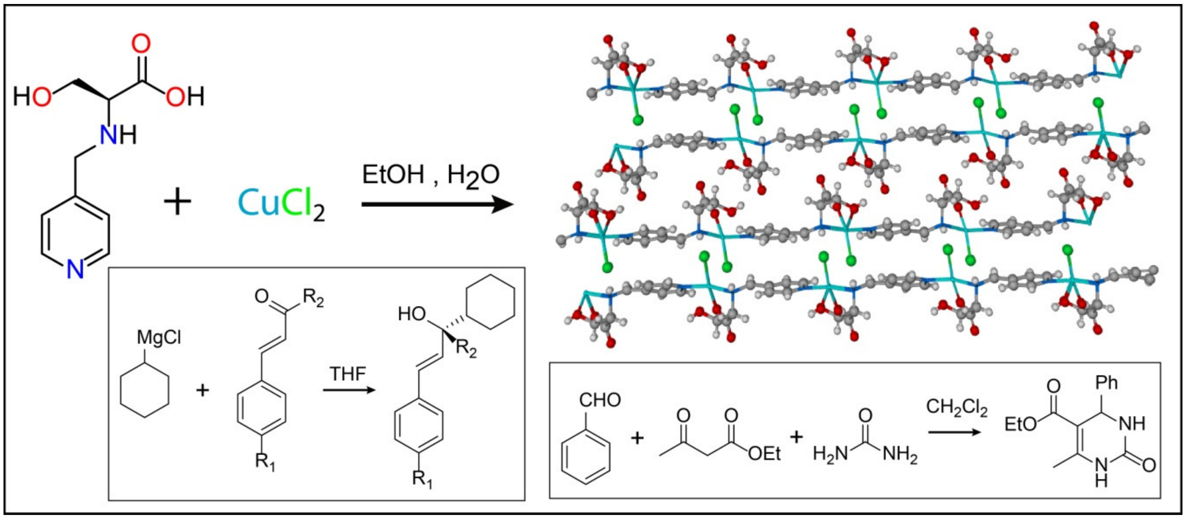

Figure 1.13: Chiral MOF synthesis from pyridyl functionalized serine linker and its catalytic activity for Biginelli reaction and α,β-unsaturated aldehyde addition reaction.

another linker. A striking feature of this coordination geometry is that the nitrogen atom of the amino group is chirally induced by the neighboring chiral carbon atom. Moreover, one copper atom is coordinated by one chlorine atom and another copper atom is coordinated by two chlorine atoms to balance the overall charge, resulting in a distorted square pyramidal and octahedral geometry along the copper unit, respectively. The 1D chains of the framework run along two different directions. These chains are held by supramolecular interactions forming a framework structure which contains one-dimensional channels with a pore size of 5.1 × 2.9 Å. Unfortunately, these channels are too small for substrate inclusion. The framework was examined for catalysis of the Biginelli reaction of benzaldehyde, urea and ethyl acetoacetate to provide dihydro-pyrimidinone. The product was isolated in ~ 90% yield without any enantioselectivity. Another test reactions of the addition of cyclohexylmagnesium chloride to various α,β-unsaturated aldehydes suggests that the reaction is assisted by the outer crystallite surface of the framework, rather than the inside channels which are too small for guest accommodation. Undoubtedly, there is an urgent need to develop amino acid based MOF with higher dimensions and pore sizes for any practical application, which is the main point addressed in this thesis.

In 2011 eight 3D MOF architectures based on 2:1 cocrystal of pure amino acid proline and Li salts were reported [1.40]. The MOFs was synthesized in water by reacting Proline with

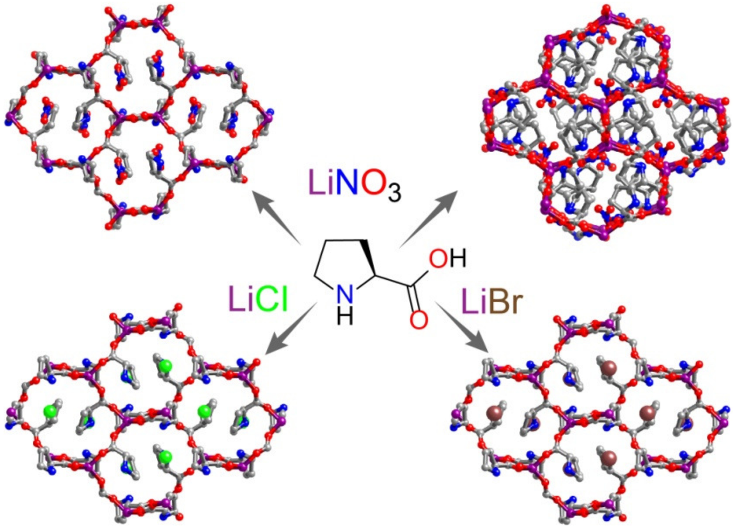

Figure 1.14: Example of a chiral MOF using Li(I) as metal source and Proline as linker.

different Li(I) salts (LiCl, LiBr, $LiNO_3$ etc.). The carboxylate groups coordinate with the Li(I) in a bridging fashion while the proline backbones remain uncoordinated. Although the resulting structures feature high dimensionality, water stability, structural diversity with interesting *dia* and *lon* topology, in all cases the proline and the non-coordinated anions (e.g. Chloride, Bromide, Nitrate) occupy the pore cavity. As a result, all the chiral MOFs are non-porous in nature and thus unsuitable for use in industrially relevant purposes.

1.5 Water stable MOFs:

The design and synthesis of moisture and water stable porous materials are crucial for their development in industrial applications e.g. gas sorption and separation, sensing, catalysis, and ion conduction. However, despite the large interest on MOFs encouraged by the high surface area and tunable pore size, full or partial degradation of them in the open atmosphere has drastically limited their competences for industrial relevance. On the one hand, solubility of MOFs in biological medium is vital for their *in vivo* applications such as drug delivery [1.41]. On the other hand, understanding of the degradation mechanisms/pathways is important for the future design of porous MOFs with appreciable water stability for industrial applications. This section will deal with the strategies to control over water stability and adsorption property in MOFs. The following discussions are largely adapted from a recent review highlighting the necessary aspects on the aforementioned notes [1.42].

Water adsorption behavior is vital for many microporous solids, and of prime importance in MOFs. For example, the water adsorption properties of molecular sieves in chromatography columns are dependent on their temperature. Although Zeolites are typically hydrophilic, hydrophobic Zeolites have particular importance for environmental applications [1.43]. Water uptake property is crucial for CO_2 capture of hydrophilic materials as water acts as a competing binder. For instance, a controlled amount of water adsorption can promote CO_2 uptake capacity in MOFs particularly in MIL-101 (Al/Cr-terephthalate), HKUST-1 (Cu-trimesate), and MIL-53 (Al/Cr-terephthalate) [1.44]. Although several applications can be envisaged for water adsorption in MOFs, few are timely relevant e.g. water purification, dehumidification, thermal batteries, heat-pumps, chillers and proton conduction [1.45]. Astonishingly, till date the structure (such as effects of pore size, pore morphology, and flexibility) and water adsorption relationship has not been studied in a systematic manner for MOFs. However, water adsorption-desorption isotherms was discretely performed on a series of MOFs with diverse structure and property. This contains a broad variety of behaviors ranging from hydrophobic ZIF-8 (Zn-methylimidazolate) to hydrophilic MIL-101. Herein, based on the water stability, MOFs can be broadly divided in 3 major sections. They are the following:

1.5.1 MOFs stable in water vapor:

The stability of a series MOFs with different organic ligands, pore apertures, metal node and coordination numbers were determined in combination with molecular modelling and experimental screening relied on X-ray diffraction (PXRD) studies [1.46]. The conclusion was that the metal-ligand bond strength is the key criterion for water-stability of the MOFs, which is more important than the metal coordination geometry or valency. The most stable MOFs emerged as MIL-101, MOF-74 and ZIF-8. More recently, Zr-MOFs e.g. UiO-66 (Zr-terephthalate) were found to be tremendously stable in water, while isostructural UiO-67 (Zr-biphenyldicarboxylate), MOF-805 and MOF-806 (Zr-bipyridinedicarboxylate) are unstable in humid condition due to the induced torsional strain inside the crystal leading to structural collapse. Similar adsorption isotherms indicate that Al-MIL-100 (Al-terephthalate) and Ni/Mg-MOF-74 (Ni/Mg-2,5-dioxidoterephthalate) MOFs are unstable leading to partial or full collapse of the framework dependent on exposure time.

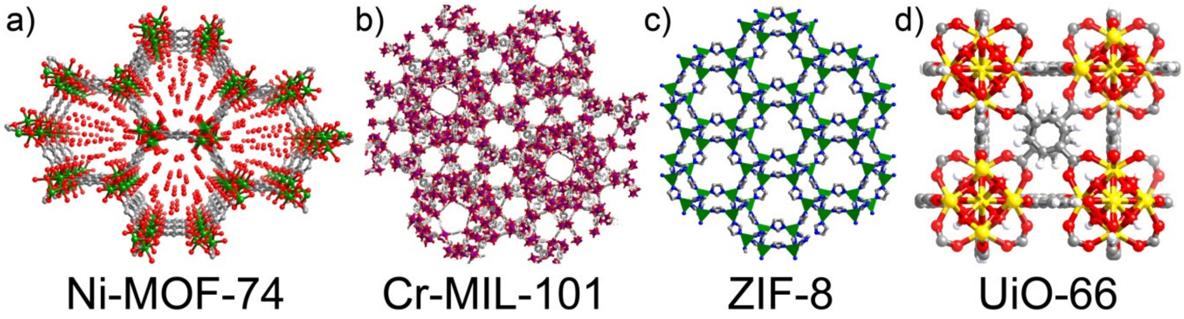

Figure 1.15: Example of MOFs used for water stability and adsorption study.

1.5.2 MOFs stable in liquid water:

The stability of various MOFs were investigated by immersing them in pure water or in wet dimethylformamide (DMF) with different H_2O : DMF ratio on a timescale ranged from hours to months and measuring patterns PXRD before and after exposure at ambient conditions [1.47]. Three well known MOFs viz. MOF 5, MOF 177 and UMCM 150 were found to be unstable in H_2O : DMF combinations with ratios greater than 1 : 4. In contrast, copper paddlewheel MOFs such as HKUST-1 were found to be stable for months in H_2O : DMF = 5 : 1, but starts to decompose in contact with pure water after 24 hours. On the other hand, the Cr-MIL-100 and ZIF-8 were stable in pure water for months and in boiling water for 24 hours. Finally, Al-MIL-53 (Al-terephthalate) undergoes degradation in boiling water to form gamma alumina (γ-Al_2O_3) under these conditions.

1.5.3 Stability in aqueous acid/base:

Most of the MOFs created from carboxylates or imidazolates linkers dissolve in acidic environment due to the protonation, such as aqueous HCl or HF solution which is common in case of silica based materials. However, a class of Zr-MOFs e.g. Zr-porphyrin PCN-222, 224, and 225 retain its crystalline architecture under extreme acidic conditions in aqueous media [1.48]. MOF stability in strong alkaline solutions has been evaluated for a few materials. In an early report of the PXRD patterns of ZIF-8 showed to remain unchanged after 24 hours in 8 M aqueous NaOH solution at 100 °C, which is superior to MCM and SBA mesoporous silicas [1.49]. On the other hand, MOFs which are designed for medical applications were studied in pH ~ 7.4 i.e. simulated physiological media. The stability of a series of seven carboxylate-based MOFs was assayed in a phosphate buffer solution at pH ~ 7.4 and 37 °C. The stability order is as follows: Fe-MIL-100 > Fe-MIL-53 > UiO-66-NH_2 > Fe-MIL-53-Br > UiO-66 > UiO-66-Br which is directly related to the donor effect of the ligand substituent as the most electron-rich linker bearing MOFs is the most stable [1.50].

1.6 Water adsorption property of MOFs:

There are three major kinds of water adsorption mechanism which dominates within the different sorts of MOF architecture based on the role of the metal centers, pore size and shape and pore functionality relied on the ligand nature.

(i) Direct water adsorption on metal nodes or metallic clusters of the MOFs involving the first coordination sphere of the metal ion. This is a typical chemisorption process and irreversible, which is primarily achieved by evacuation of the as-synthesized MOFs with coordinated water molecules at elevated temperature to generate unsaturated metal sites suitable for this process. It should be noted that sample pretreatment is a key issue in this case. For example, the shape of water adsorption isotherm in Ga-MIL-53 MOF is strongly dependant on the initial activation procedures [1.51].

(ii) Layer/cluster adsorption within the MOFs which is related to the pore size and shape for 3D MOFs and interlayer distances for 2D ones, and are generally reversible provided the MOF backbone have least interaction with the water molecules.

(iii) Capillary condensation of water molecules on the MOF particle surface or the intercrystallite spaces, where the pore surface has strong hydrophobic character to repel the incoming water molecules. This process is irreversible in nature.

All these mechanisms are well studied in MOFs and we will exemplify those using well-known MOFs including MOF-74, UiO-66, MIL-101 and ZIF-8.

Water adsorption-desorption isotherms of Ni- and Mg-MOF-74 demonstrate a type-I profile characterized by a large amount of water uptake at low partial pressure and a long saturation plateau; an usual pattern found in microporous Zeolites. The large adsorption capacity at low partial pressure makes these porous solids as promising hydrophilic adsorbents which rely on physisorptive process. The pore diameters of UiO-66 are 0.75 nm and 1.2 nm, and exhibit water adsorption-desorption isotherms of ‘‘S’’ shape with small uptake at low partial pressure followed by an adsorption step with inflexion point at P/P_o = 0.2. Interestingly, the desorption pathway do not coincide with the adsorption one, which indicates minor alterations of the structure induced by host-guest interactions and some degree of network flexibility [1.52]. Repeated adsorption-desorption cycles were carried out to evaluate the effect of hydration-dehydration on structural properties and the stability of the structure on recycling. The low temperature soft evacuation was performed to avoid the dehydration of the $Zr_6O_4(OH)_4$ cluster which shows shift with respect to hard one, indicating the operation of both physisorptive and chemisorptive phenomena. Water adsorption-desorption in MIL-101 exhibit very high water uptake within relative humidity range of P/P_o = 0.25 - 0.60. The total uptake capacity of MIL-100 (ca. 0.8 gg^{-1}) is lesser than MIL-101 (1.2 gg^{-1}), as expected from their pore volumes [1.53]. Although different Cr-MIL-101, Fe- and Cr-MIL-100, Al-MIL-100 samples give variation of adsorption capacity due to lower degree of crystallinity or ineffective evacuation procedures, the type I isotherm remains unchanged. The hydrophobic characteristic of ZIF-8 was evaluated by significantly less water uptake performance even at relative pressure $P/P_o = 1$ [1.54]. Such behaviors are usual for the hydrophobic sodalite Zeolites of similar topology. However, at large pressures, liquid water penetrate the microporous structure of ZIF-8 (0.5 mLg^{-1} at 27 mPa. A treatise of the water adsorption capacity and correlation with the surface area of the MOF can be found in the following table 1 [1.55].

MOF Structure	**Pore diameter in nm**	**BET surface area in m^2g^{-1}**	**Pore volume in cm^3g^{-1}**	**Water vapor uptake in cm^3g^{-1}**	**Ref.**
Ni-MOF-74	1.1	1040	0.46	0.50	1.55a
Mg-MOF-74	1.1	1400	0.65	0.68	1.55b
HKUST-1	0.6-0.9	1270	0.62	0.51	1.55b
Fe-MIL-100	2.5-2.9	1549	0.82	0.81	1.55c
Al-MIL-100	2.5-2.9	1814	1.14	0.50	1.55d
Cr-MIL-100	2.5-2.9	1330	0.77	0.40	1.55e
Cr-MIL-101	2.9-3.4	3124	1.58	1.40	1.55f
Cr-MIL-101-NH_2	2.9-3.4	2690	1.6	1.06	1.55g
Cr-MIL-101-NO_2	2.9-3.4	2146	1.19	1.08	1.55f
UiO-66	0.75-1.2	1290	0.49	0.42	1.55a
UiO-66-NH_2	0.75-1.2	1328	0.22	0.38	1.55h
UiO-66-NO_2	0.75-1.2	792	0.4	0.37	1.55i
UiO-67	1.2-1.6	2064	0.97	0.18	1.55h
MIL-125-NH_2	0.6-1.2	1220	0.55	0.37	1.55h
In-MIL-68-NH_2	0.6-1.2	850	0.302	0.32	1.55j
CAU-10	0.7	635	0.25	0.31	1.55k

ZIF-8	1.1	1255	0.64	0.02	1.55l
ZIF-90	1.1	1200	0.48	0.29	1.55m

1.7 Introduction to proton conductivity in MOFs:

The projected energy consumption by the world will increase by 50% from 2012 to 2030 mainly due to the rapid urbanization, booming number of industries increasing day by day and obvious population expansion [1.56]. As a result, there is urgent need to advance from fossil fuel based resources to an alternative renewable energy for environmental issues and cost-cutting measures [1.57]. Fuel cell based technology is one of the most attractive renewable energy source and gathered considerable attention in the past decades [1.58]. A fuel cell device typically converts chemical energy to electrical energy by reacting hydrogen from fuel with oxygen from the air to produce heat and water as major by-products. A basic fuel cell setup consists of a negative end (anode), a positive end (cathode) and an electrolyte media that allows charges to move freely between the both ends of the fuel cell. Different fuel cell systems have been developed over the past decades, among which the polymer electrolyte membrane fuel cells (PEMFCs) [1.59] are of prime interest, and will be discussed due to its relevance to the thesis. In PEMFCs, the basic strategy lies

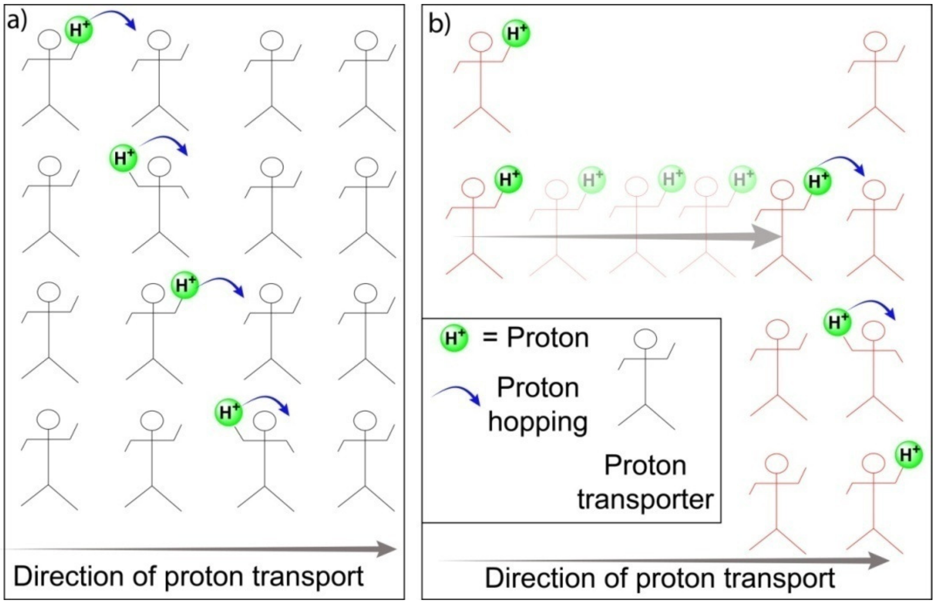

Figure 1.16: Pictorial representation of proton transport mechanism a) Grotthuss proton hopping mechanism. b) Vehicular mechanism.

on the passage of protons from anode end to cathode through the proton-exchange membrane inside the cell, while the electrons generated at the anode end pass along the external circuit to cathode generating electricity [1.59]. Although numerous proton conducting materials have been reported in the literature, till date only a group of sulfonated fluoropolymers (viz. Nafion) [1.60] (having high proton conductivity > 0.1 Scm^{-1}) has been successfully commercialized as proton exchange membrane in PEMFCs. Fluorous backbone provide additional hydrolytic, mechanical as well as oxidative stability to the material, and sulfonate groups promote high conductivity in humid conditions via uptake of several water molecules within the porous cavity of the polymers. However, this usher in another primary drawback of this material as humidified condition is required to achieve high proton conductivity without which conducting efficacy decreases drastically. Besides, there is also a need to power up a humidifier for humidity monitoring. Such bottlenecks also limit the use of Nafion at higher operating temperatures which suffer the following danger of poisoning of Pt catalysts by CO at less than 100 °C (CO is generated from the steam reforming while producing H_2) and slow reaction kinetics. Undoubtedly, there is an urgent development needed that can exhibit similar or higher proton conduction values than Nafion at lower as well as higher temperatures (100-200 °C) under both hydrous and anhydrous condition depending on the system. On this line, several new materials emerged with high proton conductivity values at different conditions, which are out of scope for this thesis, but covered in different review articles. Only during the past decade metal-organic frameworks (MOFs) have been explored as an proficient proton conducting material due to their permanent porosity, chemical functionalty and thermal stability which could be advantageous for the advancement of proton-conducting membranes. Generally, two pathways of proton conduction have been proposed for understanding the mechanisms; (1) Grotthuss proton hopping mechanism (2) Vehicular mechanism [1.61]. In Grotthuss mechanism proton transportation occurs via the ordered transporter molecules situated within close proximity so that protons can be interchanged without appreciable movement. For example, this mechanism occurs under hydrous condition and lower temperatures (< 80 °C). By contrast, vehicular mechanism, as evident from the term, happens by the activation energy induced movement of the carrier molecules (e.g. imidazole, triazole) along any direction to transfer the proton to nearby molecules

(Figure 1.16). This mechanism is of particular interest while considering conductivity at higher temperatures (i.e. near the boiling point of the transporter molecules). Based on the above discussion the proton conductivity in MOFs is divided mainly in two ways a) water mediated (hydrous) proton conductivity [1.62] b) Anhydrous proton conductivity [1.63].

1.7.1 Challenges and opportunities of proton conduction in MOFs:

The prime challenges and prospectives in designing MOF based proton conductors are many, some of which are discussed vide supra:

a) As MOFs are constructed in organic medium by joining metal ions with organic linkers via coordination bonds, reverse phenomena i.e. deconstruction of MOF backbone can be accelerated in water or simple ambient humidity to result in corresponding metal oxide/hydroxide and bare organic ligand. At present most of the MOFs cannot withstrand high humidity, which is the major operational bottleneck in developing MOF based conducting materials. In most of the cases, the water stability cannot be predicted a priori. However, few selected metal clusters linked by carboxylate moieties [e.g. $Cr_3O(COO)_6F/OH$, $Zr_6O_4(OH)_4(COO)_6$] proved to be effective in tolarating water even at higher temperatures.

b) As MOFs have high density of metal ions preferably transitional one, it is heavier and costlier than its polymer analogue and thus has to bear with gravimetric issues while considering MOFs for on board applications. MOFs based on earth abundant light weight group of metals [e.g. Mg(II), Ca(II)] can solve this issue to some extent, while high bond dissociation energy of alkali earth metal oxide can be utilized for highly water stable MOFs. For information, the chapter 6 of this thesis specifically deals with this prospect of MOFs.

c) The inherent porosity of MOFs can give rise to unwanted fuel cell crossover problem in PEMFCs, which can be effectively minimized by filling the pores with water or a nonvolatile proton carrier. In addition, providing proton conducting functional groups to the ligand backbone can serve dual purpose to assist proton transport and decrease porosity.

d) The high crystallinity of MOFs in the form of large sized crystals or microcrystalline powder create interparticle spaces while preparing a compact pellet or membrane for proton conduction measurement. This phenomenon is well-known as grain boundary and can substancially lower the proton conduction rate and also can evoke crossover problems. Diminishing the particle size of the MOFs is one strategy, while combining with polymeric binder to make a composite is another pathway to address this issue. Interestingly, pure MOF based membranes are also an active research area, which should be focused on to get added advantage to solve the current problems.

At present situation although most of the points have been addressed in the literature separately, there is an urgent development needed to combine the aforementioned aspects in a single domain to envisage MOF based proton conductor for practical applications in the near future.

1.7.2 Water assisted proton conductivity in MOFs:

Hydrous state proton conductivity occurs in MOFs in presence of certain amount of humidity (expressed in %RH) to the outer environment. Water molecules thus adsorped inside the porous cavity of the MOF architecture along with trapped within the intercrystallite spaces. Protons proceeds via simultaneous formation and breakage of covalent bonds. In this manner, the hydrogen bonded network of water molecules carry protons by a very low activation energy (< 0.4 eV) and at lower operational temperatures (below 100 °C) which is the typical characteristics of Grotthuss proton hopping mechanism. Based on the framework nature, conduction pathways and carrier molecules, proton conductivity in MOFs under humid condition can be broadly categorized into two primary sections; a) inherent water assisted proton conduction in hydrous condition and b) framework ion assisted proton conduction in humid condition.

1.7.2.1 Inherent water assisted proton conduction:

A well-organized proton conduction pathway relies on the facile movement of protons along the pores of the MOF backbone. Inherent water molecule assisted conductivity inside the MOF channels can happen through the following two categories; a) MOF backbone where water molecules are coordinated to the metal center and b) Porous MOFs with water molecules entrapped inside as lattice solvent. In both the cases, however, hydrous atmosphere enhances the proton conduction values. As most of the thesis deals with the proton conduction phenomenon in hydrous conditions, we will put particular interest to explore this section and comprehend the governing factors that promote proton conductivity in humid conditions.

Proton conducting ability has been investigated on one-dimensional metal organic chain systems with oxalate bridging moieties [1.62c]. The first system examined was ferrous oxalate dihydrate [$Fe(ox)_2.2H_2O$] which contains octahedral Fe(II) metal centers coordinated with bidentate oxalate anions and coordinated water molecules. The bridging behavior of oxalate moieties resulted in the formation of one-dimensional (1D) coordination chains (Figure 1.17a). The proton conductivity value exhibited by this material is 1.3 × 10^{-3} Scm^{-1} at 25 °C under 98% RH with an activation energy barrier of 0.37 eV. The Lewis acidic Fe(II) tend to polarize protons from the coordinated water molecules, which assist periodic arrangement of coordinated water molecules with partially acidic nature inside the structure to facilitate the proton conduction pathway under hydrous condition. Similar kind of mechanism has been observed in case of another coordination polymer viz. M(dhaq), [M = Co, Mg, Mn, Ni, Zn and dhbq = 2,5-dihydroxy-1,4-benzoquinone] (Figure 1.17b). M(dhaq) posses the same kind of structure as $Fe(ox)_2.2H_2O$ with only difference in the linker. Despite the structural similarities, the proton conductivity of these coordination polymers is comparatively low [lies in the range of 4 × 10^{-5} Scm^{-1}] in hydrous condition, suggesting that the linkers play a vital role in proton conduction.

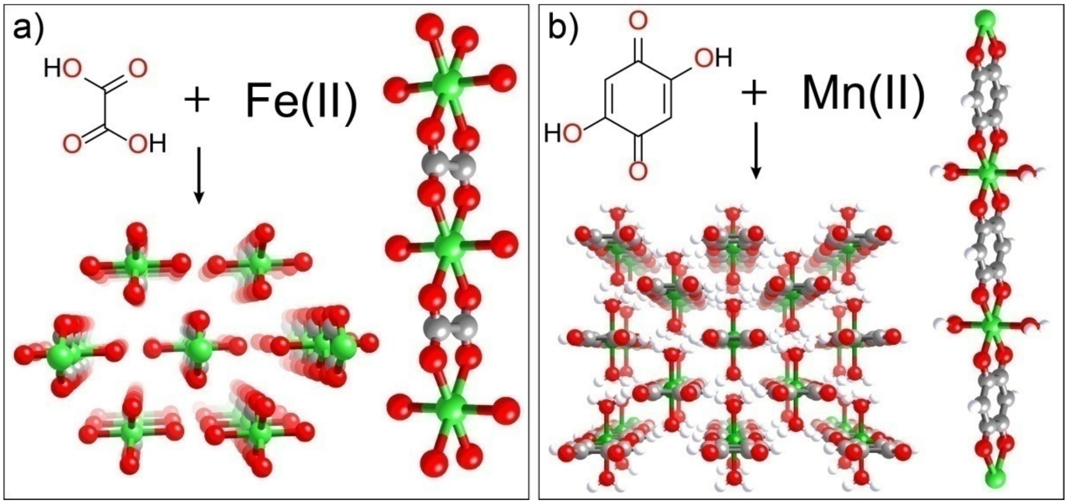

Figure 1.17: a) Constituents and packing view of Ferrous oxalate coordination polymer. b) Constituents and packing view of 2,5-dihydroxy-1,4-benzoquinone (dhbq) Mn(II) based coordination polymer. Color code: Fe/Mn green, O red, C gray and H white.

However, both of the coordination polymers do not show proton conductivity in absence of humidity which indicates that the coordinated as well as humidity induced water molecules play an important role in determining their proton conducting ability.

In another approach, proton conductivity has been examined on MOFs where the pore cavity is blocked by hydrogen bonded water molecules which can aid the conduction pathway through the MOF backbone. A perfect example of this kind is a Zn(II) based two dimensional coordination polymer PCMOF3 bearing phosphonate linker. The MOF has been synthesized under hydrothermal condition by combining the 1,3,5 benzenetriphosphonic acid and $Zn(NO_3)_2$ as metal source. The coordination of the phosphonate ligand via Zn(II) resulted in 2D layered network stacked through alternating sets of zinc metal centers. This coordination environment creates elliptical pores filled with solvent water molecules (4 in numbers per pore). The protons are presumed to [1.62b] mediate through the solvent water molecules aligned in a periodic manner through intermolecular hydrogen bonding within elliptical pores as well as further interactions with the framework backbone (Figure 1.18a). PCMOF3 showed moderate proton conductivity value of 3.5×10^{-5} Scm^{-1} at 25 °C and 98% RH. However, in anhydrous condition the conductivity decreases drastically which indicates that the conducting pathways for PCMOF3 are highly humidity dependant. To improve on the conductivity of this material, an acidic functionalization strategy has been utilized by combining with PCMOF2. The PCMOF2 structure [trisodium salt of 2,4,6-trihydroxy-1,3,5-benzenetrisulfonate (L_1)] contains pores lined with sulfonate oxygen atoms and exhibit poor proton conducting efficiency in undoped condition, while the conductivity increases many upon 1,2,4 triazole

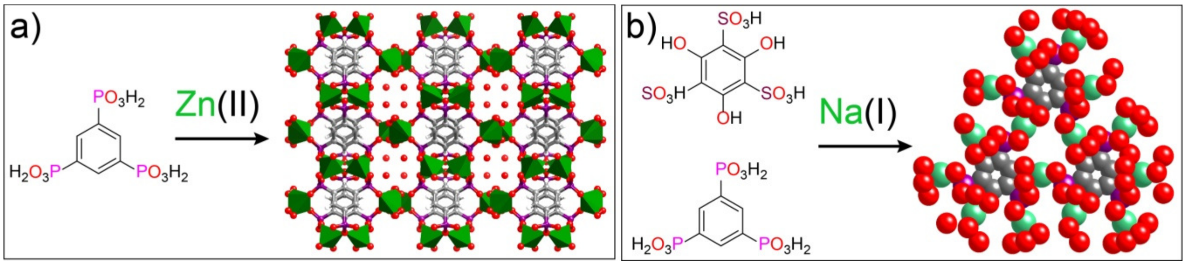

Figure 1.18: Structure of a) PCMOF-3 in polyhedral model showing 1D water filled channels. b) $PCMOF2^{1/2}$ formed by combining 1,3,5 benzene triphosphonic acid and 1,3,5 benzene trisulphonic acid. Color code: Zn green, O red, C gray P magenta and S brown.

loading (out of scope of this discussion). In order to improve on the proton conductivity of PCMOF2, partial linker replacement strategy aided by grinding with monosodium salt of 1,3,5 benzenetriphosphonic acid has been applied to get the hybrid structure comprising the characteristics of both the PCMOF2 and PCMOF3 [1.62i]. The resulting material viz. PCMOF2$^{1/2}$ has much higher proton conductivity [2.1×10^{-2} Scm^{-1} at 90% RH and 85 °C] than either of its constituting MOF [Figure 1.18b]. The incorporation of additional proton presumed to play a vital role in determining the high conductivity of the hybrid MOF. The PCMOF2$^{1/2}$ also exhibit humidity dependant proton conductivity, which confirms the role of water in assisting the conducting process. The activation energy (Ea) was measured to be 0.21 eV, which is an indicative of the Grotthuss proton hopping mechanism. In another account, a similar structure like PCMOF2 has been obtained using an extended aliphatic iminophosphonate linker L_1 = Octamethylenediamine-N,N,N′,N′-tetrakis-(methylenephos phonic acid), [H_8ODTMP] and Mg(II) as metal source [1.62t]. The MOF ($MgH_6ODTMP.2H_2O.DMF_{0.5}$) structure is 3D and posseses tetragonal pore filled with solvent water and DMF molecules (Figure 1.19). The conductivity values are a bit higher than PCMOF one, exhibiting 1.6×10^{-3} Scm^{-1} at 19 °C and ~ 100% relative humidity with activation energy value of 0.31 eV.

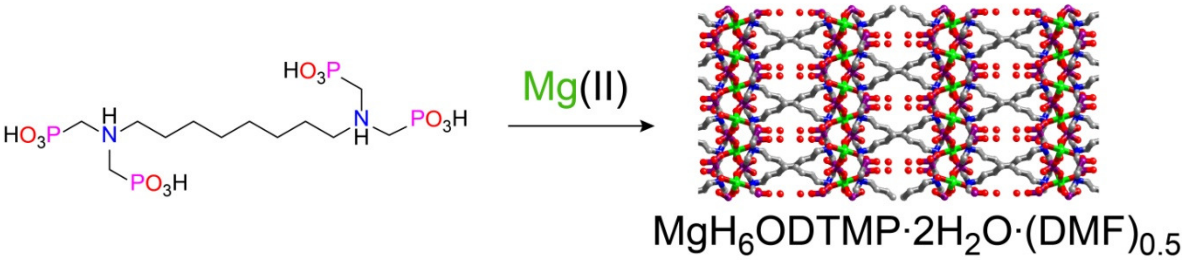

Figure 1.19: Three dimensional arrangement of Mg-iminophosphonate network starting from its constituents. Mg green, O red, C gray and N blue.

1.7.2.2 Ion assisted proton conduction:

MOFs where the coordination around the metal center creates anionic or cationic framework also have a non-coordinated countercations/anions within the pore cavity. This creates an unique opportunity to utilize the cationic/anionic guests to aid the proton conducting pathways under hydrous condition. In general, for the neutralization of the anionic framework various cationic molecules [NH_4^+, $(CH_3)_2NH_2^+$, $(C_2H_5)_2NH_2^+$ etc.] are present inside the network. A landmark example of such kind of MOF is the zinc oxalate based framework $(NH_4)_2(adp)[Zn_2(ox)_3]\cdot3H_2O$, which contains two ammonium cations, three water molecules and one adipate anions (adp) trapped inside the voids of the 2D network (Figure 1.20)[1.62e]. The interesting structural aspect is that it incorporates both cationic and anionic guests for optimized performance towards the proton conduction processes. The proton conductivity of this MOF was 8×10^{-3} Scm^{-1} at 25 °C under 98% RH. The high proton conductivity at hydrous condition is owing to the extended hydrogen-bonded network produced by both the complex intermolecular as well as intramolecular hydrogen bonding between ammonium cations, adipate anions and solvent water molecules inside the 2D architecture.

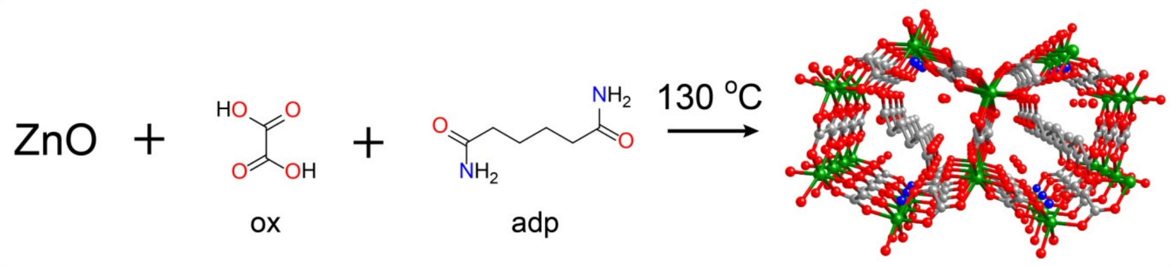

Figure 1.20: Honeycomb layered structure of Zinc oxalate framework with ammonium cation, water molecules and adipate anion trapped inside the interlayer spaces of 2D network. Color code: Zn green, O red, C gray and N blue.

A similar kind of oxalate-bridged bimetallic chiral MOF $(NH_4)_4[MnCr_2(ox)_6].4H_2O$ have been examined for proton conductivity with a helical oxalate chains (Figure 1.21)[1.62u]. The interesting aspect of this type of structure is that this is the only chiral MOF studied till date for hydrous state proton conductivity. It reveals moderate proton conductivity of ca. 1×10^{-4} Scm^{-1} where the ammonium cations in combination of solvent water molecules form

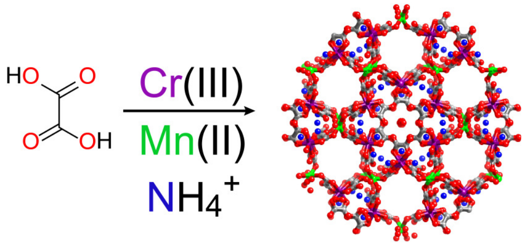

Figure 1.21: Chiral structure of mix-metal oxalate framework. Color code: Cr Violet, Mn green, O red, C gray, N blue.

the proton conduction pathways.

The hydrous state proton conductivity is reported for the MOFs are limited to mostly oxalate and phosphonate type linkers. They provide strong chelating effect to the metal ion which is suitable for the water stability of the resulting MOFs in extreme humid conditions and elevated temperatures. The following chapters of this thesis will open up new possibilities of using the chelating ability of the amino acids to design water stable MOFs which also have high water uptake capacity.

CHAPTER 2

VARIABLE WATER ADSORPTION IN A SERIES OF AMINO ACID DERIVED MOFS

2.1 Introduction:

Enantiopure amino acids and its derivatives had been a cynosure in the eyes of researchers as it serves as a backbone in the chemical processes of all flora and fauna. Extensive research on the property studies of the naturally occurring amino acids and their derivatives (e.g. peptides) as well as their synthetic analogues has been evolved in the last decades for their potential biomimetic activities [2.1]. Despite all these promising facts, till date it is extremely complicated to completely understand their structure and property relationships. For example, a small change in amino acid within the peptide backbone resulted in unexpected twist in the peptide conformers [2.2]. Hence, comprehensive understanding of the basic interactions between amino acids and other substrates would reveal the prime features of the amino acids functional property and ultimately will serve as the basis to comprehend the various chemical processes *in vivo*. In this context, several attempts have been made in order to introduce amino acid moieties in organic biopolymers [1.33]. On the other hand, organic-inorganic hybrid structures based on amino acids reveal their potential applications in enantioselective catalysis, separation, and most importantly to probe complex biochemical processes and cycles [2.3]. In this regard, metal-organic frameworks (MOFs), a class of porous organic-inorganic hybrid materials, serve as a potential platform for its application in chiral separation and sensing, nonlinear optics apart from gas sorption, catalysis, magnetism, and conductivity [1.6, 1.32, 1.35, 1.39, 1.62]. Hence, introduction of amino acid moiety in extended three dimensional backbones of MOFs assure diverse functionality and applicability due to different sidearm residue of the amino acids. In practical, high binding and chelation ability of pure amino acids with transition metals often resulted in zero/one dimensional (0D/1D) complex formation instead of higher order porous homochiral MOFs [1.34]. No surprise, till date three dimensional (3D) MOFs with amino acid backbone are only handful in numbers [1.35, 1.36, 1.40]. Moreover, rarely there has been a systematic study to directly correlate the structures and applications. Amino acids are primarily hydrophilic due to presence of polar groups; hence water and polar solvent adsorption studies will reveal important characteristics about the corresponding amino acid based MOFs. Till date, no such aspect has been revealed in the literature.

Herein, in this chapter, we report a detailed structure to property relationship in 2D and 3D amino acid based MOFs through extensive measurement of water and polar solvent adsorption isotherm; followed by their correlation with the parent MOF structure. We have developed two approaches to execute this study; a) we have examined the water and polar solvent adsorption isotherms in a series of isostructural amino acid derived MOFs with increasing hydrophilic functionality b) we have probed water sorption isotherm in a series of MOFs with different structure, different functionality and different pore sizes. In order to implement the first idea, we report three homochiral metal-organic frameworks, viz. ValZnOAc, AlaZnOAc and ThrZnOAc, a member of the extremely rare zeolitic *unh* family, having valine, alanine and threonine as the amino acid backbone [Val = (pyridin-4-yl)methylamino-valine, Ala = (pyridin-4-yl)methylamino-alanine, Thr = (pyridin-4-yl)methylamino-threonine], respectively. The pyridyl groups along with the amino and carboxylate groups of the ligands bridge Zn(II) ions to form 3D networks, whereas remaining sidearm (isopropyl, methyl and chiral 2-hydroxyethyl) can act as a functional group for desired applications like sorption, sensing and catalysis. As a proof of concept application, we have performed solvent adsorption studies, which revealed that hydrophilic interactions inside the porous cavity of ThrZnOAc increases in many fold due to poking hydroxyl group compared to isopropyl or methyl groups in case of ValZnOAc or AlaZnOAc, respectively (Figure 2.1). Extensive solvent sorption isotherms have been collected to explore their interactions with the pore surface with diverse polarity of solvents viz. water, methanol, isopropanol and toluene. ValZnOAc and AlaZnOAc show very low uptake followed by pore condensation behavior while ThrZnOAc exhibit excellent water uptake capability even at lower relative pressure (15 wt% at STP, $P/P_0 \leq 0.25$). Methanol and isopropanol sorption isotherm also reveal the enhanced uptake capacity in case of ThrZnAOc with respect to ValZnOAc and AlaZnOAc due to polar interaction inside the pore surface. However, toluene sorption profiles reveal the exact opposite trend due to hydrophobicity. ValZnOAc exhibits higher toluene sorption capacity (6 wt% at STP; $P/P_o\sim$

0.9) than AlaZnOAc (4 wt% at STP; P/P$_o$~ 0.9) and ThrZnOAc (2 wt% at STP; P/P$_o$~ 0.9). This aforementioned strategy of tuning the framework polarity for sorption of wide polarity of solvent molecule is unprecedented in amino acid based homochiral MOFs, which we believe will surely pave the way for functional amino acid based MOFs in several industrially relevant applications. Regarding implementation of the second idea, we report six new homochiral metal-organic framework isomers viz. LeuCdCl, LeuCdBr, SerCdCl, SerCdBr, ThrCdCl, ThrCdBr [Leu = (pyridin-4-yl)methylamino)-leucine, [Ser = (pyridin-4-yl)methylamino-serine] and [Thr = (pyridin-4-yl)methylamino-threonine]. These MOFs have been synthesized using pyridine derivatives of L-leucine, L-serine and L-threonine, respectively as organic link and $Cd(CH_3COO)_2 \cdot 2H_2O$ as metal precursor under hydrothermal condition. The additional pyridyl group together with the carboxylate group of the ligand can bridge transition metal ions to form three dimensional networks, while the remaining sidearms can act as a functional group for special applications. MOFs LeuCdCl/LeuCdBr, SerCdCl/SerCdBr and ThrCdCl/ThrCdBr are structural isomers with different anions (Cl^- or Br^-) coordinated to the metal atoms (Figure 2.2). MOFs LeuCdCl/SerCdCl and MOF ThrCdCl/ThrCdBr are isostructural, while MOF SerCdCl and SerCdBr posses structural diversity due to the bulkiness of coordinated halogen atoms. MOF LeuCdCl/LeuCdBr and SerCdCl/SerCdBr adopt 3D architecture while MOF ThrCdCl and ThrCdBr are 2D in nature. These MOFs exhibit distinct water adsorption nature and capacity e.g. form hydrophobic nature (in case of leucine) to high adsorption at low partial pressure (in case of serine and threonine) based on architectural diversities as well as the amino acid functionalities.

2.2 Result and discussion:

2.2.1 Structural aspects of the MOFs:

The hydrothermal synthesis has been proven to be a useful technique in the preparation of organic-inorganic framework materials. Generally, hydrothermal conditions can overcome the differential solubility of the organic and inorganic components and optimize the environment for crystal growth. All the linkers (ThrOAc, LeuCl, LeuBr, SerCl, SerBr, ThrCl, ThrBr) and the metal precursors [$Zn(OAc)_2$ and $Cd(OAc)_2$] are soluble in water, hence hydrothermal conditions have been adapted for the synthesis of the MOFs.

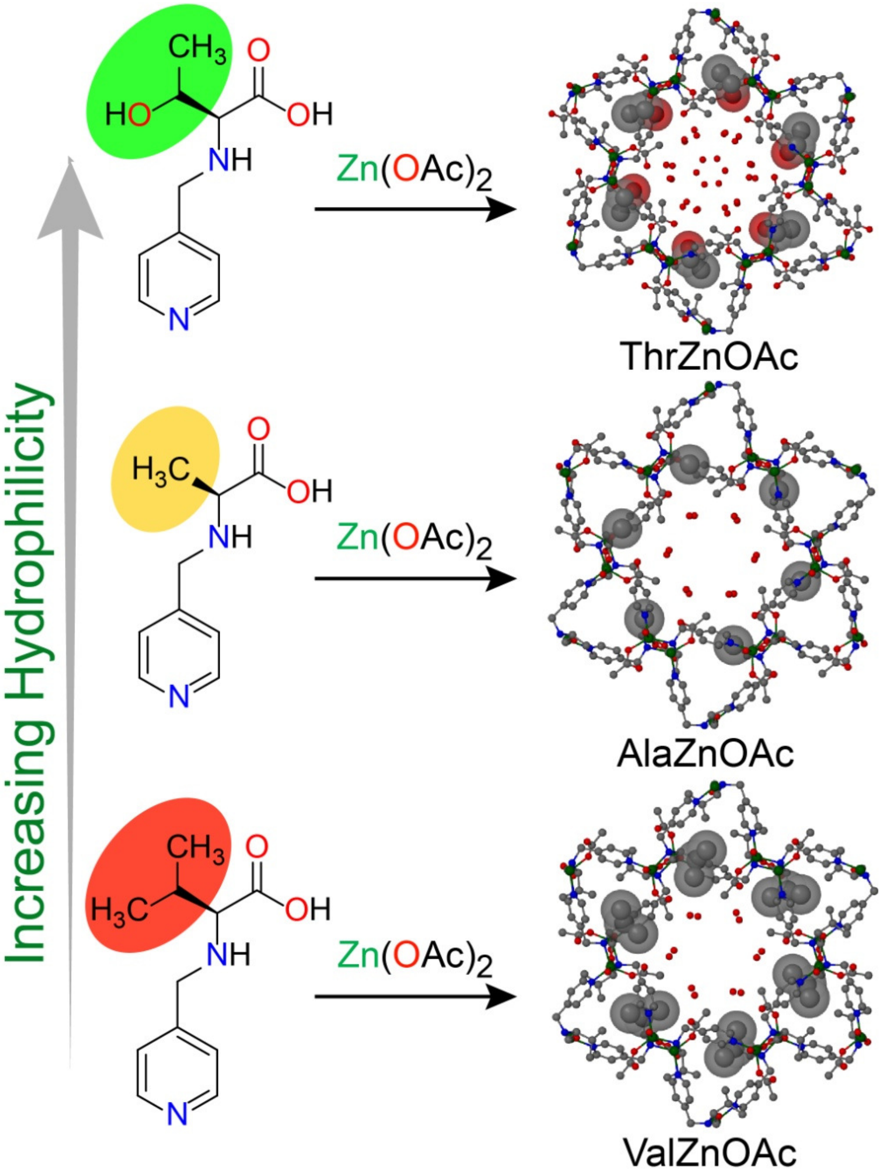

Figure 2.1: Schematic representation of the linkers ValOAc, AlaOAc and ThrOAc that react with $Zn(OAc)_2$ to produce corresponding MOF architectures (ValZnOAc, AlaZnOAc and ThrZnOAc). These MOFs possesses isostructural integrity (*unh* topology) along with linker variety (from hydrophilic to hydrophobic in order) and their framework architecture has been shown highlighting the side arms responsible for functional property. Color codes: Zn (dark green), N (blue), O (red), C (gray). Figure adapted from ref. 2.13.

ThrZnOAc crystallizes in the $P6_1$ space group, comprising one Zn(II), one Thr ligand, one OAc^- ion and five lattice H_2O molecules in the asymmetric unit. Each Zn(II) centre adopts a slightly distorted square pyramidal geometry (τ = 0.026), chelated by monodentate carboxylate [(Zn1–O1; 2.137(3) Å)], one amino functionality [(Zn1–N1; 2.080(6) Å)] of the Thr link, one pyridyl functionality and one carboxylate oxygen atom of the Thr ligand

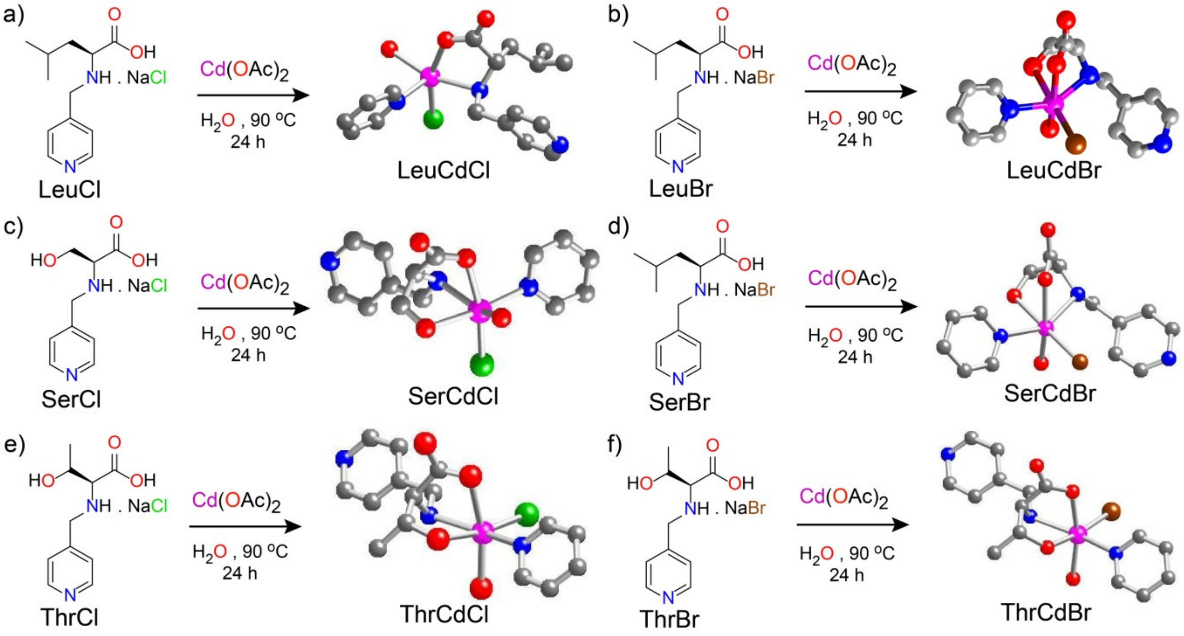

Figure 2.2: Synthesis of MOFs from the corresponding ligands a) LeuCdCl from LeuCl b) LeuCdBr from LeuBr, c) SerCdCl from SerCl, d) SerCdBr from SerBr, e) ThrCdCl from ThrCl, f) ThrCdBr from ThrBr. Color codes: Zn (dark green), N (blue), O (red), C (gray), Cl (light green) and Br (brown).

coordinate to the axial and equatorial positions of the Zn(II), respectively. One OAc^- ion coordinates to the equatorial site which balance the overall negative charge of the Zn(II) atom. All adjacent Zn(II) nodes are bridged by pyridyl functionalities to form a helical pitch along the crystallographic *a* axis. These pyridyl moieties constitute the cylindrical pore wall of the framework, which is hydrophobic in nature. Most importantly, the sidearm residue [–CH(OH)CH_3] of the threonine bears another chiral centre for functional application (Figure 2.3), which is absent in the valine/alanine counterparts. For example, the open channel along crystallographic *c* axis are filled with solvent H_2O molecules, which are two per asymmetric unit of ValZnOAc and AlaZnOAc, whereas there are five H_2O molecules present per asymmetric unit in ThrZnOAc due to enhanced hydrophilic intermolecular interactions between 2-hydroxyethyl [–CH(OH)CH_3] groups, metal-bound acetate groups (exposed towards the pore) with the water molecules. These channels have a cylindrical cross sectional area of 8.2 × 8.2 Å. A striking feature observed in this case is the interaction between ligand sidearm and solvent water molecules [O3···O10, 3.571(3) Å].

There are further intermolecular hydrogen bonds along the pore through neighboring H_2O molecules due to the short separation [O6···O7, 2.560(4) Å; O6···O9, 2.477(4) Å; O7···O10, 2.785(3) Å] (Figure 2.4). Comparing the molecular structures of these three MOFs viz. ValZnOAc, AlaZnOAc and ThrZnOAc, it is evident that change in amino acid residue in a functionalized amino acid derivate although did not exert structural transformation but provide a huge change in material property among the isostructural frameworks (Figure 2.5). This observation indicates that changing the polarity of the sidearm [from $-CH(CH_3)_2$ to $-CH_3$ to $-CH(OH)CH_3$] can create enhanced intermolecular interactions between the framework backbone and the solvent molecules, resulted in many fold increase in the guest solvent loading (increase of two to five water molecules) while keeping the pore size and the framework architecture same.

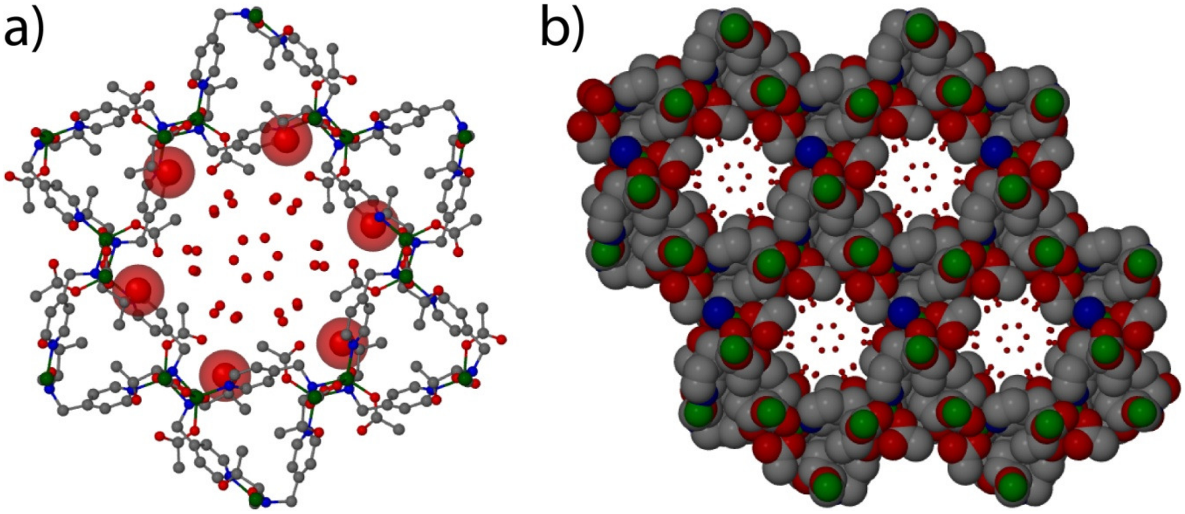

Figure 2.3: Packing view of ThrZnOAc a) single pore with hydroxy group in spacefill mode. b) Spacefill model of the ThrZnOAc featuring four pore. Figure adapted from ref. 2.13.

MOF LeuCdCl ($C_{12}H_{19}N_2O_3Cd_1Cl_1$) crystallizes in the $P2_12_12_1$ space group, comprising one Cd(II), one Leu ligand, one Cl^- ion and one lattice H_2O molecule in the asymmetric unit. The Cd(II) center adopts a slightly distorted square pyramidal geometry (τ = 0.025), chelated by monodentate carboxylate [(Cd1–O1 2.323(4) Å)], one amino functionality[(Cd1–N1 2.352(4) Å)] of the Leu link, one pyridyl functionality and one carboxylate oxygen atom of the Leu ligand coordinate to the axial and equatorial positions of the Cd(II) coordination sphere, respectively. One Cl^- ion coordinates to the equatorial site (Figure 2.6a). Noticeably, the amine group upon coordination to the Cd(II) creates one further homochiral center. All adjacent Cd(II) nodes are bridged by pyridyl groups to form a helical chain along the crystallographic *a* axis. Two carboxylate oxygens stay axial to each other. Four sets of such di-Cd-centers are bridged together by carboxylate oxygen to form an oval shaped helical channel along *a* axis while pyridyl units extend the lattice along *bc* plane (Figure 2.6b). These channels are filled with H_2O molecules despite the hydrophobic isopropyl groups and two metal bound bulky Cl^- ions are exposed towards the pore. These channels have a cross sectional area of 9.8 × 9.8 Å (Figure 2.6c). In MOF LeuCdCl the H_2O molecules are hydrogen bonded to the carboxylate oxygen [O2···O3, 3.364(1) Å]. There are no further intermolecular O—H···O hydrogen bonds along the pore as well as between the neighboring H_2O molecules (Figure 2.6d) due to large separation (~ 7.12 Å). MOF LeuCdBr is isostructural to MOF LeuCdCl with increased pore aperture (~ 10.4 × 10.0 Å). Interestingly, unlike MOF LeuCdCl, there are no lattice H_2O molecules present inside the pores of MOF LeuCdBr. We believe that the insertion of Br-atom makes

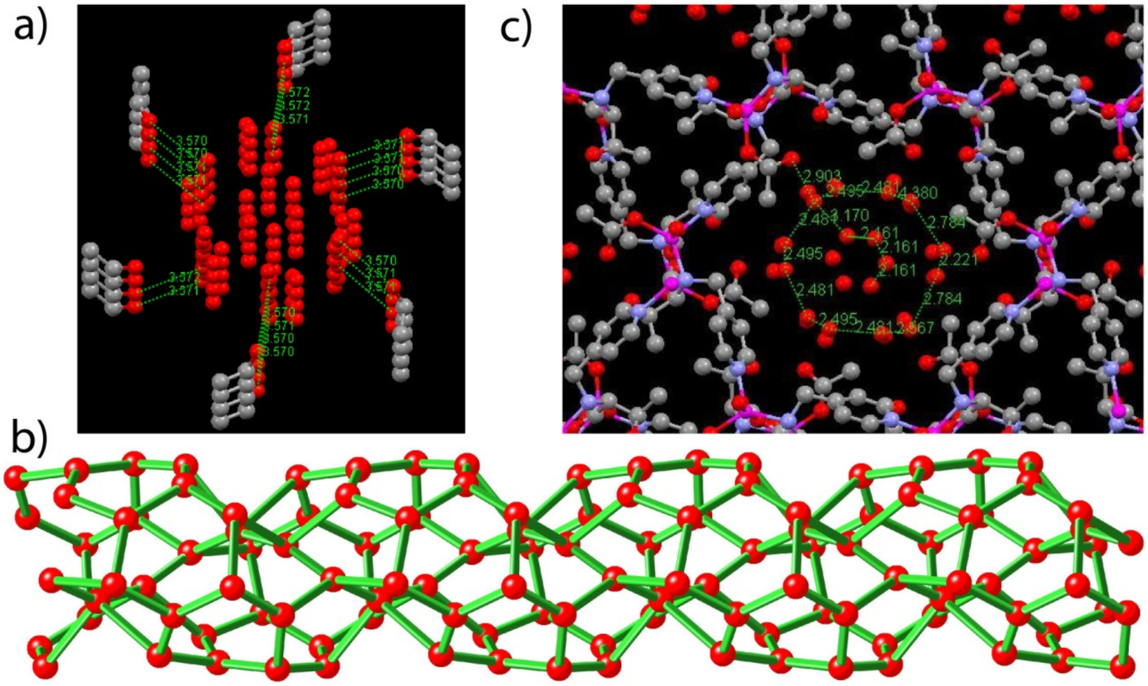

Figure 2.4: a) A snapshot of the hydrogen bonding interaction between the hydroxy group of the hydroxyethyl sidearm and the solvent water molecules (3.57 Å) along the pore. b) two dimensional view of the intermolecular hydrogen bonding interaction between the solvent water molecules inside the pore featuring high hydrophilic pore surface in case of ThrZnOAc. c) three dimensional hydrogen bonded water molecules arranged as continuous cluster along the pore of ThrZnOAc. Figure adapted from ref. 2.13.

the pore much more hydrophobic as well as less porous than MOF LeuCdCl and hence lattice H_2O molecules cannot be accommodated inside the 1D channels.

We synthesized a serine derived link (Ser) with an expectation that replacement of hydrophobic isopropyl group [$^{-}CH(CH_3)_2$] with much more hydrophilic hydroxylmethyl functionality (^{-}OH) in the side arm may play a pivotal role in molecular arrangement via different weak intermolecular interactions. In MOF SerCdCl (C_9H_{11} $N_2O_4Cd_1Cl_1$), the ^{-}OH group provide a new binding site to metal centre and coordinates to metal in its protonated form. The asymmetric unit of MOF SerCdCl contains one Cd(II) ion , one Ser ligand, one Cl^- ion and one lattice H_2O molecule. Like MOF LeuCdCl/LeuCdBr**,** The Cd(II) centre adopts a distorted octahedral geometry where one amino functionality, OH-group of the side arm of the first Ser link and one pyridyl unit and one carboxylate of second link constitutes the in-plane coordination geometry (Figure 2.7a). The monodentate carboxylate oxygen and Cl^- ion coordinates at the axial positions. In MOF SerCdCl the in-plane Cd–N_{amine} and axial Cd–$O_{carboxylate}$ bond lengths are longer [~ 2.360(1) – 2.500(1) Å] compared to the corresponding amino acid complexes (~ 1.96 Å)[2.4]. Carboxylate groups of two different ligands are bridged to form a dimeric Cd-center which repeats along the *bc* plane. Each dimeric unit is connected via pyridyl functionality in an anti-clockwise fashion to form a one dimensional pore along *a* axis (Figure 2.7b). Two Cl-atoms of each dimeric unit are exposed towards the pore and hydrogen bonded to one lattice H_2O molecule [2.5]. The cross-sectional area of this one dimensional pore is 12.0 × 8.2 Å (Figure 2.7c). The 3D

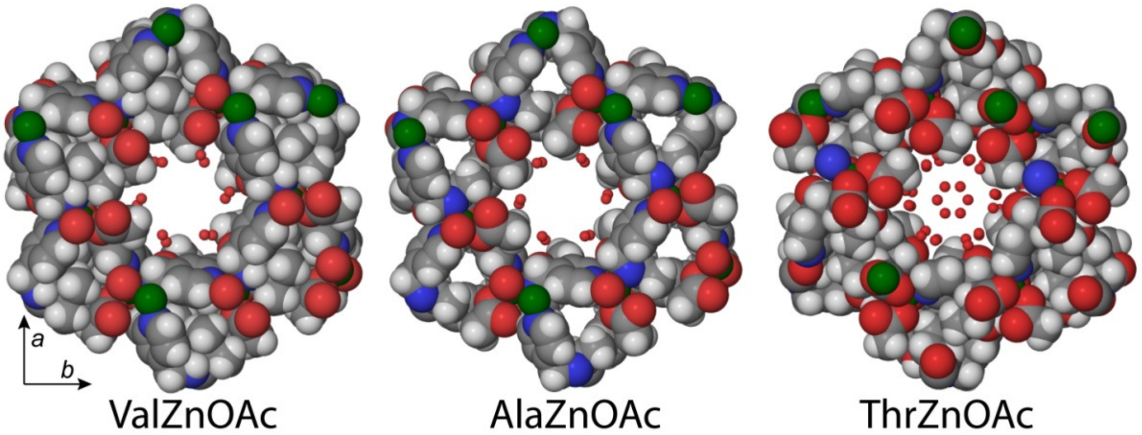

Figure 2.5: Packing diagram of ValZnOAc, AlaZnOAc and ThrZnOAc displaying cylindrical pore along crystallographic *c* axis. Figure adapted from ref. 2.13.

architecture shows a hydrophobic and hydrophilic arrangement along the *ac*-plane induced by pyridyl units and carboxylate functionality. We prepared MOF SerCdBr ($C_{18}H_{27}N_4O_9Cd_1Br_2$), a Br-analog of MOF SerCdCl ($C_9H_{13}N_2O_4Cd_1Cl_1$) to observe the effect of anion. Surprisingly, introduction of bulky Br-atom made a dramatic change in lattice arrangement. The asymmetric unit of MOF SerCdBr posses two different Cd(II) centers, and carboxylate oxygens of Ser ligand bridged to two Cd(II) centers and bound in a monodentate and bidentate fashion (Figure 2.8a). These dimeric units are arranged as a triangular repeating manner and propagate along the *bc* plane (Figure 2.8b). These

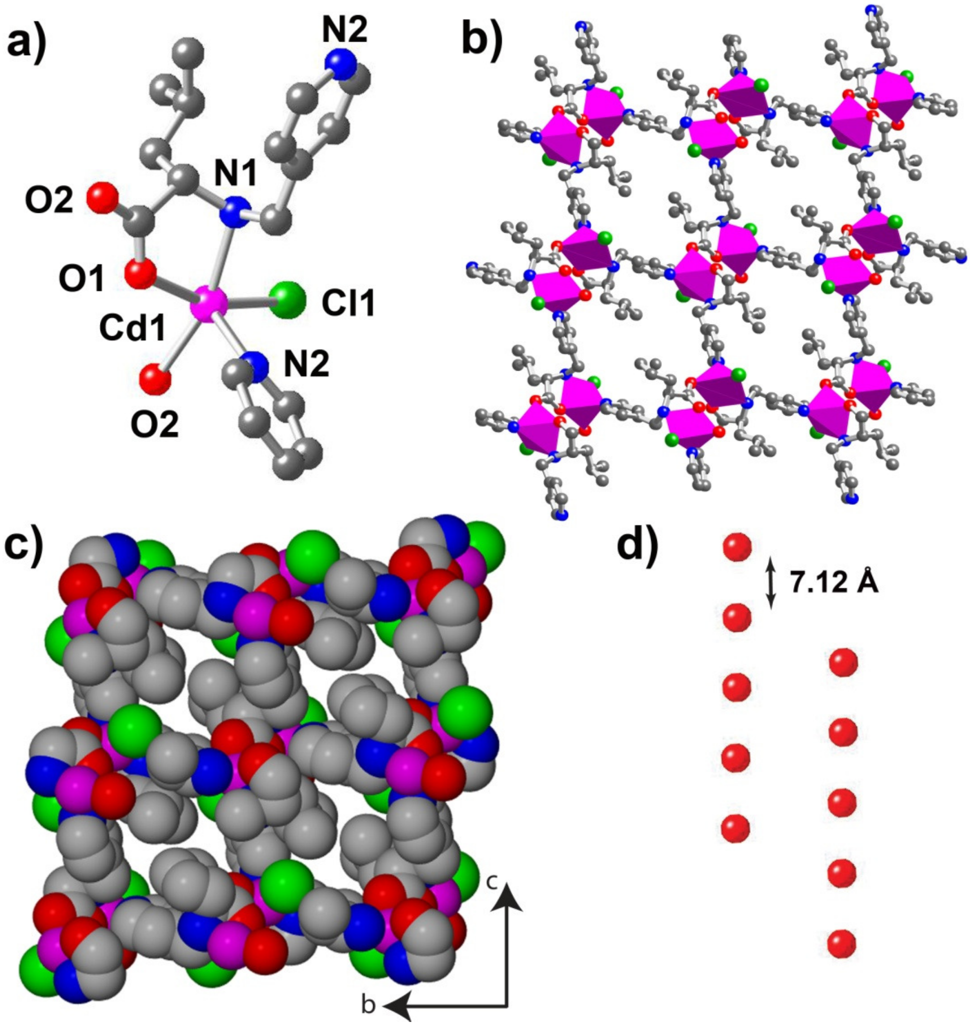

Figure 2.6: (a) SBU representation of the MOF LeuCdCl. (b) Polyhedral representation of lattice LeuCdCl viewed down the *a* axis. Magenta colored polyhedra represent Cd(II) centers, and chlorine atoms are shown as green balls. (c) 3D spacefill arrangement of MOF LeuCdCl, showing a 1D pore along the *a* axis. (d) Red colored ball represents molecular arrangement of the lattice H_2O molecules viewed along *b* axis. Figure adapted from ref. 2.14.

arrangements results in almost non-porous structure (Figure 2.8c). Viewing along *a* axis show a sheet like architecture where carboxylate bridged molecular chains (vertically) are linked by pyridyl units (horizontally). It is noteworthy that the substitution of halogen has a huge impact on structural arrangement of MOF SerCdCl and SerCdBr. In MOF SerCdCl, there is only one H_2O molecule per Cd(II) center included in the crystal lattice. These H_2O molecules stay close to the pyridyl ring and there is no interaction among the H_2O molecules along the pore due to the large separation (Figure 2.7d). But in SerCdBr, there

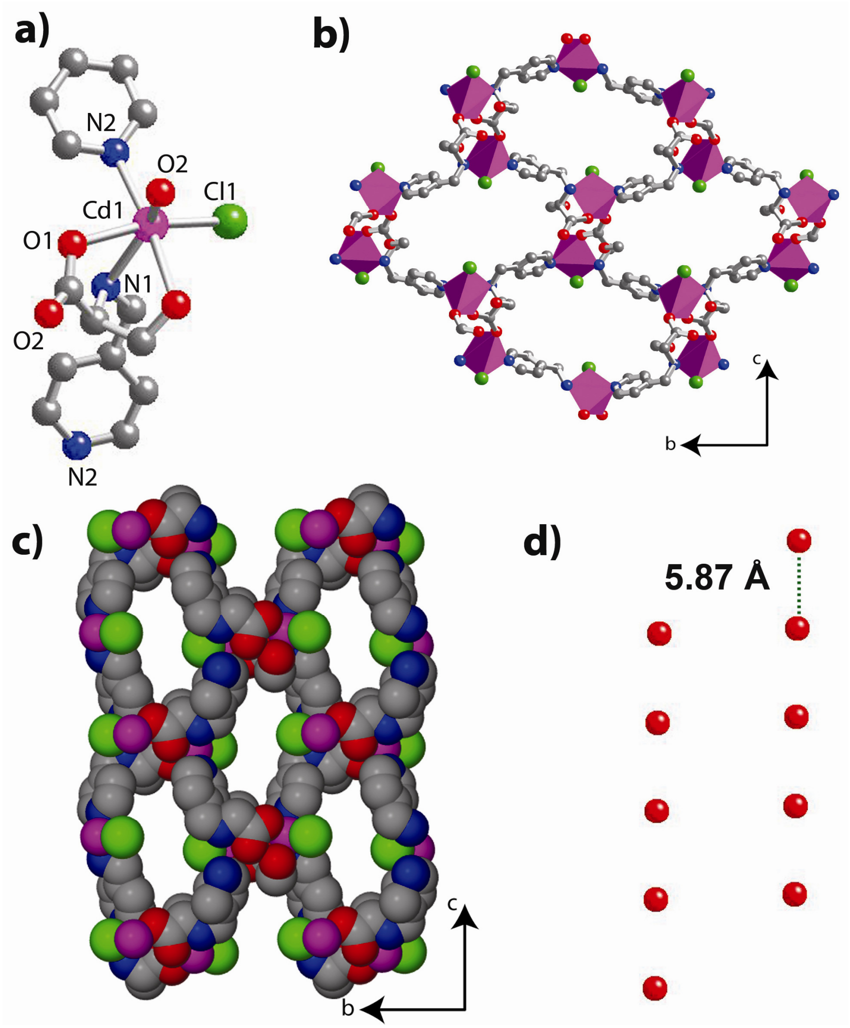

Figure 2.7: (a) SBU representation of the MOF SerCdCl. (b) Polyhedral representation of lattice SerCdCl viewed down the *a* axis. Magenta colored polyhedra represent Cd(II) centers, and chlorine atoms are shown as green balls. (c) 3D Lattice arrangement of MOF SerCdCl, showing a large 1D pore along *a* axis. Solvents are removed from the pores for clarity. (d) Lattice H_2O molecules are arranged along *b* axis with a separation of 5.87 Å. Figure adapted from ref. 2.14.

are three hydrogen-bonded H_2O molecules per asymmetric unit. All three H_2O molecules are clustered by multiple interactions and form complex hydrogen bonded network

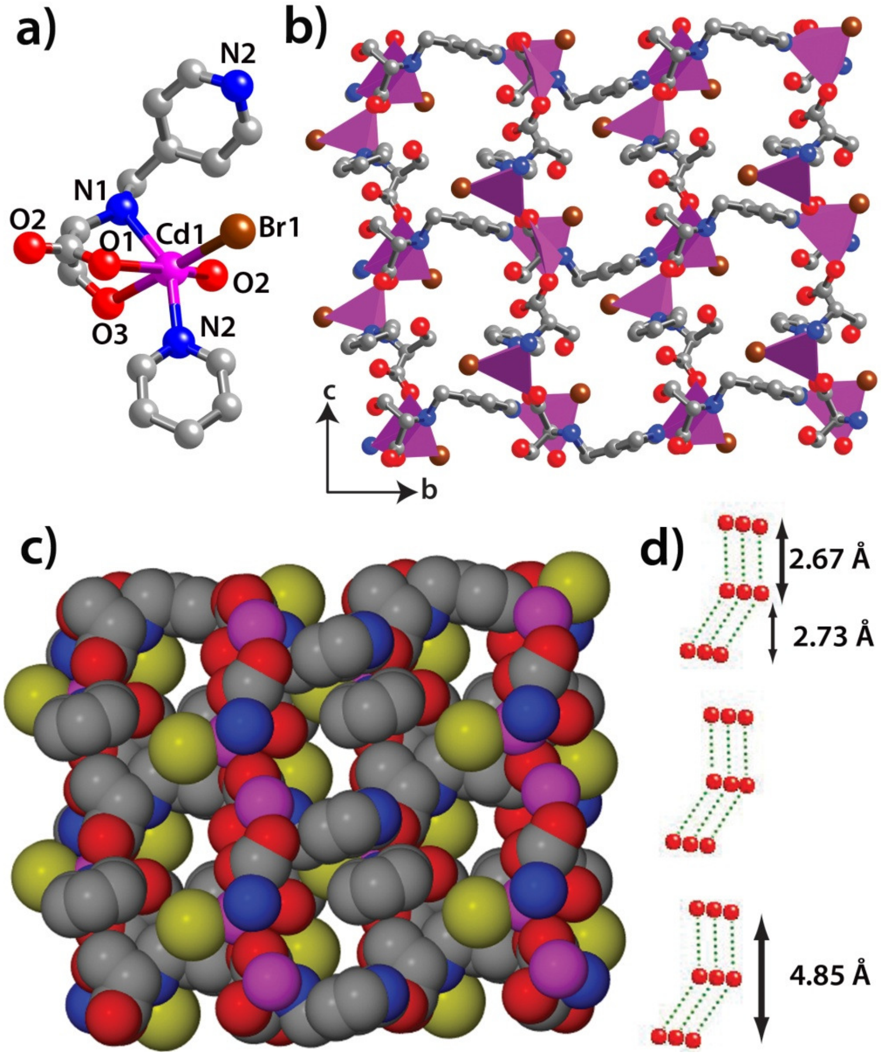

Figure 2.8: SBU representation of the MOF SerCdBr. (b) Polyhedral representation of lattice SerCdBr viewed down the *c* axis. Magenta polyhedra represent Cd(II) centers, and bromine atoms are shown as yellow balls. (c) 3D Lattice arrangement of SerCdBr, along the *a* axis. Solvents are removed from the pores for clarity. (d) Lattice H_2O molecules are arranged along *b* axis with a complex H-bonding architecture. Figure adapted from ref. 2.14.

[O8···O7, 2.730(3) Å; O7···O9, 2.667(6) Å] (Figure 2.8d). This hydrogen bonded network is further stabilized by the interaction with the metal bound Br-atoms (O8···Br1, 3.336(4); O9···Br2, 3.367(1) Å) and carboxylate groups [O7···O6, 2.714(8) Å; O8···O5, 3.003(6) Å].

We have synthesized ligand Thr, a derivate of threonine, with slight variation in the side arm keeping all binding sites same. The ligand Thr has an extra methyl ($-CH_3$) group in the side arm compared to Ser. Surprisingly the resulting MOFs ThrCdCl ($C_{10}H_{13}N_2O_5Cd_1Cl_1$) and ThrCdBr ($C_{10}H_{13}N_2O_5Cd_1Br_1$) adopts a 2D arrangement rather than the 3D network

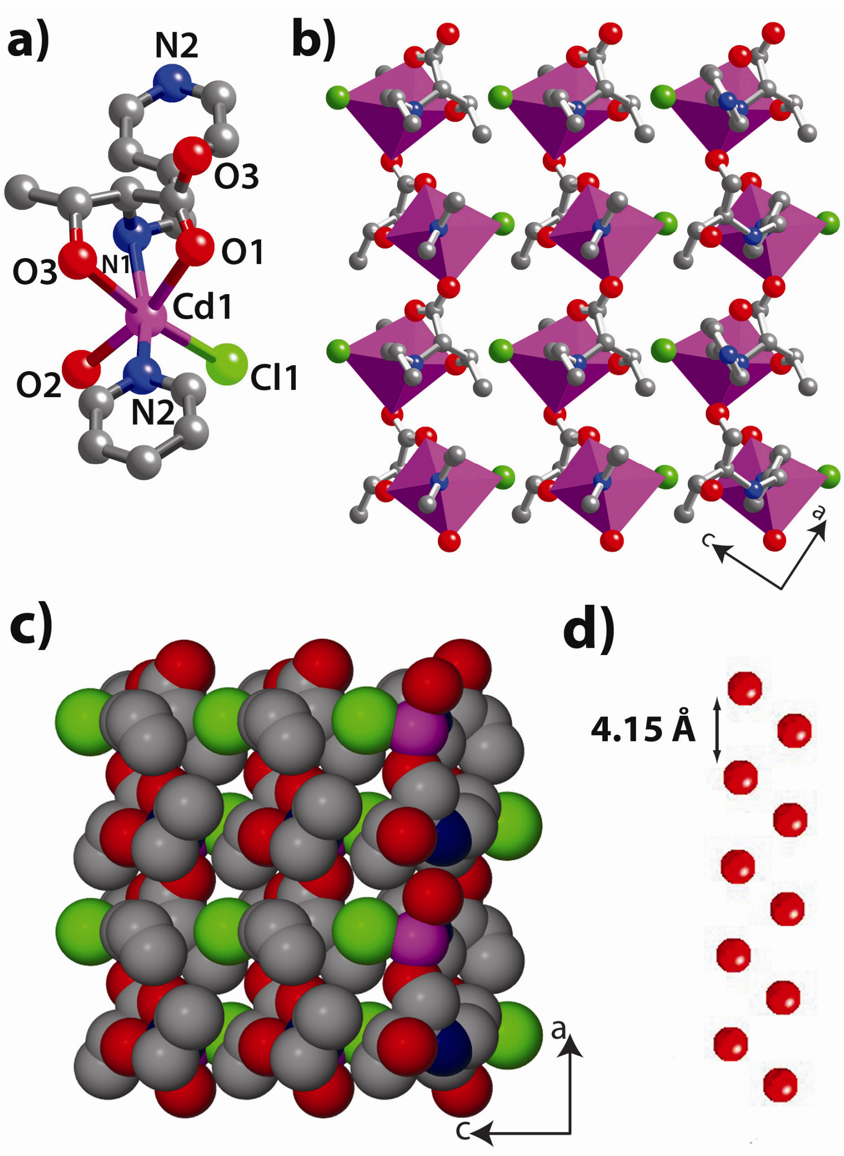

Figure 2.9: (a) SBU representation of the MOF ThrCdCl. (b) Polyhedral representation of lattice ThrCdCl viewed down the *c* axis. Magenta colored polyhedra represent Cd(II) centers, and chlorine atoms are shown as green balls. (c) 2D Lattice arrangement of ThrCdCl, along the *a* axis. Solvents are removed from the pores for clarity. (d) Lattice H_2O molecules are arranged viewed along *b* axis with a separation of 4.15 Å. Figure adapted from ref. 2.14.

found in MOFs LeuCdCl/LeuCdBr and SerCdCl/SerCdBr. MOF ThrCdCl and ThrCdBr have the halogen atoms (Cl^-/Br^-) that stay in axial positions opposite to the –OH group of the side arm (Figure 2.9a). These halogen atoms prevent this particular site to growth further. As a result these two MOFs (ThrCdCl and ThrCdBr) are forced to adopt 2D

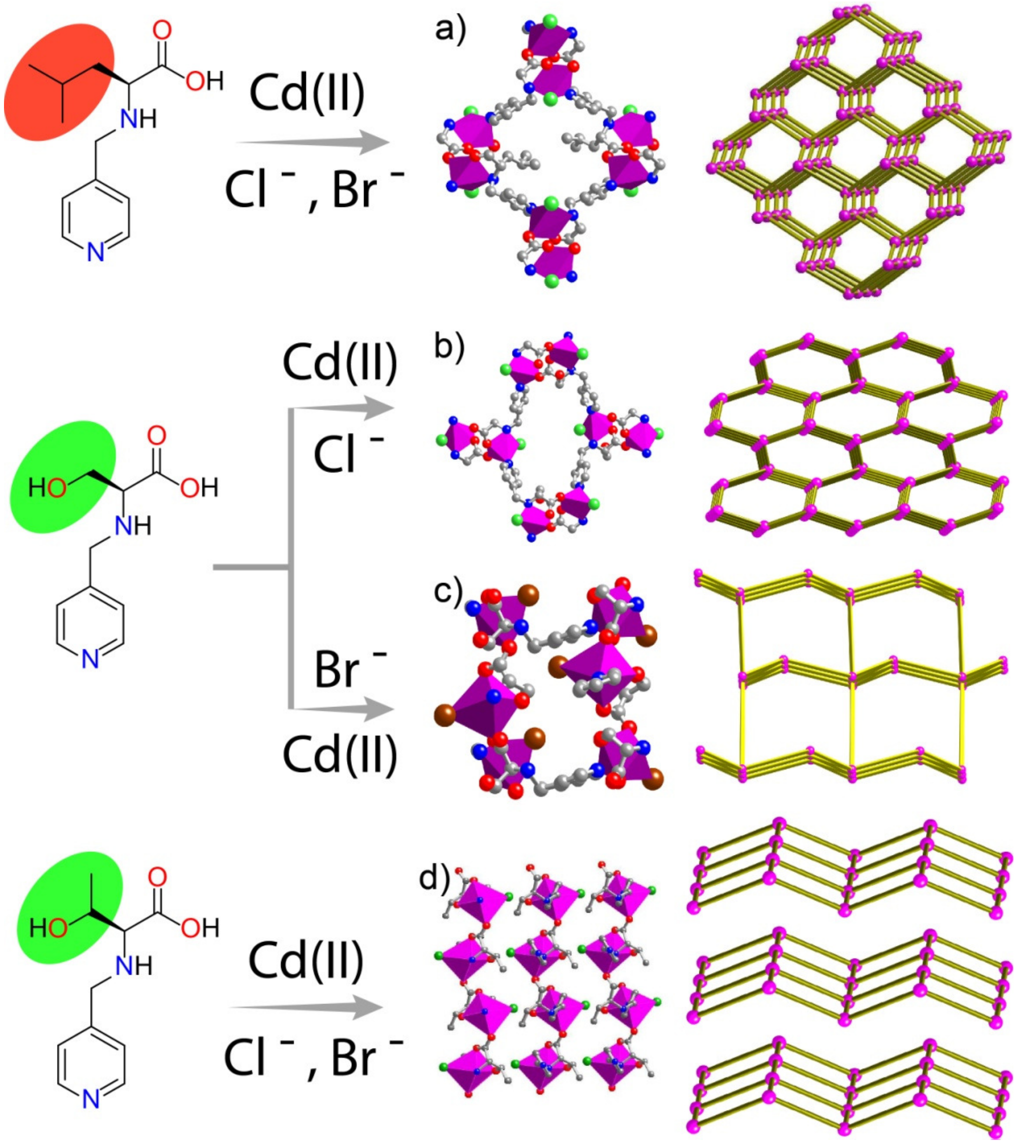

Figure 2.10: Structural comparison of the MOFs with their underlying nets. a) LeuCdCl and LeuCdBr. b) SerCdCl c) SerCdBr d) ThrCdCl and ThrCdBr. Figure adapted from ref. 2.14.

architecture. MOF ThrCdCl and ThrCdBr posses an inter-layer distance of ~6.8 Å (Figure 2.9b and 2.9c). These 2D layers propagate along *bc* plane where carboxylate bound molecular chains are linked by pyridyl units. In ThrCdCl, two H_2O molecules reside inside the crystal lattice and are strongly hydrogen bonded between each other [O19···O20, 2.741(5) Å] followed by additional weak interactions with metal bound Cl^- atoms [Cl···O19, 3.231(7); Cl···O20, 3.174(3) Å] (Figure 2.9d). Similarly in ThrCdBr, two lattice

H_2O molecules are hydrogen bonded with hydroxyl oxygens [O3···O4, 3.007(3); O3···O5, 2.690(4) Å] and halogen atoms [Br1···O4, 3.371(1); Br1···O5, 3.290(8) Å].

Comparing the molecular structures of MOF LeuCdCl, SerCdCl, and ThrCdCl (Figure 2.10), it is clear that ligand Ser contains an additional coordination site at the sidearm (-CH_2OH), compared to Leu. This plays a key role for the structural modification of MOF SerCdCl (Figure 2.10b) with respect to LeuCdCl (Figure 2.10a). Similarly comparing SerCdCl with ThrCdCl we could find that the lattice arrangement in MOF ThrCdCl is 2D (Figure 2.10d) rather than a 3D structure, even though the binding mode of Ser and Thr are similar. This observation indicates that changing the bulkiness of the sidearm [from -CH_2OH to –$CH(OH)CH_3$] create steric crowding near the carboxylate oxygen co-ordination site, which restrict the in-plane rotation of the carboxylate moiety. As a result the molecular system adopts a 2D architecture in MOF ThrCdCl**.** Moreover, architectural diversity observed from MOF SerCdCl to SerCdBr can be anticipated by the increased bulkiness of the halogen atom (from Cl^- to Br^-) and different bridging modes of the carboxylate moieties, which results in two kinds of Cd(II) centers (in MOF SerCdBr) rather than only one observed in the former case (Figure 2.10c). Hence, it is evident that those halogen atoms, along with the side arms, play a pivotal role for structural diversity among the aforementioned MOFs.

2.2.2 X-ray powder diffraction analysis and Thermo-gravimetric Analysis:

Thermo-gravimetric analysis (TGA) performed on as-synthesized MOFs revealed that ThrZnOAc has high thermal stability for all data regarding guest mobility and thermochemical stability. The TGA trace for ThrZnOAc showed a gradual weight-loss step of 19% [4.3 H_2O; calcd. 21% for 5 H_2O molecules per SBU] (25–120 °C), corresponding to the escape of all H_2O molecules trapped in the pores followed by a plateau (120–210 °C) indicating its high thermal stability in absence of guest molecules (Figure 2.11a). Further weight loss (~55%) indicates the decomposition of the framework. Similar trend has been observed in case of ValZnOAc and AlaZnOAc corresponds to escape of occluded H_2O molecules followed by framework disruption.

Confirmation of the phase purity of the bulk material was carried out on ThrZnOAc using powder X-ray diffraction (PXRD) experiments. Experimental and simulated PXRD patterns are shown in the Figure 2.11b. All the major peaks of experimental PXRD match quite well with the simulated one, indicating good crystalline phase purity in the bulk

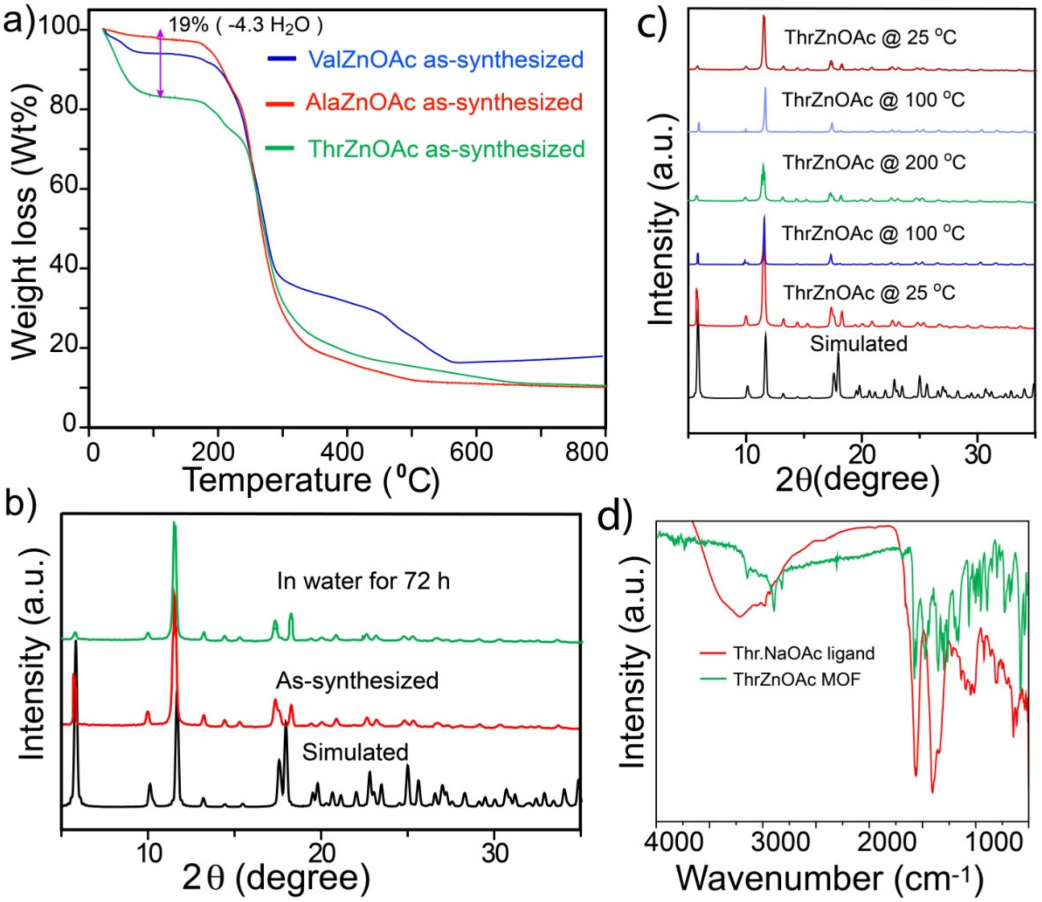

Figure 2.11: (a) Thermogravimetric analysis of ThrZnOAc compared with their valine and alanine analogue, i.e. ValZnOAc and AlaZnOAc, showing release of all guest water molecules at ~100 °C. (b) Powder XRD pattern of ThrZnOAc at different condition (red; as-synthesized at room temperature, green; in water at room temperature for 72 h. (c) VT-PXRD data for ThrZnOAc compared with simulated one shows stability upto 200 °C. d) FT-IR spectra of the ligand ThrOAc compared to MOF ThrZnOAc. Figure adapted from ref. 2.13.

material. The variable temperature PXRD measurements (VT-PXRD) (Figure 2.11c) were performed to explore the thermal stability, framework rigidity as well as crystallinity of ThrZnOAc at elevated temperature range (upto 200 °C). The VTPXRD pattern is in well agreement with the simulated one, showing the thermal stability as well as crystallinity of the material at elevated temperatures. However, the peak broadening at higher temperature might be attributed to structural flexibility of the frameworks upon desolvation as well as thermal vibration of the heavy atoms. Concisely, ThrZnOAc exhibit high thermal stability as well as degree of crystallinity even at higher temperature (upto 200 °C) as evident from VTPXRD and TGA profile. These aforementioned feature along with easy synthesis from inexpensive starting materials with bulk scale phase purity put ThrZnOAc above 0D/1D amino acid based complexes from practical application perspective.

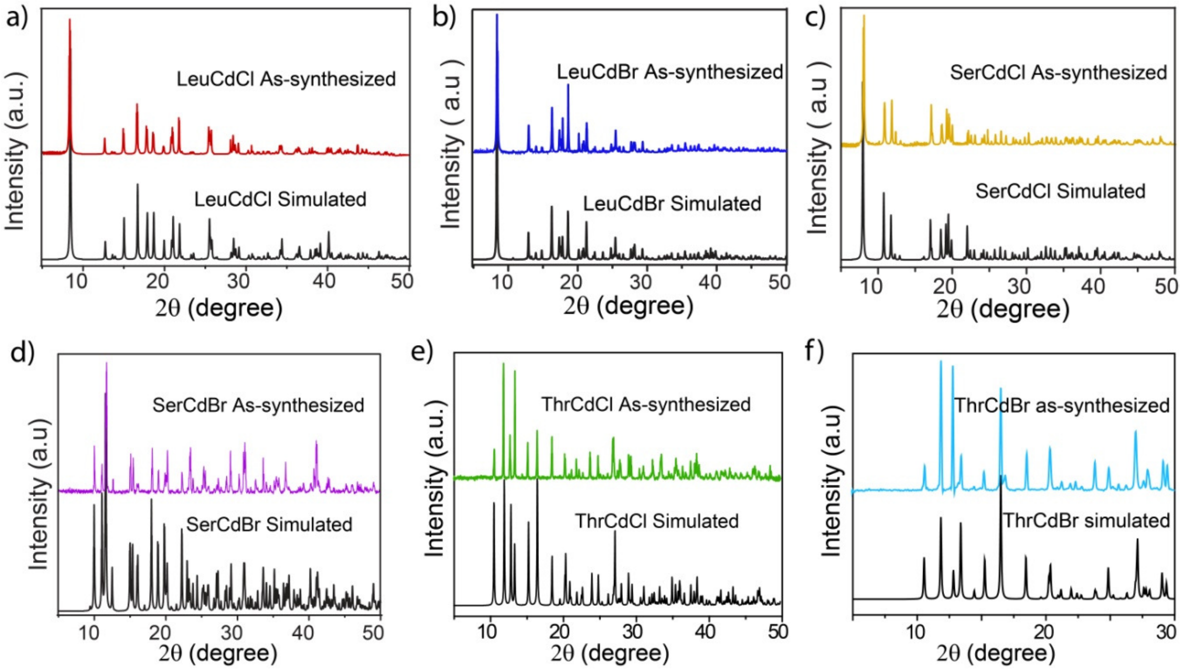

Figure 2.12: Comparison of the experimental PXRD pattern of as-synthesized MOF (top) with the simulated from its single crystal structure (bottom). a) LeuCdCl b) LeuCdBr c) SerCdCl d) SerCdBr e) ThrCdCl f) ThrCdBr. Figure adapted from ref. 2.14.

Thermal gravimetric analysis (TGA) performed on as-synthesized Cd(II) based MOFs revealed that these compounds have high thermal stability for all data regarding guest mobility and thermal stability. The TGA trace for MOF LeuCdCl showed a gradual weight-loss step of 4.3% [1 H_2O; calcd. 4.6%] (100–120 °C), corresponding to the escape of all H_2O molecules trapped in the pores followed by a plateau (120–280 °C) indicating its high thermal stability in absence of guest molecules (Figure 2.14). Further weight loss (~35%) indicates the decomposition of the framework. Similar trend has been observed in case of MOF LeuCdBr. Analysis of TGA trace for MOF SerCdCl reveals 4.4% weight loss [1 H_2O; calcd. 4.9%] (100–140 °C), and the dehydrated framework is stable upto 280 ^{0}C, as evident from the plateau region in the TGA traces. MOF SerCdBr shows weight loss step of 6.2% [$3H_2O$; calcd. 6.5%] (100–140 °C) which corresponds to the dehydration phenomena. MOF ThrCdCl exhibit 5% weight loss [$2H_2O$; calcd. 5.1%] corresponds to escape of occluded H_2O molecules. MOF ThrCdBr follows the similar trend like MOF ThrCdCl. It is noteworthy that MOFs ThrCdCl and ThrCdBr posses lower decomposition temperature (200 °C) than MOFs LeuCdCl/LeuCdBr and SerCdCl/SerCdBr (280 °C) due to lower degree of dimensionality. In order to confirm the phase purity of the bulk materials, powder X-ray diffraction (PXRD) experiments were carried out on these MOFs (LeuCdCl/LeuCdBr, SerCdCl/SerCdBr and ThrCdCl/ThrCdBr). Experimental and simulated PXRD patterns are shown in the Figure 2.12. All the major peaks of experimental PXRD of the six Cd-MOFs match quite well with those of simulated PXRD, indicating their reasonable crystalline phase purity in the bulk scale. The variable temperature PXRD measurements (Figure 2.13) were performed to explore the thermal stability, framework rigidity as well as crystallinity of these Cd-MOFs at elevated temperature ranges (upto 200 °C). The VTPXRD patterns are well matched with the simulated one, showing the thermal stability as well as crystallinity of these materials at elevated temperatures. However, peak splitting occurs (at 2θ = 16.5 for MOF ThrCdBr) at higher temperatures in some cases, which might be attributed to structural flexibility of the

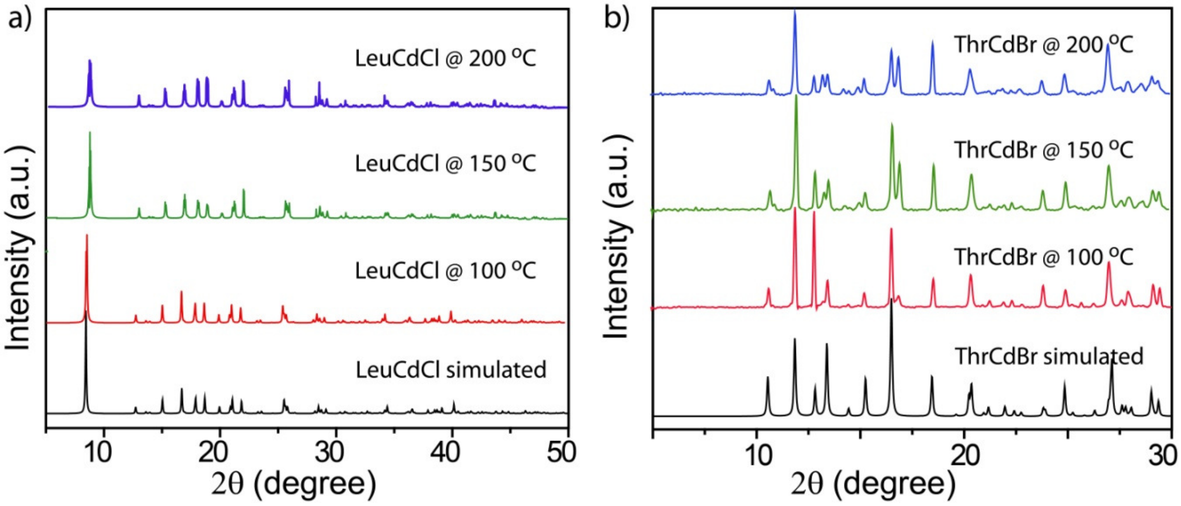

Figure 2.13: Comparison of the experimental VT-PXRD patterns of as-synthesized MOF (top) with the simulated from its single crystal structure (bottom). a) LeuCdCl b) LeuCdBr c) SerCdCl d) SerCdBr e) ThrCdCl f) ThrCdBr. Figure adapted from ref. 2.14.

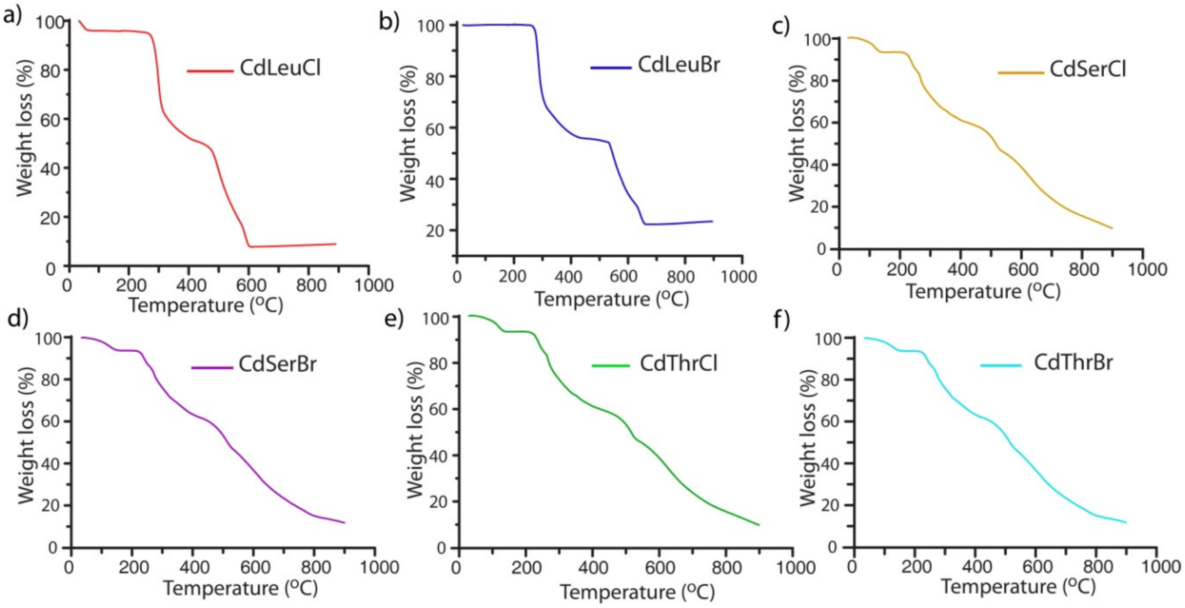

Figure 2.14: TGA analysis of the MOFs. a) LeuCdCl b) LeuCdBr c) SerCdCl d) SerCdBr e) ThrCdCl f) ThrCdBr. Figure adapted from ref. 2.14.

frameworks upon desolvation as well as thermal vibration of the heavy atoms. The high thermal stability as well as degree of crystallinity, as evident from VTPXRD and TGA profile, puts these materials above 0D/1D amino acid based complexes from practical application point of view.

2.2.3 Solvent adsorption studies on the MOFs:

MOFs, by definition, constituted from coordination bonds between metal ions and organic linkers (either anionic or neutral). Hence, major drawback of MOFs lies in their susceptibility towards hydrolysis in presence of moisture to form corresponding metal oxide/hydroxide and bare linker, followed by collapse of the porous architecture. Only few MOFs with porous architecture (e.g. ZIF 8, MIL-101, UiO-66) can withstand humidity [1.46]. In this regard, we have explored a family of porous homochiral MOFs (Val/AlaZnX, X being Cl^-, Br^-, HCO_2^- and $CH_3CO_2^-$) with *unh* topology, which exhibit excellent hydrolytic stability as well as retention of crystallinity as verified by well matched simulated and Powder XRD patterns with Powder XRD patterns collected at humidified condition Powder XRD patterns. We showed that the hydrophilicity can be finely tuned by simply changing the coordinated anions (Cl^-, Br^-, HCO_2^- and $CH_3CO_2^-$) in the framework (discussed in upcoming chapters) and same anion substitution ($CH_3CO_2^-$). In all cases, the

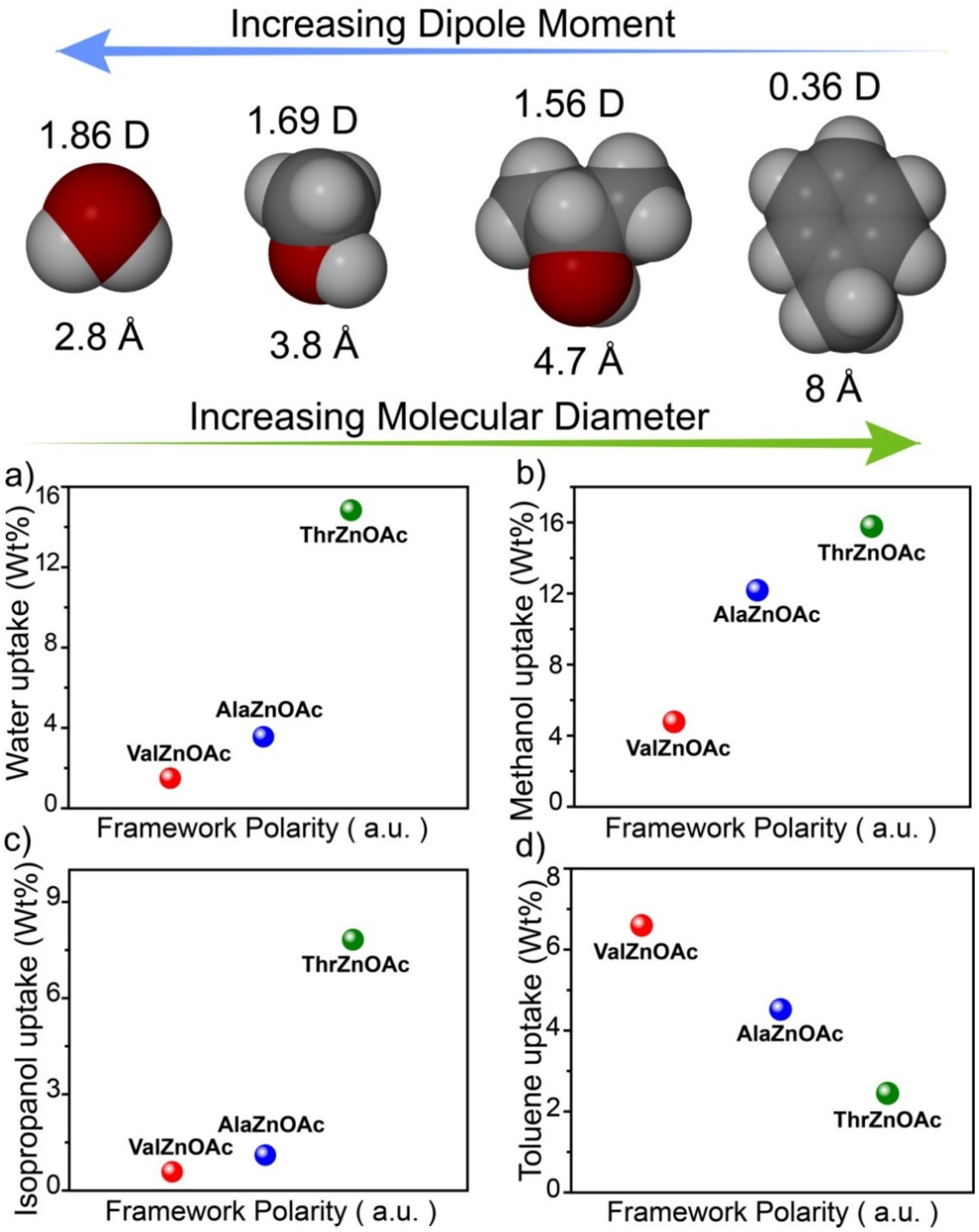

Figure 2.15: Arrangement of solvent molecules according to their polarity along with their differential dipole moment, which follow the reverse order with respect to each other. (a) Water adsorption trend (b) Methanol adsorption and (c) Isopropanol adsorption trend of the MOFs. (d) Toluene adsorption trend show the reverse trend in all three MOFs. Figure adapted from ref. 2.13.

pyridyl moieties constitute the cylindrical hydrophobic pore wall of the framework and the Zn(II) coordinated acetate groups are poking towards the pore surface to maintain a hydrophobic environment. Moreover, the hydrophobic isopropyl groups (in case of ValZnOAc) and methyl groups (in case of AlaZnOAc) are directed from the pore wall to impart additional hydrophobicity inside the pores. Although twelve water molecules per pore [two water molecules per asymmetric unit and Z (number of asymmetric unit per unit cell) being 6] are present in case of ValZnOAc and AlaZnOAc but there is no intermolecular hydrogen bonding within the water molecules or among the water molecules and the framework backbone. The only difference in ThrZnOAc is the 2-hydroxyethyl [–

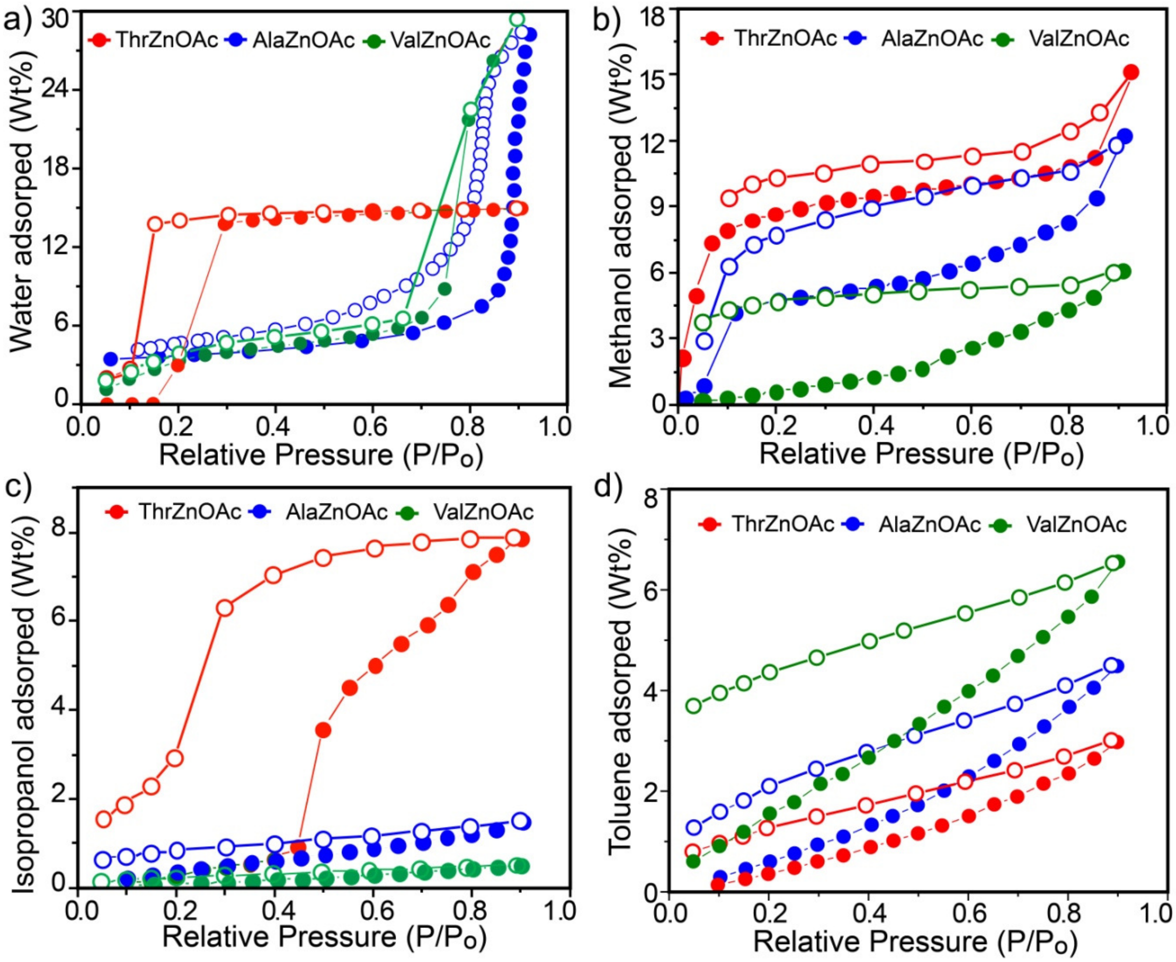

Figure 2.16: (a) Water sorption isotherm of ThrZnOAc featuring high hydrophilic interaction at low partial pressure, while ValZnOAc and AlaZnOAc exhibit pore condensation behaviour. (b) Methanol sorption profile of ValZnOAc, AlaZnOAc and ThrZnOAc at STP. (c) Isopropanol sorption isotherm reveal higher uptake in case of ThrZnOAc while ValZnOAc and AlaZnOAc remain almost non-adsorbent. (d) However, toluene sorption isotherm of all three MOFs exhibits the reverse trend. Figure adapted from ref. 2.13.

CH(OH)CH_3] sidearm where hydroxyl group (–OH) is poking through pore wall which is hydrophilic in nature, resulted in enhanced polar interactions between framework backbone and solvent water molecules, leading to increased accommodation (thirty in numbers per pore; five water molecules per asymmetric unit and Z being 6) of water molecules in case of ThrZnOAc. We have carefully unveiled the solvent uptake property using different solvent (water, methanol, isopropanol and toluene) sorption isotherm of the MOFs (Figure 2.16), which reveal their backbone, resulting in hydrophilic environment in Val/AlaZnCl whereas hydrophobic in case of ValZnOAc or AlaZnOAc (discussed in detail in the next chapters). However, effect of change in sidearm residue of the amino acid has not been

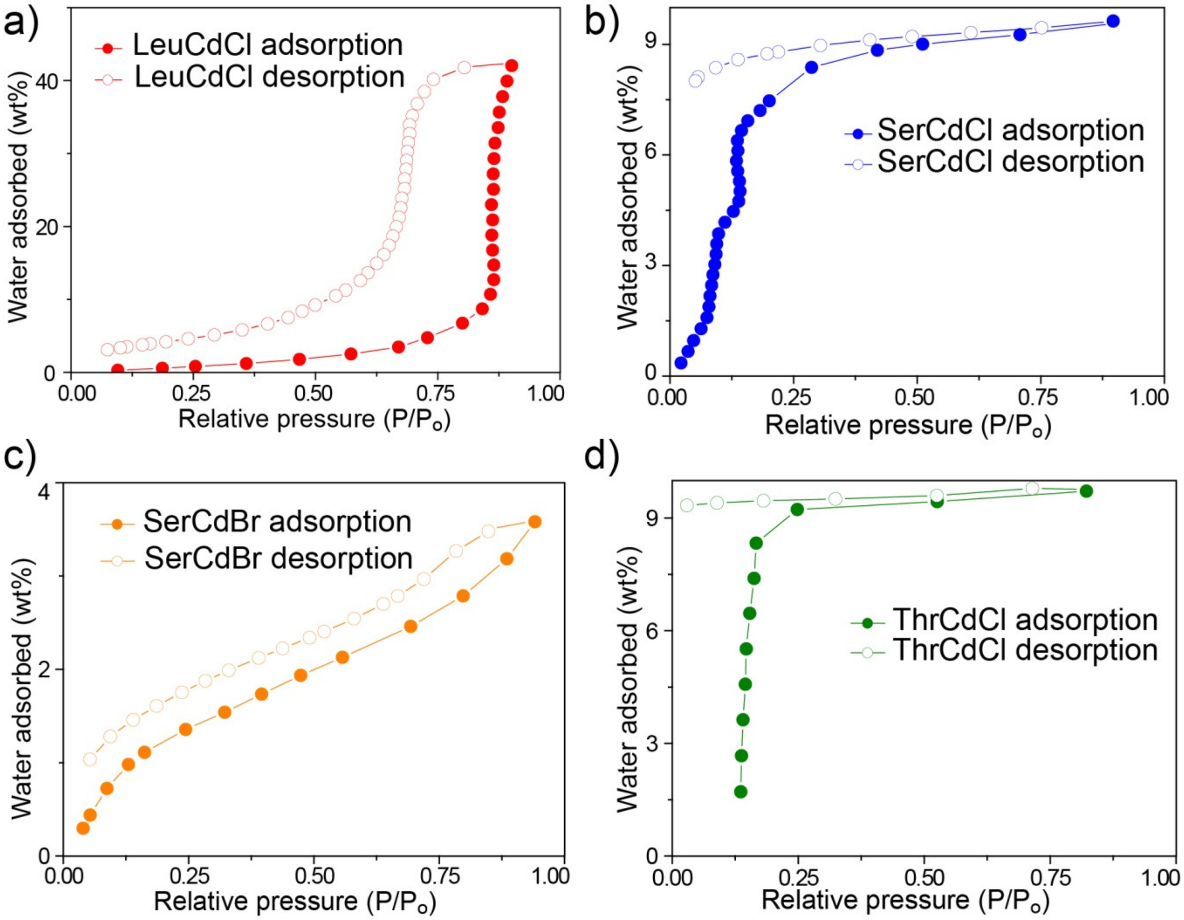

Figure 2.17: a) H_2O sorption of MOF LeuCdCl showing pore condensation behavior along with sorption hysteresis. b) H_2O sorption curve for MOF SerCdCl having ~10 wt% H_2O sorption capability and high H_2O affinity at lower humidity (P/P_0=0.0-0.2) region. c) H_2O sorption isotherm for MOF SerCdBr shows very low H_2O uptake (~3.5 wt%) due to congestion of the pore by bulky bromine atom. d) H_2O sorption profile of MOF ThrCdCl**,** which exhibit comparable uptake (~10 wt%) and high H_2O affinity at lower P/P_0 values. Figure adapted from ref. 2.14.

studied thoroughly yet, remaining a crucial part to be explored in this regime. In order to improve on the hydrophilicity of intrinsically hydrophobic MOFs, we have identified the acetate analogues of the *unh* series (viz. ValZnOAc, AlaZnOAc) as a model hydrophobic system and prepare their hydrophilic threonine analogue i.e. ThrZnOAc with isostructural integrity differential interaction with the framework backbone. The reason behind the choice of these solvents is their variable size and dipole moment (Figure 2.15). In terms of size the trend could be arranged as $H_2O < CH_3OH < (CH_3)_2CH(OH) < C_7H_8$ whereas in terms of dipole moment they follow the exact opposite order ($H_2O > CH_3OH > (CH_3)_2CH(OH) > C_7H_8$). All these MOFs show sorption hysteresis, confirming the solvophilic interaction between the pore surface and the solvent molecules. ValZnOAc and AlaZnOAc exhibit hydrophobic pores with dangling isopropyl or methyl chains poking within the molecular cavity, as evident from their very low water uptake at low pressure (less than 0.5 P/P_o) followed by pore condensation behavior at higher pressure during the water sorption isotherm measurement, measured at STP. This pore condensation of the water molecules occur on the surface of the ValZnOAc and AlaZnOAc is a common phenomenon for porous hydrophobic materials like BPL carbon [2.6]. However, ThrZnOAc, as expected, exhibit high water uptake capacity (14 wt% at STP) at very low relative pressure ($P/P_o \sim 0.25$) (Figure 2.16a). In case of methanol sorption, ValZnOAc exhibit lowest methanol uptake (6 wt% for $P/P_o \sim 0.9$ at STP) among these MOFs, which improved a bit in case of AlaZnOAc (12 wt% for $P/P_o \sim 0.9$ at STP). ThrZnOAc posses highest methanol affinity (15 wt% for $P/P_o \sim 0.9$ at STP) among these MOFs owing to the polar pore surface (Figure 2.16b). Isopropanol sorption study also revealed the similar trend. ThrZnOAc exhibit moderate isopropanol uptake (7 wt% for $P/P_o \sim 0.9$ at STP) while ValZnOAc and AlaZnOAc exhibit negligible sorption (Figure 2.16c). To assay whether solvent polarity and hydrophobicity plays a pivotal role in aforementioned MOFs, we have chosen toluene as solvent for uptake measurements, having high hydrophobicity, low dipole moment (0.36 D) and comparable molecular diameter (~8 Å) with respect to the pores of the MOFs (~8.2 Å). As expected, ValZnOAc showcases higher toluene sorption capacity (6 wt% at STP; $P/P_o \sim 0.9$) than AlaZnOAc (4 wt% at STP; $P/P_o \sim 0.9$) and ThrZnOAc (2 wt% at STP; $P/P_o \sim 0.9$) (Figure 2.16d), proving our concept that hydrophobicity as well as solvent polarity are the driving force in solvent uptake capabilities of these MOFs. Hence, we can summarize that introduction of threonine moiety inside the MOF backbone with *unh* topology proved to be an effective strategy of enhancing the solvophilic interaction inside the pore which eventually results in high polar solvent uptake.

Hydrolytic stability of MOFs is one among the most important issues for practical application. However, most of the MOFs reported till date is highly susceptible towards humidity including some well known MOFs like MOF 177, MOF 5 etc. All six MOFs reported herein exhibit excellent H_2O sustainability verified by well matched simulated and humidified Powder XRD pattern. We have explored the H_2O sorption isotherm of the MOF LeuCdCl, SerCdCl, SerCdBr and ThrCdCl (Figure 2.17), which reveals its possible application as a desiccant material like molecular sieve and silica gel. All these MOFs show sorption hysteresis, confirming the hydrophilic interaction between the polar pore surface and the solvent water molecules. Among these MOFs, MOF LeuCdCl posses the most hydrophobic pore with dangling isopropyl chain poking within the molecular cavity. It justifies the low water uptake (~5 wt%) even upto P/P_o value of 0.8. However, at higher P/P_o values (0.8-1.0), the pore condensation of the water molecules occur on the surface of the MOF LeuCdCl (Figure 2.17a) which is a common phenomenon for porous hydrophobic materials like BPL carbon [2.6]. On the contrary, MOF SerCdCl and ThrCdCl also show good sorption capacity of ~10 wt% (Figure 2.17b and 2.17d, respectively). Enrichment of highly hydrophilic chlorine, oxygen and nitrogen molecules within the framework cavity is chiefly responsible for high H_2O uptake and hysteresis of water sorption isotherm of MOF SerCdCl and ThrCdCl. In case of MOF ThrCdCl**,** highly hydrophilic interlayer void plays a pivotal role as H_2O molecules connect the 2D layers via strong interlayer hydrogen bonding. MOF SerCdBr is almost non-porous due to the presence of bulky bromine atom within the pore aperture, which is evident from its very low H_2O uptake (~3.5 wt%) (Figure 2.17c). Interestingly, MOF SerCdCl and ThrCdCl shows very high H_2O uptake at lower P/P_o values (0.0-0.2). This is due to the fact that open framework type architecture (MOF SerCdCl) as well as strong interlayer hydrogen bonding (MOF ThrCdCl) are responsible for high H_2O affinity of these MOFs, showing its capability to work as a suitable material as desiccant for packaging application.

2.3 Conclusion:

In conclusion, we have synthesized a new Zn(II) based homochiral MOF, viz. ThrZnOAc with rare *unh* topology by simply changing the amino acid residue (from valine/alanine to threonine), keeping the framework integrity same. This resulted in accommodation of more water molecules in of the pores of ThrZnOAc with respect to previously reported ValZnOAc and AlaZnOAc due to presence of intermolecular hydrogen bonding interaction between 2-hydroxyethyl [–CH(OH)CH_3] sidearm and solvent water molecule, an unique phenomenon absent in the later cases. On the other hand, Six new Cd-containing homochiral metal–organic framework materials have been synthesized hydrothermally using amino acid derived homochiral links with $Cd(CH_3COO)_2{\cdot}2H_2O$. Size of the sidearm in different amino acid derivatives and anions (Cl^-/Br^-) play an important role in the structural diversity among these MOFs. MOFs LeuCdCl and LeuCdBr show a 3D architecture with a 1D channel. On the other hand, effect of anions and sidearm dramatically produce diverse structural motifs in MOFs SerCdCl and SerCdBr. A large open spaced cavity was observed in MOF SerCdCl but it decreased subsequently after Br-substitution in MOF SerCdBr due to the structural modification. In MOF ThrCdCl and ThrCdBr, a large structural variation was clearly observed after slight variation in side arm where the resulting MOFs adopt a 2D lattice arrangement rather than 3D as compared to MOF SerCdCl and SerCdBr. These MOFs exhibit thermal stability as well as retention of crystallinity upto 200 °C. ThrZnOAc, AlaZnOAc and ValZnOAc show distinct solvatophilic characteristics and substitution of amino acid resulted in enhanced solvent (water, methanol, isopropanol sorption isotherm) uptake capacity in case of ThrZnOAc. In terms of hydrophilic solvents e.g. H_2O, CH_3OH and $(CH_3)_2CH(OH)$ uptake these MOFs align as ThrZnOAc> AlaZnOAc> ValZnOAc while in case of hydrophobic solvent e.g. toluene uptake these MOFs put themselves in reverse order. These MOFs exhibit thermal stability as well as retention of crystallinity upto 200 °C. It is noteworthy that there are very few chiral MOFs reported based on amino acids or its derivatives. Among the limited reports on amino acid based MOFs, owing to high substrate binding ability of amino acids, in most cases the resulting molecules are 0D/1D orientation with very few higher order of molecular arrangements. So introduction of amino acids/amino acid derivatives in chiral MOF synthesis will be a good roadmap for development of promising chiral catalyst or chiral separation material. The aforementioned rationale for synthesis of functionalized chiral MOFs will surely find its utility in industrially relevant chiral solvent sorption and separation. We hope that our finding will lead to incorporation of diverse amino acid moiety inside the MOF backbone for industrially relevant gas/solvent sorption and separation, and desiccant material for packaging purpose.

2.4 Experimental details:

2.4.1 Materials:

$Cd(CH_3COO)_2{\cdot}2H_2O$, $Zn(CH_3COO)_2{\cdot}2H_2O$, L-leucine, L-serine, L-threonine, sodium borohydride, and 4-pyridinecarboxaldehyde were purchased from Aldrich Chemicals. All starting materials were used without further purification. All experimental operations were performed in air.

2.4.2 Synthetic methods:

2.4.2.1 Synthesis of the ligands:

a) Synthesis of (Pyridin-4-yl)methylamino-threonine.NaOAc [ThrOAc]: To an aqueous solution (10 mL) of L-threonine (2 g, 17 mmol) and Na_2CO_3 (0.91 g, 8.5 mmol), 4-pyridinecarboxaldehyde (1.82 g, 17 mmol) in MeOH (10 mL) was added slowly. The solution was stirred for 1 h and cooled in an ice bath. $NaBH_4$ (0.76 g, 20.4 mmol) in 5 mL of H_2O was added. The mixture was stirred for 3 h, and 3 N AcOH was used to adjust the pH to 5−6. The clear solution was stirred further for 2 h and then evaporated to dryness. The solid was extracted in hot and dry MeOH (150 mL×3), and the filtrate was evaporated to get the ligand along with sodium acetate salt in form of a white powder. Yield: 2.7 g, 70%. ^1H NMR (D_2O, ppm): -CH_3 (1.12, d, 3H), -CH (1.66, m, 1H), -CH_2 (2.19, dd, 2H), -HN-CH (3.55, d, 1H), -HN (3.69, m, 1H), -CH_2 (4.19, s, 2H), py-H (7.49, d, 2H), py-H (8.56, d, 2H).m.p.200 °C. Elemental Analysis: C, 53.79; H, 6.60; N, 9.65; (calc.); C, 53.12; H, 6.21; N, 9.38; (obs.).

b) Synthesis of (Pyridin-4-yl)methylamino-leucine.NaCl [LeuCl]: The ligand (LeuCl) was prepared using a modified literature procedure. To an aqueous solution (10 mL) of L-leucine (2 g, 15 mmol) and Na_2CO_3 (0.78 g, 7.5 mmol), 4-pyridinecarboxaldehyde (1.60 g, 15 mmol) in MeOH (10 mL) was added slowly. The solution was stirred for 1 h and cooled in an ice bath. $NaBH_4$ (0.76 g, 20.4 mmol) in 10 mL of water was added. The mixture was stirred for 1 h, and 3 N HCl was used to adjust the pH to 5−6. The solution was stirred further for 2 h and then evaporated to dryness. The solid was extracted in hot and dry MeOH (150 mL×3), and the filtrate was evaporated to get a white powder. Yield: 2.7 g, 70%. IR (KBr, cm^{-1}): ν_{OH}, 3406; ν_{as}(CO2), 1626; ν_s(CO2), 1412. ^{1}H NMR (D_2O, ppm): -CH_3 (0.90, d, 6H), -CH (1.66, m, 1H), -CH_2 (2.19, dd, 2H), -HN-CH (3.55, d, 1H), -HN (3.69, m, 1H), -CH_2 (4.19, s, 2H), py-H (7.49, d, 2H), py-H (8.56, d, 2H).

c) Synthesis of (Pyridin-4-yl)methylamino-leucine.NaBr [LeuBr]: The ligand (LeuBr) was prepared exactly as LeuCl, except HBr was used instead of HCl for pH adjustment. Yield: 3.0 g, 66%. IR (KBr, cm^{-1}): ν_{OH}, 3414; ν_{as}(CO2), 1612; ν_s(CO2), 1409. ^{1}H NMR (D_2O, ppm): -CH_3 (0.92, d, 6H), -CH (1.65, m, 1H), -CH_2 (2.19, dd, 2H), -HN-CH (3.57, d, 1H), -HN (3.71, m, 1H) -CH_2 (4.17, s, 2H), py-H (7.48, d, 2H), py-H (8.46, d, 2H).

d) Synthesis of (Pyridin-4-yl)methylamino-serine.NaCl [SerCl]: To an aqueous solution (10 mL) of L-serine (2 g, 19 mmol) and Na_2CO_3 (0.99 g, 9.5 mmol), 4-pyridinecarboxaldehyde (2.03 g, 19 mmol) in MeOH (10 mL) was added slowly. The solution was stirred for 1 h and cooled in an ice bath. $NaBH_4$ (0.76 g, 20.4 mmol) in 10 mL of water was added. The mixture was stirred for 1 h, and 3 N HCl was used to adjust the pH to 5−6. The solution was stirred further for 2 h and then evaporated to dryness. The solid was extracted in hot and dry MeOH (150 mL×3), and the filtrate was evaporated to get a white powder. Yield: 2.6 g, 60%. IR (KBr, cm^{-1}): ν_{OH}, 3420; ν_{as}(CO2), 1602; ν_s(CO2), 1410. ^{1}H NMR (D_2O, ppm): -CH_2 (3.65, dd, 2H), -HN-CH (3.58, m, 1H), -CH_2 (4.19, s, 2H), py-H (7.45, d, 2H), py-H (8.52, d, 2H).

e) Synthesis of (Pyridin-4-yl)methylamino-serine.NaBr [SerBr]: The ligand SerBr was prepared exactly as SerCl except HBr was used instead of HCl for pH adjustment. Yield: 3.3 g, 63%. IR (KBr, cm^{-1}): ν_{OH}, 3382; ν_{as}(CO2), 1619; ν_s(CO2), 1412. ^{1}H NMR (D_2O, ppm): -CH_2 (3.61, dd, 2H), -HN-CH (3.53, m, 1H), -CH_2 (4.22, s, 2H), py-H (7.47, d, 2H), py-H (8.52, d, 2H).

f) Synthesis of (Pyridin-4-yl)methylamino-threonine.NaCl [ThrCl]: To an aqueous solution (10 mL) of L-threonine (2 g, 16 mmol) and Na_2CO_3 (0.84 g, 8.0 mmol), 4-pyridinecarboxaldehyde (1.71 g, 16 mmol) in MeOH (10 mL) was added slowly. The solution was stirred for 1 h and cooled in an ice bath. $NaBH_4$ (0.75 g, 20.0 mmol) in 10 mL of water was added. The mixture was stirred for 1 h, and 3 N HCl was used to adjust the pH to 5–6. The solution was stirred further for 2 h and then evaporated to dryness. The solid was extracted in hot and dry MeOH (150 mL×3), and the filtrate was evaporated to get a white powder. Yield: 2.7 g, 70% yield. IR (KBr, cm^{-1}): ν_{OH}, 3353; $\nu_{as}(CO2)$, 1597; $\nu_{s}(CO2)$, 1412. ^1H NMR (D_2O, ppm): -CH_3 (1.18, dd, 2H), -CH (3.72, dd, 1H), -HN-CH (3.55, m, 1H), -CH_2 (4.20, s, 2H), py-H (7.46, d, 2H), py-H (8.50, d, 2H).

g) Synthesis of (Pyridin-4-yl)methylamino-threonine.NaBr [ThrBr]: The ligand ThrBr was prepared exactly as ThrCl except HBr was used instead of HCl for pH adjustment. Yield: 3.4 g, 75% yield. IR (KBr, cm^{-1}): ν_{OH}, 3382; $\nu_{as}(CO2)$, 1607; $\nu_{s}(CO2)$, 1409. ^1H NMR (D_2O, ppm): -CH_3 (1.21, dd, 2H), -CH (3.74, dd, 1H), -HN-CH (3.53, m, 1H), -CH_2 (4.21, s, 2H), py-H (7.44, d, 2H), py-H (8.49, d, 2H).

2.4.2.2 Synthesis of the MOFs:

a) Synthesis of ValZnCl and AlaZnCl: Detailed synthesis of ValZnOAc and AlaZnOAc is described in the next chapters.

b) Synthesis of $[\{Zn(Thr)(OAc)\}(H_2O)_5]_\infty$ (ThrZnOAc): To an aqueous solution (1 mL) of Thr.NaOAc (0.05 g, ~0.2 mmol), $Zn(CH_3COO)_2{\cdot}2H_2O$ (0.022 g, 0.1 mmol) in 5ml MeOH was added and sonicated for 10 min to produce a clear solution, which was left for evaporation for 48-72 h to produce rod-shaped transparent crystals. Although NaOAc has been used, no incorporation of Na(I) ion incorporated in the crystal structure. Yield: 0.025 g, 59%. Elemental analysis: calcd C (37.22%), H (4.94%), N (7.23%); found C (38.20%), H (4.88%), N (7.25%).

c) Synthesis of $[\{Cd(Leu)(Cl)\}(H_2O)]_\infty$ (LeuCdCl): To an aqueous solution (2 mL) of LeuCl (0.05 g, 0.2 mmol), $Cd(CH_3COO)_2{\cdot}2H_2O$ (0.027 g, 0.1 mmol) was added and sonicated for 10 min. The clear solution was kept in a tightly capped 5 mL vial for 24 h at 90 °C to produce rod-shaped transparent crystals. Yield: 0.025 g, 65%. IR (KBr, cm^{-1}): ν_{OH}, 3421; ν_{N_H}, 2927; $\nu_{as}(CO2)$, 1598; $\nu_{s}(CO2)$, 1400. Elemental analysis: calcd C (37.22%), H (4.94%), N (7.23%); found C (38.20%), H (4.88%), N (7.25%).

d) Synthesis of $[Cd(Leu)(Br)]_\infty$ (LeuCdBr): To an aqueous solution (2 mL) of LeuBr (0.05 g, 0.2 mmol), $Cd(CH_3COO)_2{\cdot}2H_2O$ (0.027 g, 0.1 mmol) was added and sonicated for 10 min. The clear solution was kept in a tightly capped 5 mL vial for 24 h at 90 °C to produce rod-shaped transparent crystals. Yield: 0.025 g, 65%. IR (KBr, cm^{-1}): ν_{OH}, 3421;

ν_{N_H}, 2927; ν_{as}(CO2), 1598; ν_s(CO2), 1400. Elemental analysis: calcd C (37.22%), H (4.94%), N (7.23%); found C (38.20%), H (4.88%), N (7.25%).

e) Synthesis of [{Cd(Ser)(Cl)}(H_2O)]$_\infty$ (SerCdCl): To an aqueous solution (2 mL) of SerCl (0.046 g, 0.2 mmol), Cd($CH_3COO)_2{}^{\cdot}2H_2O$ (0.027 g, 0.1 mmol) was added and sonicated for 10 min. The clear solution was kept in a tightly capped 5 mL vial for 24 h at 90 °C to produce rod-shaped transparent crystals. Yield: 0.023 g, 62%. IR (KBr, cm^{-1}): ν_{as}(CO2), 1625; ν_s(CO2), 1512. Elemental analysis: calcd C (32.19%), H (3.51%), N (7.50%); found C (32.2%), H (3.48%), N (7.47%).

f) Synthesis of [{Cd(Ser)(Br)}($H_2O)_{1.5}$]$_\infty$ (SerCdBr): To an aqueous solution (2 mL) of SerBr (0.055 g, 0.2 mmol), Cd($CH_3COO)_2{}^{\cdot}2H_2O$ (0.027 g, 0.1 mmol) was added and sonicated for 10 min. The clear solution was kept in a tightly capped 5 mL vial for 24 h at 90 °C to produce rod-shaped transparent crystals. Yield: 0.024 g, 58%. IR (KBr, cm^{-1}): ν_{OH}, 3445; ν_{as}(CO2), 1550; ν_s(CO2), 1427. Elemental analysis: calcd C (26.07%), H (3.40%), N (6.75%); found C (26.0%), H (3.41%), N (6.69%).

g) Synthesis of [{Cd(Thr)(Cl)}($H_2O)_2$]$_\infty$ (ThrCdCl): To an aqueous solution (2 mL) of ThrCl (0.05 g, 0.2 mmol), Cd($CH_3COO)_2{}^{\cdot}2H_2O$ (0.027 g, 0.1 mmol) was added and sonicated for 10 min. The clear solution was kept in a tightly capped 5 mL vial for 24 h at 90 °C to produce rod-shaped transparent crystals. Yield: 0.027 g, 70%. IR (KBr, cm^{-1}): ν_{OH}, 3642; ν_{as}(CO2), 1593; ν_s(CO2), 1433. Elemental analysis: calcd C (30.55%), H (4.35%), N (7.12%); found C (30.52%), H (4.36%), N (7.14%).

h) Synthesis of [{Cd(Thr)(Br)}($H_2O)_2$]$_\infty$ (ThrCdBr): To an aqueous solution (2 mL) of ThrBr (0.058 g, 0.2 mmol), Cd($CH_3COO)_2{}^{\cdot}2H_2O$ (0.027 g, 0.1 mmol) was added and sonicated for 10 min. The clear solution was kept in a tightly capped 5 mL vial for 24 h at 90 °C to produce rod-shaped transparent crystals. Yield: 0.028 g, 65%. IR (KBr, cm^{-1}): ν_{OH}, 3686; ν_{N_H}, 2924; ν_{as}(CO2), 1580; ν_s(CO2), 1395. Elemental analysis: calcd C (27.44%), H (3.91%), N (6.40%); found C (27.41%), H (3.92%), N (6.41%).

2.5 General characterization methods:

a) Powder X-Ray Diffraction (PXRD): Powder XRD patterns of the aforementioned MOF samples were analyzed to confirm the crystallinity as well as the phase purity of the bulk materials. Powder X-ray diffraction (PXRD) patterns were recorded on a Phillips

PANalytical diffractometer equipped with Cu K_α radiation (λ = 1.5406 Å), with a scan speed of 2° min^{-1} and a step size of 0.02° in 2θ. 50 mg of as synthesized materials were made pellet and subjected to analysis over glass slides.

b) Thermogravimetric Analysis (TGA) and Differential Scanning Calorimetry (DSC): TGA and DSC were performed on a SDT Q600 TG-DTA instrument. ca. 8 mg of the MOFs were heated from 25 to 800 °C under the N_2 flow at heating rate of 5 °C min^{-1}.

c) IR Spectroscopy: The Fourier transform (FT) infrared spectra of the MOFs were collected on a *PERKIN ELMER FT-IR SPECTRUM* (Nicolet) spectrometer. KBr pellets (2 mg MOF in 20 mg of KBr) were prepared and 50 scans were measured at 2 cm^{-1} resolution for each sample. The spectra were measured over the range of 4000-600 cm^{-1}.

b) Solvent Adsorption Analysis: Solvent adsorption studies were done to confirm the permanent porosity of the as synthesized sample as well as to determine the surface area accessible to the solvent molecules to get adsorbed onto the surface of the MOFs. All low-pressure Gas adsorption experiments (up to 1 bar) were performed on a *Quantachrome Quadrasorb* automatic volumetric instrument. 100 mg sample were evacuated for 6 h at room temperature and subsequently loaded for adsorption analysis.

2.6 X-ray Crystallography

General Data Collection and Refinement Procedures:

All single crystal data were collected on a Bruker SMART APEX three circle diffractometer equipped with a CCD area detector and operated at 1500 W power (50 kV, 30 mA) to generate Mo Kα radiation (λ = 0.71073 Å). The incident X-ray beam was focused and monochromated using Bruker Excalibur Gobel mirror optics. All crystals reported in this chapter were mounted on nylon CryoLoops (Hampton Research) with Paraton-N (Hampton Research).

Initial scans of each crystal were performed to obtain preliminary unit cell parameters and to determine the mosaicity (breadth of spots between frames) of the crystal to select the required frame width for data collection. In every case frame widths of 0.5° were judged to be appropriate and full hemispheres of data were collected using the *Bruker* SMART software suite. Following data collection, reflections were sampled from all regions of the Ewald sphere to redetermine unit cell parameters for data integration and to check for rotational twinning using CELL_NOW [2.7]. Fortunately, no crystal decay was encountered in case of the data collection. Following exhaustive review of the collected frames the resolution of the dataset was judged. Data were integrated using Bruker SAINT [2.8] software with a narrow frame algorithm and a 0.400 fractional lower limit of average intensity. Data were subsequently corrected for absorption by the program SADABS [2.9]. The space group determinations and tests for merohedral twinning were carried out using XPREP [2.9]. In all cases, the highest possible space group was chosen.

All structures were solved by direct methods and refined using the SHELXTL 97 [2.10] software suite. Atoms were located from iterative examination of difference F-maps following least squares refinements of the earlier models. Final models were refined anisotropically (if the number of data permitted) until full convergence was achieved. Hydrogen atoms were placed in calculated positions (C–H = 0.93 Å) and included as riding atoms with isotropic displacement parameters 1.2-1.5 times U_{eq} of the attached C atoms. All structures were examined through the *Adsym* subroutine of PLATON [2.11] to ensure that no additional symmetry could be applied to the models. All ellipsoids in ORTEP diagrams are displayed at the 50% probability level unless stated otherwise. For all structures we observed elevated R-values; a problem commonly encountered in MOF crystallography [2.12].

Experimental and refinement details for ThrZnOAc: Colorless rod shaped crystal ($0.60 \times 0.20 \times 0.20$ mm^3) was mounted on 0.7 mm diameter nylon CryoLoops (Hampton Research) with Paraton-N (Hampton Research). The loop was mounted on a *SMART APEX* three circle diffractometer equipped with a CCD area detector (Bruker Systems Inc., 1999) and operated at 1500 W power (50 kV, 30 mA) to generate Mo K_α radiation ($\lambda = 0.71073$ Å). The incident X-ray beam was focused and monochromated using Bruker Excalibur Gobel mirror optics. Analysis of the data showed negligible decay during collection. The structure was solved in the hexagonal $P6_1$ space group, with $Z = 6$, using direct method. All non-hydrogen atoms were refined anisotropically. Very high displacement parameters, high esd's and partial occupancy due to the disorder make it impossible to determine accurate positions for the hydrogen atoms in water molecules. Crystallographic data (excluding structure factors) for this structure have been deposited with the CCDC as deposition No. CCDC 943050. The ORTEP diagram is provided with 50% probability (Figure 2.18g).

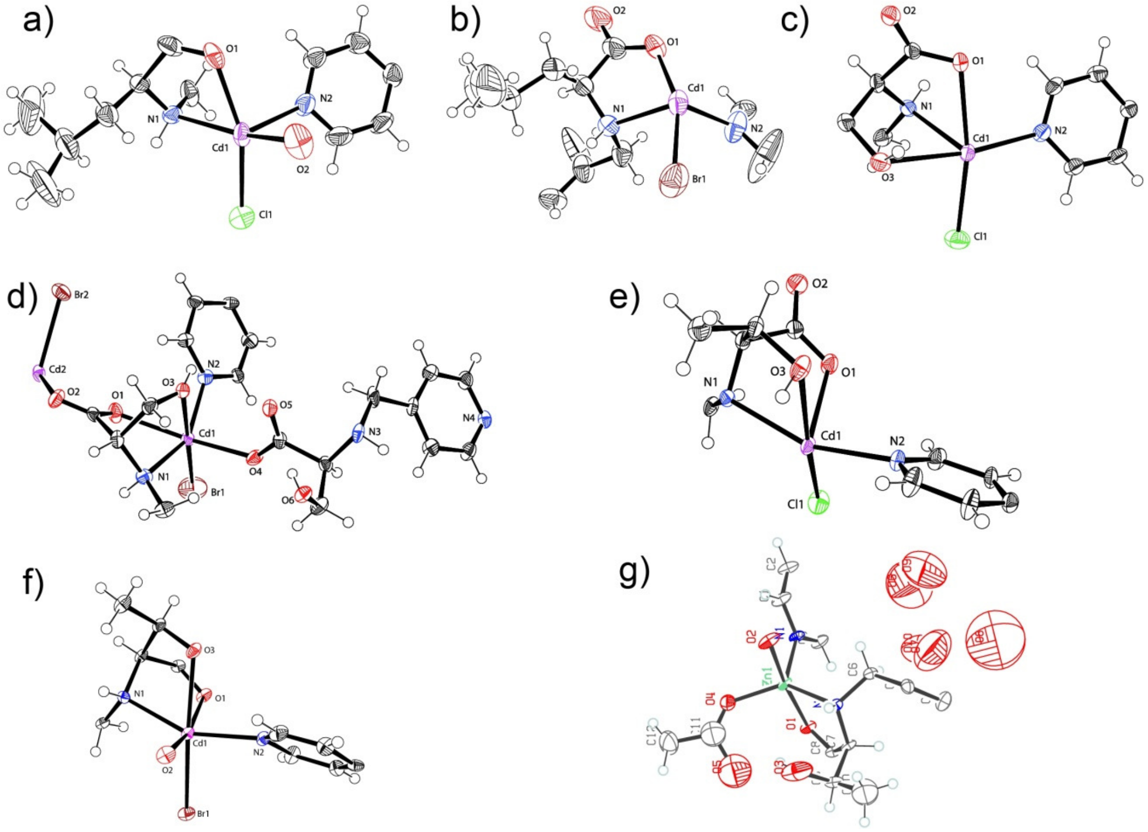

Figure 2.18: ORTEP diagrams for the asymmetric unit of the MOFs in 50% probability level. a) LeuCdCl b) LeuCdBr c) SerCdCl d) SerCdBr e) ThrCdCl f) ThrCdBr g) ThrZnOAc. Figure adapted from ref. 2.13 and 2.14.

Experimental and refinement details for LeuCdCl: A colourless rod shaped crystal of LeuCdCl (0.3 × 0.2× 0.1 mm^3) was placed in 0.7 mm diameter nylon CryoLoops (Hampton Research) with Paraton-N (Hampton Research). The loop was mounted on a SMART APEX three circle diffractometer. All non-hydrogen atoms were refined anisotropically. Hydrogen atoms attached to the lattice water molecules in LeuCdCl could not be located or fixed. MOF LeuCdCl contains one ligand and one chloride atom and metal atom with one lattice water in the asymmetric unit. It should be noted that other supporting characterization data are consistent with the crystal structure. Final full matrix least-squares refinement on $F2$ converged to $R1 = 0.0475$ ($F > 2\sigma F$)) and $wR2 = 0.1079$ (all data) with GOF = 1.033. Crystallographic data (excluding structure factors) for this structure have been deposited with the CCDC as deposition No. CCDC 851353. The ORTEP diagram is provided with 50% probability (Figure 2.18a).

Experimental and refinement details for LeuCdBr: A colourless rod shaped crystal of LeuCdBr (0.3 × 0.21 × 0.12 mm^3) was placed in 0.7 mm diameter nylon CryoLoops (Hampton Research) with Paraton-N (Hampton Research). The loop was mounted on a SMART APEX three circle diffractometer. All non-hydrogen atoms were refined anisotropically. MOF LeuCdBr contains one ligand and one bromine atom and metal atom in the asymmetric unit. It should be noted that other supporting characterization data are consistent with the crystal structure. Final full matrix least-squares refinement on $F2$ converged to $R1 = 0.0461$ ($F > 2\sigma F$)) and $wR2 = 0.1342$ (all data) with GOF = 1.066. Crystallographic data (excluding structure factors) for this structure have been deposited with the CCDC as deposition No. CCDC 851354. The ORTEP diagram is provided with 50% probability (Figure 2.18b).

Experimental and refinement details for SerCdCl: A colourless rod shaped crystal of SerCdCl (0.3 × 0.2 × 0.1 mm^3) was placed in 0.7 mm diameter nylon CryoLoops (Hampton Research) with Paraton-N (Hampton Research). The loop was mounted on a SMART APEX three circle diffractometer. All non-hydrogen atoms were refined anisotropically. Hydrogen atoms attached to the lattice water molecules of SerCdCl could not be located or fixed. MOF SerCdCl contains one ligand and one chloride atom and metal atom in the asymmetric unit. It should be noted that other supporting characterization data are consistent with the crystal structure. Final full matrix least-squares refinement on $F2$ converged to $R1 = 0.0341$ ($F > 2\sigma F$)) and $wR2 = 0.0956$ (all data) with GOF = 1.097. Crystallographic data (excluding structure factors) for this structure have been deposited with the CCDC as deposition No. CCDC 851355. The ORTEP diagram is provided with 50% probability (Figure 2.18c).

Experimental and refinement details for SerCdBr: A colourless rod shaped crystal of SerCdBr (0.3 × 0.2 × 0.1 mm^3) was placed in 0.7 mm diameter nylon CryoLoops (Hampton Research) with Paraton-N (Hampton Research). The loop was mounted on a SMART APEX three circle diffractometer. All non-hydrogen atoms were refined anisotropically. Hydrogen atoms attached to the lattice water molecules in and one side arm oxygen atoms of SerCdBr could not be located or fixed. MOF SerCdBr contains one ligand and one bromine atom and metal atom in the asymmetric unit. It should be noted that other supporting characterization data are consistent with the crystal structure. Final full matrix least-squares refinement on *F*2 converged to *R*1 = 0.0506 (*F* >2σ*F*)) and *wR*2 = 0.1344 (all data) with GOF = 1.067. Crystallographic data (excluding structure factors) for this structure have been deposited with the CCDC as deposition No. CCDC 851356. The ORTEP diagram is provided with 50% probability (Figure 2.18d).

Experimental and refinement details for ThrCdCl: A colourless rod shaped crystal of ThrCdCl (0.3 × 0.2 × 0.1 mm^3) was placed in 0.7 mm diameter nylon CryoLoops (Hampton Research) with Paraton-N (Hampton Research). The loop was mounted on a SMART APEX three circle diffractometer. All non-hydrogen atoms were refined anisotropically. Hydrogen atoms attached to the lattice water molecules of ThrCdCl could not be located or fixed. MOF ThrCdCl contains one ligand and one chloride atom and metal atom in the asymmetric unit. It should be noted that other supporting characterization data are consistent with the crystal structure. Final full matrix least-squares refinement on *F*2 converged to *R*1 = 0.0189 (*F* >2σ*F*)) and *wR*2 = 0.0501 (all data) with GOF = 1.021. Crystallographic data (excluding structure factors) for this structure have been deposited with the CCDC as deposition No. CCDC 851357. The ORTEP diagram is provided with 50% probability (Figure 2.18e).

Experimental and refinement details for ThrCdBr: A colourless rod shaped crystal of ThrCdBr (0.3 × 0.1 × 0.1 mm^3) was placed in 0.7 mm diameter nylon CryoLoops (Hampton Research) with Paraton-N (Hampton Research). The loop was mounted on a SMART APEX three circle diffractometer. All non-hydrogen atoms were refined anisotropically. Hydrogen atoms attached to the lattice water molecules and side arm oxygen atoms of ThrCdBr could not be located or fixed. MOF ThrCdBr contains one ligand and one bromine atom and metal atom in the asymmetric unit. It should be noted that other supporting characterization data are consistent with the crystal structure. Final full matrix least-squares refinement on *F*2 converged to *R*1 = 0.0630 (*F* >2σ*F*)) and *wR*2 = 0.1450 (all data) with GOF = 1.081. Crystallographic data (excluding structure factors) for this structure have been deposited with the CCDC as deposition No. CCDC 851358. The ORTEP diagram is provided with 50% probability (Figure 2.18f).

NOTE: The results of this chapter have already been published in *Cryst. Growth Des.* 2012, **12**, 4633-4640 with the title: "*Variable Water Adsorption in Amino Acid Derivative Based Homochiral Metal Organic Frameworks*" and *CrystEngComm*, 2013, **15**, 9634-

9640. with the title “Relating pore hydrophilicity with vapour adsorption capacity in a series of amino acid based metal organic frameworks”. These publications were the results from the group of Dr. Rahul Banerjee and his students Subash Chandra Sahoo and Tanay Kundu from CSIR-National Chemical Laboratory, Pune, India. Major experimental works, data interpretation and manuscript preparation were contributed by Tanay Kundu using instrumental facilities of CSIR-National Chemical Laboratory. Subash Chandra Sahoo did the crystallization.

CHAPTER 3

RARE *unh* TOPOLOGY OF AMINO ACID DERIVED MOFS WITH DIFFERENT PROTON CONDUCTING ABILITY

3.1 Introduction:

The art of knitting molecular building units by coordination bonds are leading to the formation of extended structures with novel architectures. Thus, realization of new structures in which typically metal ion acting as nodes or joints are used in connecting organic linkers or spacers to make porous metal-organic frameworks (MOFs). At present, researchers from different fields are involved in the design and study of MOF structures and their properties. As expected, a system of organization and nomenclature should be developed to facilitate the navigation within the field for current and future researchers. Knowledge on Self organization of molecular components is essential for the pre-designed

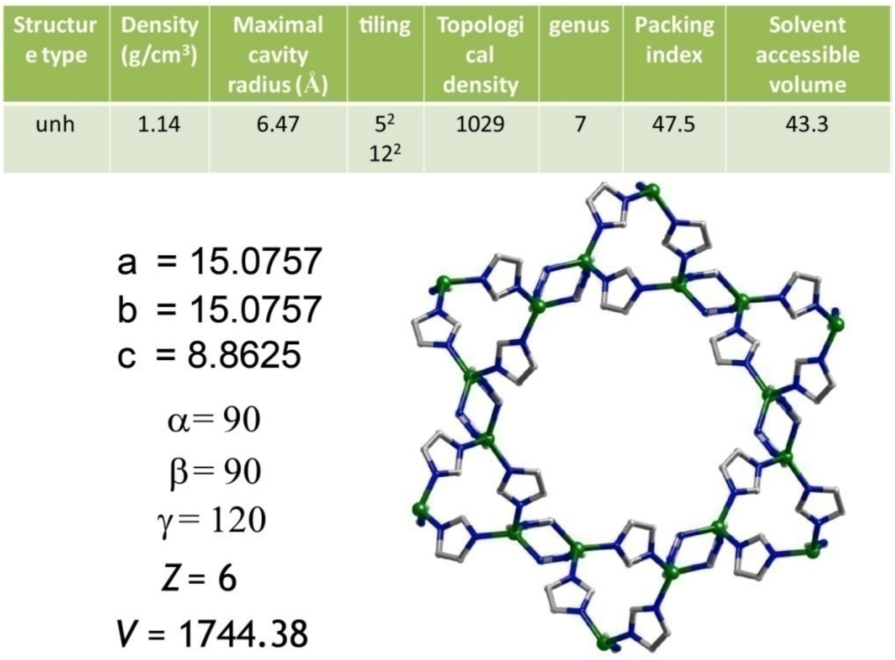

Structure type	Density (g/cm³)	Maximal cavity radius (Å)	tiling	Topological density	genus	Packing index	Solvent accessible volume
unh	1.14	6.47	5^2 12^2	1029	7	47.5	43.3

a = 15.0757
b = 15.0757
c = 8.8625
α = 90
β = 90
γ = 120
Z = 6
V = 1744.38

Figure 3.1: Predicted structural details (but not yet synthesized) of the Zeolitic Imidazolate Framework (ZIF) having *unh* topology.

synthesis of MOFs and related materials. For proper understanding of Nets, breaking down MOF architectures into its fundamental units without sacrificing its chemical importance is necessary. One can also think of it as a top down approach. Another aspect for knowing about nets and their occurrences is their application in computer simulation of MOF adsorbate interactions, adsorption isotherms, prescreening of MOF as an emergent aspect [3.1].

Recent advances on three-periodic nets have come from the tiling theory. In a natural tiling, the tiling has the same symmetry as the natural symmetry of the net. Subject to these limitations, the natural tiling is composed of the smallest possible tiles. For example, in a polyhedron three edges meet at each vertex. Similarly, in a simple tiling four tiles meet at a vertex and exactly three meet at an edge. A suitable regularity of a net is measured as transitivity, composed of a set of four integers, abcd, that represents a tiling has a kinds of vertex, b kinds of edge, c kinds of face, and d kinds of tile [3.1].

In this regard, the concept of secondary building units (SBUs) has been proposed as a harmonizing concept for the classification of the MOF structures into their underlying topology. Typically MOFs are composed of two types of secondary building units (SBUs) or points of extension. One type is essentially organic ligands, which could be multitopic in nature. The second type of SBU is a metal atom or finite polyatomic clusters having two or more metal atoms of same (homometallic, e.g. Zn_4O,Zr_6O_4) or different kinds (heterometallic, e.g. Polyoxometallates). The two types of SBU exhibit their different roles in the construction of three dimensional MOF architectures. The details of nets are available as searchable database known as the Reticular Chemistry Structure Resource (RCSR), having a collection of more than 2000 different nets. There nets are assigned three-letter symbols such as ***abc*** *(pts, soc, rht* etc.*)*. TOPOS, a computer generated program which identifies underlying nets within a structure, have a huge database over 70,000 nets. Olaf Delgado Friedichs' developed a complex mathematical program called *Systre*, which even identifies new nets that are not included in RSCR database. Nets with one type of vertex are called uninodal, whereas with two types of vertex are binodal, and so on. Metal-containing SBUs are produced during synthesis, which are generally polygonal or polyhedral. On the other hand, although organic SBUs have predetermined shape and geometry, flexibility often determine the final architecture [3.1]. Hence, it is vital to identify all vertices and edges rather than just identifying the nets. Identification of novel nets always has been a cynosure in the eyes of the researchers in MOF or any other fields. Typically, new nets provide more opportunities to study metal-ligand organization strategies. In this respect, we report a novel *unh* topology in MOFs built with amino acid derived linkers and Zn(II) as metal ion. Additionally, these MOFs show single crystal to single crystal structural dehydration-rehydration phenomenon, structural dependant water adsorption and proton conducting ability.

3.2 Result and discussion:

3.2.1 Structural aspects of the MOFs:

Chirality, helicity and porosity play important roles in chemistry and biology and it is indeed a challenge to combine all the aspects in a single entity. The construction of helical MOFs are considered to be a fascinating structure as helical assemblies such as protein bundles and DNA are ubiquitous in biological systems and play key roles in molecular recognition, replication, and catalysis [3.2]. Several approaches have been developed for constructing chiral MOFs and their potential applications in the field of chiral synthesis, optical devices, sensory functions, modelling of biological compounds etc. Multitopic linkers derived from natural amino acids are an attractive choice for chiral MOF synthesis because of their functional biological properties along with highly selective substrate-binding abilities. Based on the above facts it is evident that amino acid derivatives (naturally available and pure enantiomer) are good choice as chiral links for designing 3D homochiral MOFs for various promising applications.

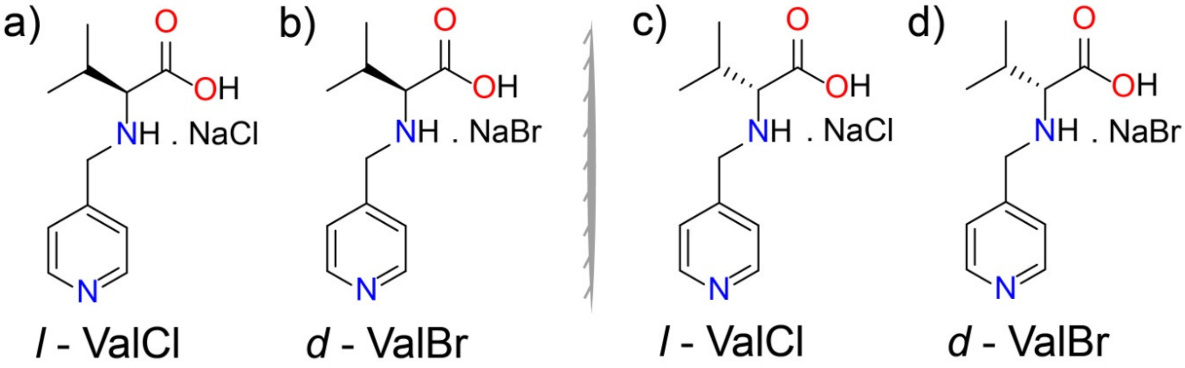

Figure 3.2: Schematic representation of the chiral linkers used for MOF synthesis.

MOFs reported in this chapter were synthesized by mixing $Zn(CH_3COO)_2.2H_2O$ and (Pyridine-4-yl)methylamino-valine (a valine derived link) (Figure 3.2) using hydrothermal condition in water medium. Phase pure rod shape crystals were grown in the caped vial at 90 °C within 5-6 h, while optimal growths were accomplished at 12 h. All the MOFs are structural isomers with respect to either different anions ($–Cl^-$ or $–Br^-$) coordinated to metal atoms or enantiomers with respect to (*–d* or *–l*) ligand backbone. *l*-ValZnCl crystallizes in the $P6_1$ space group, which consists of one Zn(II), one *l*-ValCl ligand and two lattice water molecules in the asymmetric unit. The Zn(II) center adopts a distorted square pyramidal geometry ($\tau = 0.88$) chelated by monodentate carboxylate [(Zn1–O2 2.170(3) Å)] anion, and one neutral amino functionality [(Zn1–N1 2.092(4) Å)] of first *l*-ValCl link. One pyridyl functionality and one carboxyl oxygen atom of the second *l*-ValCl ligand coordinates to the equatorial positions, and one free chloride anion occupies the axial site (Figure 3.3) for charge balance. Noticeably, the amine group is induced by the neighboring chiral carbon center into a homochiral unit to coordinate the Zn(II) ion. As a result, the Zn(II) acquires a third homochiral center associated with two homochiral centers. All adjacent zinc nodes are bridged by pyridyl group to form a 6_1 helical chain with a pitch of 12 Å through the crystallographic *c* axis (Figure 3.3). The two coordinated carboxylate oxygens stay opposite to each other along *c* axis through which link to additional molecules form the wall of the helical chain. Among the pyridyl rings, one set of pridyl rings run in clockwise direction while other run anti-clockwise to extend (linking two molecular chains) the lattice along the *ab* plane. This result in a 3D architecture containing close-packed 1D open channel along the *c* axis filled with solvent water molecules (Figure 3.4a). All pyridyl rings and isopropyl groups constitute the wall of the helical channel and provide a hydrophobic environment to it. This molecular arrangements result in a unprecedented zeolitic *unh* topology which has not been perceived till date by any other synthetic means even though it is theoretically proposed in ZIFs (Figure 3.1)[3.3]. The *unh* topology has a vertex symbol $5.5.5.5_2.12.12$. We analyzed the complexity of the nets in terms of their natural tiling, where the set of edges and vertices of the tiles is the same as that of the net. All the MOFs reported in this chapter have the transitivity value of 1221, which means that the tiling has one kind of vertices, two kinds of edges, two kinds of faces, and one kind of tiles. The MOFs comprise a uninodal nets having an isohedral kind of tile. The tile has two five-sided and two twelve-sided faces with face symbol $5^2.12^2$ (Figure 3.4b). The Lattice water molecules are weakly H-bonded to Zn–Cl atom [(O···Cl–Zn, 3.175(1) Å)] run along

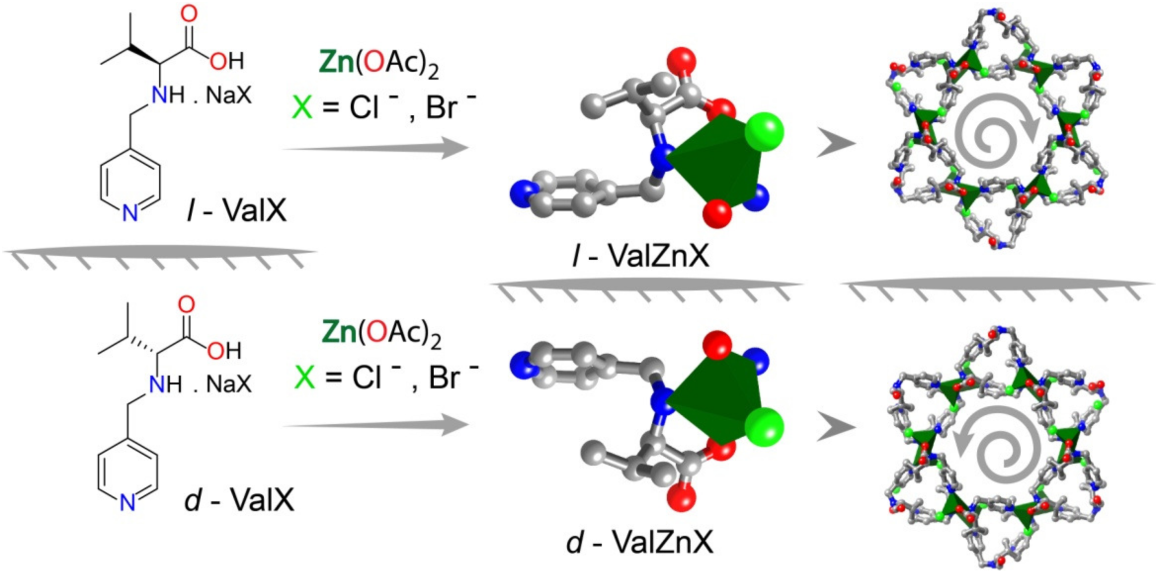

Figure 3.3: Schematic representation of the chiral MOF synthesis starting from chiral links.

the helical channel (Figure 3.4c) in case of *l*-ValZnCl. The second water molecule resides within the H-bonding distance of the 1st water molecule ($D_{O.....O}$ = 3.234(3) Å) to make a continuous water channel along crystallographic *c* axis. This H-bonding distance is well within the range of $D_{O.....O}$ of O–H···O hydrogen bonding reported in the literature. As a result a secondary helical water chain surrounded by the molecular helix is formed. Week (O–H···Cl–Zn) H-bonding facilitate the water protons to become more acidic in nature. It was found that helical orientation of water molecules are the structural basis by which the K^+ ion and proton transport occurs inside KcsA K^+ channel and in protein aquaporin-1, respectively [3.4]. 1D water chains also play vital roles in stabilizing the native conformation of several biopolymers, but such helical water chains are less observed in synthetic homochiral crystal hosts and particularly rare in MOFs, because most of the high boiling solvents like DMF, DMA, DMSO, DEF are used for MOF synthesis instead of water [3.5]. Single crystal X-ray diffraction analysis revealed that MOF *d*-ValZnCl, *l*-ValZnBr, and *d*-ValZnBr are isomorphous to *l*-ValZnCl where *l*-ValZnCl and *l*-ValZnBr are isomers with respect to substituted halogen atoms. On the other hand, *l*-ValZnCl and *d*-ValZnCl pair and *l*-ValZnBr and *d*-ValZnBr pair are enantiomers to each other. In *l*-ValZnBr each Zn(II) cation has similar coordination environment except the axial position is occupied by Br-atom. The τ (trigonality factor) is almost same (τ = 0.89) as that of *l*-ValZnCl. The Lattice water molecules in *l*-ValZnBr are weakly H-bonded and placed

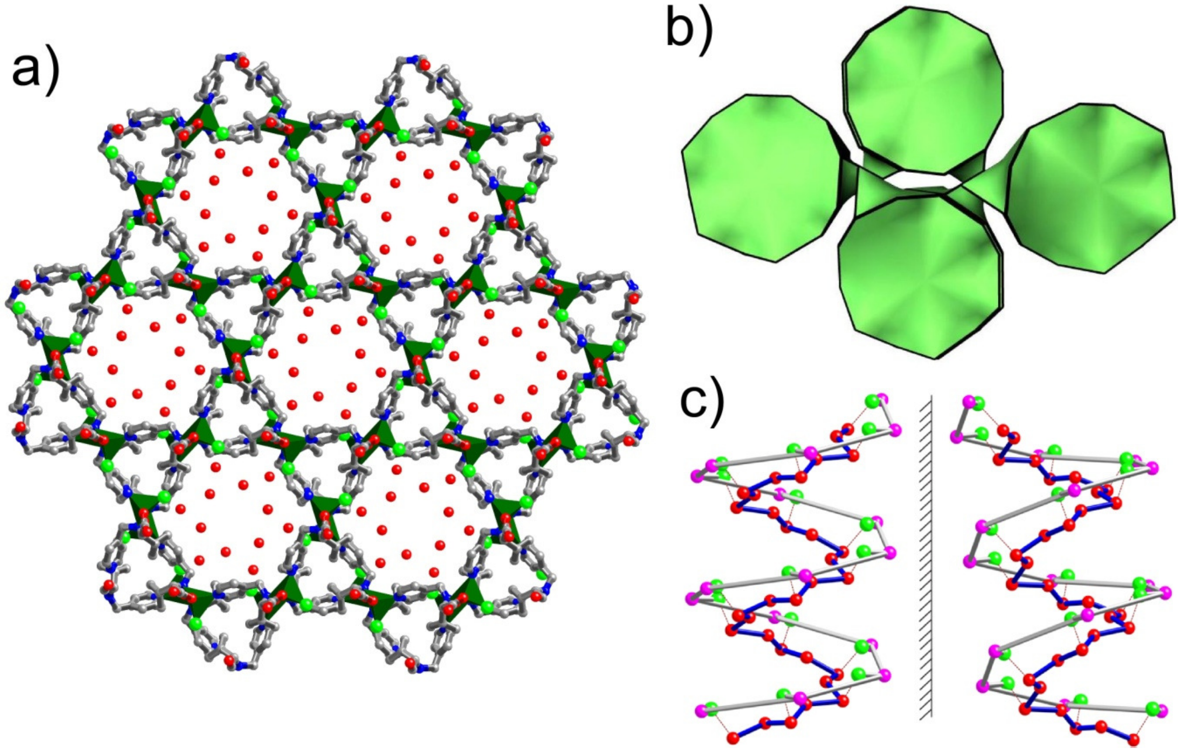

Figure 3.4: a) Polyhedral packing image of *l*-ValZnCl along crystallographic *c* axis. b) Topological representation of the *l*-ValZnCl tiling image. c) Hydrogen bonded helical chain along crystallographic *b* axis. Figure adapted from ref. 3.13.

almost in equivalent position with respect to –Br atom show a helical arrangement similar to *l*-ValZnCl. For comparative purpose, we prepared enantiomer analogue of *l*-ValZnCl i.e. *d*-ValZnCl. The O···Br–Zn and O···O hydrogen bonding distance in *d*-ValZnCl is 3.175(1) and 3.341(7) Å, respectively. We obtained two enantiomorphic frameworks, *l*-ValZnBr and *d*-ValZnBr based on self-assembly between *d*-ValCl and *d*-ValBr with $Zn(CH_3COO)_2.2H_2O$ under identical hydrothermal synthetic conditions. The CD measurements on bulk crystals of *l*-ValZnCl and of *d*-ValZnCl show opposite Cotton effects at ~ 238 and 265 nm (Figure 3.5), indicating that they are enantiomers. MOF *l*-ValZnBr and *d*-ValZnBr have similar coordination environment to that of *l*-ValZnCl and *d*-ValZnCl except the resulting crystal structure adopts opposite handedness. *l*-ValZnBr and *d*-ValZnBr also contain two water molecules as lattice solvent having week H-bonding interactions distance 3.158(3) Å (for O···Cl–Zn) and 3.175(1) Å (for O···Br–Zn), respectively. Overall it has been confirmed that all the four MOF isomers have similar lattice arrangements (*unh* topology) and the helical water chain persists irrespective of the different halogen substitutions or change in chirality of the ligand backbone.

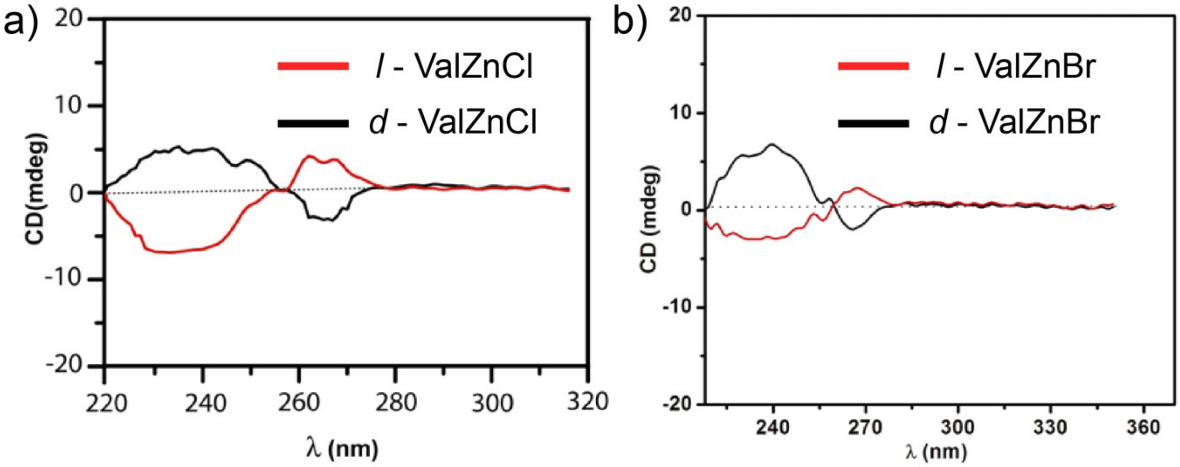

Figure 3.5: CD spectra of the enantiomorphic MOFs a) *l*-ValZnCl and *d*-ValZnCl b) *l*-ValZnBr and *d*-ValZnBr. Figure adapted from ref. 3.13.

3.2.2 X-ray powder diffraction analysis and Thermo-gravimetric Analysis:

The phase purity of the bulk materials were confirmed by powder X-ray diffraction (PXRD) experiments which are in well agreement with the simulated PXRD patterns (Figure 3.6). Thermogravimetric analysis (TGA) performed on as-synthesized MOFs revealed that these compounds have thermal stability upto ~270 °C (Figure 3.7). The TGA trace for as-synthesized MOFs exhibit a gradual weight-loss step of ~ 7 wt% [2 H_2O in *l*-ValZnCl and *d*-ValZnCl; calcd. 10.5 wt%] and ~ 6 wt% [2 H_2O in *l*-ValZnBr and *d*-ValZnBr; calcd. 9.3 wt%] at temperature range of 40–100 °C, corresponding to escape of guest water molecules from the pores (Figure 3.7). We note that the water molecules of *l*-ValZnCl and *l*-ValZnBr were released without damaging the framework architecture, as evidenced by the coincidence of the PXRD patterns of the MOF samples heated and held at 150 °C in N_2 atmosphere with the PXRD patterns simulated from single-crystal structures. The above fact is also supported by *in situ* VT-PXRD of *l*-ValZnCl (Figure 3.9a). All major peaks of experimental and simulated PXRDs are well matched, indicating the sample's phase purity. A combined heating and cooling *in situ* VT-PXRD experiment reveals that the frame work is stable and remain crystalline over a wide temperature range (heating from 25 to 200 °C and then cooling from 200 to 25 °C) and remain stable after solvent removal (solvent escapes ~100 °C, confirmed by TGA). Escape of solvent water molecules from the crystals were also monitored by hot stage microscopy at different temperature intervals (25–270 °C). Pictures taken on hot stage microscope reveals that the trapped water molecules escape the lattice in between 60–120 °C as heating goes on and cracking appears on the crystal surface, but crystallinity remain intact up to 250 °C (Figure 3.9b). This observation indicated that it is possible to monitor the arrangement of water molecules with respect to temperature and we can realize a solvent free framework after successful removal of solvents at the higher temperatures.

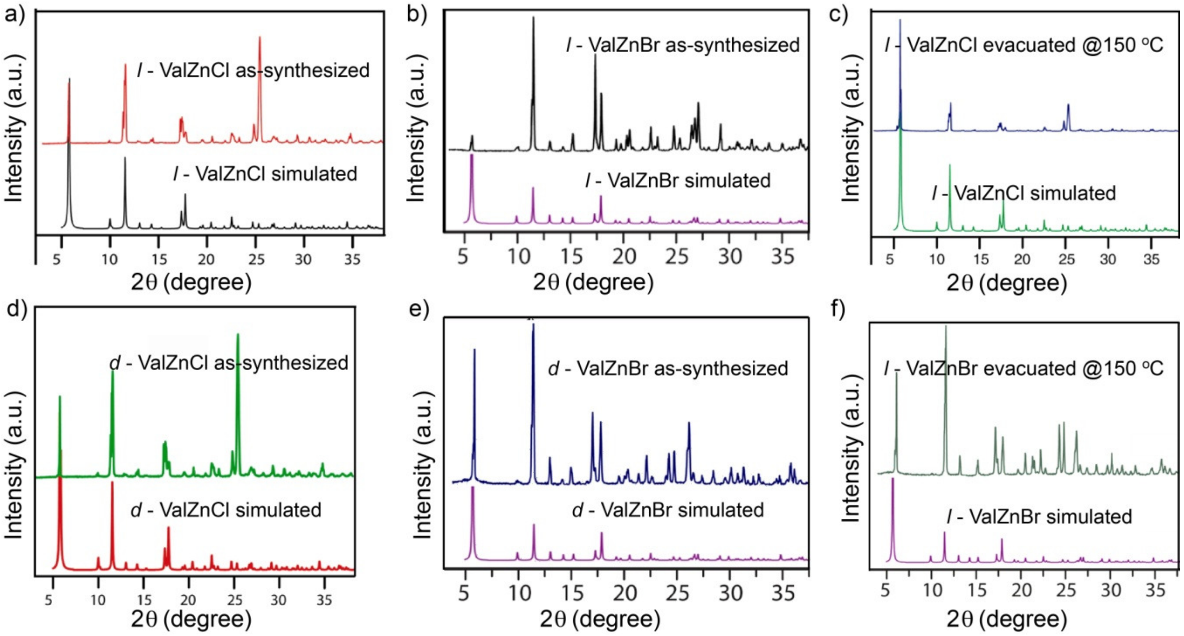

Figure 3.6: PXRD patterns of the MOFs compared with the simulated one. a) *l*-ValZnCl b) *l*-ValZnBr c) *d*-ValZnCl d) *d*-ValZnBr e) evacuated *l*-ValZnCl f) evacuated *l*-ValZnBr. Figure adapted from ref. 3.13.

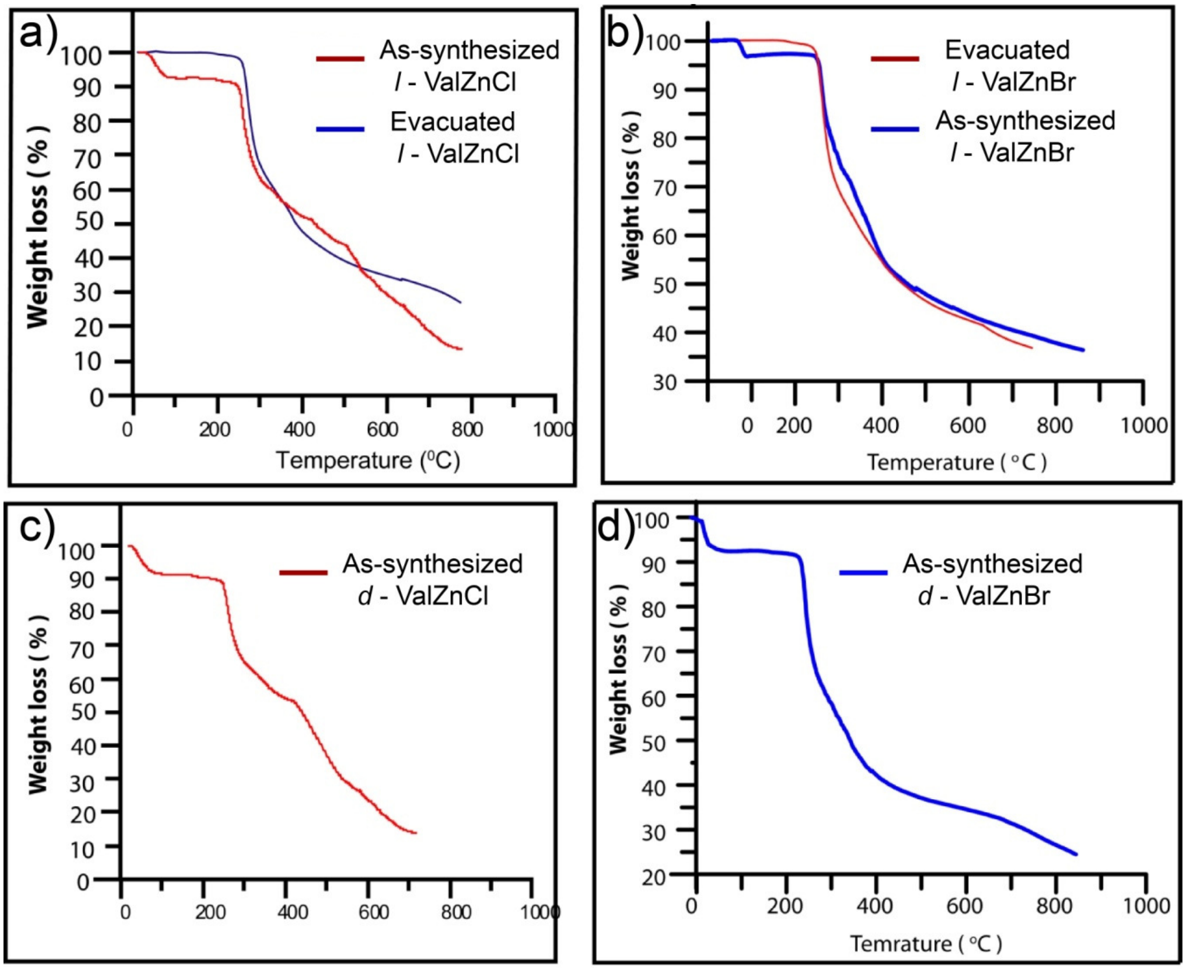

Figure 3.7: TGA analysis of the as-synthesized MOFs compared with the evacuated one. a) *l*-ValZnCl b) *l*-ValZnBr c) *d*-ValZnCl d) *d*-ValZnBr. Figure adapted from ref. 3.13.

3.2.3 Single crystal to single crystal transformation studies on the MOFs:

It is noteworthy that the water molecules adopt similar arrangements in all MOFs reported in this chapter except the handedness. The guest free frameworks of MOFs show high affinity for water irrespective of different structural variations. It is worth mentioning that only a handful of Zn(II) based MOFs reported in literature can withstand moisture [3.6]. To provide a further evidence of water affinity apart for crystallographic information, MOFs were extensively studied by various experiments. *l*-ValZnCl shows a reversible transformation in presence of water vapor. After evacuation at 150 °C for two days, the dehydrated polycrystalline sample of *l*-ValZnCl was exposed in a closed chamber saturated with water vapor. Single crystalline nature of *l*-ValZnCl comes back within 6-12 h (Figure

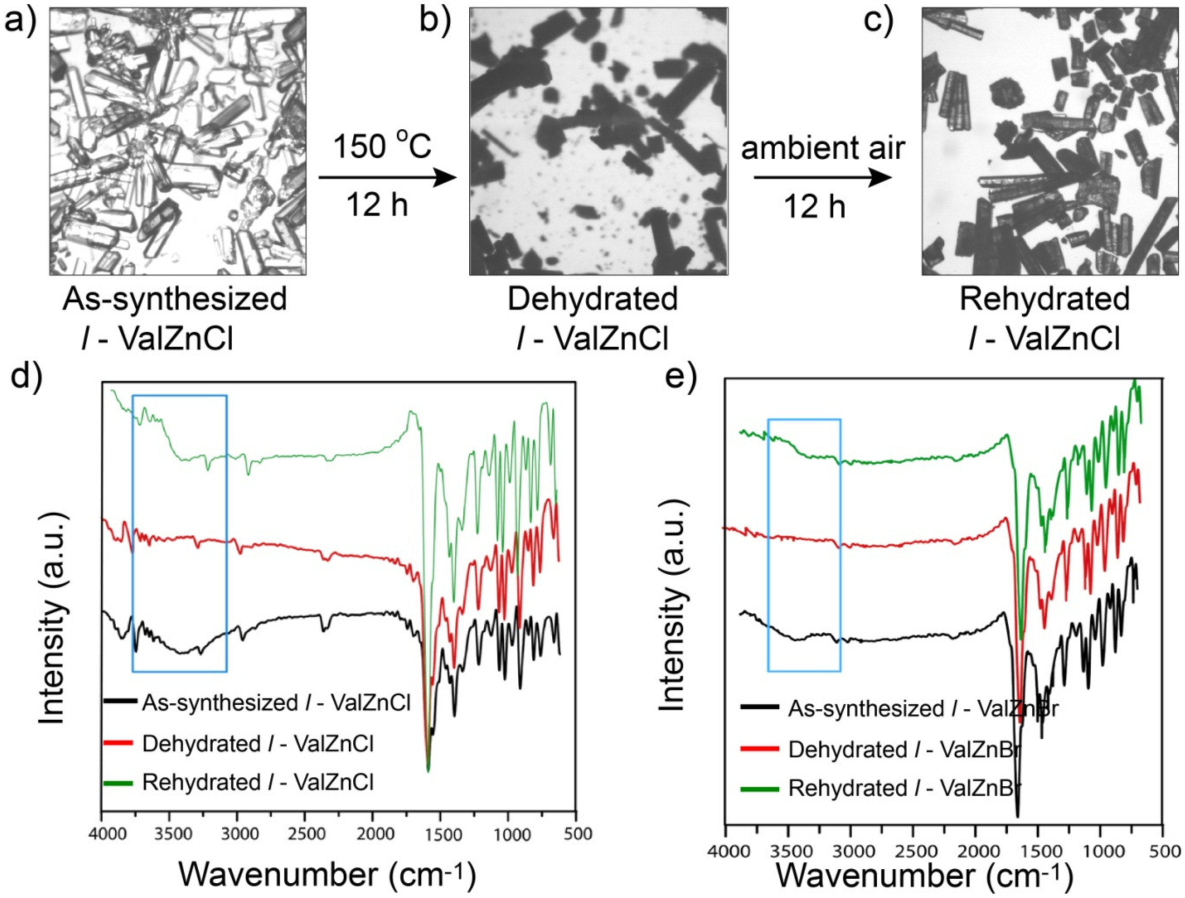

Figure 3.8: a) Structural reversibility in the light of optical microscopy in case of *l*-ValZnCl b) FT-IR spectra comparison study in case of b) *l*-ValZnCl c) *l*-ValZnBr. Figure adapted from ref. 3.13.

3.8a), which is confirmed by IR, TGA, and crystallography. FT-IR spectra of the evacuated *l*-ValZnCl sample collected at a time interval of one hour showed gradual increase in intensity of water peaks after exposed to moisture (Figure 3.8b), which further confirms the high affinity of *l*-ValZnCl for water. Further, the water affinity of *l*-ValZnCl and *l*-ValZnBr were examined by water adsorption isotherm. Surprisingly we found that *l*-ValZnCl shows 12 wt% water vapor uptake (150 cc/g at STP) (Figure 3.9c) whereas *l*-ValZnBr shows 6 wt % (75 cc/g at STP) (Figure 3.9d) which is almost half at relative pressure (P/P_o) of 0.9. It is quite clear that *l*-ValZnBr has less water affinity compared to *l*-ValZnCl, though framework arrangements of both the MOFs are similar. N_2 adsorption isotherm indicates very less uptake which signifies low degree of interaction points inside the pore.

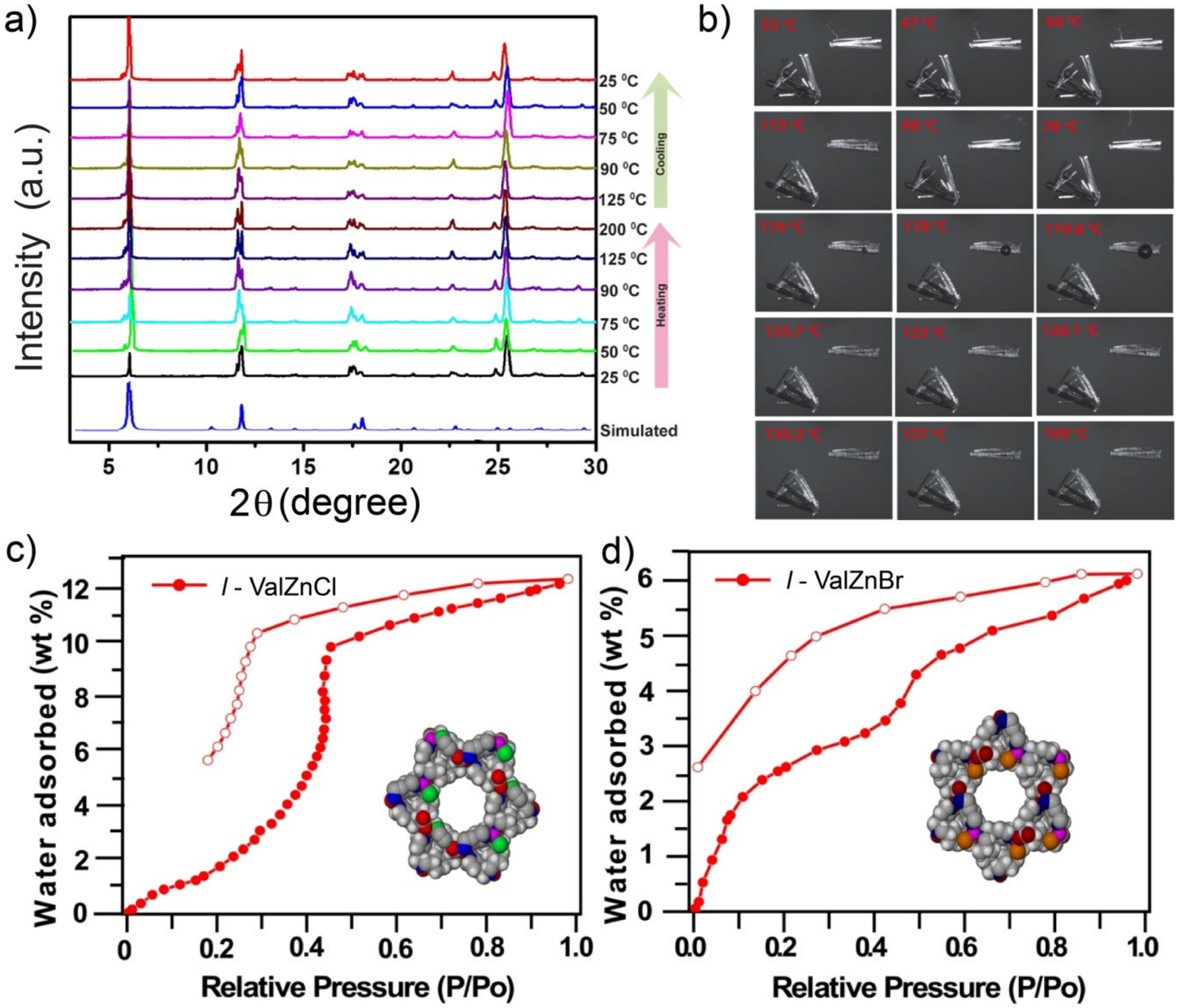

Figure 3.9: a) VT-PXRD pattern compared with simulated one in case of *l*-ValZnCl b) Hot stage microscopy images at different temperatures in case of *l*-ValZnCl. Water adsorption isotherms in case of c) *l*-ValZnCl and d) *l*-ValZnBr. Figure adapted from ref. 3.13.

Inspired by the above results we considered to establish the abovementioned fact by *in situ* variable temperature single crystal x-ray diffraction experiment (SCXRD). Variable temperature SCXRD on MOF *l*-ValZnCl (Figure 3.10a) and *l*-ValZnBr (Figure 3.10b) are performed at different temperature interval of 25, 40, 50, 60, 70, 80, 90, 100 and 115 °C. Before data collection, single crystallinity of MOFs suitable for single crystal diffraction were checked by taking snap shots and unit cell determination at that particular temperature which confirms that the sample's crystallinity remain intact for suitable data collection. From TGA experiments it was found that the MOFs loose lattice water molecules during a temperature range of 40–100 °C. Taking clue from the above observations we anticipated that not only we could possibly achieve an evacuated framework via a single-crystal to single-crystal (SC-SC) transformation but also can monitor the dynamics of H_2O inside the molecular framework over the temperature range. After carefully solving the above collected data sets we found that 80 °C is the ideal temperature at which we could able to achieve stable and solvent free framework of *l*-ValZnCl with reasonable good structural parameters [(R_1) = 6.4%, weighted R (wR_2) = 14.7%, GOF = 1.005] below which water stay at lattice as solvents and the framework remains intact but high thermal vibration observed in some of the atom sites results in high refinement parameters i.e. thermal ellipsoids. Similar experiment performed on *l*-ValZnBr reveals that we can achieve an evacuated framework at much lower temperature of 40 °C [(R_1) = 5.7%, weighted R (wR_2) = 15.12%, GOF = 1.071]. So far the amount of water uptake of *l*-ValZnCl with respect to *l*-ValZnBr and achieving evacuated framework of *l*-ValZnBr at only 40 °C clearly indicates that *l*-ValZnBr has lower water affinity than *l*-ValZnCl**.**

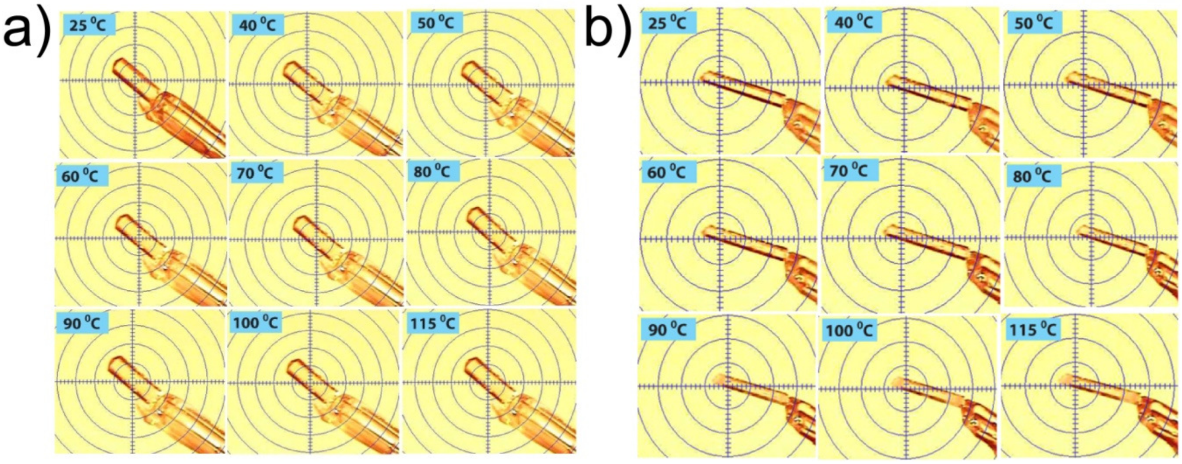

Figure 3.10: Single crystal to single crystal dehydration phenomena in case of a) *l*-ValZnCl and b) *l*-ValZnBr. Figure adapted from ref. 3.13.

It has been mentioned already that the structural arrangement of the MOFs are all similar except the handedness and halogen atoms in the framework [Zn–X (X = –Cl, –Br)]. It is well established that metal halides (M–X) have shown to be strong hydrogen bond acceptors, compared to organic halides (e.g. C–Cl and C–Br bonds). The normalized distance function, R_{HX}, for D–H····X–M hydrogen bonds [($R_{HX} = d(\mathrm{H}\cdots \mathrm{X})/(r_H + r_X)$)][$R_{HX}$ value of 0.799 and 0.820 for O–H····X–M (X = Cl^-, Br^-)] show a acceptor capabilities of halogens. It is anticipated that due to increase in polarity of the D–H bond, for a given halide ion, O–H donors can contribute stronger interaction than N– H donors. Similarly comparison of halide ion acceptors for a given donor are compared, interactions follow an order H····F > H····Cl > H····Br > H····I. In the present scenario for MOFs *l*-ValZnCl and *l*-ValZnBr, it is expected that O–H····X–Zn interaction is stronger in *l*-ValZnCl than *l*-ValZnBr.

3.2.4 Proton conductivity studies on the MOFs

The X-ray crystal structures of the MOFs established that these materials are amenable to proton conducting property owing to the continuous (O···O) helical 1D water chain ($D_{O\cdots O}$ = 3.234(3) Å) in a confined hydrophobic and acidic environment [$D_{O\cdots Cl–Zn}$ = 3.164(3) Å, $D_{O\cdots Br–Zn}$ = 3.175(2) Å]. The proton conductivities of two halogen isomers *l*-ValZnCl and *d*-ValZnCl were measured by a quasi-two-probe method, with a Solartron 1287 Electrochemical Interface with frequency response Analyzer. The conductivities were determined from the semicircles in the Nyquist plots (Figure 3.11). The proton conductivities of *l*-ValZnCl and *d*-ValZnCl were 4.45 × 10^{-5}, 4.42 × 10^{-5} S cm^{-1}, respectively, at 304 K and 98% relative humidity (RH). This value was highly humidity-dependent and dropped to 1.49 × 10^{-5} S cm^{-1}, 1.22 × 10^{-5} S cm^{-1} at 75%, and 60% RH respectively at 304 K (Figure 3.11b). Surprisingly, *l*-ValZnBr and *d*-ValZnBr show almost zero proton conductivity. Before coming to any conclusion, the reproducibility was tested by measuring the aforementioned proton conduction 4-5 times on different batch of samples. Each experiment revealed similar result. The above anomalous behavior is attributed to the following reasons. (a) Water holding capacity of *l*-ValZnBr (6 wt%) is less than *l*-ValZnCl (12 wt%) confirmed by water adsorption. (b) At room temperature (~35 °C), *l*-ValZnCl has a continuous water chain while *l*-ValZnBr has a discrete water assembly confirmed by VT-SCXRD experiments. (c) Interior cavity decorated with halogen atoms with different electronegativity are hydrogen bonded to water molecules. To prove the role of water molecules, we synthesized *l*-ValZnCl taking D_2O as solvent of synthesis, studied further by IR and solid sate ^2H SSNMR (Figure 3.11d) which confirmed the D_2O incorporation in *l*-ValZnCl. Impedance studies on the deuterated sample in an atmosphere humidified (98%) with D_2O, gave a conductivity value of 1.33 × 10^{-5} Scm^{-1}. The lower value is expected due to the heavier isotopic substitution. Proton conductivity measurements performed at different temperature shows gradual increase in proton conductivity value from 3.13 × 10^{-5} to 4.45 × 10^{-5} Scm^{-1} as the temperature increases from 299 K to 304K, respectively (Figure 3.11a). At higher temperature, above 40 °C the proton conductivity of *l*-ValZnCl vanishes due to partial dehydration as indicated by TGA plot and the VT-SCXRD data. Similar property was also observed by a previously reported PCMOF2 [1.62b]. The activation energy (Ea) for the proton transfer derived from the bulk conductivity of *l*-ValZnCl and *d*-ValZnCl were 0.34 and 0.36 eV, respectively, as determined by least-square fitting of the slopes. *l*-ValZnCl show high Ea value than Nafion (0.22 eV) [3.7], but comparable with $Zr(HPO_4)_2$ (0.33 eV)[3.8] and HUO_2PO_4[3.9] (0.32

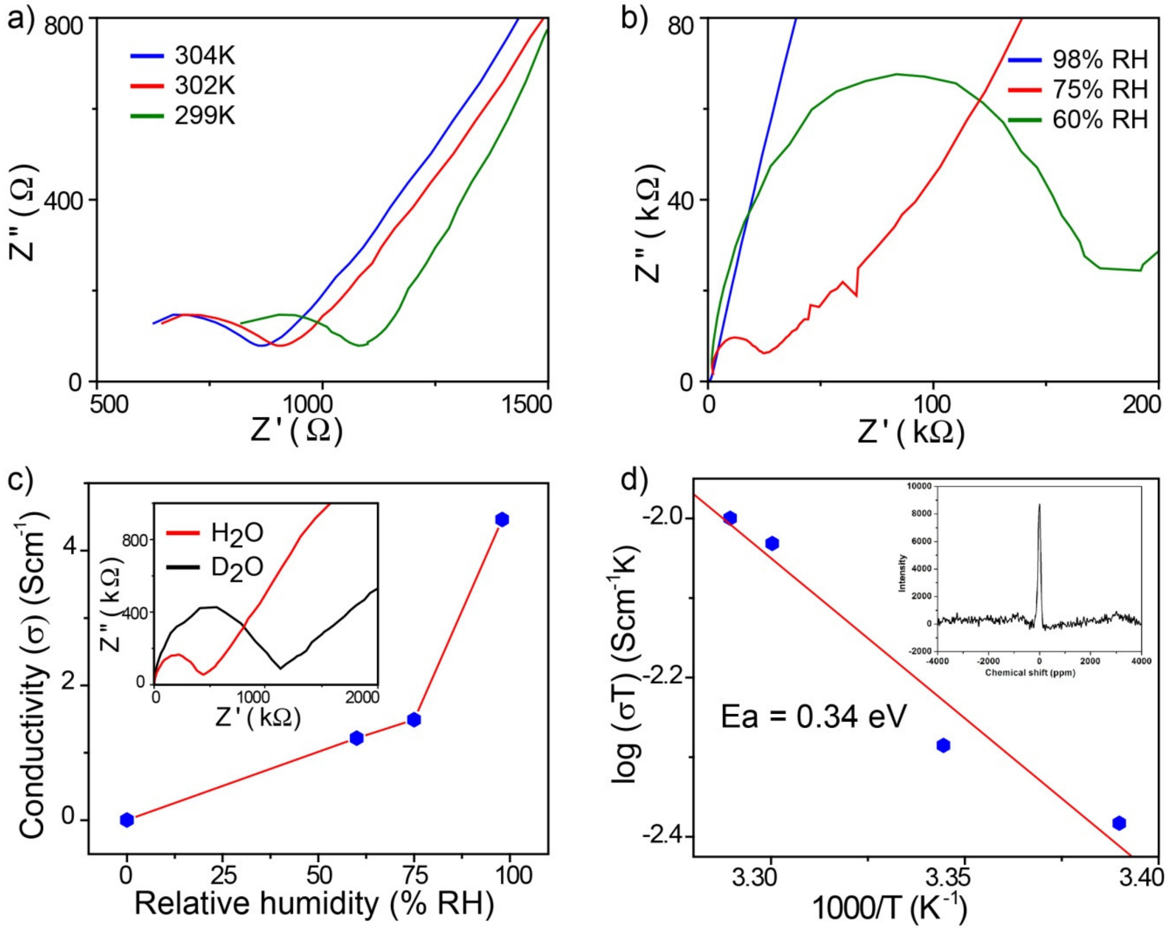

Figure 3.11: a) Nyquist plot for *l*-ValZnCl at different temperatures. b) Nyquist plot for conductivity as a function of relative humidity and c) its graphical representation. Inset shows Nyquist plots for conductivity as a function of carrier molecules i.e. H_2O vs. D_2O. d) Arrhenius plot for the activation energy showing least square fitting. Inset shows ^2H SS NMR data potraying incorporation of D_2O molecules. Figure adapted from ref. 3.13.

eV). This low Ea observed in *l*-ValZnCl indicates that the ordered helical water chain (observed crystallographically) function to transport protons via a Grotthuss hopping mechanism as opposed to the higher Ea value observed for vehicular transfer mechanism. Proton conductivity value of *l*-ValZnCl is higher than MIL-53 (~10^{-6}–10^{-9} studied at 25 °C, 95% RH), and comparable to PCMOF3 (1.33×10^{-5} S cm^{-1} at 25 °C, 98% RH)[1.62b] and possess a lower value as compared to $Fe(ox)_2$ (1.3×10^{-3} S cm^{-1} at 25 °C, 98% RH)[1.62c] and under similar condition.

3.3 Conclusion:

In conclusion, we have synthesized four new homochiral Zn-MOFs using amino acid derived links. These MOFs adopt 3D periodic architecture with 1D helical water chains irrespective of type of halogen atom substitutions or enantiomeric differences. All four MOFs show an unprecedented zeolitic (*unh*) topology which are not perceived so far by any other synthetic means. Two Lattice water molecules hydrogen bonded with the framework and also among them, form a secondary helical water chain inside the molecular helix. In MOFs *l*-ValZnCl and *l*-ValZnBr, water escapes at ~40–100 °C but show reversible crystallization by readily re-absorbing moisture which is also confirmed by VT-FT-IR and VT-PXRD experiments. The hydrophobic environment of the 1D channel along with the weak H-bonding with halogen atoms provide a helical pathway for proton conduction in humid conditions. In *l*-ValZnCl and *d*-ValZnCl this is the first example in which proton conductivity has been observed in chiral MOFs having helical water chains confined in hydrophobic and acidic environment controlled by metal bound halogen atoms. Substitution of different halogen atom results an anomalous behavior in proton conductivity of *l*-ValZnCl and *d*-ValZnCl with respect to *l*-ValZnBr and *d*-ValZnBr. High Water uptake capacity**,** high water holding capacity and high electronegativity of chlorine with respect to bromine may be the possible reason for high proton conductivity value of *l*-ValZnCl than *l*-ValZnBr**.** Stronger O–H···Cl–Zn interaction results in the increasing acidity of the water protons and subsequently becomes the major driving force of the proton conduction in *l*-ValZnCl and *d*-ValZnCl. The role of water chain in proton conduction has been further confirmed by D_2O exchanged experiments. These results will provide good roadmap towards tuning and precise control over the proton conductivity and consequently enable us to develop useful materials both for solid electrolytes and biological perspectives.

3.4 Experimental details:

3.4.1 Materials:

$Zn(CH_3COO)_2{\cdot}2H_2O$, *l*-valine, *d*-valine, sodium borohydride, and 4-pyridine carboxaldehyde were purchased from Aldrich Chemicals. All starting materials were used without further purification. All experimental operations were performed in air.

3.4.2 Synthetic methods:

3.4.2.1 Synthesis of the ligands:

a) Synthesis of (Pyridin-4-ylmethyl)-*l*-valine.NaCl [*l*-ValCl]: To an aqueous solution (10 mL) of *l*-valine (2 g, 17 mmol) and Na_2CO_3 (0.91 g, 8.5 mmol), 4-pyridinecarboxaldehyde (1.82 g, 17 mmol) in MeOH (10 mL) was added slowly. The solution was stirred for 1 h and cooled in an ice bath. $NaBH_4$ (0.76 g, 20.4 mmol) in 5 mL of H_2O was added. The mixture was stirred for 3 h, and 3 N HCl was used to adjust the pH to 5–6. The clear solution was stirred further for 2 h and then evaporated to dryness. The solid was extracted in hot and dry MeOH (150 mL × 3), and the filtrate was evaporated to get the ligand along with sodium Chloride salt in form of a white powder. Yield: 2.9 g, 70%. IR (KBr, cm^{-1}): ν_{OH}, 3421; $\nu_{as}(CO_2)$, 1562; $\nu_s(CO_2)$, 1409. ^1H NMR (D_2O, ppm): $-CH_3$ (1.21, d, 3H), $-CH_3$ (1.35, d, 3H), -CH (3.20, m, 1H), -HN-CH (3.65, m, 1H), $-CH_2$ (3.82, dd, 2H), py-H (7.34, d, 2H), py-H (8.38, d, 2H).

b) Synthesis of (Pyridin-4-ylmethyl)-*l*-valine.NaBr [*l*-ValBr]: The ligand (*l*-ValBr) was prepared exactly as *l*-ValCl only HBr was used instead of HCl for pH adjustment. Yield = 3.4 g (70%). IR (KBr, cm^{-1}): ν_{OH}, 3420; $\nu_{as}(CO_2)$, 1560; $\nu_s(CO_2)$, 1411. ^1H NMR (D_2O, ppm): $-CH_3$ (1.20, d, 3H), $-CH_3$ (1.33, d, 3H), -CH (3.24, m, 1H), -HN-CH (3.63, m, 1H), $-CH_2$ (3.79, dd, 2H), py-H (7.34, d, 2H), py-H (8.37, d, 2H).

c) Synthesis of (Pyridin-4-ylmethyl)-*d*-valine.NaCl [*d*-ValCl]: The ligand (*d*-ValCl) was prepared exactly as *l*-ValCl only *d*-valine was used instead of *l*-valine. Yield: 3.1 g, 72%. IR (KBr, cm^{-1}): ν_{OH}, 3417; $\nu_{as}(CO_2)$, 1564; $\nu_s(CO_2)$, 1415. ^1H NMR (D_2O, ppm): $-CH_3$

(1.21, d, 3H), -CH_3 (1.34, d, 3H), -CH (3.22, m, 1H), -HN-CH (3.65, m, 1H), -CH_2 (3.78, dd, 2H), py-H (7.30, d, 2H), py-H (8.36, d, 2H).

d) Synthesis of (Pyridin-4-ylmethyl)-*d*-valine.NaCl [*d*-ValCl]: The ligand (*d*-ValBr) was prepared exactly as *l*-ValBr only *d*-valine was used instead of *l*-valine. Yield: 3.6 g, 72%. IR (KBr, cm^{-1}): ν_{OH}, 3419; $\nu_{as}(CO_2)$, 1570; $\nu_s(CO_2)$, 1421. ^1H NMR (D_2O, ppm): -CH_3 (1.20, d, 3H), -CH_3 (1.34, d, 3H), -CH (3.24, m, 1H), -HN-CH (3.63, m, 1H), -CH_2 (3.80, dd, 2H), py-H (7.35, d, 2H), py-H (8.37, d, 2H).

3.4.2.2 Synthesis of the MOFs:

a) Synthesis of [{Zn(*l*-Val)(Cl)}(H_2O)$_2$]$_\infty$ (*l*-ValZnCl): To an aqueous solution (2 mL) of *l*-ValCl (0.044 g, 0.2 mmol), $Zn(CH_3COO)_2.2H_2O$ (0.022 g, 0.1 mmol) was added and sonicated for 10 min. The clear solution was kept in a tightly capped 5 mL vial for 24 h at 90 °C to produce rod shaped transparent crystals. Yield: 0.025 g, 71%. Elemental analysis: calcd- C (38.8%), H (4.44%), N (8.23%); found C (38.78%), H (4.41%), N (8.25%).

b) Synthesis of [{Zn(*l*-Val)(Br)}(H_2O)$_2$]$_\infty$ (*l*-ValZnBr): To an aqueous solution (2 mL) of *l*-ValBr (0.044 g, 0.2 mmol), $Zn(CH_3COO)_2.2H_2O$ (0.022 g, 0.1 mmol) was added and sonicated for 10 min. The clear solution was kept in a tightly capped 5 mL vial for 24 h at 90 °C to produce rod shaped transparent crystals. Yield: 0.026 g, 67%. Elemental analysis: calcd- C (34.37%), H (3.90%), N (7.29%); Found C (34.35%), H (3.92%), N (7.25%).

c) Synthesis of [{Zn(*d*-Val)(Cl)}(H_2O)$_2$]$_\infty$ (*d*-ValZnCl): To an aqueous solution (2 mL) of *d*-ValCl (0.044 g, 0.2 mmol), $Zn(CH_3COO)_2.2H_2O$ (0.022 g, 0.1 mmol) was added and sonicated for 10 min. The clear solution was kept in a tightly capped 5 mL vial for 24 h at 90 °C to produce rod shaped transparent crystals. Yield: 0.023 g, 67%. Elemental analysis: calcd- C (38.82%), H (4.44%), N (8.23%); Found C (38.79%), H (4.42%), N (8.24%).

d) Synthesis of [{Zn(*d*-Val)(Br)}(H_2O)$_2$]$_\infty$ (*d*-ValZnBr): To an aqueous solution (2 mL) of *d*-ValBr (0.044 g, 0.2 mmol), $Zn(CH_3COO)_2.2H_2O$ (0.022 g, 0.1 mmol) was added and sonicated for 10 min. The clear solution was kept in a tightly capped 5 mL vial for 24 h at 90 °C to produce rod shaped transparent crystals. Yield: 0.026 g, 69%. Elemental analysis: calcd- C (34.37%), H (3.90%), N (7.29%); Found C (34.36%), H (3.91%), N (7.27%).

3.5 General characterization methods:

a) Powder X-Ray Diffraction (PXRD): Powder XRD patterns of the aforementioned MOF samples were analyzed to confirm the crystallinity as well as the phase purity of the bulk materials. Powder X-ray diffraction (PXRD) patterns were recorded on a Phillips PANalytical diffractometer equipped with Cu K_α radiation (λ = 1.5406 Å), with a scan speed of 2° min^{-1} and a step size of 0.02° in 2θ. 50 mg of as-synthesized materials were made pellet and subjected to analysis over glass slides.

b) Thermogravimetric Analysis (TGA) and Differential Scanning Calorimetry (DSC): TGA was performed on a SDT Q600 TG-DTA instrument. ca. 8 mg of the MOFs were heated from 25 to 800 °C under the N_2 flow at heating rate of 5 °C min^{-1}.

c) IR Spectroscopy: The Fourier transform (FT) infrared spectra of the MOFs were collected on a *PERKIN ELMER FT-IR SPECTRUM* (Nicolet) spectrometer. KBr pellets (2 mg MOF in 20 mg of KBr) were prepared and 50 scans were measured at 2 cm^{-1} resolution for each sample. The spectra were measured over the range of 4000-600 cm^{-1}.

d) Water Adsorption Analysis: All low-pressure water adsorption experiments (up to 1 bar) were performed on a BELSORP-max volumetric instrument. Approximately 50 mg of the sample was activated after solvent exchange by the use of activation chamber. The activated sample was loaded inside the glass bulb of water adsorption instrument and measured the capacity.

e) Hot-Stage Microscopy: Leica M-80 optical microscope with hot stage and camera attachment was used for collecting photographs.

f) Proton Conductivity: Proton Conductivities were measured using Solartron 1287 Electrochemical Interface with 1255B frequency response analyzer via a quasi-four-probe method. ca. 120 mg of the as-synthesized MOFs were pressed in a pellet maker to obtain uniform pellets of ca. 0.38 mm, which was subject to humidification (98% RH) for 24 h and subsequently measured the proton conductivity. Resistances were measured from the semicircle of the Nyquist plots. Proton conductivity was measured by the following equation; $\sigma = L/(R.A)$ where σ = proton conductivity, L = thickness of the pellet, R = resistance of the pellet and A = area of the pellet = πr^2 where r = radius of the pellet.

For high-temperature proton conductivity measurements, the pellets were inserted within a humidification chamber, which was encircled with a controlled heating coil attached with an automated temperature controller. The heat flow within the temperature controller was controlled by a dimmerstat accordingly. The temperature of the chamber was measured by an infrared temperature sensor attachment, having a sensing accuracy of ±0.5 °C.

For low-temperature proton conductivity measurements, the pellets were inserted within a humidification chamber, which was encircled with a water circulation coil attached with a chiller integrated with an automated temperature controller. The heat flow within the chamber was controlled by the chiller accordingly. The temperature of the chamber was measured by an infrared temperature sensor attachment, having a sensing accuracy of ±0.5 °C.

3.6 X-ray Crystallography:

General data collection and refinement procedures:

All single crystal data were collected on a Bruker SMART APEX three circle diffractometer equipped with a CCD area detector and operated at 1500 W power (50 kV, 30 mA) to generate Mo Kα radiation (λ = 0.71073 Å). The incident X-ray beam was focused and monochromated using Bruker Excalibur Gobel mirror optics. All crystals reported in this chapter were mounted on nylon CryoLoops (Hampton Research) with Paraton-N (Hampton Research).

Initial scans of each crystal were performed to obtain preliminary unit cell parameters and to determine the mosaicity (breadth of spots between frames) of the crystal to select the required frame width for data collection. In every case frame widths of 0.5° were judged to be appropriate and full hemispheres of data were collected using the *Bruker* SMART software suite. Following data collection, reflections were sampled from all regions of the Ewald sphere to redetermine unit cell parameters for data integration and to check for rotational twinning using CELL_NOW [2.7]. Fortunately, no crystal decay was encountered in case of the data collection. Following exhaustive review of the collected frames the resolution of the dataset was judged. Data were integrated using Bruker SAINT [2.8] software with a narrow frame algorithm and a 0.400 fractional lower limit of average intensity. Data were subsequently corrected for absorption by the program SADABS [2.9]. The space group determinations and tests for merohedral twinning were carried out using XPREP [2.9]. In all cases, the highest possible space group was chosen.

All structures were solved by direct methods and refined using the SHELXTL 97 [2.10] software suite. Atoms were located from iterative examination of difference F-maps following least squares refinements of the earlier models. Final models were refined anisotropically (if the number of data permitted) until full convergence was achieved. Hydrogen atoms were placed in calculated positions (C–H = 0.93 Å) and included as riding atoms with isotropic displacement parameters 1.2-1.5 times U_{eq} of the attached C atoms. All structures were examined through the *Adsym* subroutine of PLATON [2.11] to ensure that no additional symmetry could be applied to the models. All ellipsoids in ORTEP diagrams are displayed at the 50% probability level unless stated otherwise. For all structures we observed elevated R-values; a problem commonly encountered in MOF crystallography [2.12].

Experimental and refinement details for *l*-ValZnCl: A colourless rod shaped crystal ($0.80 \times 0.16 \times 0.12$ mm^3) of *l*-ValZnCl was placed in a 0.7 mm diameter nylon CryoLoops (Hampton Research) with Paraton-N (Hampton Research). The loop was mounted on a SMART APEX three circle diffractometer. The range of θ was from 2.30 to 26.81º. All nonhydrogen atoms were refined anisotropically. *l*-ValZnCl contains one ligand and one chloride atom and metal atom in the asymmetric unit. It should be noted that other supporting characterization data are consistent with the crystal structure. Final full matrix least-squares refinement on $F2$ converged to $R1= 0.0384$ ($F > 2\sigma F$) and $wR2 = 0.1203$ (all data) with GOF = 1.017. Very high displacement parameters, high esd's and partial occupancy due to the disorder make it impossible to determine accurate positions for the hydrogen atoms in water molecules. Crystallographic data (excluding structure factors) for this structure have been deposited with the CCDC as deposition No. CCDC 831054. The ORTEP diagram is provided with 50% probability (Figure 3.12a).

Experimental and refinement details for *l*-ValZnBr: A colourless rod shaped crystal of *l*-ValZnBr was placed in 0.7 mm diameter nylon CryoLoops (Hampton Research) with Paraton-N (Hampton Research). The loop was mounted on a SMART APEX three circle diffractometer. The range of θ was from 2.29 to 20.90º. All nonhydrogen atoms were refined anisotropically. *l*-ValZnBr contains one ligand and one bromine atom and metal atom in the asymmetric unit. It should be noted that other supporting characterization data are consistent with the crystal structure. Final full matrix least-squares refinement on $F2$

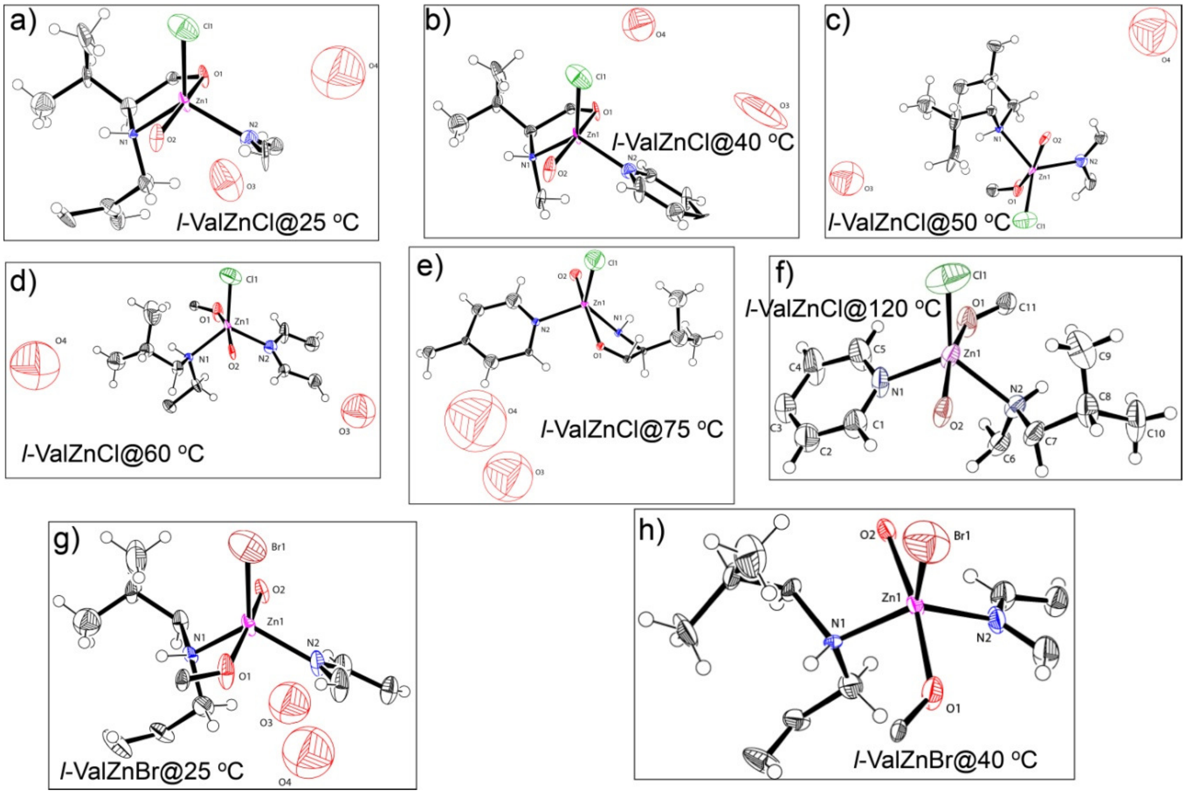

Figure 3.12: ORTEP diagrams for the asymmetric unit of the MOFs at different temperatures in 50% probability level. Figure adapted from ref. 3.13.

converged to $R1 = 0.0618$ ($F > 2\sigma F$)) and $wR2 = 0.2133$ (all data) with GOF = 1.017. Very high displacement parameters, high esd's and partial occupancy due to the disorder make it impossible to determine accurate positions for the hydrogen atoms in water molecules. Crystallographic data (excluding structure factors) for this structure have been deposited with the CCDC as deposition No. CCDC 831055. The ORTEP diagram is provided with 50% probability (Figure 3.12g).

Experimental and refinement details for *d*-ValZnCl: A colorless rod shaped crystal of *d*-ValZnCl was placed in 0.7 mm diameter nylon CryoLoops (Hampton Research) with Paraton-N (Hampton Research). The loop was mounted on a SMART APEX three circle diffractometer. The range of θ was from 2.34 to 27.13º. All nonhydrogen atoms were refined anisotropically. *d*-ValZnCl contains one ligand and one chloride atom and metal atom in the asymmetric unit. It should be noted that other supporting characterization data are consistent with the crystal structure. Final full matrix least-squares refinement on $F2$

converged to *R*1= 0.0469 (*F* >2σ*F*)) and *wR*2 = 0.1387 (all data) with GOF = 1.053. Very high displacement parameters, high esd's and partial occupancy due to the disorder make it impossible to determine accurate positions for the hydrogen atoms in water molecules. Crystallographic data (excluding structure factors) for this structure have been deposited with the CCDC as deposition No. CCDC 831056.

Experimental and refinement details for *d*-ValZnBr: A colorless rod shaped crystal of *d*-ValZnBr was placed in 0.7 mm diameter nylon CryoLoops (Hampton Research) with Paraton-N (Hampton Research). The loop was mounted on a SMART APEX three circle diffractometer. The range of θ was from 2.29 to 22.66º. All nonhydrogen atoms were refined anisotropically. *d*-ValZnBr contains one ligand and one bromine atom and metal atom in the asymmetric unit. It should be noted that other supporting characterization data are consistent with the crystal structure. Final full matrix least-squares refinement on *F*2 converged to *R*1= 0.0583 (*F* >2σ*F*)) and *wR*2 = 0.1859 (all data) with GOF = 1.046. Very high displacement parameters, high esd's and partial occupancy due to the disorder make it impossible to determine accurate positions for the hydrogen atoms in water molecules. Crystallographic data (excluding structure factors) for this structure have been deposited with the CCDC as deposition No. CCDC 831057.

NOTE: The results of this chapter have already been published in *J. Am. Chem. Soc.,* 2011, **133**, 17950. with the title: "*Helical Water Chain Mediated Proton Conductivity in Homochiral Metal–Organic Frameworks with Unprecedented Zeolitic unh-Topology*" The publication was resulted from the group of Dr. Rahul Banerjee and his students Subash Chandra Sahoo and Tanay Kundu from CSIR-National Chemical Laboratory, Pune, India. Major experimental works were contributed by Tanay Kundu using instrumental facilities of CSIR-National Chemical Laboratory. Subash Chandra Sahoo did the data interpretation and manuscript preparation.

CHAPTER 4

HYDROLYTIC REGENERABILITY IN A SERIES OF AMINO ACID DERIVED MOFS

4.1 Introduction:

Metal-organic frameworks (MOFs) are structured by linking metal ions or clusters by organic connecting units called linkers via coordination bonds. The reversibility of the coordination bonds in high boiling solvents (DMF, DMA, DEF, NMP, DMSO etc.) resulted in single crystallinity of the MOFs. However, the same phenomena become irreversible in water, leading to the formation of metal oxides or hydroxides and the bare organic links, as the case happens for majority of the MOFs (> 90%). Well known MOFs like MOF 5 [1.4] and MOF 177 [1.5b] shows this kind of behavior. The abovementioned bottleneck of MOFs restricts its application (e.g. catalysis) in toxic organic solvents (e.g. DMF, DMSO, CH_3CN) rather than environmentally benign H_2O. Only limited number of water stable MOFs (e.g. MIL-101, ZIF-8, UiO-66) [1.46] have been reported in the literature for their practical utility in aqueous medium. Researchers approach involves incorporation of multiple alkane and fluorine functionality. For example, methyl modified MOFs was successfully synthesized by incorporation methyl group in the parent ligand [4.1]. In another case, fluorine atoms have been decorated in the ligand to repel water molecules [4.2]. However, such approach involves diminished pore aperture and further functionalization of the framework backbone for industrial relevance remains a challenge. As a result, a simple design for MOFs having water stability and structural reversibility is highly anticipated.

In this chapter, we present the design of amino acid derived MOFs which possesses ambient temperature hydrolytic stability as well as high temperature hydrolytic regenerability. A series of eight homochiral metal-organic frameworks (MOFs) (ValZnCl, ValZnBr, ValZnFor, ValZnOAc, AlaZnCl, AlaZnBr, AlaZnFor, AlaZnOAc) have been synthesized by using pyridyl derivative of *l*–valine or *l*–alanine, and Zn(II) salt as metal precursor with different coordinated anions (Cl^-, Br^-, HCO_2^- and $CH_3CO_2^-$). A 3D homochiral architecture with parallel 1D helical channel along the crystallographic *c* axis results in extremely rare zeolitic *unh* topology in all the cases. Interestingly, lattice water molecules hydrogen bonded to the coordinated anions (Cl^-, Br^-, HCO_2^- and $CH_3CO_2^-$) form a secondary double helical arrangement of water molecules inside the homochiral frameworks. Replacement of valine (amino acid residue of the ligand) with more hydrophilic alanine results in enhanced polar intermolecular interaction, higher water sorption capability of the aforestated MOFs. The coordinated anions largely determine the differential regenerability of the aforementioned MOFs. A solution state processing method has been demonstrated to utilize the unique water soluble property to yield completely different MOF architectures.

4.2 Result and discussion:

4.2.1 Structural aspects of the MOFs:

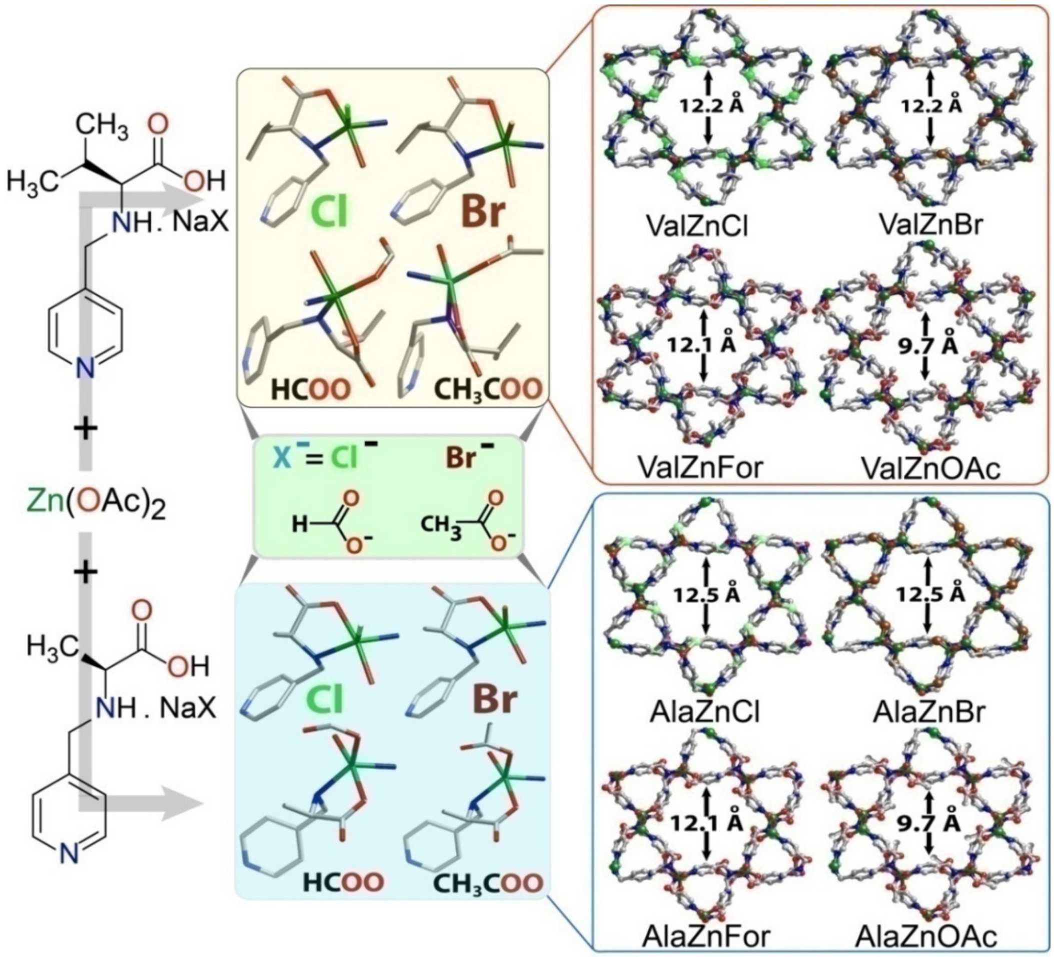

Figure 4.1: Schematic representation of the chiral MOF synthesis starting from chiral links. Figure adapted from ref. 4.3.

MOFs reported in this chapter were synthesized by mixing Zn(CH_3CO_2)$_2$.2H_2O and (pyridine-4-yl)methylamino-valine (a valine derived link for ValZnX) or

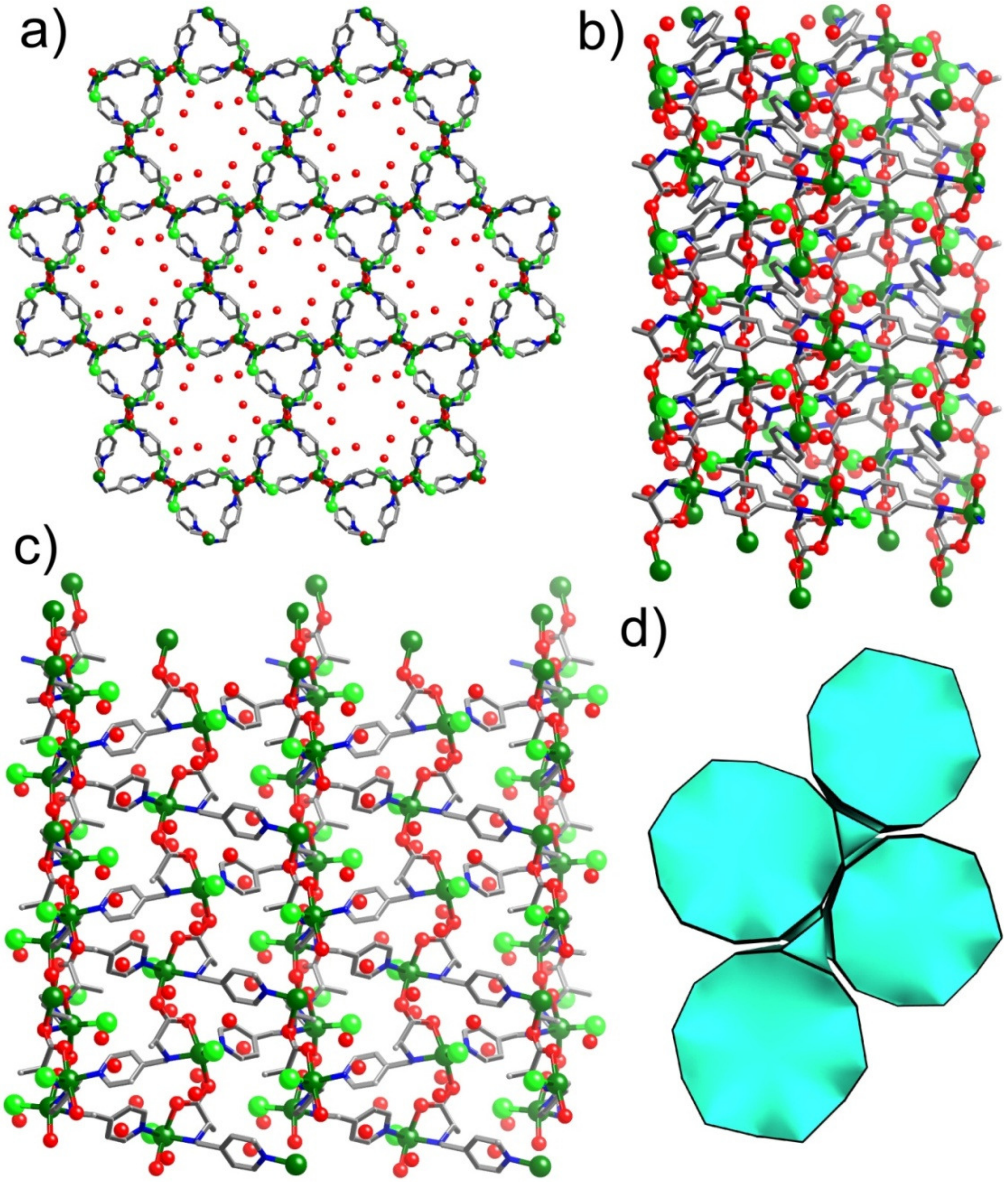

Figure 4.2: a) Polyhedral packing image of AlaZnCl along crystallographic *c* axis. b) *b* axis. c) Helical packing of AlaZnCl backbone. b) Topological representation of the AalZnCl tiling image. Figure adapted from ref. 4.3.

(pyridin-4-yl)methylamino-alanine (an alanine derived link for AlaZnX) either in caped vial at 90 °C or in an open vial by slow evaporation within 12-48 h. Interestingly, the as-synthesized bulk ligand is composed of neutral pyridyl substituted valine or alanine link

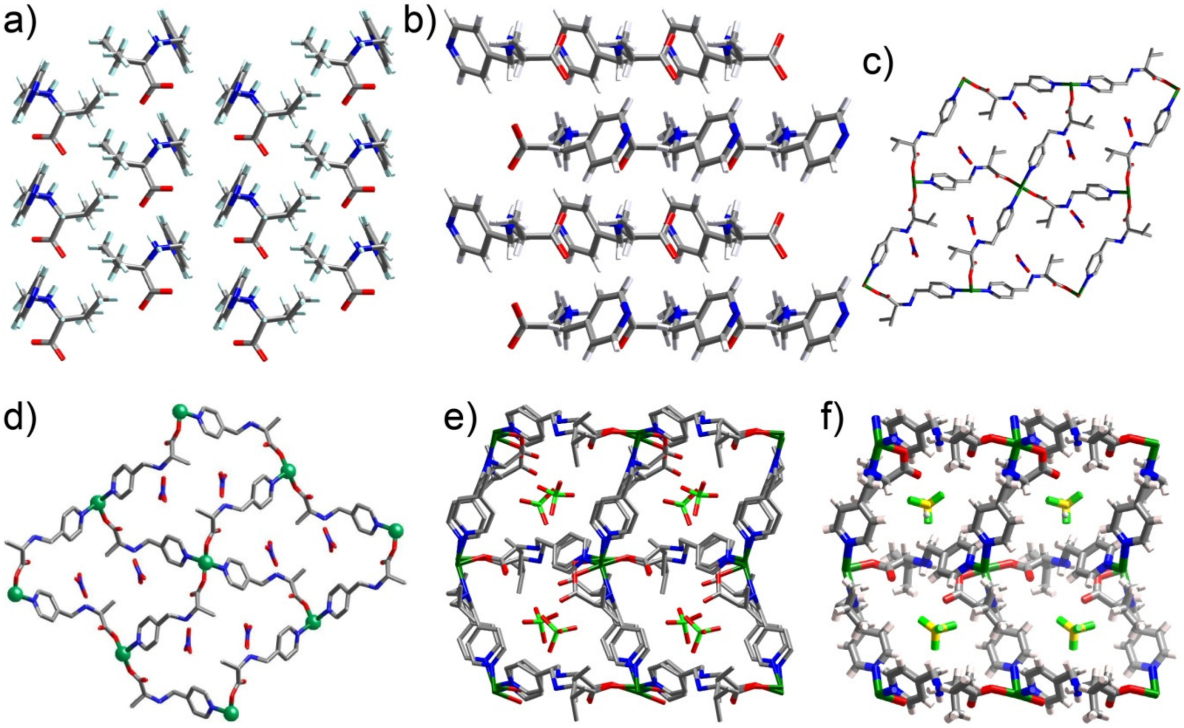

Figure 4.3: Crystal packing view of a) Val ligand through crystalligraphic *b* axis, b) Ala ligand from *a* axis c) ValZnNO$_3$ from *b* axis d) AlaZnNO$_3$ through *c* axis e) ValZnClO$_4$ and f) ValZnBF$_4$through *a* axis. Figure adapted from ref. 4.3.

and corresponding Na(I) salt of anions (Cl$^-$, Br$^-$, HCO$_2$$^-$ and CH$_3$CO$_2$$^-$). AlaZnCl crystallizes in the *P*6$_1$ space group, which comprises of one Zn(II), one AlaCl ligand and two lattice water molecules in the asymmetric unit [$a = b = 17.4587(2)$, $c = 10.24475(14)$]. All adjacent square pyramidal zinc nodes are bridged by AlaCl to form a 6$_1$ helical chain with a pitch of 12.9 Å along the crystallographic *c* axis. Clockwise and anti-clockwise coordination of the pyridyl groups extend the lattice along the *ab* plane resulting in 3D framework architecture with extremely rare zeolitic *unh* topology containing close-packed 1D open channel (1.2 nm) along the *c* axis filled with solvent water molecules (Figure 4.1). AlaZnBr, AlaZnFor and AlaZnOAc possess similar framework architecture as compared to AlaZnCl, only difference is coordinated anions (Br$^-$, HCO$_2$$^-$ and CH$_3$CO$_2$$^-$) in place of Cl$^-$. However, the anions are decorated towards the pore aperture. As a result, in every case there are subtle changes in the pore cavity (Figure 4.1). On the other hand, ValZnCl (structure discussed in detail in the earlier chapter) exhibit analogous structural integrity with AlaZnCl, albeit with increased hydrophobicily as well as less porosity owing to replacement of methyl (–CH_3) group by comparatively bulky and hydrophobic isopropyl [–$CH(CH_3)_2$] group in the side chain of the amino acid derived links. ValZnBr, ValZnFor and ValZnOAc are different isomers of ValZnCl with respect to different coordinated anions

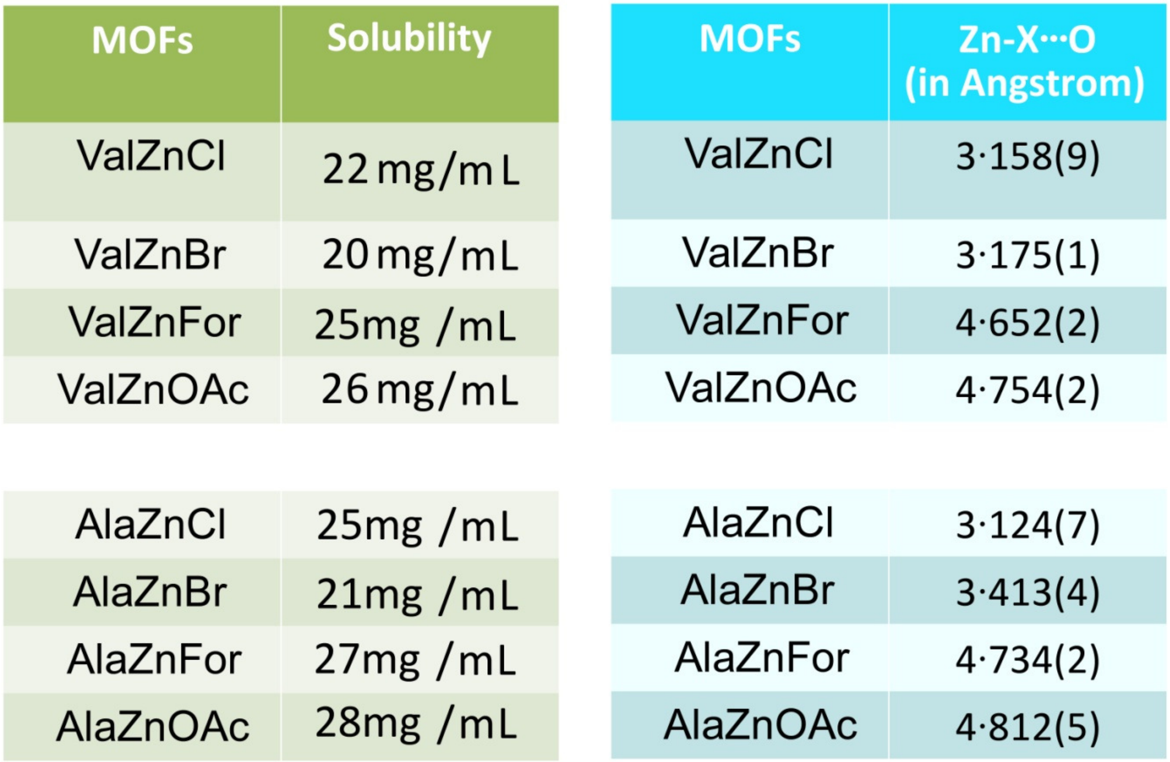

MOFs	Solubility
ValZnCl	22 mg/mL
ValZnBr	20 mg/mL
ValZnFor	25mg /mL
ValZnOAc	26 mg/mL
AlaZnCl	25mg /mL
AlaZnBr	21mg /mL
AlaZnFor	27mg /mL
AlaZnOAc	28mg /mL

MOFs	Zn-X···O (in Angstrom)
ValZnCl	3·158(9)
ValZnBr	3·175(1)
ValZnFor	4·652(2)
ValZnOAc	4·754(2)
AlaZnCl	3·124(7)
AlaZnBr	3·413(4)
AlaZnFor	4·734(2)
AlaZnOAc	4·812(5)

Figure 4.4: Solubility chart and hydrogen bonding distance for the MOFs.

(Br^-, HCO_2^- and $CH_3CO_2^-$). All the alanine based MOFs possess higher pore aperture as well as framework polarity than its valine counterparts due to substitution of bulky and hydrophobic isopropyl group [–$CH(CH_3)_2$] with methyl group (–CH_3). The lattice water molecules are weakly H-bonded to the Zn–Cl unit [(O···Cl–Zn, 3.124(7) Å) in AlaZnCl] which run along the helical channels, resulting secondary helical water arrangement. The different polarity of the Zn–X bond (Cl^-, Br^-, HCO_2^- or $CH_3CO_2^-$) largely determine their distance from adjacent water molecules, which is lowest for Zn–Cl [3.124(7) Å in AlaZnCl] and highest for Zn-OAc [4.812(5) Å in AlaZnOAc] (Figure 4.4). Moreover, the distances are shorter in alanine than its valine congeners, justified from the fact that enhanced intermolecular interaction resulted due to the enhancement of hydrophilicity at the side chain (isopropyl in valine to methyl in alanine) (Figure 4.4). Single-crystal X-ray diffraction analysis revealed that all the eight MOFs are structural isomers with respect to either coordinated anions (Cl^-, Br^-, HCO_2^- or $CH_3CO_2^-$) or side chain substitution (isopropyl in case of valine and methyl group in case of alanine) and helical water arrangement persists irrespective of the different coordinated anion substitution or change in the ligand backbone (Figure 4.1).

4.2.2 X-ray powder diffraction analysis and Thermo-gravimetric Analysis:

The phase purity of the bulk MOFs were confirmed by powder X-ray diffraction (PXRD) experiments which are in well agreement with the simulated PXRD patterns (Figure 4.5). The coordination polymers synthesized from the MOFs are also exhibit bulk phase purity and the peak positions matched exactly with that of the simulated ones. Thermogravimetric analysis (TGA) performed on as-synthesized MOFs revealed that these compounds have thermal stability upto ~270 °C (Figure 4.8). Interestingly, the chloride (Cl^-) and bromide (Br^-) coordinated valine and alanine MOFs (i.e. ValZnCl, ValZnBr, AlaZnCl and AlaZnBr) possess higher thermal stability (upto 270 °C) than the formate (HCO_2^-) and acetate

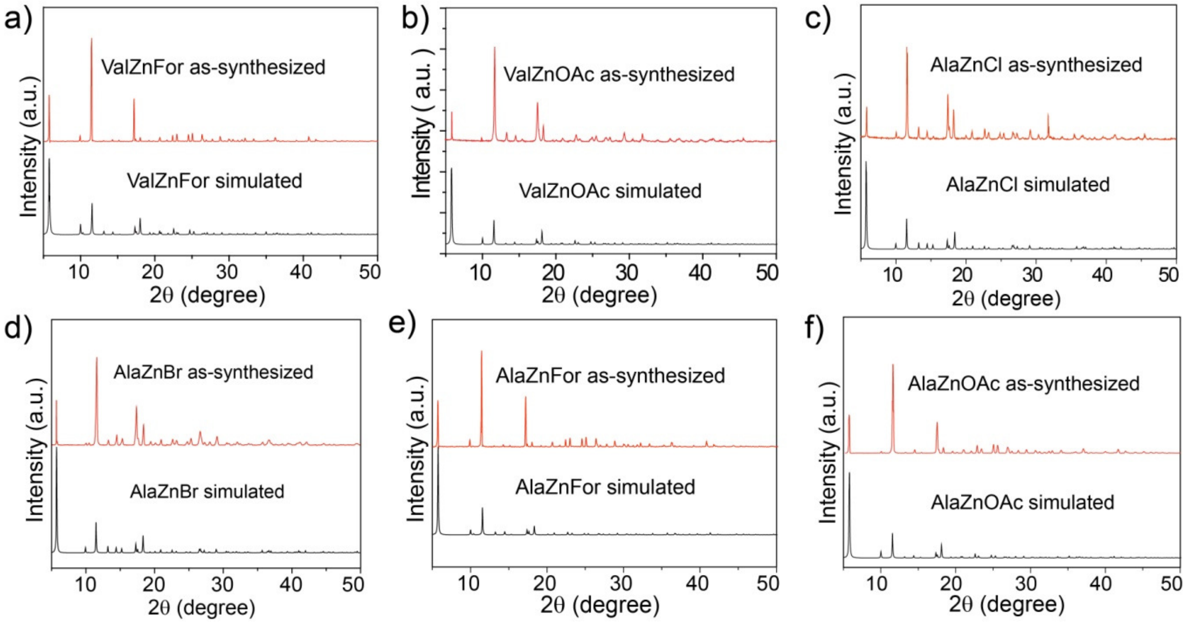

Figure 4.5: PXRD patterns of the MOFs compared with the simulated one. a) ValZnFor b) ValZnOAc c) AlaZnBr d) AlaZnCl e) AlaZnFor f) AlaZnOAc. Figure adapted from ref. 4.3.

($CH_3CO_2^-$) counterparts (ValZnFor, ValZnOAc, AlaZnFor and AlaZnOAc), having thermal stability upto ~210 °C. TGA traces for the as-synthesized MOFs showed a gradual weight-loss step at temperature range of 40–100 °C, corresponding to escape of guest water molecules from the pores (Figure 4.8). The other two coordination polymers viz. $ValZnNO_3$ and $AlaZnNO_3$ exhibits thermal stability of the frameworks after guest removal upto ~270 °C (Figure 4.7c and d). Interestingly, the water molecules were released without damaging the frameworks, as evidenced by Variable Temperature Single Crystal XRD data and coincidence of the PXRD patterns of the as-synthesized samples heated to and held at 200 °C in N_2 atmosphere with the PXRD patterns simulated from single-crystal structures. All major peaks of experimental VT-PXRD and simulated PXRDs are well matched,

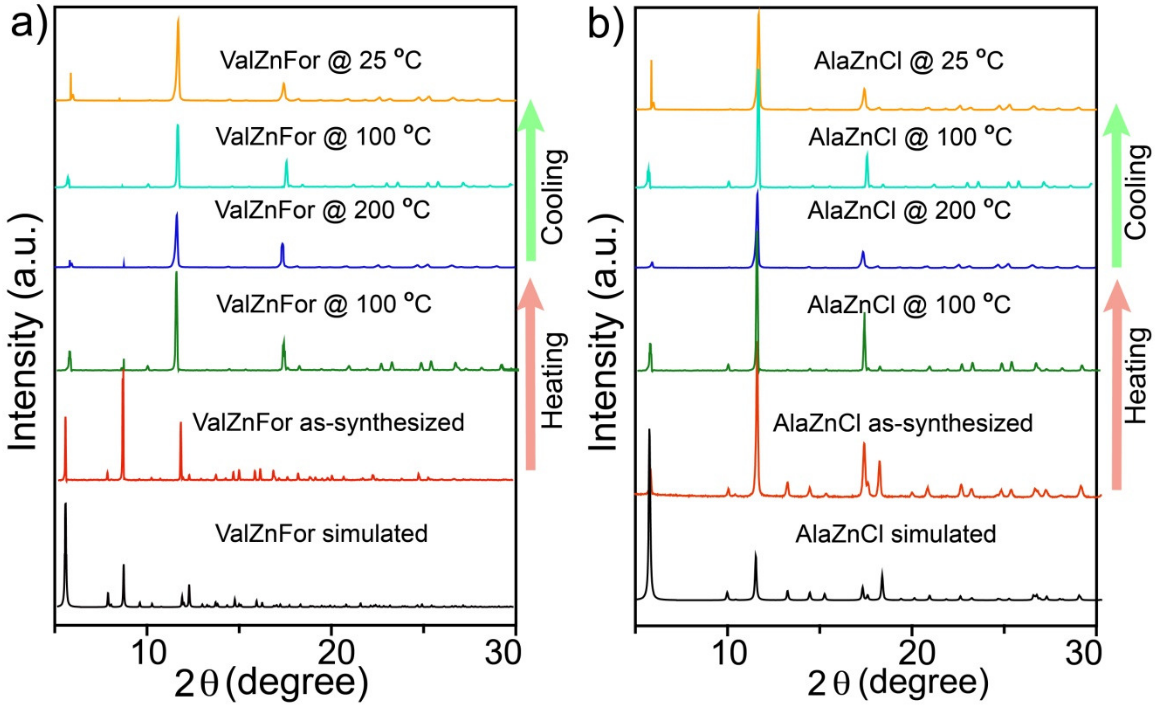

Figure 4.6: VT-PXRD patterns of the a) ValZnFor b) AlaZnCl. Figure adapted from ref. 4.3.

indicating the sample's phase purity (Figure 4.6). A combine heating and cooling *in situ* VT-PXRD experiment reveals that the frameworks are stable and remain crystalline over a

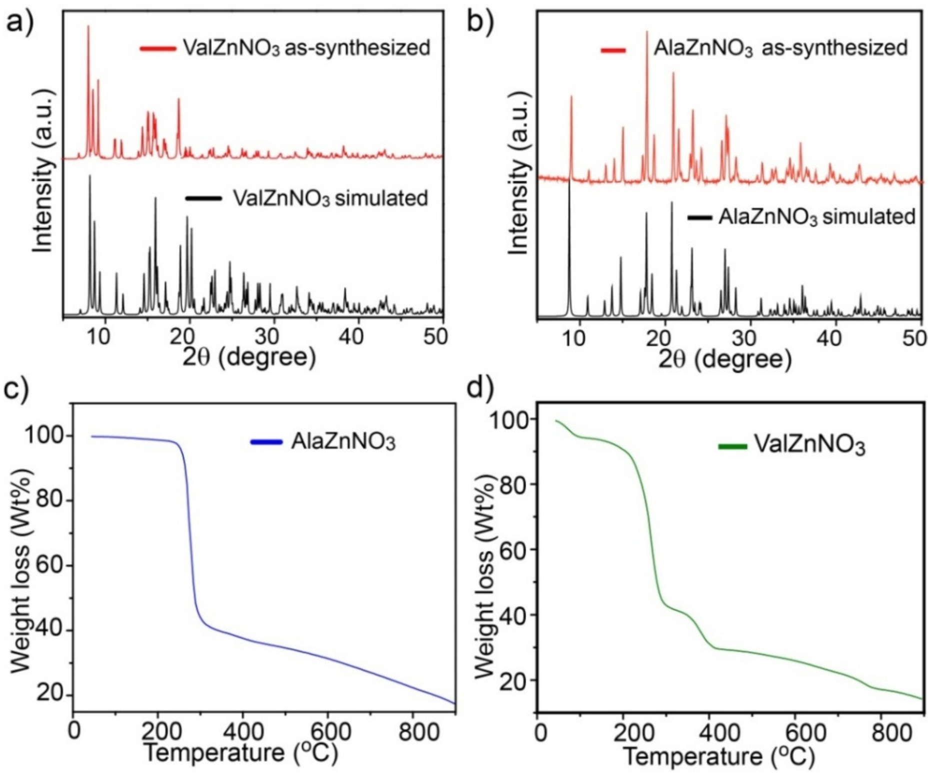

Figure 4.7: PXRD patterns compared with the simulated one. a) ValZnNO$_3$ and b) AlaZnNO$_3$. TGA analysis of c) ValZnNO$_3$ and d) AlaZnNO$_3$. Figure adapted from ref. 4.3.

wide temperature range (heating from 25 to 200 °C followed by cooling from 200 to 25 °C) and remain stable after solvent removal (H_2O escapes ~100 °C, confirmed by TGA) (Figure 4.6).

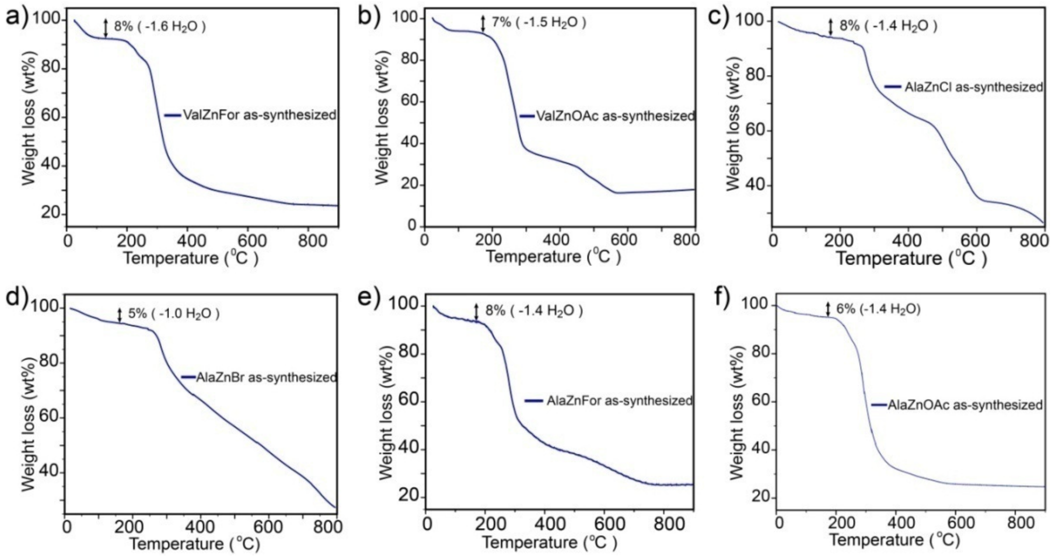

Figure 4.8: TGA analysis of the MOFs a) ValZnFor b) ValZnOAc c) AlaZnCl d) AlaZnBr e) AlaZnFor f) AlaZnOAc. Figure adapted from ref. 4.3.

4.2.3 Single crystal to single crystal transformation studies on the MOFs:

It is noteworthy that the water molecules adopt almost similar arrangements in all the MOFs reported in this chapter except the relative distances from the framework backbone and the distance between themselves let alone their handedness. However, the guest free frameworks of the MOFs show high affinity towards water molecules irrespective of their different structural variations. In the previous chapter we have shown that ValZnCl shows a reversible transformation in presence of water vapor, which was proved by various experiments. To provide evidence of water affinity from crystallographic point of view, MOFs were extensively studied by numerous in situ VT-SCXRD experiments. The single crystal data of AlaZnCl collected at 100 K shows well resolved two water molecules hydrogen bonded with the coordinated chloride anion. At near ambient temperature, we evidenced only one water molecule in AlaZnCl crystals. At higher temperatures (>50 °C) an evacuated framework with no trace of solvent water molecules observed crystallographically. This phenomenon is reversible like the ValZnCl. From the abovementioned experiment it is evident that it is possible to obtain a desolvated framework with high crystalline architecture in amino acid derived MOFs.

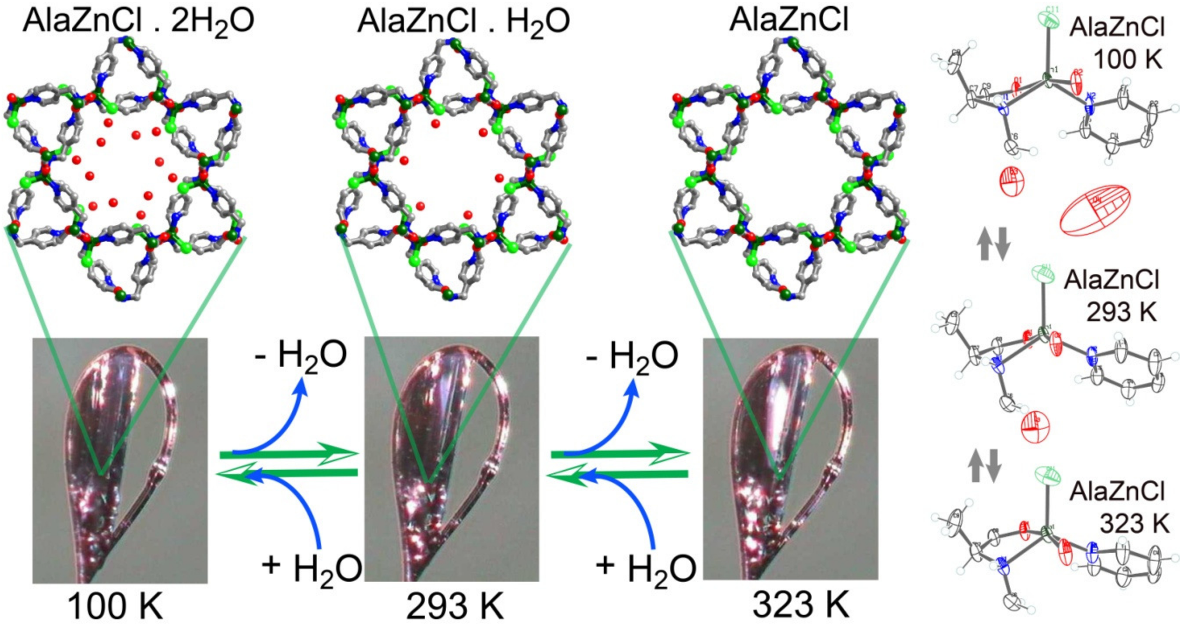

Figure 4.9: a) Structural reversibility in the light of VT-SCXRD in case of AlaZnCl.

4.2.4 Water adsorption studies on the MOFs:

To further explore the relationship between the framework modulation and material characteristics, water sorption experiment have been performed. AlaZnCl possess highest

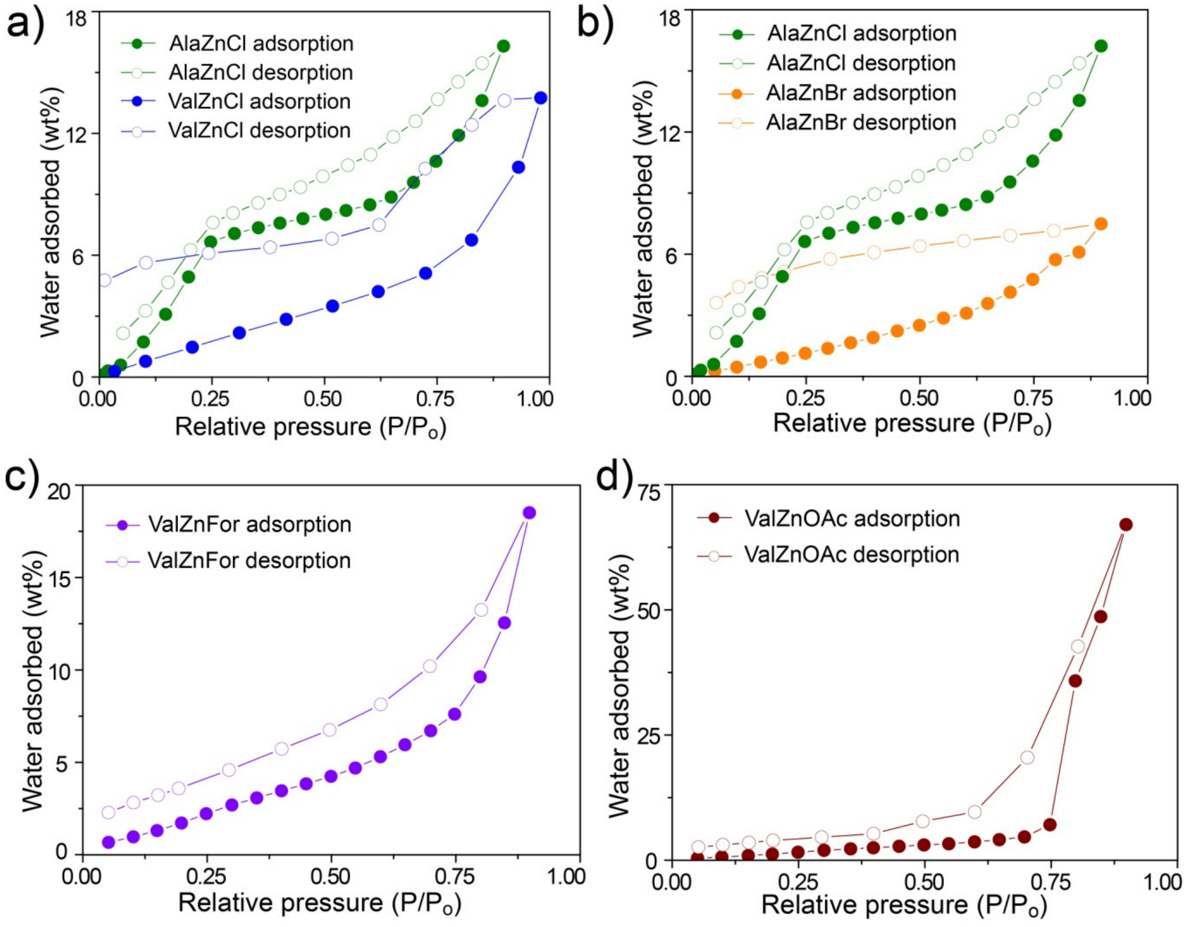

Figure 4.10: Water adsorption isotherms for the MOFs a) AlaZnCl compared with ValZnCl b) AlaZnCl compared with AlaZnBr. c) ValZnFor and d) ValZnOAc. Figure adapted from ref. 4.3.

water adsorbing capacity [210 cc/g (~17 wt%) at $P/P_0 = 0.89$ and STP] among all these MOFs reported in this chapter (Figure 4.10a). In cases of AlaZnBr, however, decrease in hydrophilicity resulted in low water sorption of 80 cc/g (~6 wt%) at similar conditions. Their corresponding valine congeners (i.e. ValZnCl and ValZnBr) exhibit even lesser sorption capacity owing to hydrophobic isopropyl groups. However, formate (HCO_2^-) and acetate ($CH_3CO_2^-$) based valine and alanine MOFs (ValZnFor, ValZnOAc, AlaZnFor and AlaZnOAc) exhibit low water uptake followed by pore condensation behavior (Figure 4.10d). From the above behavior of the MOFs towards water adsorption, it is evident that the hydrophobicity is controlled by both the framework backbone (amino acid sidearm) as well as the coordinated anions. The water affinity order is also a reminiscent of the relative distances of the water molecules from the corresponding frameworks (Figure 4.4).

4.2.5 Hydrolytic regenerability studies on the MOFs:

The most important aspect, however, we believe these MOFs possess is their unprecedented hydrolytic regenerability i.e. deconstruction of the MOF in water and regeneration of the same framework from aqueous solution. Water degradability of MOFs and coordination polymers are common due to hydrolysis of coordination bonds in aqueous medium. These homochiral MOFs are stable towards moisture in room temperature for over 6 months irrespective of the framework constituents (Figure 4.12e). However, at elevated temperature (50–120 °C) these homochiral MOFs (Figure 4.11a) get deconstructed in water to form initially a turbid solution, which in turn forms a clear solution after continual refluxing at 90 °C (0.5–6 h) (Figure 4.11b), confirming completion of the deconstruction

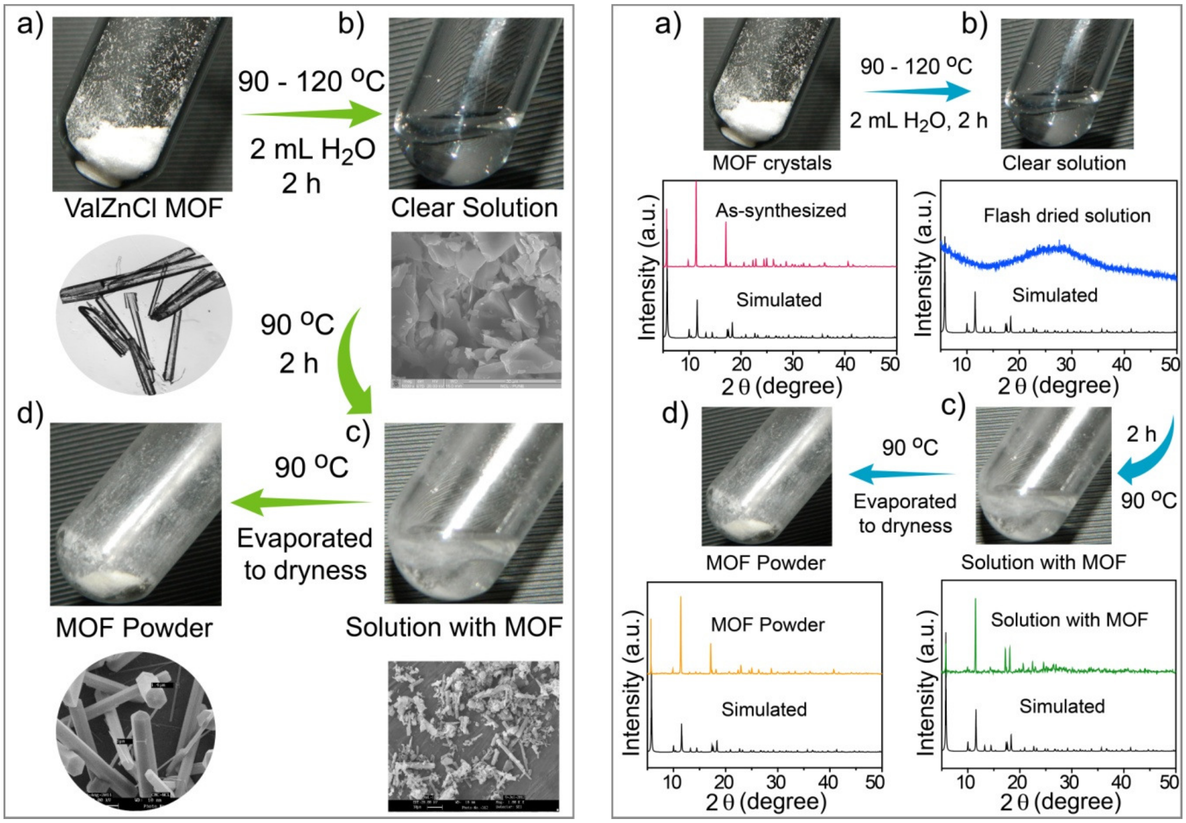

Figure 4.11: Regenerability process in the light of a) electron microscopy and b) Powder XRD. Figure adapted from ref. 4.3.

process. This clear solution when further heated continually at 90 °C for 2 h, the regenerated MOF crystals started to precipitate out from the solution (Figure 4.11c). After that, complete regeneration of the MOFs was completed when water molecules were evaporated completely (Figure 4.11d). Valine based MOFs deconstruct slowly and

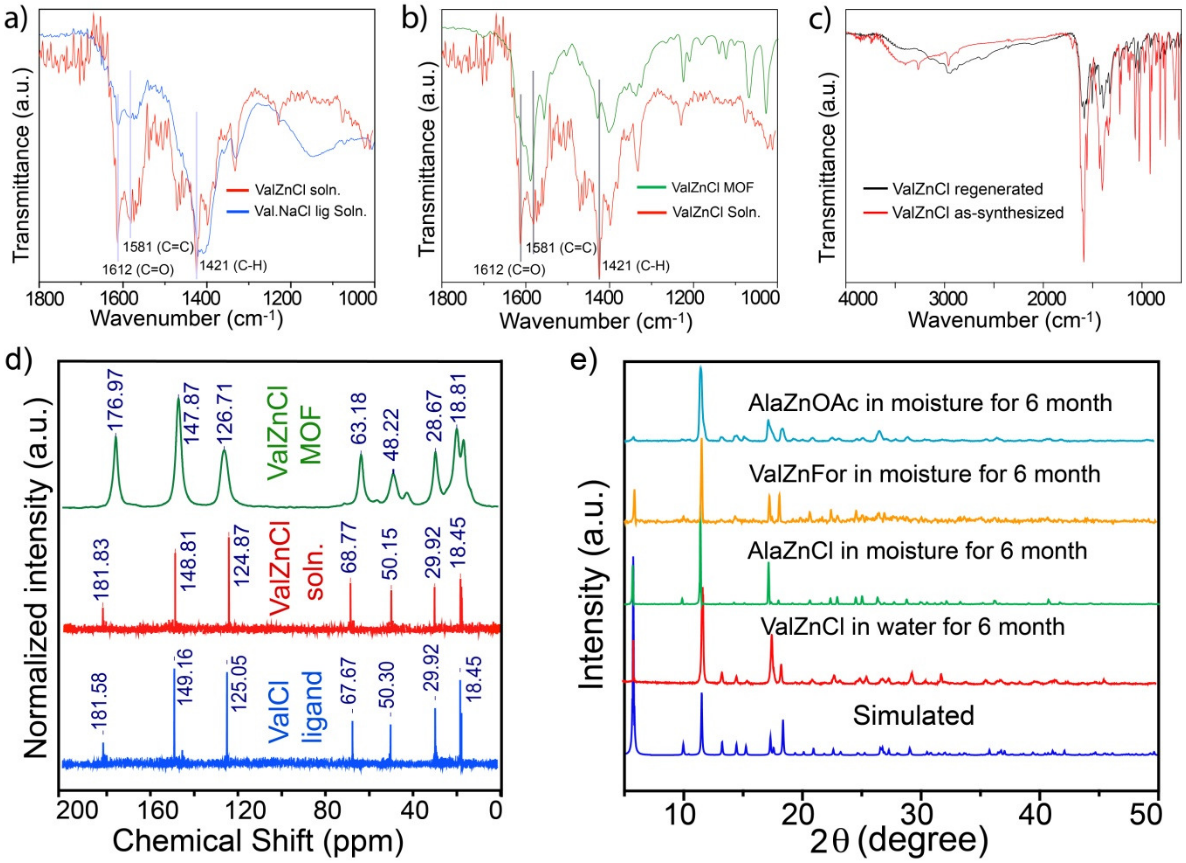

Figure 4.12: Regenerability process in the light of FT-IR spectra (a,b,c). d) The solution state ^{13}C NMR of deconstructed solution of ValZnCl (red) matches well with the ligand solution (blue). However, the MOF possess distinct peak positions (green). e) Water stability of the MOFs. Figure adapted from ref. 4.3.

recrystallized faster than their Alanine congeners due to hydrophobicity of the former. Originally rod shaped crystals get deconstructed and looses crystallinity in the aqueous solution at boiling temperatures, as evident from the Powder XRD pattern of the flash-dried solution (Figure 4.11b). The SEM of the flash-dried solution (Figure 4.11b) also yielded amorphous material with random morphology in contrast to parent rod shaped crystals (Figure 4.11a). The FT-IR spectra of the solution exactly matched with the corresponding ligands (Val/Ala), where carboxy stretching frequency remain centered at 1612 cm^{-1} in all cases, further confirming the deconstruction phenomena (Figure 4.12b). In addition, significant agreement was observed between the ^{13}C NMR characteristic peaks of the solution with the ligands, where identical chemical shift of carbon (of the carboxy group) at 181.8 ppm eludes to the deconstruction of the framework in solution (Figure 4.12d). Further evaporation of water leads to saturation of the solution resulting recrystallization of the corresponding MOFs. The Powder XRD patterns of this regenerated material (Figure 4.11d) shown well agreement with the simulated one, confirming precise reconstruction of the building blocks. The FT-IR patterns of the as-synthesized materials exactly match with the FT-IR patterns of the regenerated MOFs (Figure 4.12c). Furthermore, the SEM images of the MOF powder thus obtained finally after the regeneration process recapitulate the rod shaped morphology of the as-synthesized MOFs. To explore the solution state properties of these MOFs, we have performed salt metathesis reaction using different Ag(I) salts e.g. $AgNO_3$, $AgBF_4$, $AgClO_4$ and studied the reorganization pathway critically. The idea is to identify the constituents individually in solution and correlate with the mechanism proposed. The deconstructed ValZnCl (20 mg in 2 mL water) when treated with 250 µl 1N $AgNO_3$, resulted in creamy white precipitation of AgCl. The solution was filtered using Whatman filter paper and one part (containing Zn(II) ion, bare ligand and NO_3^- anion) was

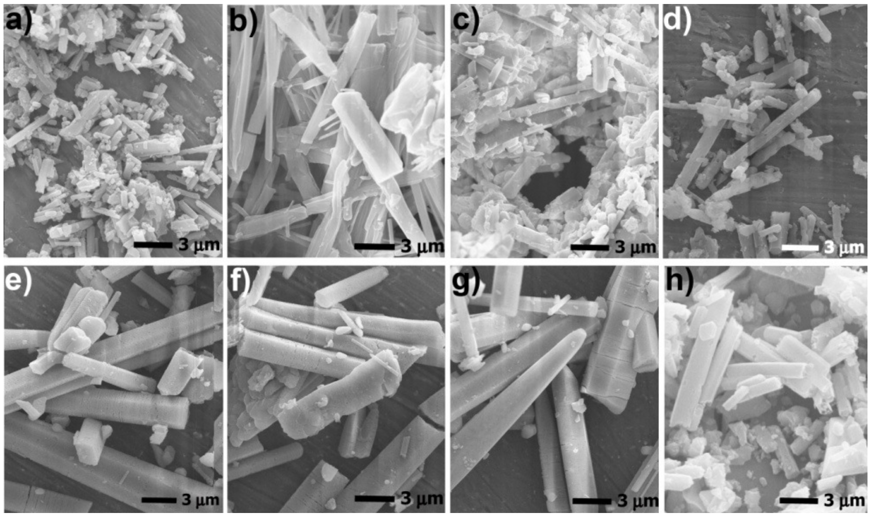

Figure 4.13: SEM image of the regenerated MOFs revealed retention of parent rod shaped morphology a) ValZnCl, b) ValZnBr, c) ValZnFor, d) ValZnOAc, e) AlaZnCl, f) AlaZnBr, g) AlaZnFor and h) AlaZnOAc. Figure adapted from ref. 4.3.

treated with either NaCl or NH_4Cl, which yielded rod shaped transparent ValZnCl crystals [$P6_1$, $a = b$ =17.691(2), c = 10.5617(12)], thus confirming the reconstitution in presence of Cl^- anions (Figure 4.14). Furthermore, another part when kept at room temperature for slow evaporation crystallizes into another new cationic homochiral framework, $ValZnNO_3$ ($C2$, a = 25.117(2), b = 5.7802(4), c = 21.993(2), β = 120°) (Figure 4.3c). Change in the Ag precursor generalizes the salt metathesis reaction with ValZnCl resulting in two more coordination polymers viz. $ValZnBF_4$ (Figure 4.3e) and $ValZnClO_4$ (Figure 4.3f). In a similar fashion, neutral AlaZnCl can be converted to a new coordination polymer,

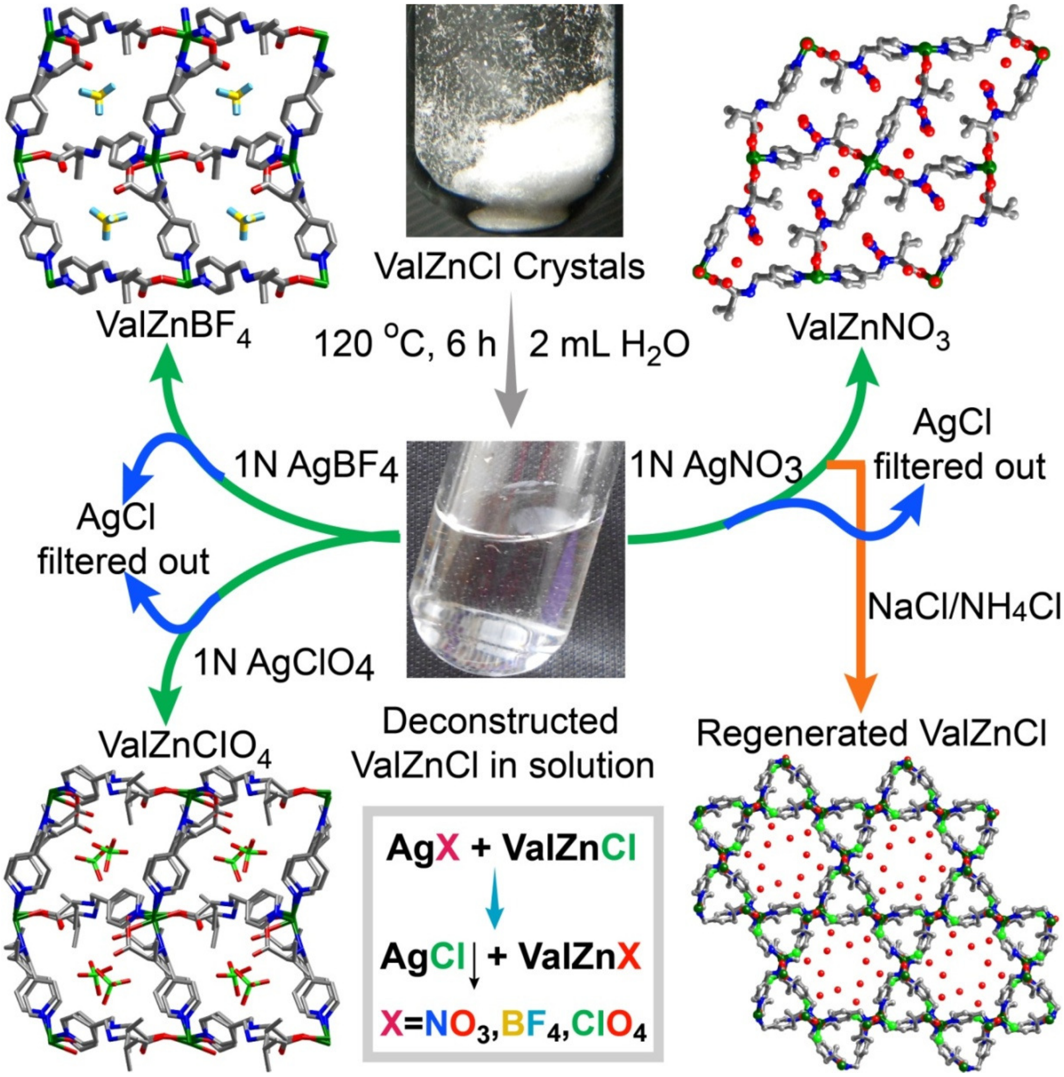

Figure 4.14: Schematic representation of the salt metathesis reaction on ValZnCl by addition of different Ag salts ($AgNO_3$,$AgBF_4$,$AgClO_4$) to yield 2D coordination polymers $ValZnNO_3$,$ValZnBF_4$,$ValZnClO_4$. The filtrate on addition of $NaCl/NH_4Cl$ yielded prototypical ValZnCl. Figure adapted from ref. 4.3.

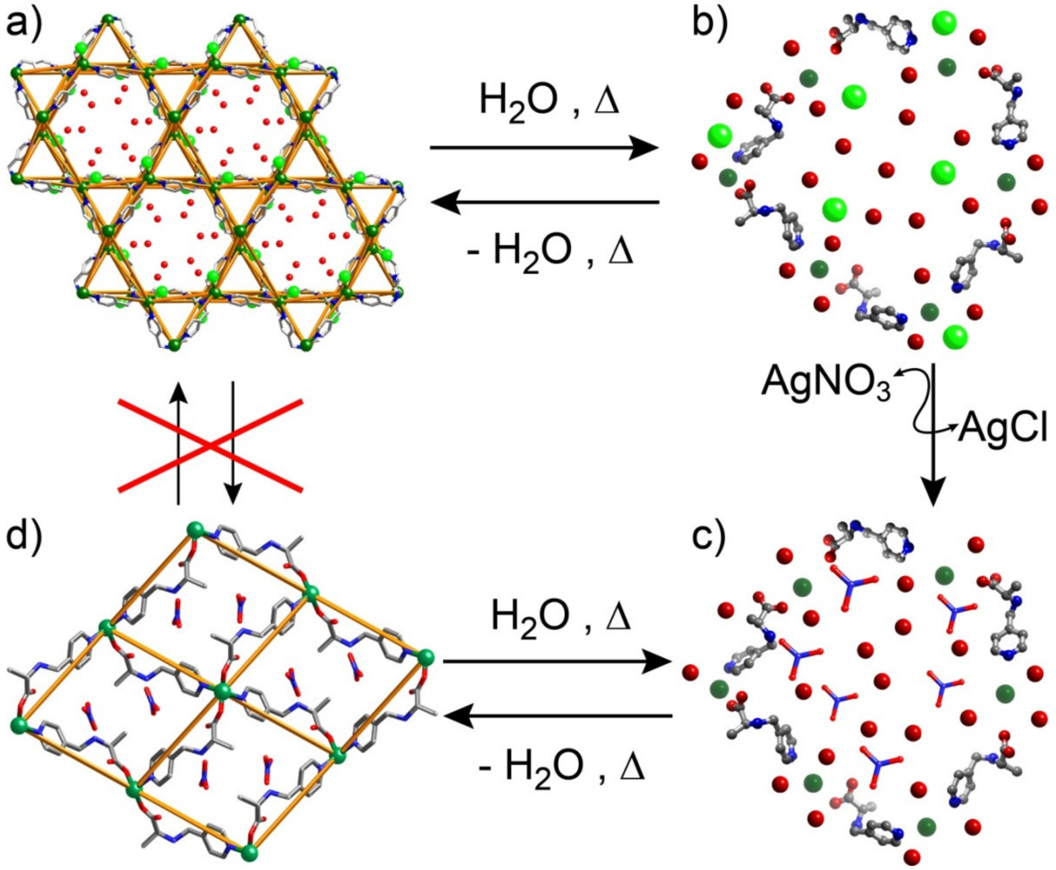

Figure 4.15: Schematic representation of the regenerability and salt metathesis process.

AlaZnNO$_3$ [$P2_12_12$, a = 12.8683(3), b = 16.2028(4), c = 5.4706(1)] (Figure 4.3d). Interestingly, ValZnNO$_3$ contains both tetra and pentacoordinated Zn(II) nodes, whereas AlaZnNO$_3$ contains solely tetracoordinated Zn(II) centers. ValZnBF$_4$ and ValZnClO$_4$ are isostructural in nature ($P2_1$) with Pentacoordinated Zn(II) and coordinated as well as uncoordinated (protonated) amine groups, where BF_4^- or ClO_4^- lie within pore cavity to neutralize the cationic framework. This experiment precisely confirms that the deconstructed solution is expected to be composed of Zn(II) ions, corresponding uncoordinated ligands and the anions in their hydrated form. Presence of free Cl^- has been confirmed by precipitation of AgCl upon addition of AgNO$_3$. Furthermore, the coordination environment as well as the coordination number change of the Zn(II) ion can only be possible in case of complete separation of the metal ligand assembly (Figure 4.15b). Hence we conclude that in presence of boiling water the MOF get deconstructed to form bare ligand, hydrated metal ion and anions of the corresponding MOFs (Figure 4.15b). We, for the first time, studied this unprecedented hydrolytic regenerable nature in 3D MOFs and utilized this property to perform salt metathesis reaction (Figure 4.15c) which in turn yielded 2D ionic coordination polymers (Figure 4.15d).

4.3 Conclusion:

In conclusion, we have synthesized eight porous homochiral Zn based MOFs using two different amino acid derived links. These MOFs adopt 3D periodic architecture with 1D helical water arrangement irrespective of the type of anion (Cl^-, Br^-, HCO_2^- and $CH_3CO_2^-$) substitution or side chain difference (methyl and isopropyl). All MOFs exhibit extremely rare zeolitic (unh) topology. Lattice water molecules are weakly hydrogen bonded to the coordinated anions to form a helical water arrangement inside the framework. Owing to hydrophilic nature of the pore aperture these MOFs exhibit diverse water sorption capacity subject to framework integrity. More importantly, These MOFs are regenerable from water via unprecedented deconstruction-reconstitution pathway, which has not been reported in MOF literature so far. For the first time, salt metathesis reaction has been performed on 3D MOFs to demonstrate the solution state property and utilized the same to synthesize different homochiral 2D coordination polymers with different architectures. Markedly different water solubility of these MOFs along with the unique regenerable property will surely open up numerous possibility of fabrication of these materials onto supporting surfaces for industrially relevant applications.

4.4 Experimental details:

4.3.1 Materials:

$Zn(CH_3COO)_2{\cdot}2H_2O$, *l*-valine, *l*-alanine, sodium borohydride, and 4-pyridinecarboxaldehyde were purchased from Aldrich Chemicals. All starting materials were used without further purification. All experimental operations were performed in air.

4.4.2 Synthetic methods:

4.4.2.1 Synthesis of the ligands:

a) Synthesis of (Pyridin-4-yl)methylamino-*l*-valine.HCOONa [ValFor]: To an aqueous solution (10 mL) of *l*-valine (2 g, 17 mmol) and Na_2CO_3 (0.91 g, 8.5 mmol), 4-pyridinecarboxaldehyde (1.82 g, 17 mmol) in MeOH (10 mL) was added slowly. The solution was stirred for 1 h and cooled in an ice bath. $NaBH_4$ (0.76 g, 20.4 mmol) in 5 mL of H_2O was added. The mixture was stirred for 3 h, and 3 N HCOOH was used to adjust the pH to 5–6. The clear solution was stirred further for 2 h and then evaporated to dryness. The solid was extracted in hot and dry MeOH (150 mL × 3), and the filtrate was evaporated to get the ligand along with sodium formate salt in form of a white powder. Yield: 2.9 g, 70%. IR (KBr, cm^{-1}): ν_{OH}, 3421; $\nu_{as}(CO_2)$, 1562; $\nu_s(CO_2)$, 1409. ^1H NMR (D_2O, ppm): -CH_3 (1.21, d, 3H), -CH_3 (1.35, d, 3H), -CH (3.20, m, 1H), -HN-CH (3.65, m, 1H), -CH_2 (3.82, dd, 2H), py-H (7.34, d, 2H), py-H (8.38, d, 2H).

b) Synthesis of (Pyridin-4-yl)methylamino-*l*-valine.CH_3COONa [ValOAc]: The ligand (ValOAc) was prepared exactly as *l*-ValCl only HBr was used instead of HCl for pH adjustment. Yield = 3.4 g (70%). IR (KBr, cm^{-1}): ν_{OH}, 3420; $\nu_{as}(CO_2)$, 1560; $\nu_s(CO_2)$, 1411. ^1H NMR (D_2O, ppm): -CH_3 (1.20, d, 3H), -CH_3 (1.33, d, 3H), -CH (3.24, m, 1H), -HN-CH (3.63, m, 1H), -CH_2 (3.79, dd, 2H), py-H (7.34, d, 2H), py-H (8.37, d, 2H).

c) Synthesis of (Pyridin-4-yl)methylamino-*l*-alanine.NaCl [AlaCl]: The ligand (*d*-ValCl) was prepared exactly as *l*-ValCl only *d*-valine was used instead of *l*-valine. Yield: 3.1 g, 72%. IR (KBr, cm^{-1}): ν_{OH}, 3417; $\nu_{as}(CO_2)$, 1564; $\nu_s(CO_2)$, 1415. ^1H NMR (D_2O, ppm): -CH_3 (1.21, d, 3H), -CH_3 (1.34, d, 3H), -CH (3.22, m, 1H), -HN-CH (3.65, m, 1H), -CH_2 (3.78, dd, 2H), py-H (7.30, d, 2H), py-H (8.36, d, 2H).

d) Synthesis of (Pyridin-4-yl)methylamino-*l*-alanine.NaBr [AlaBr]: The ligand (*d*-ValBr) was prepared exactly as *l*-ValBr only *d*-valine was used instead of *l*-valine. Yield: 3.6 g, 72%. IR (KBr, cm^{-1}): ν_{OH}, 3419; $\nu_{as}(CO_2)$, 1570; $\nu_s(CO_2)$, 1421. ^1H NMR (D_2O, ppm): -CH_3 (1.20, d, 3H), -CH_3 (1.34, d, 3H), -CH (3.24, m, 1H), -HN-CH (3.63, m, 1H), -CH_2 (3.80, dd, 2H), py-H (7.35, d, 2H), py-H (8.37, d, 2H).

e) Synthesis of (Pyridin-4-yl)methylamino-*l*-alanine.HCOONa [AlaFor]: The ligand (*d*-ValBr) was prepared exactly as *l*-ValBr only *d*-valine was used instead of *l*-valine. Yield: 3.6 g, 72%. IR (KBr, cm^{-1}): ν_{OH}, 3419; $\nu_{as}(CO_2)$, 1570; $\nu_s(CO_2)$, 1421. ^1H NMR (D_2O, ppm): -CH_3 (1.20, d, 3H), -CH_3 (1.34, d, 3H), -CH (3.24, m, 1H), -HN-CH (3.63, m, 1H), -CH_2 (3.80, dd, 2H), py-H (7.35, d, 2H), py-H (8.37, d, 2H).

f) Synthesis of (Pyridin-4-yl)methylamino-*l*-alanine.CH_3COONa [AlaOAc]: The ligand (*d*-ValBr) was prepared exactly as *l*-ValBr only *d*-valine was used instead of *l*-valine.

Yield: 3.6 g, 72%. IR (KBr, cm^{-1}): ν_{OH}, 3419; $\nu_{as}(CO_2)$, 1570; $\nu_s(CO_2)$, 1421. ^1H NMR (D_2O, ppm): $-CH_3$ (1.20, d, 3H), $-CH_3$ (1.34, d, 3H), -CH (3.24, m, 1H), -HN-CH (3.63, m, 1H), $-CH_2$ (3.80, dd, 2H), py-H (7.35, d, 2H), py-H (8.37, d, 2H).

4.4.2.2 Synthesis of the MOFs:

a) Synthesis of [{Zn(Val)(HCOO)}$(H_2O)_2]_\infty$ (ValZnFor): To an aqueous solution (2 mL) of ValFor (0.055 g, 0.2 mmol), $Zn(CH_3COO)_2.2H_2O$ (0.022 g, 0.1 mmol) was added and sonicated for 10 min. The clear solution was kept in a tightly capped 5 mL vial for 24 h at 90 °C to produce rod shaped transparent crystals. Yield: 0.023 g, 71%. IR (KBr, cm^{-1}): ν_{OH}, 3420; ν_{N-H}, 2975; $\nu_{as}(CO_2)$, 1589; $\nu_s(CO_2)$, 1397. ν_{C-N},1627. Elemental Analysis: Calcd- C (40.51%), H (5.25%), N (8.59%); Found C (40.54%), H (5.28%), N (8.57%). CCDC No. 918487.

b) Synthesis of [{Zn(Val)(CH_3COO)}$(H_2O)_2]_\infty$ (ValZnOAc): To an aqueous solution (2 mL) of ValOAc (0.058 g, 0.2 mmol), $Zn(CH_3COO)_2.2H_2O$ (0.022 g, 0.1 mmol) was added and sonicated for 10 min. The clear solution was kept in a tightly capped 5 mL vial for 24 h at 90 °C to produce rod shaped transparent crystals. Yield: 0.026 g, 72%. IR (KBr, cm^{-1}): ν_{OH}, 3425; ν_{N-H}, 2970; $\nu_{as}(CO_2)$, 1592; $\nu_s(CO_2)$, 1395. ν_{C-N},1622. Elemental Analysis: Calcd- C (35.65%), H (4.62%), N (7.60%); Found C (35.60%), H (4.64%), N (7.62%). CCDC No. 918488.

c) Synthesis of [{Zn(Ala)(Cl)}$(H_2O)_2]_\infty$ (AlaZnCl): To an aqueous solution (0.5 mL) of AlaCl (0.048 g, 0.2 mmol), $Zn(CH_3CO_2)_2.2H_2O$ (0.022 g, 0.1 mmol) in 5 mL MeOH was added and sonicated for 10 min. The clear solution was kept in a 15 mL vial for 24 h at room temperature to produce rod shaped transparent crystals (0.025 g, 75% yield). IR (KBr, cm^{-1}): ν_{OH}, 3421; ν_{N-H}, 2977; $\nu_{as}(CO_2)$, 1589; $\nu_s(CO_2)$, 1395. ν_{C-N}, 1626. Elemental Analysis: Calcd- C (40.51%), H (5.25%), N (8.59%); Found C (40.57%), H (5.21%), N (8.62%). CCDC No. 918489.

d) Synthesis of [{Zn(Ala)(Br)}$(H_2O)_2]_\infty$ (AlaZnBr): To an aqueous solution (0.75 mL) of AlaBr (0.048 g, 0.2 mmol), $Zn(CH_3CO_2)_2.2H_2O$ (0.022 g, 0.1 mmol) in 5 mL MeOH was added and sonicated for 10 min. The clear solution was kept in a 15 mL vial for 24 h at room temperature to produce rod shaped transparent crystals (0.026 g, 70% yield). IR (KBr, cm^{-1}): ν_{OH}, 3427; ν_{N-H}, 2974; $\nu_{as}(CO_2)$, 1590; $\nu_s(CO_2)$, 1394. ν_{C-N},1623. Elemental

Analysis: Calculated- C (34.45%), H (4.62%), N (7.60%); Found C (35.68%), H (4.60%), N (7.63%). CCDC No. 918490.

e) Synthesis of $[\{Zn(Ala)(HCOO)\}(H_2O)_2]_\infty$ (AlaZnFor): To an aqueous solution (0.5 mL) of AlaFor (0.05 g, 0.2 mmol), $Zn(CH_3CO_2)_2.2H_2O$ (0.022 g, 0.1 mmol) in 5 mL MeOH was added and sonicated for 10 min. The clear solution was kept in a 15 mL vial for 24 h at room temperature to produce rod shaped transparent crystals (0.023 g, 71% yield). IR (KBr, cm^{-1}): ν_{OH}, 3424; $\nu_{N\text{-}H}$, 2975; $\nu_{as}(CO_2)$, 1589; $\nu_s(CO_2)$, 1397. $\nu_{C\text{-}N}$,1627. Elemental Analysis: Calculated- C (40.51%), H (5.25%), N (8.59%); Found C (40.54%), H (5.28%), N (8.57%). CCDC No. 918491.

f) Synthesis of $[\{Zn(Ala)(CH_3COO)\}(H_2O)_2]_\infty$ (AlaZnOAc): To an aqueous solution (0.25 mL) of AlaOAc (0.044 g, 0.2 mmol), $Zn(CH_3CO_2)_2.2H_2O$ (0.022 g, 0.1 mmol) in 5 mL MeOH was added and sonicated for 10 min. The clear solution was kept in a 15 mL vial for 24 h at room temperature to produce rod shaped transparent crystals (0.026 g, 72% yield). IR (KBr, cm^{-1}): ν_{OH}, 3423; $\nu_{N\text{-}H}$, 2970; $\nu_{as}(CO_2)$, 1592; $\nu_s(CO_2)$, 1395. $\nu_{C\text{-}N}$,1622. Elemental Analysis: Calculated- C (35.65%), H (4.62%), N (7.60%); Found C (35.60%), H (4.64%), N(7.62%). CCDC No. 918492.

4.5 General characterization methods:

a) Powder X-Ray Diffraction (PXRD): Powder XRD patterns of the aforementioned MOF samples were analyzed to confirm the crystallinity as well as the phase purity of the bulk materials. Powder X-ray diffraction (PXRD) patterns were recorded on a Phillips PANalytical diffractometer equipped with Cu K_α radiation (λ = 1.5406 Å), with a scan speed of 2° min^{-1} and a step size of 0.02° in 2θ. 50 mg of as synthesized materials were made pellet and subjected to analysis over glass slides.

b) Thermogravimetric Analysis (TGA): TGA was performed on a SDT Q600 TG-DTA instrument. ca. 8 mg of the MOFs were heated from 25 to 800 °C under the N_2 flow at heating rate of 5 °C min^{-1}.

c) IR Spectroscopy: The Fourier transform (FT) infrared spectra of the MOFs were collected on a *PERKIN ELMER FT-IR SPECTRUM* (Nicolet) spectrometer. KBr pellets (2 mg MOF in 20 mg of KBr) were prepared and 50 scans were measured at 2 cm^{-1} resolution for each sample. The spectra were measured over the range of 4000-600 cm^{-1}.

d) Water Adsorption Analysis: All low-pressure water adsorption experiments (up to 1 bar) were performed on a BELSORP-max volumetric instrument. Approximately 50 mg of the sample was activated after solvent exchange by the use of activation chamber. The activated sample was loaded inside the glass bulb of water adsorption instrument and measured the capacity.

e) Nuclear Magnetic Resonance (NMR) spectroscopy: Solid state NMR spectra (SSNMR) of the MOFs were taken in a Bruker 300 MHz NMR spectrometer while the solution state ligand NMR data were taken in Bruker 200 MHz NMR spectrometer.

4.6 X-ray Crystallography:

General data collection and refinement procedures:

All single crystal data were collected on a Bruker SMART APEX three circle diffractometer equipped with a CCD area detector and operated at 1500 W power (50 kV, 30 mA) to generate Mo Kα radiation (λ = 0.71073 Å). The incident X-ray beam was focused and monochromated using Bruker Excalibur Gobel mirror optics. All crystals reported in this chapter were mounted on nylon CryoLoops (Hampton Research) with Paraton-N (Hampton Research).

Initial scans of each crystal were performed to obtain preliminary unit cell parameters and to determine the mosaicity (breadth of spots between frames) of the crystal to select the required frame width for data collection. In every case frame widths of 0.5° were judged to be appropriate and full hemispheres of data were collected using the *Bruker* SMART software suite. Following data collection, reflections were sampled from all regions of the Ewald sphere to redetermine unit cell parameters for data integration and to check for rotational twinning using CELL_NOW [2.7]. Fortunately, no crystal decay was encountered in case of the data collection. Following exhaustive review of the collected frames the resolution of the dataset was judged. Data were integrated using Bruker SAINT [2.8] software with a narrow frame algorithm and a 0.400 fractional lower limit of average intensity. Data were subsequently corrected for absorption by the program SADABS [2.9].

The space group determinations and tests for merohedral twinning were carried out using XPREP [2.9]. In all cases, the highest possible space group was chosen.

All structures were solved by direct methods and refined using the SHELXTL 97 [2.10] software suite. Atoms were located from iterative examination of difference F-maps following least squares refinements of the earlier models. Final models were refined anisotropically (if the number of data permitted) until full convergence was achieved. Hydrogen atoms were placed in calculated positions (C–H = 0.93 Å) and included as riding atoms with isotropic displacement parameters 1.2-1.5 times U_{eq} of the attached C atoms. All structures were examined through the *Adsym* subroutine of PLATON [2.11] to ensure that no additional symmetry could be applied to the models. All ellipsoids in ORTEP diagrams are displayed at the 50% probability level unless stated otherwise. For all structures we observed elevated R-values; a problem commonly encountered in MOF crystallography [2.12].

Experimental and refinement details for MOFs:

Colorless rod shaped crystals were mounted on 0.7 mm diameter nylon CryoLoops (Hampton Research) with Paraton-N (Hampton Research). The loop was mounted on a *SMART APEX* three circle diffractometer equipped with a CCD area detector (Bruker Systems Inc., 1999) and operated at 1500 W power (50 kV, 30 mA) to generate Mo K_{α} radiation ($\lambda = 0.71073$ Å). The incident X-ray beam was focused and monochromated using Bruker Excalibur Gobel mirror optics. Analysis of the data showed negligible decay during collection. The structure was solved in the hexagonal $P6_1$ space group, with $Z = 6$, using direct methods. All non-hydrogen atoms were refined anisotropically. Very high displacement parameters, high esd's and partial occupancy due to the disorder make it impossible to determine accurate positions for the hydrogen atoms in water molecules. Crystallographic data (excluding structure factors) reported in this chapter have been deposited with the CCDC as deposition No. CCDC 918487–918500, 926615–926616. The ORTEP diagrams are provided with 50% probability (Figure 4.16 and 4.17).

ORTEP Diagrams for the MOFs and Coordination Polymers

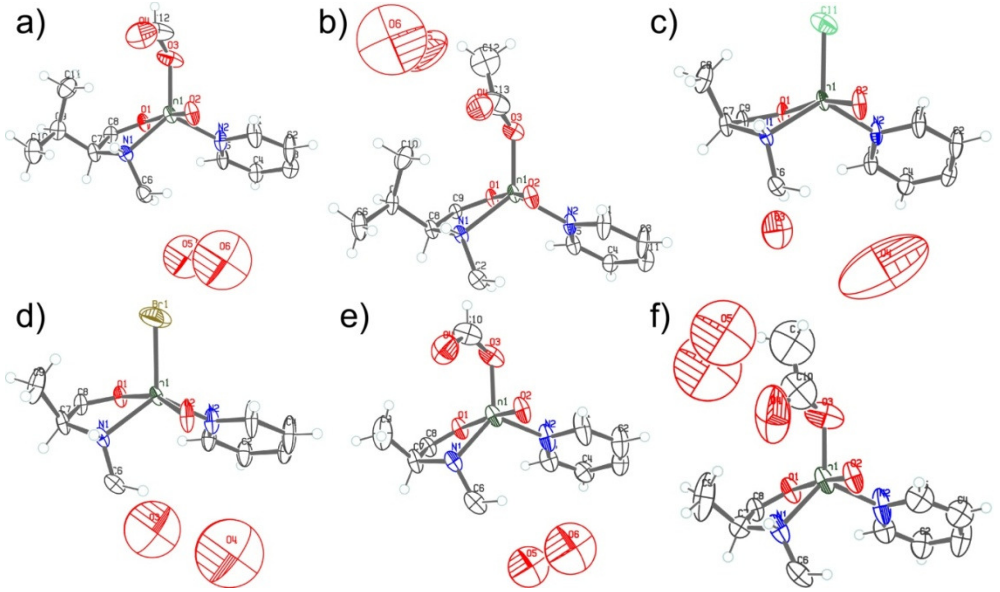

Figure 4.16: ORTEP diagrams for the asymmetric unit of the MOFs in 50% probability level. a) ValZnFor b) ValZnOAc c) AlaZnCl d) AlaZnBr e) AlaZnFor and f) AlaZnOAc. Figure adapted from ref. 4.3.

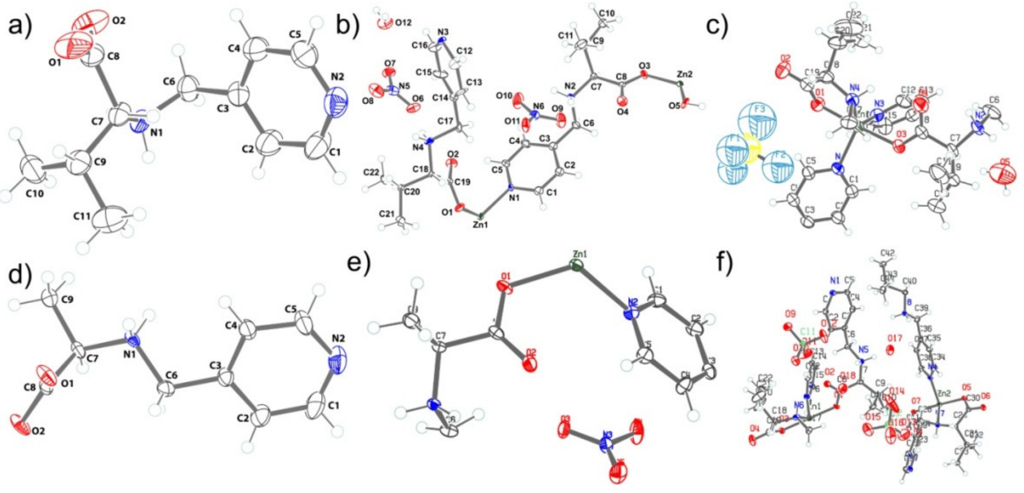

Figure 4.17: ORTEP diagrams for the asymmetric unit of the ligands and coordination polymers in 50% probability level. a) Val b) ValZnNO$_3$ c) ValZnBF$_4$ d) Ala e) AlaZnNO$_3$ f) ValZnClO$_4$. Figure adapted from ref. 4.3.

NOTE: The results of this chapter have already been published in *Chem. Commun.* 2013, **49**, 5262. with the title: "*Salt metathesis in three dimensional metal–organic frameworks*

(MOFs) with unprecedented hydrolytic regenerability” The publication was resulted from the group of Dr. Rahul Banerjee and his students Subash Chandra Sahoo, Subhadeep Saha and Tanay Kundu from CSIR-National Chemical Laboratory, Pune, India. Major experimental works and manuscript preparation were contributed by Tanay Kundu using instrumental facilities of CSIR-National Chemical Laboratory. Subash Chandra Sahoo and Subhadeep Saha did the crystallization.

CHAPTER 5

ANION INDUCED MORPHOLOGICAL IMPACT ON ZINC OXIDE BY THERMOLYSIS OF AMINO ACID DERIVED MOFS

5.1 Introduction:

In recent years, the synthesis and characterization of the transition-metal oxides with controlled size and shape have gathered huge interest among researchers. In particular, unique physical and chemical properties made them attractive towards potential applications e.g. catalysis and photo-electronic devices [5.1]. Among those transition-metal oxides, zinc oxide (ZnO) is of very high importance owing to its multifaceted properties in catalysis [5.2], gas sensing [5.3], varistors [5.4], piezoelectric actuator [5.5], oxide layer for solar cell applications [5.6], semiconductors or transparent conductors, UV-protection

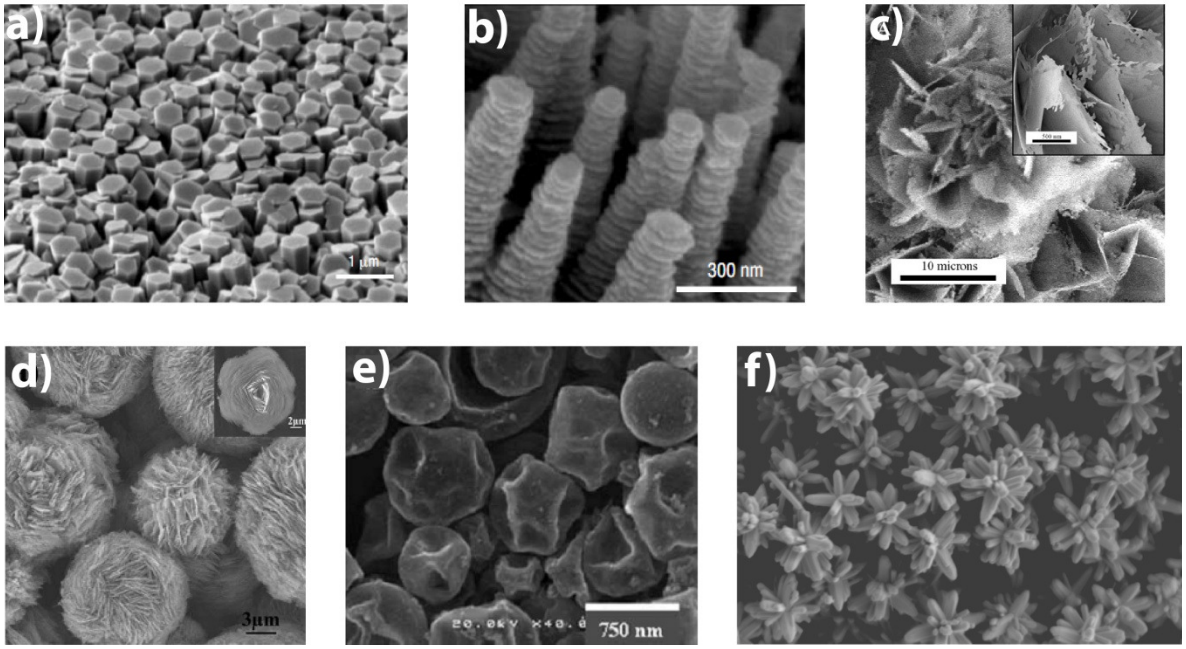

Figure 5.1: Morphological diversity of ZnOs synthesized by various methods; a) hexagonal plate shaped b) vertically oriented one dimensional spike shaped c) flake shaped d) flower shaped e) dry pea shaped f) multipod shaped ZnOs [5.8].

films, and chemical sensors [5.7]. ZnO nanoparticles are well-known for wide band gap semiconductors and environment-friendly oxide semiconductors. In the last decade, great progresses have been made in the synthesis of diverse morphological variations of ZnO [5.8] including stars, rods, snow flakes and spheres in anticipation of various targeted applications (Figure 5.1). For example, fabrication of long, vertically aligned ZnO nanowire arrays by economically viable methods provide a definite solution for Dye Sensitized Solar Cell (DSSC) applications with high power conversion efficiency due to significantly increase in electron diffusion length [5.9]. Among many methods of synthesis of ZnO, the sol–gel route remains favorable because of the low cost, easiness of fabrication and non-destructive nature of processing [5.10]. Different synthetic conditions result in ZnO particles with uncommon morphologies as well as diverse properties with moderate yields. Still, the control of ZnO in terms of type, shape, morphology, and especially large-scale synthesis of ZnO particles from a simple, controllable, low-cost and environmentally viable method remains a challenge. Recently, solid-state pyrolysis of metal-organic frameworks (MOFs) has emerged as an alternative

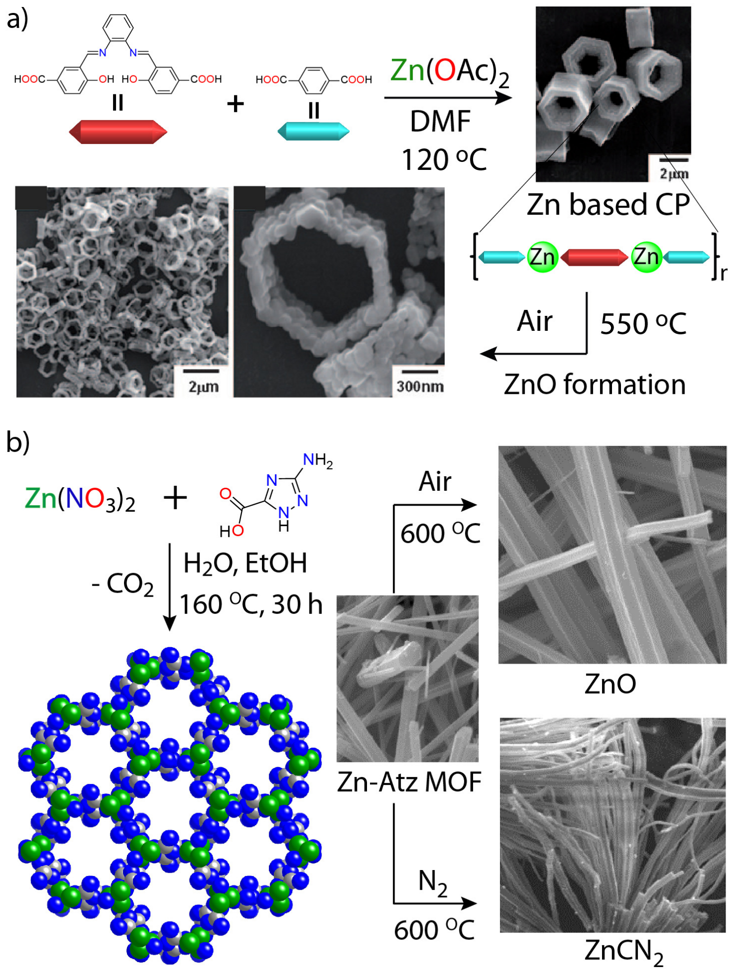

Figure 5.2: Synthesis of ZnOs from MOFs via thermolysis methods; a) hexagonal rod shaped mix-linker coordination polymer derived ZnOs of similar shape and size [5.13] b) hexagonal fibre shaped ZnO and $ZnCN_2$ obtained from similar structured Zn-aminotriazolate MOF [5.15].

route to synthesize ZnO with diverse morphologies [5.11]. MOFs are crystalline solids composed of single or multi-nuclear metal ions as the building units with tunable organic linkers as the two key components [5.12]. Advantage of MOFs over the other precursors are its porosity and long range ordering that offers unique opportunity to synthesize unusual ZnO morphologies. In this regard, a mix-ligand approach (i.e. mixture terephthalic acid and salen based dicarboxylic acid or acetylene dicarboxylic acid) have been used to synthesize hexagonal columnar like hollow core coordination polymer, which upon heat treatment in air led to ZnO structures with shape persistency (Figure 5.2a) [5.13]. Researchers have heated Zn based materials in air or in N_2 environments, to get pure ZnO or ZnO nanoparticles embedded in carbon matrix [5.14]. The intrinsic porous backbone of MOFs retained its shape even upon solid state calcination, which provided us a direct route to envisage porous, shape persistent ZnO structures. In another account, the Zn based amino-triazolate framework exhibit hexagonal rod like morphology, which upon heating in air at

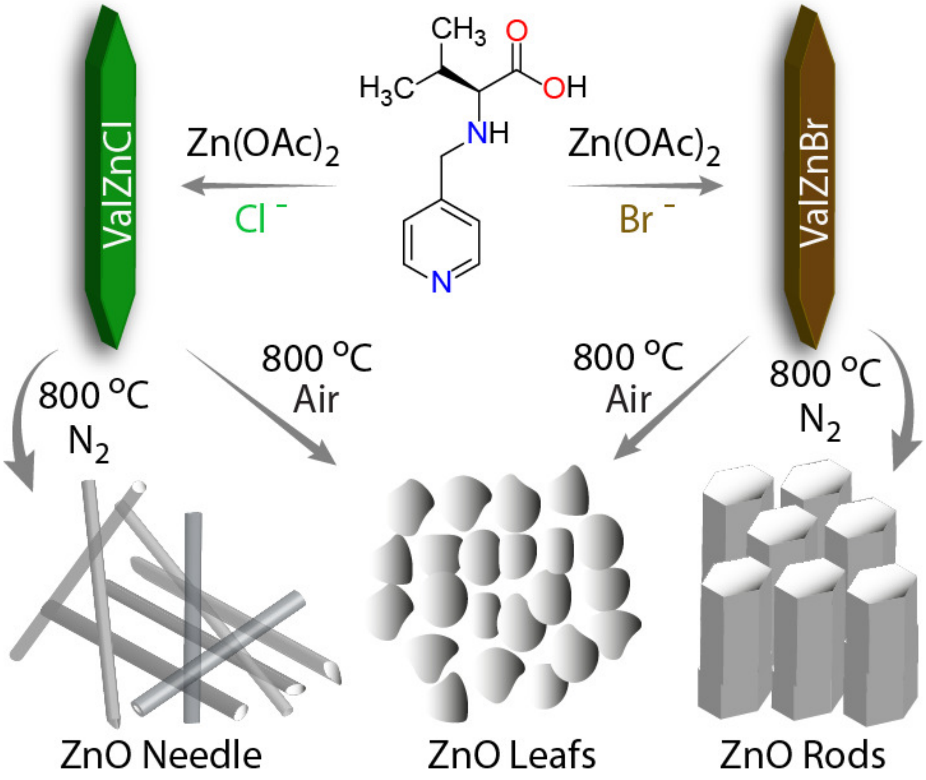

Figure 5.3: Schematic synthesis of diverse ZnOs from amino acid derived MOFs reported in this chapter via thermolysis methods.

600 °C resulted in ZnO microparticles with similar size and shape compared to the pristine MOF. On the other hand, pyrolysis at 600 °C in absence of O_2 environment led to the formation of $ZnCN_2$ with retention of the pristine architecture (Figure 5.2b) [5.15]. However, all these attempts lack systematic investigation on impact of framework constituents as templating effect, as well as judicious choice of environment to control the size and shape of ZnO micro-texture, which, in turn, manifested in their potential application in DSSCs.

In this chapter, we will discuss a systematic investigation and analysis of diverse ZnO morphologies derived from calcination or pyrolysis of porous isostructural amino acid derived 3D MOFs with only difference in coordinated halogen anions. Herein, we report the synthesis of two homochiral 3D MOF isomers (ValZnCl and ValZnBr), derived from $Zn(CH_3COO)_2.2H_2O$ and amino acid (valine) derived ligand, with different halogen substitutions (Cl, Br). These MOFs have been synthesized in both bulk crystals as well as in microcrystalline forms. Systematic calcination and pyrolysis of both the microcrystalline MOFs under air and nitrogen environment lead to ZnO and carbon matrix embedded ZnO, respectively. When ValZnCl and ValZnBr were calcined in air, elliptical aggregations of ZnO microparticles with average aspect ratio of 3 were obtained in both cases (termed as $ZnO(O_2)_{Cl}$ and $ZnO(O_2)_{Br}$, respectively). On the contrary, when the same MOF was pyrolysed in N_2 environment, rod like ZnO microparticles (termed as $ZnO(N_2)_{Cl}$) with very high aspect ratio of 20 was obtained. However, when ValZnBr was pyrolysed under similar condition**,** hexagonal columnar of ZnO microparticles ($ZnO(N_2)_{Br}$) with much lower average aspect ratio of 3 were obtained (Figure 5.4). Both MOFs (ValZnCl and ValZnBr) possesses similar architecture and the only difference lies in halogen substitutions (-Cl, -Br) in the crystal structure. In comparison with other conventional synthesis of ZnO, the advantage of this synthetic route lies in its simplicity by one step thermolysis technique without using any template, surfactant, and other additives. We have thoroughly characterized these ZnO microparticles and evaluated its efficacy in terms of photoluminescence and solar cell activity. In this chapter, we have achieved distinct morphological diversity of ZnO microstructures from isostructural MOFs. We believe that our findings will motivate researchers to design suitable MOFs for the solid state synthesis of ZnO with uncommon size and shape for its application in solar cells.

5.2 Result and discussion:

5.2.1 Structural aspects of the MOFs:

The hydrothermal synthesis has been proven to be a useful technique in the preparation of organic–inorganic framework materials. Generally, hydrothermal conditions can overcome the differential solubility of the organic and inorganic components and optimize the environment for crystal growth. Both the linkers (ValCl and ValBr) and the metal precursor ($Zn(OAc)_2.2H_2O$) are highly soluble in water. As a result, we choose water as a suitable solvent for the synthesis of the MOF crystals, which resulted in high quality large sized (0.5 mm) crystals with random size distribution (0.3 mm to 0.6 mm length). For any material

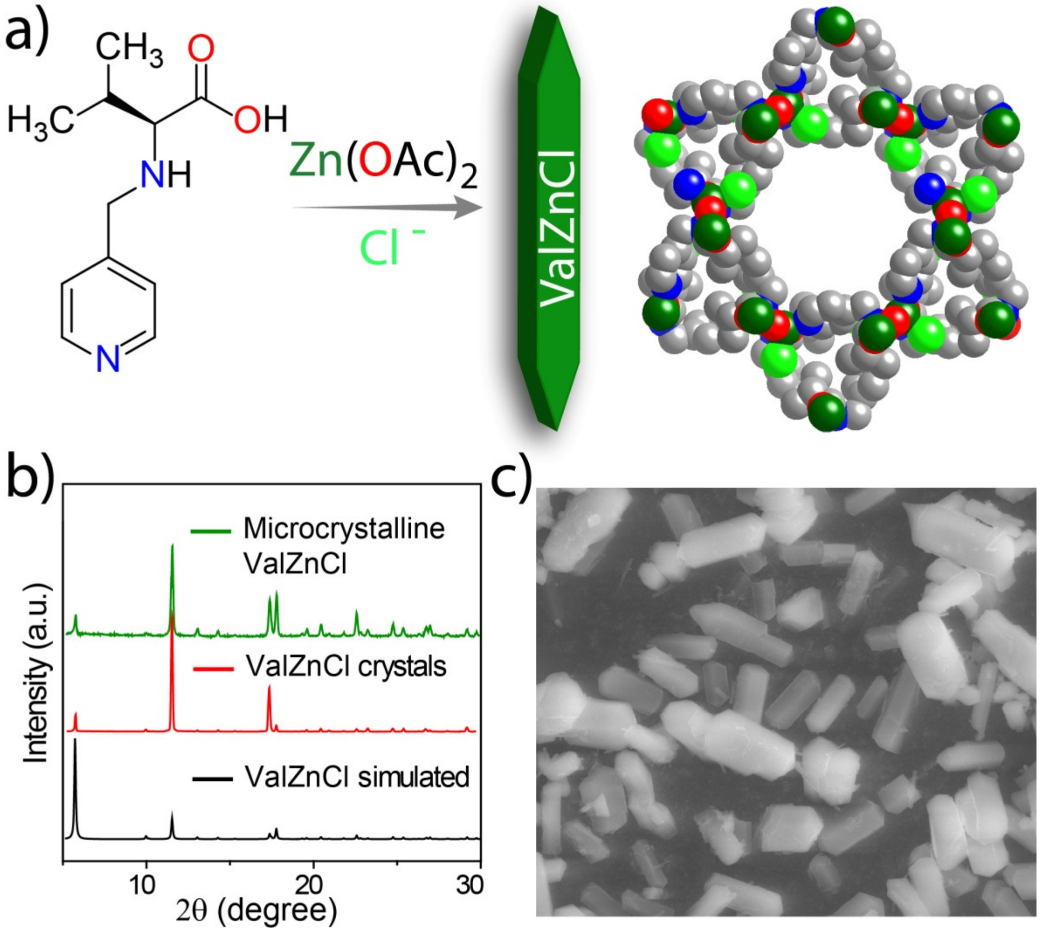

Figure 5.4: a) Schematic synthesis of microcrystalline ValZnCl MOF reported in this chapter. b) PXRD pattern comparison of the MOFs with simulated one. c) SEM images of the microcrystalline ValZnCl MOFs. Color codes: Zn (dark green), N (blue), O (red), C (gray) and Cl (light green).

synthesis, effective size distribution always stands at the top priority as properties of materials vary widely with respect to the size and shape of the nanoparticles. Hence, to obtain any functional property with reproducible results, control over size and shape are the two key issues which needed to be addressed during the synthesis of the materials. Unfortunately, our initial attempts to synthesize ZnO particles from the pristine MOF crystals resulted in inhomogeniety of the size and shape of the ZnO particles. As a result, we opt for the synthesis of microcrystalline MOFs with both size and shape uniformity (see experimental section). In order to get a good size and shape distribution of the MOF materials, we have synthesized ValZnCl and ValZnBr in different synthetic environment (1:5 H_2O/Et_2O media; see details in experimental section) by room temperature

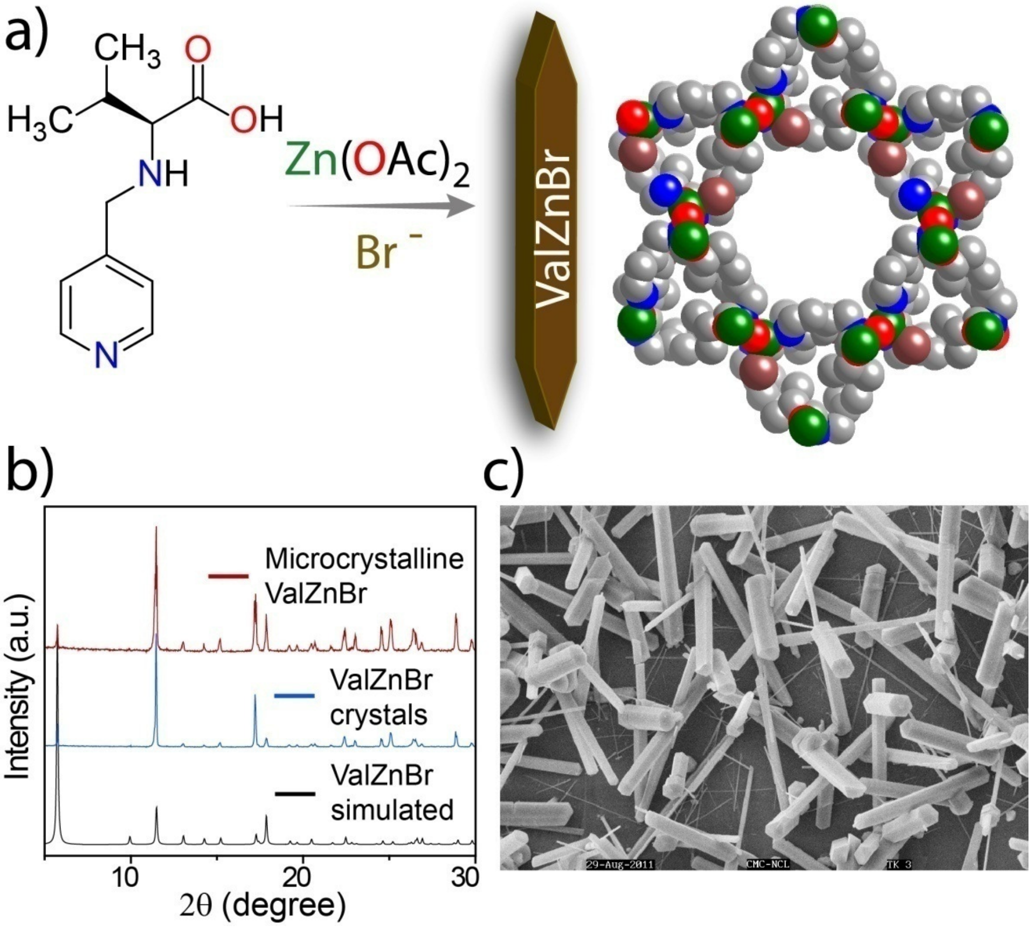

Figure 5.5: a) Schematic synthesis of microcrystalline ValZnBr MOF reported in this chapter. b) PXRD pattern comparison of the MOFs with simulated one. c) SEM images of the microcrystalline ValZnBr MOFs. Color codes: Zn (dark green), N (blue), O (red), C (gray) and Br (dark brown).

precipitation method. These synthetic modulations led to better homogeneity and uniform particle morphology distribution in terms of the size and shape. The ValZnCl (Figure 5.4) and ValZnBr (Figure 5.5) exhibit lesser dimensions (15 μm length and 5 μm width) compared to the pristine MOF crystals (300-600 μm length and 100-150 μm width). It is noteworthy to mention that, crystallinity of both these MOFs remains intact in their microcrystalline forms, evident from the peak to peak match of the simulated powder XRD patterns of the MOF crystals and the microcrystalline form of both these MOFs (Figure 5.4c and 5.5c). Henceforth, through the entire chapter, we will denote the microcrystalline form of the MOFs as ValZnCl and ValZnBr.

Both the microcrystalline MOFs viz. ValZnCl and ValZnBr synthesized in the aforementioned way were calcinated or pyrolysed to 800 °C in either air or N_2 atmosphere. Diffraction patterns of individual ZnO produced correspond to the ISCD reference for polycrystalline zinc oxide [5.16] with no unidentified phases detected. XRD studies of the material synthesized reveals wurtzite ZnO has been produced in all cases.

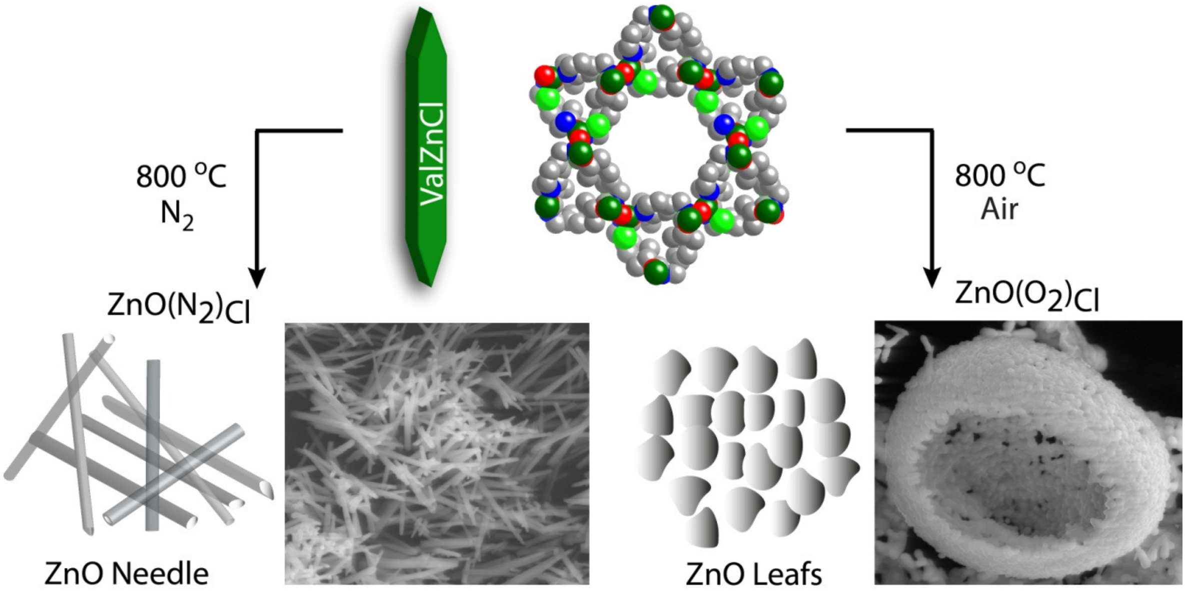

Figure 5.6: a) Schematic synthesis of ZnOs from ValZnCl MOF in different conditions.

Investigation of the as-synthesized MOFs via scanning electron microscopy (SEM) revealed uniform rod shape morphologies. The scale range was taken as 10 μm at a magnification of 5000×. The phase purity of the rod shape crystals confirmed by well matched peaks (Figure 5.4c and 5.5c) of simulated and as-synthesized PXRD data. When

ValZnCl was pyrolysed at 800 °C in N_2 environment, narrow needle shaped ZnO was formed (Figure 5.6). The resulting ZnO morphology adopts the parent MOF shape with increased aspect ratio. The as-synthesized ValZnCl have ca. 5 µm width and 15 µm length. However, the ZnO adopts ca. 0.4 µm width and 8 µm length. Hence, the parent MOF posses an aspect ratio of 1.5/0.5 = 3 whereas the resulting ZnO adopts a much higher aspect ratio of 8/0.4 = 20.

Surprisingly, when the same ValZnCl was subjected to calcination under air at the same temperature (800 °C), aggregated elliptical microparticles of ZnO with the similar wurtzite phase (Figure 5.6) was obtained. In this case, the ZnO particle posses 2 µm length and 0.7 µm width (the aspect ratio being 2/0.7 = 3). This result clearly indicates that the oxygen atom source in as-synthesized ValZnCl (two oxygen atom per Zn atom in the unit cell of dehydrated ValZnCl) is sufficient enough for the production of ZnO. However, presence of air i.e. excess oxygen makes a dramatic difference in size and shape of the ZnO although both morphologies are in wurtzite phase. As compared to various procedures reported in the literature for synthesis of ZnO particles, it is among the most convenient methods as it is free from any template and surfactants. There exists only a handful report where MOFs have been used as precursors for ZnO synthesis with a hope that Zn-based MOFs can

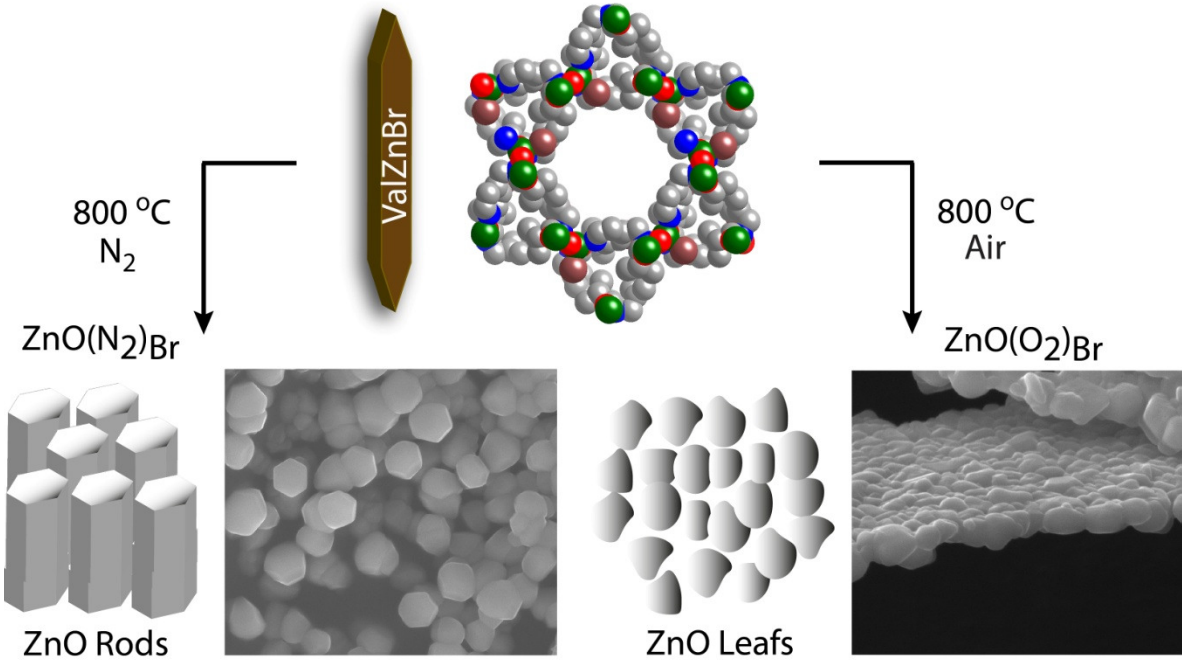

Figure 5.7: Schematic synthesis of ZnOs from ValZnBr MOF in different conditions.

provide a metal source and different MOF topology will directly produce ZnO particle with various shape and size. Till now it is not clear, so as in the present case, weather the MOF integrity is playing any key role or not. To confirm the same we subjected the calcination and pyrolysis of ValZnBr, which has almost similar crystallographic parameters as well as morphological architecture like ValZnCl, except the –Cl atom is substituted by the –Br in the crystal structure (Figure 5.3). Phase pure ValZnBr was synthesized via the same room temperature precipitation method, confirmed by the peak to peak match of the powder XRD patterns of the simulated and as-synthesized ValZnBr (Figure 5.5b). When ValZnBr was subjected to calcination or pyrolysis in an identical environment with respect to ValZnCl, a dramatic morphological change was encountered. When ValZnBr was pyrolysed at 800 °C

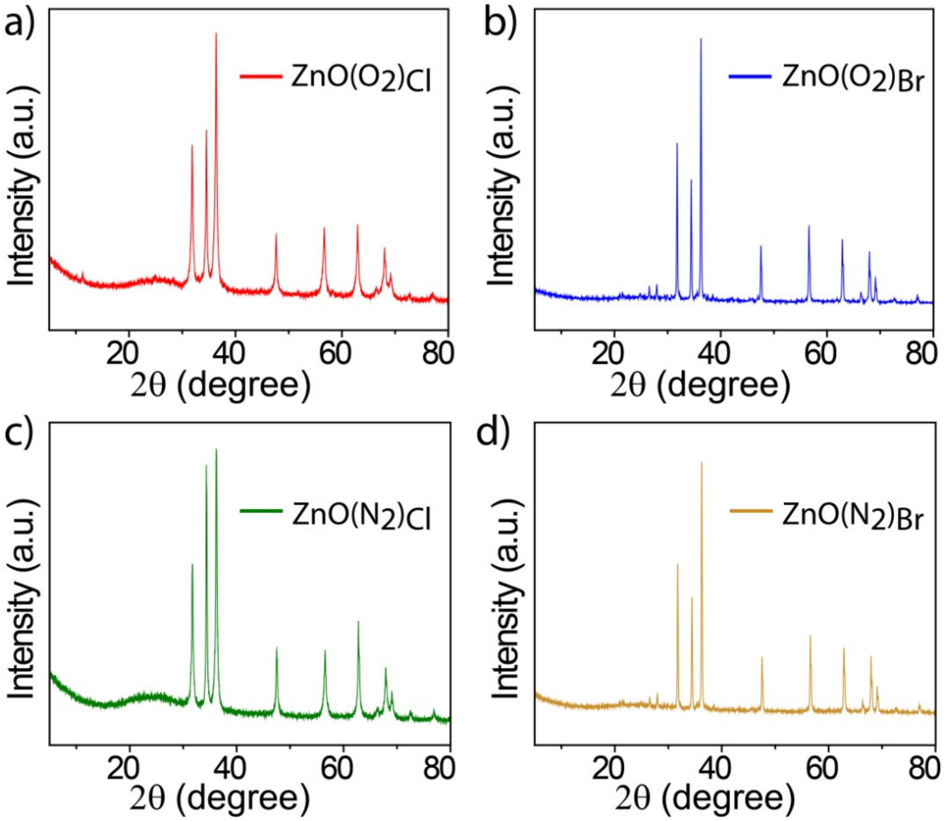

Figure 5.8: PXRD pattern of the ZnOs derived in different conditions from the MOFs; a) $ZnO(O_2)_{Cl}$ b) $ZnO(O_2)_{Br}$ c) $ZnO(N_2)_{Cl}$ d) $ZnO(N_2)_{Br}$.

in N_2, it produces uniform hexagonal columnar shaped ZnO microparticles of 1.5 μm length and 0.5 μm width, aspect ratio being 1.5/0.5 = 3 (Figure 5.7). However, when we calcined ValZnBr in air, elliptical ZnO microparticles resulted with length of 2 μm and width of 0.7

μm (aspect ratio being 2/0.7 = 3). Figure 5.7 shows a hexagonal wurtzite phase confirmed by PXRD of ZnO. However, pyrolysis at lower temperatures (600 °C) resulted in non-homogeneity of morphology of the ZnO microparticles.

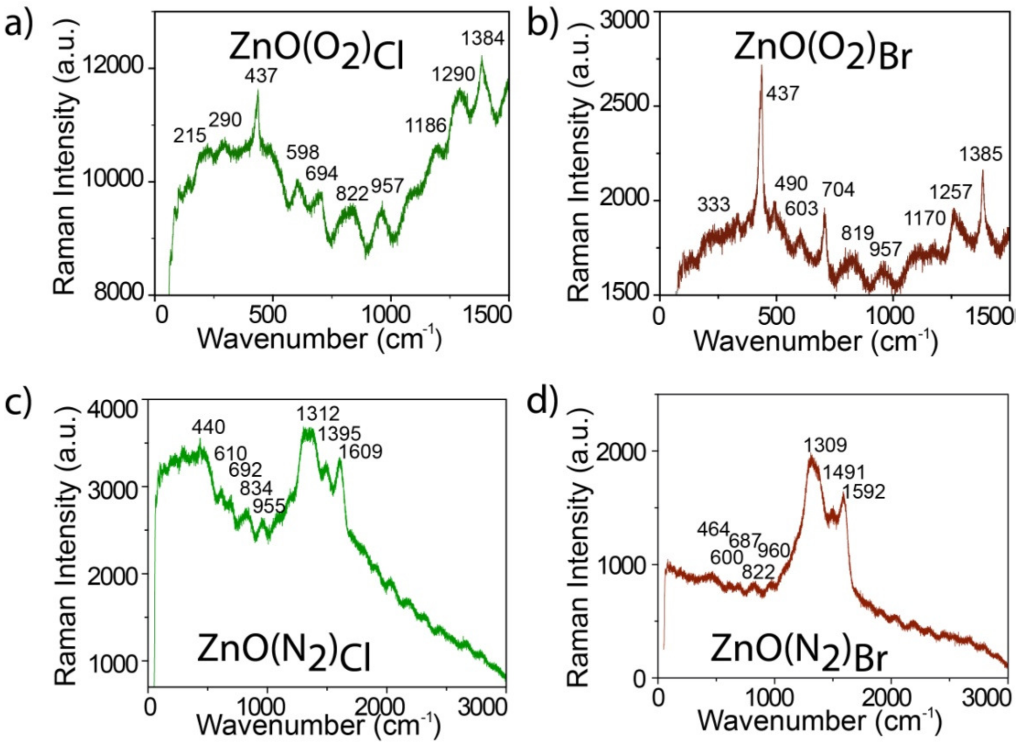

Figure 5.9: Raman spectra of the ZnOs derived from the MOFs; a) $ZnO(O_2)_{Cl}$ b) $ZnO(O_2)_{Br}$ c) $ZnO(N_2)_{Cl}$ d) $ZnO(N_2)_{Br}$.

The aforementioned observations indicate that anions (-Cl and -Br) play a very vital role in controlling the resulting ZnO morphology. As mentioned above, ValZnCl and ValZnBr, although posses similar crystal structures, resulted in completely different size and shaped ZnO microparticles while calcined or pyrolysed in exactly similar temperature (800 °C) and environment (N_2 or air). Hence, the template effect of the halogen atoms should be the factor responsible for these morphological diversities. Moreover, heating environment also controls the aspect ratio of the aforementioned ZnO. ValZnCl and ValZnBr, while calcined in air, produced completely different size and shape of ZnO microparticles than that obtained by pyrolysis in inert, O_2 free environment (N_2 atmosphere). This result hints towards the fact that aspect ratio of ZnO microparticles also can be tuned by controlling the O_2 content of the heating environment.

5.2.2 X-ray powder diffraction analysis, Transmission Electron Microscopy (TEM) and gas adsorption analysis:

In order to confirm the phase purity of the bulk materials, powder X-ray diffraction (PXRD) experiments were carried out on ValZnCl and ValZnBr. All major peaks of experimental PXRD patterns of as-synthesized MOFs matches well with simulated PXRDs, indicating their reasonable crystalline phase purity (Figure 5.4b and 5.5b). We have collected the PXRD data to confirm the phase purity of ZnO microstructures. All the diffraction patterns of the synthesized ZnO microparticles correspond to the ISCD reference for polycrystalline zinc oxide [5.16] with no unidentified phases detected. XRD

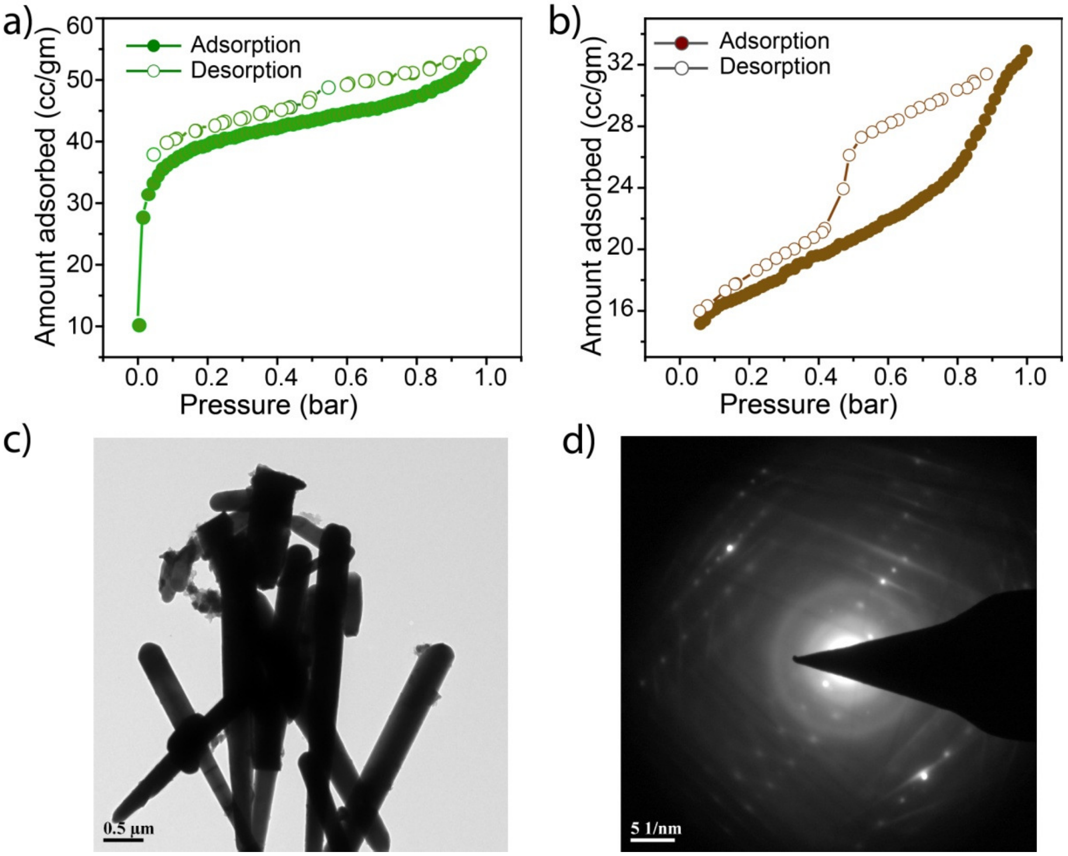

Figure 5.10: Nitrogen adsorption isotherms for a) $ZnO(N_2)_{Cl}$ and b) ZnO $ZnO(N_2)_{Br}$. c) TEM imaging of $ZnO(N_2)_{Cl}$ showed needle type morphology as observed in SEM. d) SAED pattern of the ZnO showing diffraction patterns.

studies of the as-synthesized ZnO revealed wurtzite phase produced in all the cases, irrespective of the MOF template and calcination or pyrolysis environment (Figure 5.8).

TEM analysis of as-synthesized materials revealed that $ZnO(N_2)_{Cl}$ have ~7-8 μm length and ~0.35-0.40 μm width, which was also consistent with the SEM imaging. Additionally, we have got the Selected Area Diffraction patterns having the distances as 1.18 Å and 1.63 Å, which corresponds to (110) and (104) plane of ZnO microstructure with hexagonal wurtzite phase (Figure 5.10d). N_2 adsorption analysis of as-synthesized $ZnO(N_2)_{Cl}$ exhibit its BET surface area of 120 m^2g^{-1}, having a mesoporous nature of the pore, which is evident from the hysteresis (type IV isotherm) of the N_2 adsorption curve. However, in case of $ZnO(N_2)_{Br}$ a much less surface area of 60 m^2g^{-1} was obtained. The $ZnO(O_2)_{Cl}$ and $ZnO(O_2)_{Br}$ materials have negligible surface area. These observations revealed that the different synthetic conditions not only change their external morphologies but also affect their intrinsic properties.

5.2.3 Photoluminescence properties of zinc oxide microparticles:

The room temperature solid-state photoluminescence spectra of as-synthesized the ZnO microstructures obtained from ValZnCl MOF and ValZnBr MOF under different conditions were shown in figure 5. $ZnO(O_2)_{Cl}$ shows a weak wide emission at 325 nm, observed by solid state UV-Vis spectra and a strong wide band emission from 450 nm to 740 nm centered at 605 nm were observed from solid state PL spectra (Figure 5.10a). Similar study for $ZnO(O_2)_{Br}$ shows excitation maxima at 325 nm, observed by solid state UV-Vis spectra and a wide emission from 400 nm to 600 nm centered at 510 nm was observed for solid state PL spectra and coined as maximum emission (Figure 5.10c). It is well known that these wide emissions represent the intrinsic emission and defect related emission of the ZnO particles (wurtzite phase), respectively. To confirm the mechanism of above emission of ZnO microparticles, the Fourier transform infrared (FT-IR) spectrum was measured at room temperature, which shows bands at 3440 cm^{-1} and 1636 cm^{-1} are attributed to the existence of hydroxyl groups of water molecules adsorbed on the surface of microparticles. It is to be noted that the constituent of parent MOFs play a vital role for resulting different ZnO morphology followed by PL spectra (Figure 5.10). The above result is attributed to the fact that facile synthesis of ZnO with different morphology can be tuned

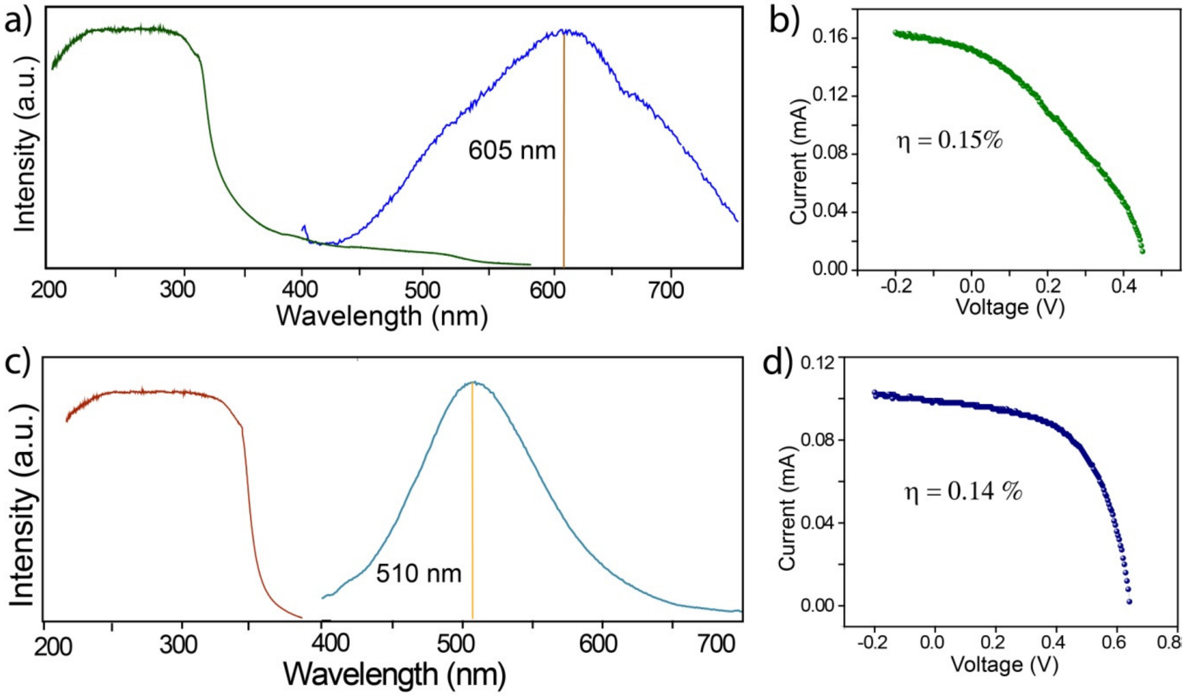

Figure 5.10: UV-Vis and PL spectra patterns in case of a) $ZnO(O_2)_{Cl}$ and c) $ZnO(O_2)_{Br}$. Solar cell efficiency studies on b) $ZnO(O_2)_{Cl}$ and d) $ZnO(O_2)_{Br}$.

with respect to MOF morphology as far as the development of MOF field in recent years is concerned. The PL spectra of each of these abovementioned ZnO particles are again repeated after five month of interval and show almost no change in PL maxima position and intensity.

5.2.4 Dye sensitized solar sell activity measurements:

Use of ZnO in DSSC serves the advantage of increase in diffusion rate without increasing the recombination rate, ease processability and low cost [5.17]. The most interesting part of this work is of course the DSSC activity measurement data. We have studied the potential of ZnO particles derived from thermolysis of MOF for DSSC applications. The DSSC activity measurement data reveals 0.15% power conversion efficiency for the $ZnO(O_2)_{Cl}$ and 0.14% DSSC activity for the $ZnO(O_2)_{Br}$, which lie below than typical ZnO DSSC activity of ~1-2%. However, we could not able to get DSSC activity measurement data for the $ZnO(O_2)_{Cl}$ and $ZnO(O_2)_{Br}$ due to poor conductivity and crystallinity of the carbon present in as-synthesized ZnO samples.

5.3 Conclusion:

In conclusion, anion and environment controlled zinc oxide microstructures are obtained by one step solid state thermolysis of two Zn(II) based homochiral MOFs both in air and in nitrogen. Apart from diverse morphologies, these ZnO microparticles show visible light emission centered at 605 nm or 510 nm. These ligand free ZnO microparticles are very stable and their PL spectra show almost no change after keeping samples in air for at least 5 months. The visible light emission band may be attributed to one of the following i.e. singly charged oxygen vacancy or surface defects. These ZnO microparticles show potential for DSSC applications. The advantage of this work is that a simple experiment leads us to understand the role of the anions as the structural directing agent and effect of environment on the ZnO morphologies. The produced ZnO particles with stable visible emission bears huge possible applications in the field of optical devices, fluorescent labeling in biomedical applications by various surface modifications. This solid state transformation of ZnO microparticles with tunable morphology using different Zn(II) based MOFs provides an important sign for facile synthesis of various metal oxide functional materials.

5.4 Experimental details:

5.4.1 Materials:

All starting materials were purchased from the Sigma Aldrich Chemicals and used without further purification.

5.4.2 Synthetic methods:

a) Synthesis of microcrystalline ValZnCl: To an aqueous solution (2 mL) of ValCl (0.044 g, 0.2 mmol), $Zn(CH_3COO)_2.2H_2O$ (0.022 g, 0.1 mmol) was added and sonicated for 10 min. Then it was placed on a hot plate for stirring at 50 °C, and then slowly dropwise diethyl ether was added. Crystalline precipitates begin to separate within an hour. The precipitate was washed firstly with water for 3 times (2 mL × 3), then with diethyl ether for 2 times (3 mL × 2), dried in air and characterized by powder XRD, SEM, and EDX.

b) Synthesis of microcrystalline ValZnBr: To an aqueous solution (2 mL) of ValBr (0.055 g, 0.2 mmol), $Zn(CH_3COO)_2.2H_2O$ (0.022 g, 0.1 mmol) was added and sonicated for 10 min. Then it was placed on a hot plate for stirring at 50 °C, and then slowly drop wise diethyl ether was added. Crystalline precipitates begin to separate within an hour. The precipitate was washed firstly with water for 3 times (2 mL × 3), then with diethyl ether for 2 times (3 mL × 2), dried in air and characterized by powder XRD, SEM, and EDX.

c) Calcination of ValZnCl and ValZnBr in air: 100 mg sample of ValZnCl MOF or ValZnBr MOF was placed in a silica combustion boat, inserted within a quartz tube, in which moisture free air ($O_2 : N_2 = 1:4$) was passed. Then the tube was slowly heated (5 °C min^{-1}) up to 800 °C, kept for 2 h and then slowly cooled (2 °C min^{-1}) to room temperature. Heating and cooling rate is essential for uniform particle size distribution. The product appears as whitish crystalline powder, which was characterized by powder XRD, SEM, EDX and TEM (Yield ~ 20% for ValZnCl MOF and ~ 18% for ValZnCl MOF).

d) Pyrolysis of ValZnCl and ValZnBr in N_2: 100 mg sample of ValZnCl MOF or ValZnBr MOF was placed in a silica combustion boat, inserted within a quartz tube, in which 99.99% pure N_2 was passed. Then the tube was slowly heated (5 °C min^{-1}) up to 800 °C, kept for 2 h and then slowly cooled (2 °C min^{-1}) to room temperature. Heating and cooling rate is essential for uniform particle size distribution. The product appears as blackish crystalline powder, which was characterized by powder XRD, SEM, EDX and TEM (yield ~ 50% for ValZnCl MOF and ~ 40% for ValZnBr MOF).

5.5 General characterization methods:

a) Powder X-Ray Diffraction (PXRD): Powder XRD patterns of the aforementioned ZnO samples were analyzed to confirm the crystallinity as well as the phase purity of the bulk materials. Powder X-ray diffraction (PXRD) patterns were recorded on a Phillips PANalytical diffractometer equipped with Cu K_α radiation (λ = 1.5406 Å), with a scan speed of 2° min^{-1} and a step size of 0.02° in 2θ. 50 mg of as synthesized materials were made pellet and subjected to analysis over glass slides.

b) Gas Adsorption Analysis: Gas adsorption studies were done to confirm the permanent porosity of the as synthesized sample as well as to determine the surface area accessible to dye molecules to get adsorbed onto the surface of the ZnO microparticles. All low-pressure Gas adsorption experiments (up to 1 bar) were performed on a *Quantachrome Quadrasorb* automatic volumetric instrument. 100 mg sample were evacuated for 6 h at room temperature and subsequently loaded for adsorption analysis.

c) Scanning Electron Microscopy (SEM): SEM images were recorded using a Zeiss DSM 950 scanning electron microscope and FEI Quanta 200 3D scanning electron microscope with tungsten filament as electron source. Samples for SEM analysis were prepared by dropcasting one drop of the sample dispersion (1 mg/ 2 mL isopropanol) onto a silicon wafer and allowed to dry for 24 h to 36 h at ambient temperature followed by gold coating (3 nm) before subjection to SEM analysis.

d) Transmission Electron Microscopy (TEM): An FEI Tecnai F30 electron microscope operating at 100 kV was used for HRTEM sample observation. It was equipped with a Gatan digital camera for recording micrographs. Samples were prepared from 1 mg/5 mL isopropanol ZnO dispersion and one drop was dropcasted onto a holey carbon-coated copper grid of 200 mesh size (Ted Pella) and allowed to dry at room temperature for 24 to 36 h. The size of microrods was analyzed from TEM images using ImagePro software.

e) Raman Spectroscopy: Raman spectroscopic analysis was performed on the as-synthesized sample to obtain the Raman shift. Raman analysis were obtained from HORIBA Jobin Yvon raman Spectrometer with model number HR800. Helium- Neon laser Excitation source (632.81 mm) were taken for all analysis, with slit width of 100 mm and hole width 400 mm. The resolution of the instrument is 0.35 cm^{-1} per pixel. The magnification of the instrument was maintained as 50X zoom for ZnO obtained in N_2 environment and 10X zoom for ZnO obtained from air. The grating was maintained as 800 and activation parameters were a) RTD exposure 15 sec, b) Exposure time 20 sec and c) accumulation number was 2. 50 mg of as-synthesized samples were handled once, made thin pellet using glass slide and subject to Raman analysis.

f) Photoluminescence Spectroscopy: Solid state UV/Vis spectra were recorded using a Perkin–Elmer Lambda 35 UV/Vis spectrometer, with solid state sample holder attachment. Steady-state fluorescence emission measurements were performed using a Fluorolog HORIBA Jobin Yvon fluorescence spectrophotometer. The emission as well as excitation slit width was maintained at 1 nm throughout the experiments, and the data was obtained in S1c/R1 mode (to account for the variations in lamp intensity). Measurements were made at 908 positions for solution/dispersions and 22.58 in front-face films.

g) Dye Sensitized Solar Cell (DSSC) activity Measurements: DSSC activity measurements were done on as-synthesized ZnO microparticles to account for its efficiency in DSSCs. Solar cell tests were performed on Newport USA Solar simulator and incident-photon-to-current conversion efficiency (IPCE) instrument (Toy model) and all measurements were carried out in power of the solar simulator as 1 sun (100 MW/cm^2). The formation of ZnO films was carried out by the doctor blade method, and the films were then annealed at 450 °C for 30 min. The thickness of as-prepared ZnO films was ~ 12 μm. For sensitization, the ZnO films were impregnated with 0.5 mM N719 dye in ethanol for 24 h at room temperature. The sensitizer-coated ZnO films were washed with ethanol. The FTO electrodes were washed with acetone, ethanol, and deionized water (18.2 MΩ·cm) in an ultra-sonication bath for 15 min with a final wash in isopropyl alcohol.

NOTE: The results of this chapter have already been published in *Cryst. Growth & Des.* 2012, **12**, 2572-2578. with the title: "*Solid-State Thermolysis of Anion Induced Metal–Organic Frameworks to ZnO Microparticles with Predefined Morphologies: Facile Synthesis and Solar Cell Studies*". The publication was resulted from the group of Dr. Rahul Banerjee and his students Subash Chandra Sahoo and Tanay Kundu from CSIR-National Chemical Laboratory, Pune, India. Major experimental works and manuscript preparation were contributed by Tanay Kundu using instrumental facilities of CSIR-National Chemical Laboratory. Subash Chandra Sahoo did the data interpretation.

CHAPTER 6

ALKALI EARTH METAL DERIVED MOFS FOR PROTON CONDUCTION

6.1 Introduction:

Past decades have witnessed tremendous growth in the field of metal-organic frameworks (MOFs), a crystalline class of compounds, with diverse topological architectures and promising applications like gas sorption, catalysis, magnetism, and conductivity. In particular, proton conductivity in MOFs is of recent interest, where either MOF backbone and/or guests therein lead the pathway to transport protons. For majority of the cases, proton conducting MOFs are synthesized by combining transition such as Mn, Cr, Fe, Cu, Zn(II) or lanthanide e.g. Gd(III) metals and suitable organic linkers. However, uses of lightweight group of metals (e.g. alkaline earth metals) are far less explored. Alkaline earth metals (Ca, Sr, Ba) are relatively cheaper than transition and lanthanide metals, have less toxicity and appreciable earth abundance, which could be beneficial for designing inexpensive proton conducting materials. Alkaline earth metals also posses high binding affinity towards oxygen (high bond energy of M–O, M = Mg, Ca, Ba, Sr), which could impart thermochemical stability in MOF backbone. Additionally, alkaline earth metals have different coordination numbers despite having same valency, which may lead to architectural variety. However, till date alkali earth metal based MOFs are scarce, and a handful of them exhibit promising applications like gravimetric hydrogen uptake, catalysis, proton conductivity [6.1]. For the aforesaid reasons, we have chosen group II alkali earth metals as an appropriate candidate for synthesizing a series of MOFs. Recently, a systematic study revealed the effect of ligand substitution on the proton conductivity nature of MOFs [1.62a]. These results demonstrated increasing acidic nature of the ligand by imparting acidic functional group (phenolic OH, COOH) within the ligand backbone, increases proton conduction and decreases activation energy required for this process. However, till date effect of metal ion substitution in a series of MOFs and its impact on proton transport is still unprecedented. Hence, a systematic approach might unfold us the needful characteristics for judicious choice of the metal node to design organic–inorganic hybrid materials with enhanced proton conducting ability. As a part of our ongoing research on proton conducting MOFs, we pursue our interest to explore the proton conductivity of a specific group of metals, i.e. alkali earth metals, keeping the ligand constant.

For the abovementioned purpose, we opt for 4,4′-sulphobisbenzoic acid (SBBA), a suitable linker to construct MOFs for a number of reasons; a) SBBA has a bent (V shaped) geometry with two carboxylate groups which could provide structural diversity towards different metals, b) SBBA has high thermal stability (ca. 400 °C) which could be utilized to design thermally stable MOFs, c) the sulfone group provide additional scope to functionalize the linker backbone with acidic (e.g. sulfonic acid, carboxylic acid) groups for high proton conductivity. In polymeric backbone, the SBBA moiety provides additional mechanical and oxidative stability with the opportunity of ortho functionalization through lithiation (Figure 6.1a) [6.2]. Surprisingly, SBBA based MOFs are rare, and a handful of them exhibit practical applicability. For example, till date only one Zn(II) based 1D coordination polymer bearing sulfone group i.e. Zn-SDBA (SDBA: sulfone biphenyldicarboxylic acid) has been reported for the application in proton conductivity (Figure 6.1b) [6.3]. Although the framework consists of free SDBA ligand hydrogen bonded with the coordination polymer chains and water molecules, the material exhibit low proton conductivity of 2.5 × 10^{-7} Scm^{-1}. We, upon judicious arrangement of the metal nodes and organic spacer, took the opportunity to prepare alkali earth metal based

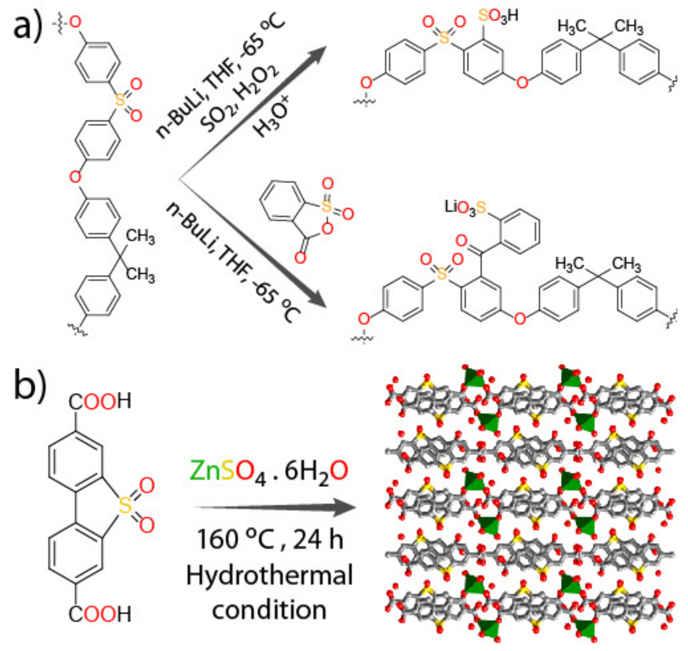

Figure 6.1: a) Functionalization scheme of sulfone group bearing membranes for high proton conductivity [6.2]. b) Synthetic scheme of reported Zn-SDBA coordination polymer [6.3]. Color codes: Zn (green), N (blue), O (red), C (gray). and S (yellow).

MOFs with SBBA as a linker and unveil their structural diversity and proton transporting ability.

Herein, we present three 2D MOFs, namely Ca-SBBA, Sr-SBBA and Ba-SBBA, constructed from alkaline earth metals i.e. Ca(II), Sr(II) and Ba(II) as metal nodes and 4,4′-sulphobisbenzoic acid (SBBA) as an organic linker. Interestingly, the structures are completely different from each other although they bear same group of metal atoms and the same linker. They have remarkable thermal stability up to 500 °C. Moreover, they exhibit noticeable difference in proton conductivity under hydrous condition. Ca-SBBA shows proton conductivity of 8.58×10^{-6} Scm^{-1}, whereas Sr-SBBA shows proton conductivity of 4.4×10^{-5} Scm^{-1} at 298 K in 98% relative humidity (RH). Ba-SBBA does not show any proton conductivity due to structural instability under similar condition. We hope that these findings will lead the systematic exploration of proton conducting MOFs with high thermal and chemical stability.

6.2 Result and discussion:

6.2.1 Structural aspects of the MOFs:

The solvothermal synthesis has been proven to be a useful technique in the preparation of organic–inorganic framework materials. Generally, solvothermal conditions can overcome the differential solubilities of the organic and inorganic components and optimize the environment for crystal growth. SBBA linker is partially soluble in DMF and DEF at ambient temperature and pressure; hence solvothermal route has been chosen to crystallize Ca-SBBA, Sr-SBBA and Ba-SBBA materials.

Ca-SBBA crystallizes in $P2_1/c$ space group, which contains only one type of Ca(II) SBU. The asymmetric unit of Ca-SBBA contains one Ca atom, one deprotonated SBBA ligand, two coordinated and one solvent DMF molecule. The Ca(II) center adopts an octahedral geometry; where four μ_2 carboxylate oxygen of SBBA coordinates in the equatorial position. The axial positions are occupied by two coordinated DMF molecules. These μ_2 carboxylate connects another Ca(II) to form one dimensional Ca(II) chains (Figure 6.2a). These Ca(II) chains are linked through SBBA ligands, resulting 2D sheet like structure (Figure 6.2b). In the 2D sheets, the sulfone groups of the SBBA linker are coordinated in a zigzag fashion. The coordinated DMF molecules are interdigitated within two sheets (Figure 6.2c). These sheets are further self assembled through the interaction between coordinated and solvent DMF molecules (3.35 Å and 4.68 Å, respectively) entrapped within two sheets to form the 3D supramolecular architecture.

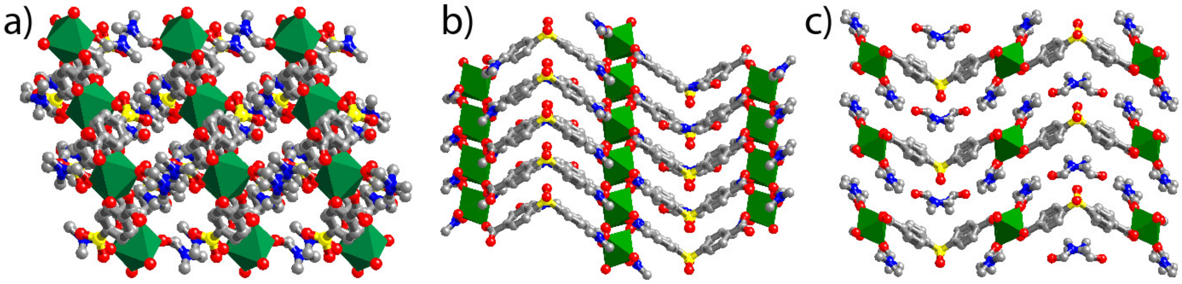

Figure 6.2: a) Crystal structure of Ca-SBBA in polyhedral mode viewed through crystallographic *b* axis. b) 2D layer structure of Ca-SBBA and c) stacking of the 2D layers. Color codes: Ca (green), N (blue), O (red), C (gray) and S (yellow).

Sr-SBBA crystallizes in *P*-1 space group. The asymmetric unit of Sr-SBBA contains three Sr(II) atoms, two deprotonated SBBA ligand, one formate anion (generated by *in situ* decomposition of DMF molecules) and four coordinated and two solvent DMF molecules. The crystal structure of Sr-SBBA consists of a pentanuclear Sr(II) cluster linked through carboxylate groups of the SBBA ligand (Figure 6.3a), creating three distinct type of SBU (SBU-1, SBU-2 and SBU-3). The Sr(II) centers are either ten coordinated SrO_{10} (SBU-1) or eight coordinated SrO_8 polyhedra. Among these three SBUs, SBU-1 consists of one Sr(II) atom coordinated by two μ_1 carboxylate groups, six μ_2 carboxylate groups. SBU-2 contains one Sr(II) atom coordinated by two μ_1 carboxylate groups, two μ_2 carboxylate oxygen and two coordinated DMF molecules, whereas SBU-3 consists one μ_1 formate anion, four μ_2

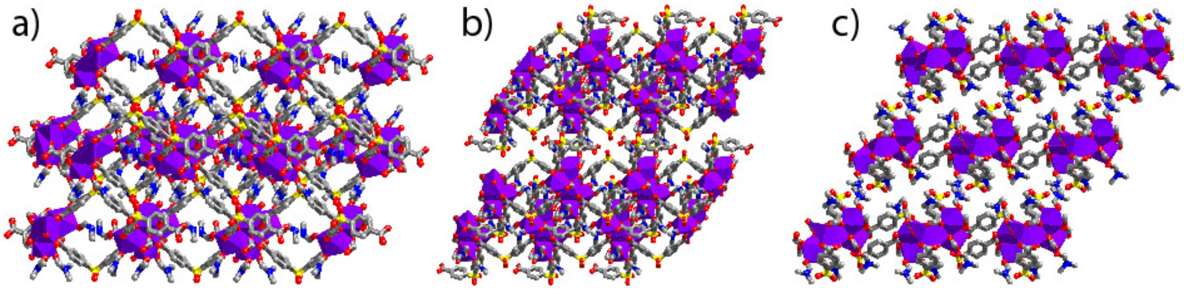

Figure 6.3: a) Crystal structure of Sr-SBBA in polyhedral mode viewed along crystallographic *c* axis, b) *b* axis and c) *a* axis. Color codes: Sr (violet), N (blue), O (red), C (gray) and S (yellow).

carboxylate oxygen and two coordinated DMF molecules. These clusters are connected to the neighboring clusters via four SBBA ligands to form the 2D architecture (Figure 6.3b). Interestingly, the pentanuclear cluster posses two fold rotation symmetry (C_2), but due to solvent ordering the resulting crystal structure adopts asymmetric space group (Figure 6.3c).

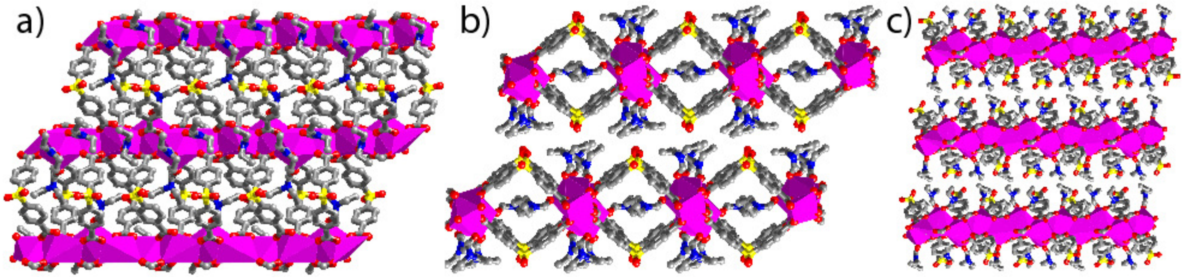

Figure 6.4: a) Crystal structure of Ba-SBBA in polyhedral mode viewed along crystallographic *c* axis, b) *a* axis and c) *b* axis. Color codes: Ba (magenta), N (blue), O (red), C (gray) and S (yellow).

Ba-SBBA crystallizes in *P*-1 space group. The asymmetric unit of Ba-SBBA consists of two Ba(II) atom, two deprotonated SBBA ligand and three coordinated DEF molecules. In the crystal structure of Ba-SBBA, three types of SBUs are present, where the Ba(II) metal centers form nine coordinated BaO_9 polyhedra (SBU-1 and -2) and ten coordinated BaO_{10} polyhedra (SBU-3). The carboxylate group of the ligand SBBA are linked with Ba(II) atoms in a μ_3 fashion, with η_4 connectivity (Figure 6.4a). Among these three SBUs, SBU-1 consists of one Ba(II) atom coordinated with two μ_1 carboxylate groups, three μ_2 carboxylate groups and two coordinated DEF molecules, whereas SBU-2 consists of one Ba(II) atom coordinated with two μ_1 carboxylate groups, four μ_2 carboxylate groups and one coordinated DEF molecule. SBU-3 consists of one Ba(II) atom coordinated with two μ_1 carboxylate groups, three μ_2

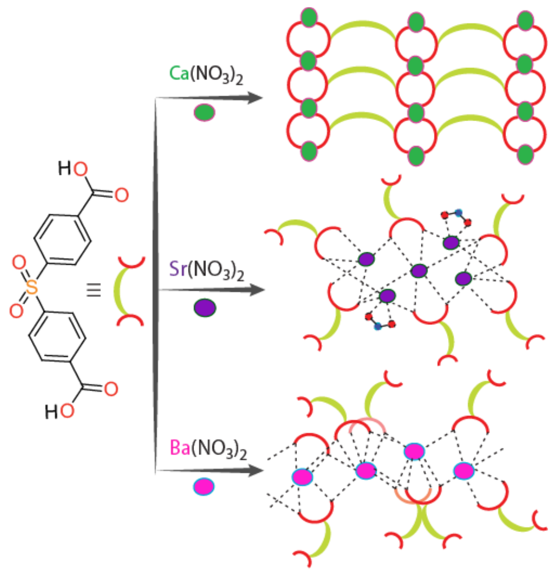

Figure 6.5: Schematic structural differences between the three MOFs viz. Ca-SBBA, Sr-SBBA and Ba-SBBA.

carboxylate groups and three coordinated DEF molecules. These μ_2 carboxylate groups links two neighboring Ba(II) to form an one dimensional Ba(II) chain along crystallographic *a* axis. SBBA links two Ba(II) chain in a zigzag fashion to construct the two dimensional architecture, which forms square shaped pores (Figure 6.4b). However, the coordinated DEF molecules are poking inside the pore to block the pore aperture. Further self assembly of these 2D motifs via var der Waal interaction forms the 3D lattice (Figure 6.4c).

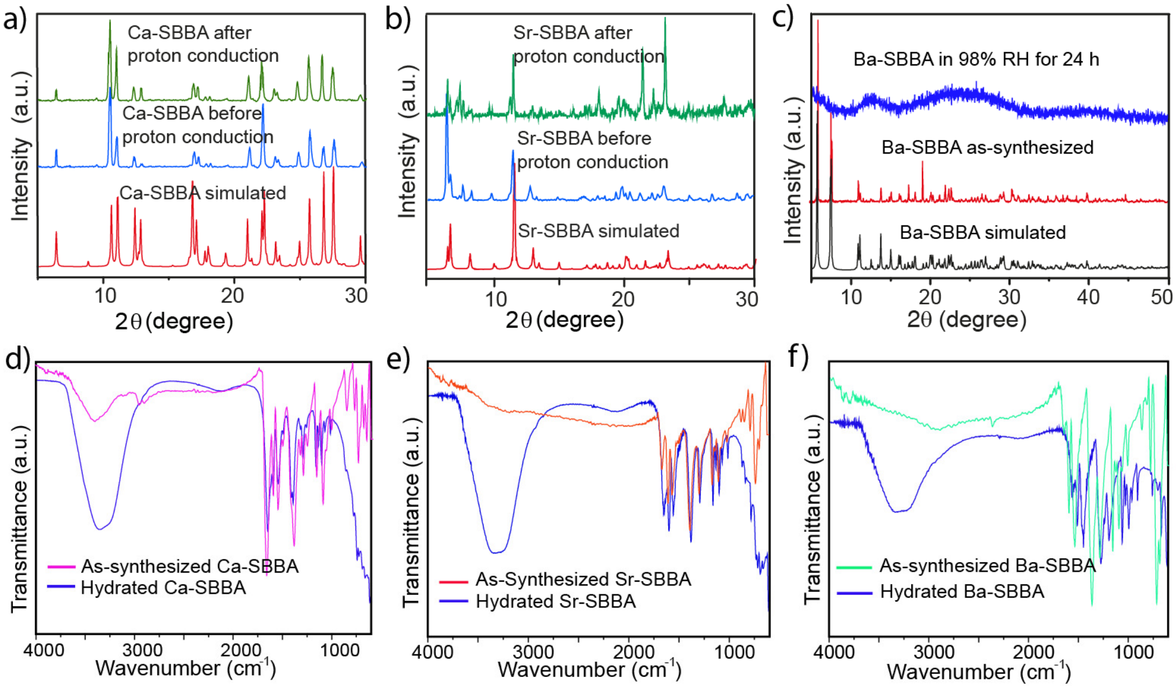

Figure 6.6: Structural stability of the MOFs in humid conditions (98% humidity for 24 h); exhibited by comparison of simulated, as-synthesized (before proton conduction) and after proton conduction experiment in case of a) Ca-SBBA b) Sr-SBBA and c) Ba-SBBA. FT-IR spectra comparison reveals the same fact by comparing as-synthesized and hydrated (98% humidity for 24 h) d) Ca-SBBA e) Sr-SBBA and f) Ba-SBBA.

Collectively, crystal structure analysis of the three MOFs reveals that the metal-carboxylate chain (in case of Ca and Ba) or the metal cluster-carboxylate chain (in case of Sr) are linked through the organic linker SBBA to form a 2d sheet like structure (Figure 6.5). Further stacking of these sheets built the 3D MOF architecture. In all the cases, the interlayer and intralayer voids are occupied by coordinated or non-coordinated DMF or DEF molecules. As a result, all these MOFs are non-porous to gases (e.g. CO_2, N_2, O_2). This feature is desired in fuel cell membrane, where materials having low gas permeation and high proton diffusion is preferred.

Architectural stability of the MOF structures is an essential step towards their practical utility in various industrial processes. All the MOF crystals are stable in common organic solvents (DMF, MeOH, Dioxane etc.). Moreover, water stability of the MOFs are verified by exposing them in 98% relative humidity for 24 h. Ca-SBBA and Sr-SBBA show retention of the framework architecture; as evident from the comparison between as-synthesized and humidity exposed materials. Ca-SBBA exhibited identical peak intensity in case of humidity exposed materials as compared with the simulated one (Figure 6.6a). The FT-IR spectra of as-synthesized Ca-SBBA also matches well with the humidity exposed material; with increase in O–H stretching frequency in the later case due to incorporation of water within the crystals (Figure 6.6d). Similar phenomena are observed in case of Sr-SBBA (Figure 6.6b and 6.6e). However, Ba-SBBA shows collapse of the framework integrity in humid condition. The PXRD pattern of humidity exposed Ba-SBBA exhibit amorphous phase (Figure 6.6c). In addition, FT-IR spectroscopy reveals different peak position and intensity compared with the as-synthesized one (Figure 6.6f). The aforementioned results clearly suggest that although Ca-SBBA and Sr-SBBA is stable for their utility in proton conduction, Ba-SBBA is not suitable for this application. As a result, we have performed proton conductivity experiments using the humidified Ca-SBBA and Sr-SBBA materials.

6.2.2 X-ray powder diffraction analysis and Thermo-gravimetric Analysis:

In order to confirm the phase purity of the bulk materials, powder X-ray diffraction (PXRD) experiments were carried out on Ca-SBBA, Sr-SBBA and Ba-SBBA. All major peaks of experimental PXRDs of as-synthesized compounds matches well with simulated PXRDs, indicating their reasonable crystalline phase purity (Figure 6.6a-6c). One of the major concerns regarding MOFs is their limited thermal stability, which prevents them from competing with inorganic Silica and Zeolites in practical applications. Variable temperature PXRD experiments (VTPXRD) reveals all the materials viz. Ca-SBBA, Sr-SBBA and Ba-SBBA undergo irreversible structural transformation above 100 °C, which results from the irreversible loss of the solvent molecules at elevated temperatures (Figure

6.7a and 6.7b). However, the structural integrity remains intact till 500 °C. The structurally transformed materials exhibit appreciable crystalline peaks, and no abrupt change in peak position and intensity was observed till 500 °C. The DSC curves for the three MOFs also reflect similar fact; indicating irreversible structural changes above 100 °C (Figure 6.8). We anticipate that above 100 °C, the loss of the interlayer solvent molecules that hold the 3D motifs as well as structural reordering of the 2D sheets at elevated temperature are responsible for the irreversible architectural transformation as observed in many 2D MOFs.

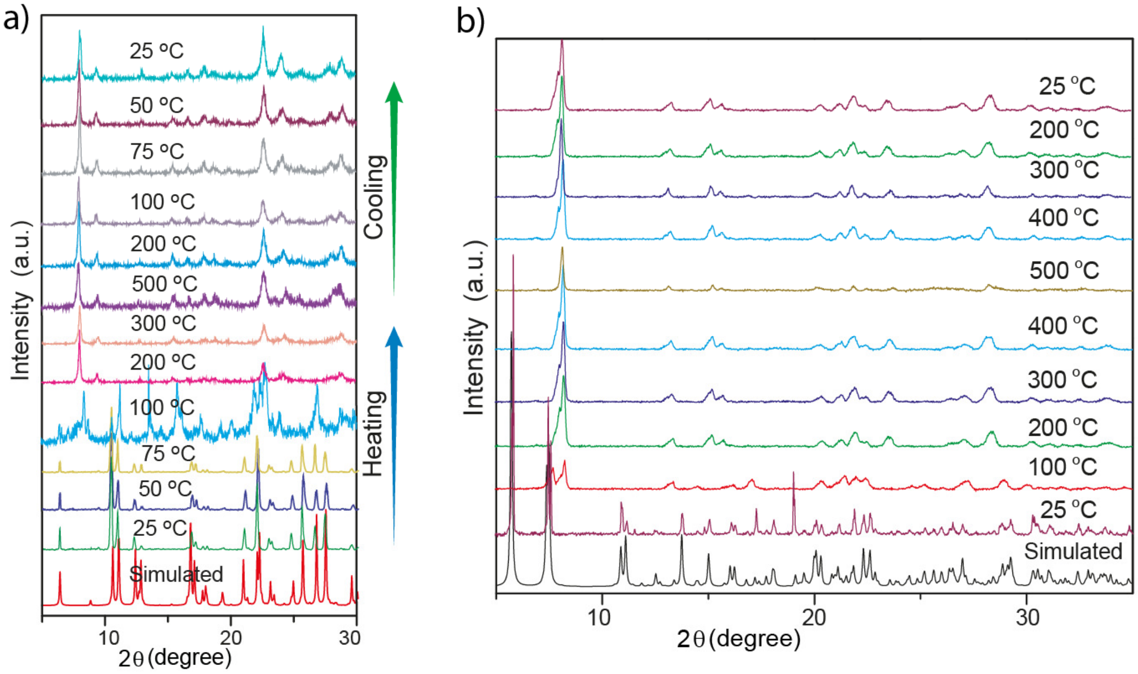

Figure 6.7: VT-PXRD patterns (upto 500 °C) in comparison with the simulated patterns in case of a) Ca-SBBA and b) Sr-SBBA.

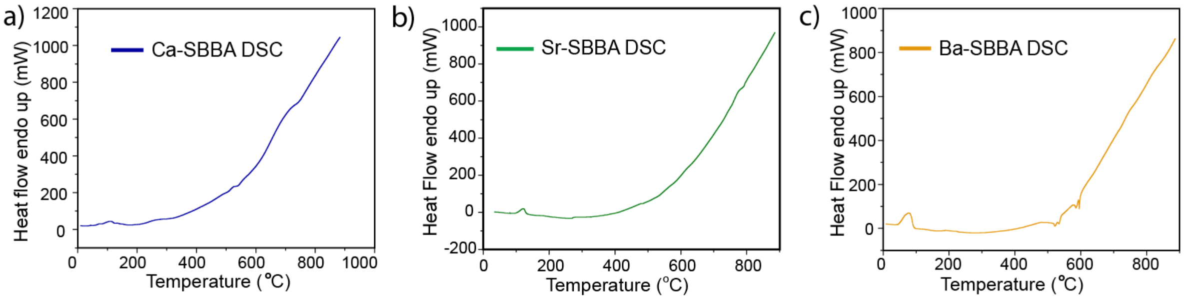

Figure 6.8: The DSC data for (a) Ca-SBBA (b) Sr-SBBA and (c) Ba-SBBA.

Moreover, The FT-IR spectroscopy reveals that the thermally treated (ca. 500 °C) materials have identical peak position and intensity than the pristine materials (Figure 6.9); with significant decrease in the peak intensity correspond to the DMF and DEF molecules (ca. 1700 cm^{-1}). Collectively, these experiments hint at the architectural rigidity as well as the thermal stability of all the MOFs. Finally, the TGA traces well reflect the aforementioned fact, showing remarkable thermal stability upto 500 °C (Figure 6.10). High bond energy between the alkali earth metals and the carboxylate oxygens are presumed to be primarily accountable for the high thermal stability. The thermograms for the as-synthesized Ca-SBBA, Sr-SBBA and Ba-SBBA showed a weight-loss step of ca. 10 wt% (25–95 °C), 5 wt% (25–95 °C) and 10 wt% (25–95 °C) respectively, which corresponds to the escape of the adsorbed moisture and solvent molecules from the frameworks. Further weight loss step [19 wt% (95–182 °C) for Ca-SBBA, 14 wt% (95–203 °C) for Sr-SBBA and 9 wt% (95–205 °C) for Ba-SBBA] signifies escape of solvent DMF molecules. The stable plateau from ca.

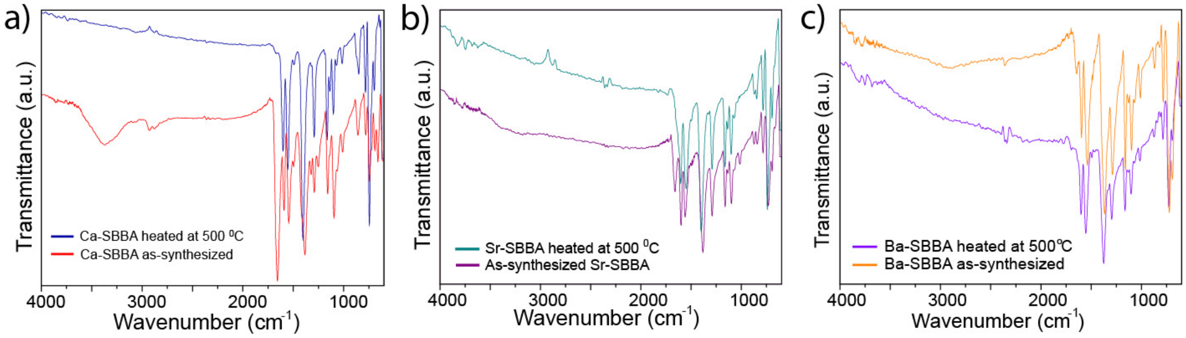

Figure 6.9: FT-IR comparison between as-synthesized MOFs and thermally treated MOFs at 500 °C in case of a) Ca-SBBA, b) Sr-SBBA and c) Ba-SBBA.

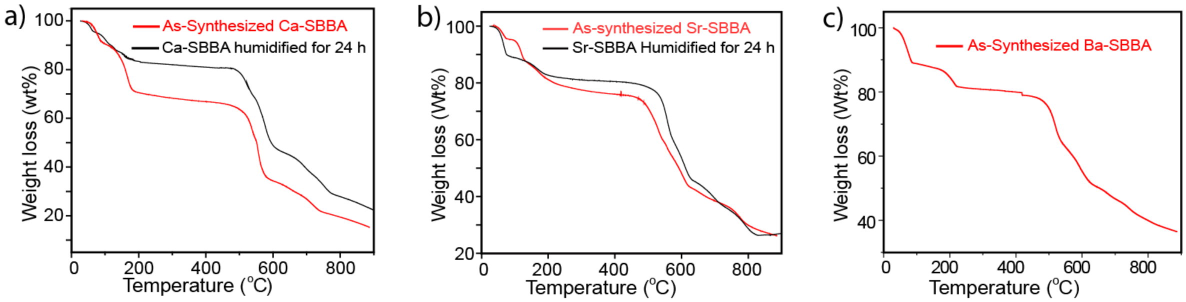

Figure 6.10: TGA data for (a) Ca-SBBA (b) Sr-SBBA and (c) Ba-SBBA.

200-500 °C landmarks the thermal stability of the frameworks at elevated temperatures. We have also performed the TGA analysis of the humidity exposed Ca-SBBA and Sr-SBBA materials. As expected, they exhibit less weight loss than as-synthesized MOFs, which justifies the fact that the high molecular weight DMF molecules have been replaced by the low molecular weight water molecules. The abovementioned experiments confirm the potential of Ca-SBBA and Sr-SBBA as a proton conductor discussed *vide infra*.

6.2.3 Proton conducting properties of the MOFs:

Proton transport under hydrous condition occurs in solid state materials via the framework backbone or some carrier mediated pathways (e.g. H_2O, H_3O^+, HO^-). We have used the

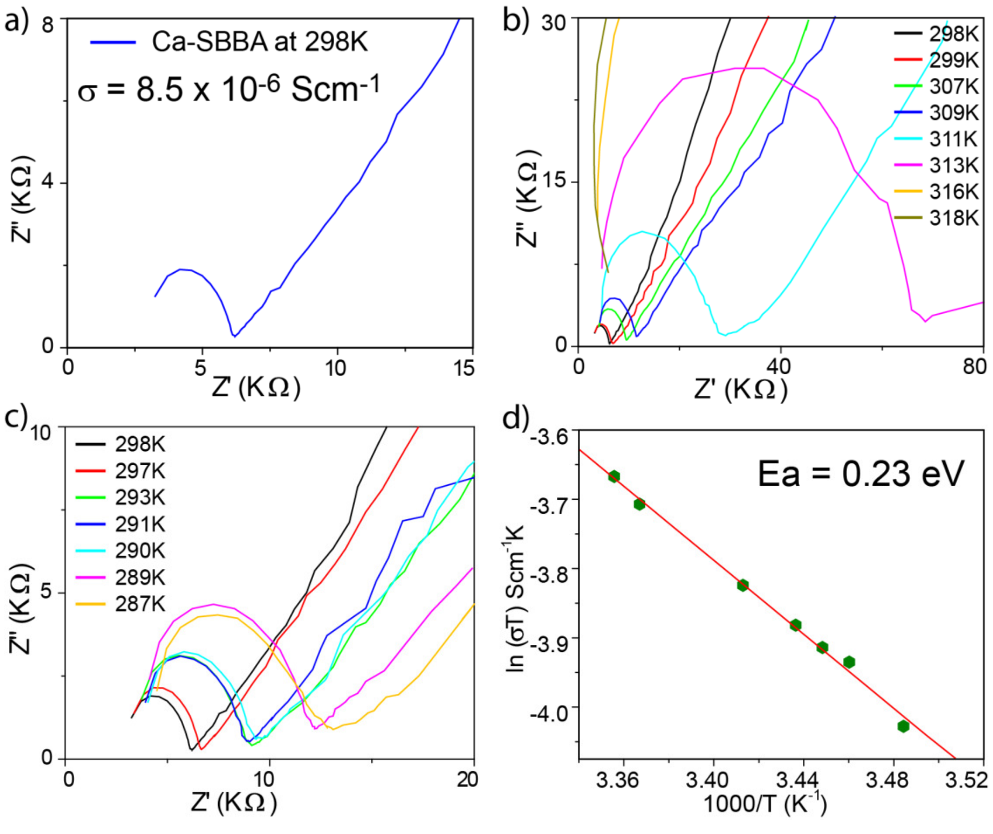

Figure 6.11: a) Nyquist plots for Ca-SBBA at ambient temperature. b) Nyquist plots for Ca-SBBA at elevated temperatures. c) Nyquist plots for Ca-SBBA at lower temperatures. d) Arrhenius plot for activation energy calculation.

pelletized MOFs (details in experimental section) for proton conductivity studies. Interestingly, the as-synthesized Ca-SBBA and Sr-SBBA compounds are highly resistive and do not show any proton conductivity. However, after humidification for 24 h they exhibit proton conduction, which eventually confirms the role of water as proton transporter. Presumably, the water molecules are absorbed within the crystal (confirmed from FT-IR spectroscopy and TGA analysis discussed *vide supra*) by hydrogen bonding with the carboxylate bound metal clusters, highly electronegative sulfone group and the non-coordinated DMF molecules to facilitate the proton conduction pathways. The proton conductivity value (Figure 6.11) was measured for Ca-SBBA as 8.5×10^{-6} $\mathrm{Scm^{-1}}$ at ambient temperature (298 K) in 98% relative humidity (RH). In the identical condition, Sr-SBBA shows proton conductivity (Figure 6.12) of 4.4×10^{-5} $\mathrm{Scm^{-1}}$. We have also performed a variable humidity proton conduction experiment to assay the role of humidity in proton transport. The proton conductivity values were highly humidity-dependent and dropped to 2.8×10^{-7} $\mathrm{Scm^{-1}}$ in case of Ca-SBBA at 60% RH at 298 K. Similar phenomenon was

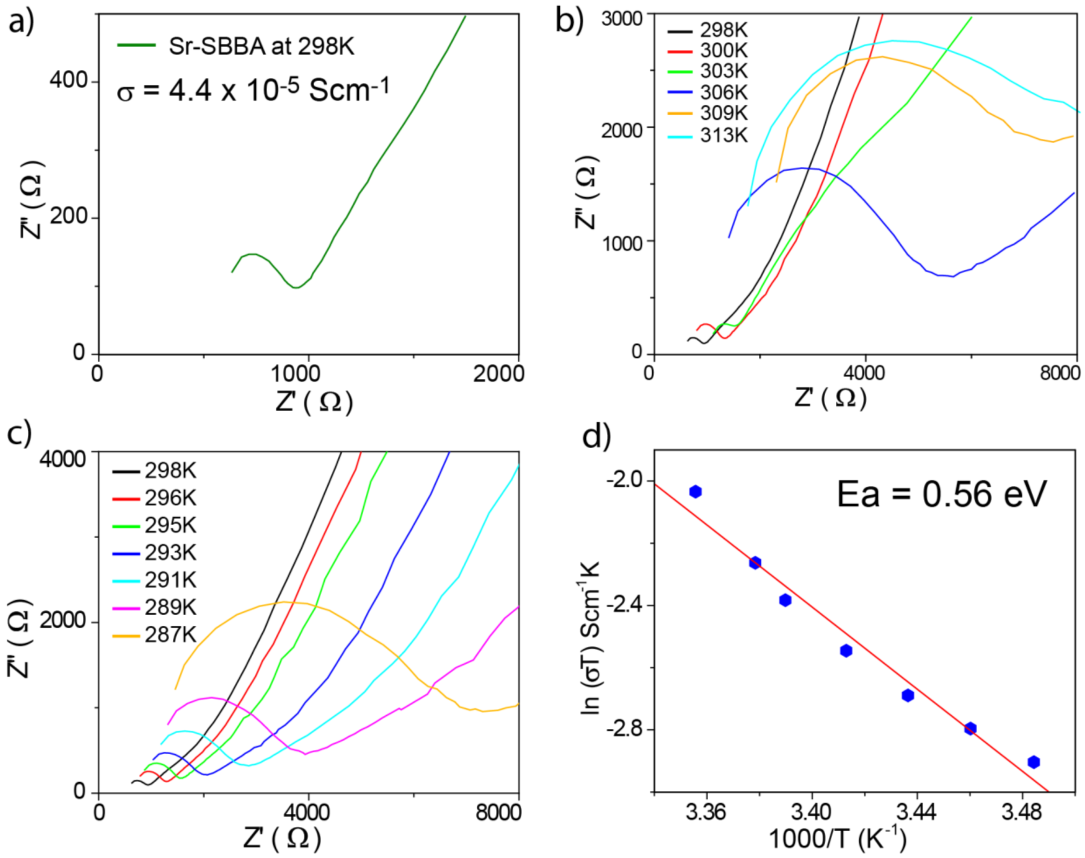

Figure 6.12: a) Nyquist plots for Sr-SBBA at ambient temperature. b) Nyquist plots for Sr-SBBA at elevated temperatures. c) Nyquist plots for Sr-SBBA at lower temperatures. d) Arrhenius plot for activation energy calculation.

observed in Sr-SBBA which exhibit 3.4 × 10^{-6} Scm^{-1} in identical experimental condition. Finally, we have carried out both low and high temperature proton conduction experiments to evaluate the proton conductivity as a function of temperature (Figure 6.13) as well as to calculate the respective activation energy values. Ca-SBBA and Sr-SBBA shows high proton conductivity upto 318 K and 313 K, respectively. The proton conductivity value of

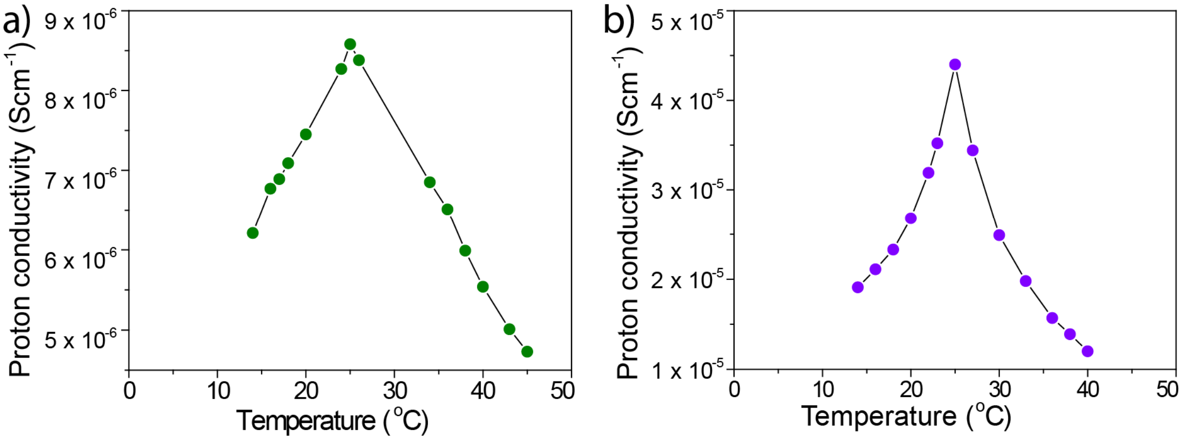

Figure 6.13: Proton conductivity as a function of temperature in a) Ca-SBBA and b) Sr-SBBA.

Ca-SBBA is comparable with MIL-53 (10^{-6}-10^{-7} Scm^{-1}) [1.62a] whereas the proton conductivity value of Sr-SBBA is similar to PCMOF3 (3.5 × 10^{-5} Scm^{-1}) [1.62b] and ValZnCl (4.4 × 10^{-5} Scm^{-1}) [3.13] where identical hydrous conditions had been applied. Moreover, the conductivity value is two order higher than the literature reported Zn-SDBA coordination polymer. The low temperature proton conductivity experiments reveal the activation energy of 0.23 eV and 0.56 eV for Ca-SBBA and Sr-SBBA, respectively. Hence, the proton conduction for Ca-SBBA follows the Grotthuss proton hopping mechanism. However, higher activation energy for Sr-SBBA indicates Grotthuss mechanism along with some other process such as direct diffusion of additional protons with water molecules or DMF molecules (vehicle mechanism). The fact that Sr-SBBA exhibits higher proton conduction than Ca-SBBA despite the large Ea is indicative of a high carrier concentration, originating from the combination of metal clusters along with coordinated and non-coordinated solvent molecules. Ba-SBBA fails to show reproducible conductivity results owing to its structural instability in humid conditions. Thus, the three alkali earth metal based MOFs exhibit significant difference in their proton conducting ability owing to structural variation as well as physico-chemical properties. We believe that our findings will motivate researchers to employ eco-friendly alkali earth metal to design functional MOFs with high stability to compete with polymers and Zeolite based materials in practical applications.

6.3 Conclusion:

In summary, we have successfully synthesized three new 2D MOFs (Ca-SBBA, Sr-SBBA, Ba-SBBA) from alkali earth metal (Ca, Sr, Ba) salts and 4,4′-sulphobisbenzoic acid (SBBA) as a linker. These MOFs exhibit interesting structural variation although they are derived from the same group of metals and same SBBA ligand. They show remarkable thermal stability upto 500 °C. Most interestingly, these three MOFs show significant difference in their proton conducting ability. We hope that our study will motivate researchers to systematically explore proton conducting MOFs with high thermal stability to compete with Nafion and Zeolite based materials in practical applications.

6.4 Experimental details:

6.4.1 Materials:

All starting materials (e.g. metal salts, SBBA, DMF, DEF) were purchased from the Sigma Aldrich Chemicals and used without further purification.

6.4.2 Synthetic procedure of the MOFs:

Synthesis of Ca-SBBA: 1 mL 0.2 M DMF stock solution of $Ca(NO_3)_2.4H_2O$ was mixed with 1 mL 0.2 M DMF stock solution of SBBA in a 5 mL screw capped vial and sonicated briefly. The vial was then inserted in a preheated oven at 100 °C for 48 h. The block shaped colorless crystals were isolated by filtration and washed with DMF (× 2) and acetone (× 2) followed by drying in air (10 min). [**Yield:** 70 %, 0.013 g based on $Ca(NO_3)_2.4H_2O$]. ***FT-IR*** **:** (KBr 4000-600 cm^{-1}): 3369(br), 3051(w), 1656(s), 1591(s), 1545(s), 1384(s), 1158(s), 1095(s), 744(s), 660(s).

Elemental Analysis: $C_{23}N_3O_9H_{29}S_1Ca_1$= [Ca(SBBA).$(DMF)_2$].DMF:

Calcd. C, 49.02; H, 5.15; N, 7.46. Found C, 49.41; H, 5.72; N, 7.23.

Synthesis of Sr-SBBA: 1 mL 0.2 M DMF stock solution of $Sr(NO_3)_2$ was mixed with 1 mL 0.2 M DMF stock solution of SBBA in a 5 mL screw capped vial and sonicated for 30 min. The vial was then inserted in a preheated oven at 100 °C for 96 h. The block shaped colorless crystals were isolated by filtration and washed with DMF (× 2) and acetone (× 2) followed by drying in air (10 min). [**Yield:** 74%, 0.0074 g based on $Sr(NO_3)_2$]. ***FT-IR:*** (KBr 4000-600 cm^{-1}): 3463(br), 3051(w), 1659(s), 1598(s), 1560(s), 1383(s), 1098(w), 1290(s), 1161(s), 1098(s), 783(s), 730(s).

Elemental Analysis: $C_{82}H_{88}N_8O_{36}S_4Sr_5$ = $[Sr_5(SBBA)_4.(HCOO)_2.(DMF)_8].2DMF$:

Calcd. C, 42.72; H, 4.16; N, 5.66. Found C, 42.41; H, 4.09; N, 5.47.

Synthesis of Ba-SBBA: 11 mL 0.2 M DEF stock solution of $Ba(NO_3)_2$ was mixed with 1 mL 0.2 M DEF stock solution of SBBA in a 5 mL screw capped vial and sonicated for 20 minutes. The vial was then inserted in a preheated oven at 100 °C for 72 h. The colorless plate crystals were isolated by filtration and washed with DMF (× 2) and acetone (× 2) followed by drying in air (10 min). [**Yield:** 74%, 0.0074 g depending on $Ba(NO_3)_2$. ***FT-IR*** **:** (KBr 4000-600 cm^{-1}): 2880(br), 1596(s), 1538(s), 1367(s), 1288(s), 1098(w), 1037(m), 783(s), 722(s).

Elemental Analysis: $C_{48}H_{56}Ba_2N_4O_{16}S_2$ = $[Ba_2(SBBA)_2].4DEF$:

Calcd. C, 44.86; H, 4.44; N, 4.36. Found C, 44.39; H, 4.46; N, 4.39.

6.5 General characterization methods:

a) Powder X-Ray Diffraction (PXRD): The PXRD patterns were collected on a Phillips PANalytical diffractometer on a CuKα radiation (λ = 1.5406 Å), with a scan speed of 2° min^{-1}. The tube voltage and amperage were set at 40 kV and 30 mA, respectively. Each sample was scanned between 5 and 50° 2θ with a step size of 0.02°.

b) Thermogravimetric Analysis (TGA) and Differential Scanning Calorimetry (DSC): TGA and DSC were performed on a SDT Q600 TG-DTA instrument. ca. 8 mg of the MOFs were heated from 25 to 800 °C under the N_2 flow at heating rate of 5 °C min^{-1}.

c) IR Spectroscopy: The Fourier transform (FT) infrared spectra of the MOFs were collected on a *PERKIN ELMER FT-IR SPECTRUM* (Nicolet) spectrometer. KBr pellets (2 mg MOF in 20 mg of KBr) were prepared and 50 scans were measured at 2 cm^{-1} resolution for each sample. The spectra were measured over the range of 4000-600 cm^{-1}.

d) Proton Conductivity: Proton Conductivities were measured using Solartron 1287 Electrochemical Interface with 1255B frequency response analyzer via a quasi-four-probe method. ca. 120 mg of the as-synthesized MOFs were pressed in a pellet maker to obtain uniform pellets of ca. 0.38 mm, which was subject to humidification (98% RH) for 24 h and subsequently measured the proton conductivity. Resistances were measured from the semicircle of the Nyquist plots. Proton conductivity was measured by the following equation; $\sigma = L/(R.A)$ where σ = proton conductivity, L = thickness of the pellet, R = resistance of the pellet and A = area of the pellet = πr^2 where r = radius of the pellet.

For high-temperature proton conductivity measurements, the pellets were inserted within a humidification chamber, which was encircled with a controlled heating coil attached with an automated temperature controller. The heat flow within the temperature controller was controlled by a dimmerstat accordingly. The temperature of the chamber was measured by an infrared temperature sensor attachment, having a sensing accuracy of ±0.5 °C.

For low-temperature proton conductivity measurements, the pellets were inserted within a humidification chamber, which was encircled with a water circulation coil attached with a chiller integrated with an automated temperature controller. The heat flow within the chamber was controlled by the chiller accordingly. The temperature of the chamber was measured by an infrared temperature sensor attachment, having a sensing accuracy of ±0.5 °C.

6.6 X-ray Crystallography

General data collection and refinement procedures:

All single crystal data were collected on a Bruker SMART APEX three circle diffractometer equipped with a CCD area detector and operated at 1500 W power (50 kV, 30 mA) to generate Mo Kα radiation (λ = 0.71073 Å). The incident X-ray beam was focused and monochromated using Bruker Excalibur Gobel mirror optics. All crystals reported in this chapter were mounted on nylon CryoLoops (Hampton Research) with Paraton-N (Hampton Research).

Initial scans of each crystal were performed to obtain preliminary unit cell parameters and to determine the mosaicity (breadth of spots between frames) of the crystal to select the required frame width for data collection. In every case frame widths of 0.5° were judged to be appropriate and full hemispheres of data were collected using the *Bruker* SMART software suite. Following data collection, reflections were sampled from all regions of the Ewald sphere to redetermine unit cell parameters for data integration and to check for rotational twinning using CELL_NOW [2.7]. Fortunately, no crystal decay was encountered in case of the data collection. Following exhaustive review of the collected frames the resolution of the dataset was judged. Data were integrated using Bruker SAINT [2.8] software with a narrow frame algorithm and a 0.400 fractional lower limit of average intensity. Data were subsequently corrected for absorption by the program SADABS [2.9]. The space group determinations and tests for merohedral twinning were carried out using XPREP [2.9]. In all cases, the highest possible space group was chosen.

All structures were solved by direct methods and refined using the SHELXTL 97 [2.10] software suite. Atoms were located from iterative examination of difference F-maps following least squares refinements of the earlier models. Final models were refined anisotropically (if the number of data permitted) until full convergence was achieved. Hydrogen atoms were placed in calculated positions (C–H = 0.93 Å) and included as riding atoms with isotropic displacement parameters 1.2-1.5 times U_{eq} of the attached C atoms. All structures were examined through the *Adsym* subroutine of PLATON [2.11] to ensure that no additional symmetry could be applied to the models. All ellipsoids in ORTEP diagrams are displayed at the 50% probability level unless stated otherwise. For all structures we observed elevated R-values; a problem commonly encountered in MOF crystallography [2.12].

Experimental and refinement details for Ca-SBBA: A Colorless block like crystal (0.3 × 0.2 × 0.1 mm^3) of Ca-SBBA was placed in 0.7 mm diameter nylon CryoLoops (Hampton Research) with Paraton-N (Hampton Research). The loop was mounted on a SMART APEX three circle diffractometer equipped with a CCD area detector and operated at 1500 W power (50 kV, 30 mA) to generate Cu Kα radiation (λ = 1.54184 Å) at 296(2) K. A total of 4407 reflections were collected of which 3315 were unique. The range of θ was from 1.71 to 24.99. Analysis of the data showed negligible decay during collection. The structure was solved in the monoclinic $P2_1/c$ space group, with Z = 4, using direct methods. All non-hydrogen atoms were refined anisotropically with hydrogen atoms generated as spheres riding the coordinates of their parent atoms. Final full matrix least-squares refinement on F^2 converged to $R_1 = 0.0386$ ($F > 2\sigma F$) and $wR_2 = 0.1045$ (all data) with GOF = 1.028. All the atoms were made anisotropic and the ORTEP diagram is provided with 50% probability (Figure 6.14a).

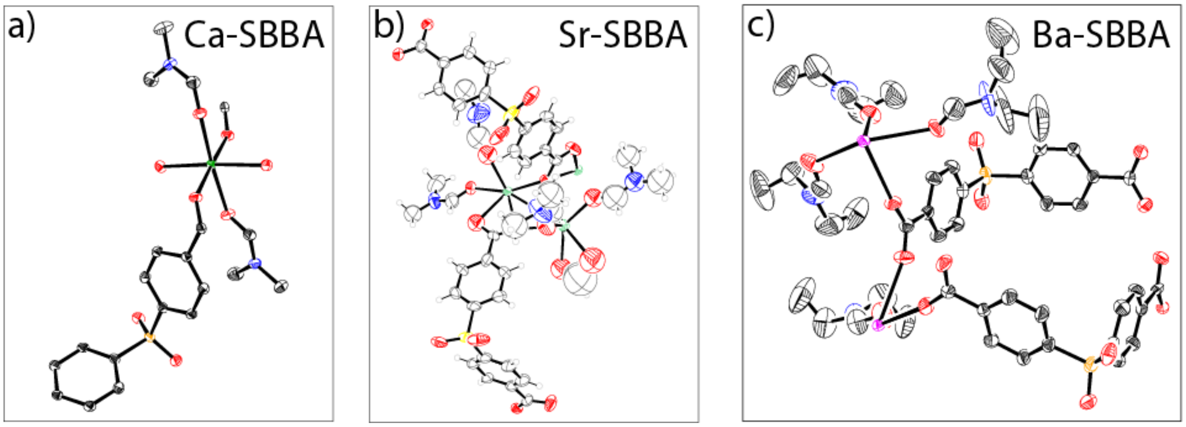

Figure 6.14: ORTEP diagrams for the asymmetric unit of Ca-SBBA, Sr-SBBA and Ba-SBBA in 50% probability level.

Experimental and refinement details for Sr-SBBA:

A colorless needle like crystal (0.28 × 0.16 × 0.08 mm^3) of Sr-SBBA was placed in 0.7 mm diameter nylon CryoLoops (Hampton Research) with Paraton-N (Hampton Research). The loop was mounted on a SMART APEX three circle diffractometer equipped with a CCD area detector and operated at 1500 W power (50 kV, 30 mA) to generate Cu Kα radiation (λ = 1.54184 Å) at 293(2) K. A total of 11542 reflections were collected of which 8511 were unique. The range of θ was from 3.26 to 73.36. Analysis of the data showed negligible decay during collection. The structure was solved in the monoclinic *P*-1 space group, with Z = 1, using direct methods. All non-hydrogen atoms were refined anisotropically with hydrogen atoms generated as spheres riding the coordinates of their parent atoms. Final full matrix least-squares refinement on F^2 converged to $R_1 = 0.0825$ ($F > 2\sigma F$) and $wR_2 = 0.2534$ (all data) with GOF = 1.116.

Modeling of electron density within the voids of the frameworks did not lead to identification of guest entities in Sr-SBBA structure due to the disordered contents of the pores in the frameworks. Increasing the exposure time of the crystal to x-rays did not improve the quality of the high angle data, as the intensity from low angle data saturated the detector. The only optimal crystals suitable for analysis were generally small and weakly diffracting, and unfortunately, larger crystals, which would usually improve the quality of the data, presented a lowered degree of crystallinity and attempts to optimize the crystal growing conditions for large high-quality specimens has not yet been fruitful.

Electron density within void spaces, which could not be assigned to any definite guest entity, was modeled as highly disordered DMF molecules and isolated oxygen and carbon atoms, and the foremost errors in all the models lies with assignment of guest electron density. To prove the correctness of the atomic positions in the framework the application of the SQUEEZE routine of A. Spek had been performed. The SQUEEZE structure is devoid of any solvent entity, and matches well with the elemental analysis value of the evacuated Sr-SBBA sample. We have provided the squeezed structure of Sr-SBBA. The formate anion (O8, C44, O7), symmetry generated DMF (O12, C18, C19) and disordered DMF [(O13, C41, C42, C43, N5) and (C20, C21, C39)] were kept isotropic. Except these all the atoms were made anisotropic and the ORTEP diagram is provided with 50% probability (Figure 6.14b).

Experimental and refinement details for Ba-SBBA:

A colorless rod shaped crystal (0.3 × 0.2 × 0.2 mm^3) of Ba-SBBA was placed in 0.7 mm diameter nylon CryoLoops (Hampton Research) with Paraton-N (Hampton Research). The loop was mounted on a SMART APEX three circle diffractometer equipped with a CCD area detector and operated at 1500 W power (50 kV, 30 mA) to generate Mo Kα radiation (λ = 0.71073 Å) at 296(2) K. A total of 12609 reflections were collected of which 8752 were unique. The range of θ was from 1.71 to 24.99. Analysis of the data showed negligible decay during collection. The structure was solved in the triclinic P-1 space group, with Z = 2, using direct methods. All non-hydrogen atoms were refined anisotropically with hydrogen atoms generated as spheres riding the coordinates of their parent atoms. Final full matrix least-squares refinement on F^2 converged to $R_1 = 0.0557$ ($F > 2\sigma F$) and $wR_2 = 0.1413$ (all data) with GOF = 1.074. All the atoms were made anisotropic and the ORTEP diagram is provided with 50% probability (Figure 6.14c).

NOTE: The results of this chapter have already been published in *Chem. Commun.* 2012, **48**, 4998. with the title: "*Alkali earth metal (Ca, Sr, Ba) based thermostable metal–organic frameworks (MOFs) for proton conduction*". The publication was resulted from the group of Dr. Rahul Banerjee and his students Subash Chandra Sahoo and Tanay Kundu from CSIR-National Chemical Laboratory, Pune, India. Major experimental works and manuscript preparation were contributed by Tanay Kundu using instrumental facilities of

CSIR-National Chemical Laboratory. Subash Chandra Sahoo did the X-ray data interpretation.

CHAPTER 7

CONCLUSION OF ALL CHAPTERS AND FUTURE DIRECTION

7.1 Conclusion:

In this dissertation, the applications of MOFs have been emphasized on high H_2O storage capacity and proton transporting ability. A series of MOFs have been synthesized, characterized and screened successfully for such aspects.

The conclusion of chapter 2 is divided in two parts. In first part, the MOFs are arranged according to their hydrophilicity with almost similar structural backbone and pore size/shape with only difference in the poking sidearm of the amino acids. Thus, the incoming guest solvent molecules interact with the MOFs based on their differential polarity and hydrophilicity. It has been concluded from extensive solvent uptake (water, methanol, isopropanol and toluene) studies that the hydrophilic MOFs prefer hydrophilic guest over the hydrophobic one. In the second part, we have demonstrated the effects of changing MOF structure and pore size/shapes to assay their effect on water adsorption affinity. In this case, hydrophobic MOFs showed pore condensation behaviour while hydrophilic MOFs allow water inclusion regardless of their pore size albeit with varying capacity.

In chapter 3, we have demonstrated the chirality of amino acid derived MOFs and their isomerism with respect to change in anions. These subtle changes usher in drastic change in water adsorption capacity, proton conducting capability and single crystal to single crystal transformation ability.

In chapter 4, we have presented the design of amino acid derived MOFs which possesses ambient temperature hydrolytic stability as well as high temperature hydrolytic regenerability. A series of eight homochiral MOFs have been synthesized by using pyridyl derivative of *l*–valine or *l*–alanine, and Zn(II) salt as metal precursor with different coordinated anions. Replacement of valine (amino acid residue of the ligand) with more hydrophilic alanine results in enhanced polar intermolecular interaction, higher water sorption capability of the aforestated MOFs. The coordinated anions largely determine the differential regenerability of the aforementioned MOFs. A solution state processing method via salt metathesis has been demonstrated to utilize the unique water soluble property of these MOFs to yield completely different MOF architectures from a single precursor solution.

In chapter 5, anion and environment controlled ZnO microstructures are obtained by one step solid state thermolysis of two Zn based homochiral MOFs both in air and in N_2. Apart from diverse morphologies, these ZnO microparticles show visible light emission centered at 605 nm or 510 nm. These ligand free ZnO microparticles are very stable and their PL spectra show almost no change after keeping samples in air for at least 5 months. These ZnO microparticles show potential for DSSC applications. The advantage of this work is that a simple experiment leads us to understand the role of the anions as the structural directing agent and effect of environment on the ZnO morphologies.

In chapter 6, we have successfully synthesized three new 2D MOFs (Ca-SBBA, Sr-SBBA, Ba-SBBA) from alkali earth metal (Ca, Sr, Ba) salts and 4,4′-sulphobisbenzoic acid (SBBA) as a linker. These MOFs exhibit interesting structural variation although they are derived from the same group of metals and same SBBA ligand. They show remarkable thermal stability upto 500 °C. Most interestingly, these three MOFs show significant difference in their proton conducting ability, which could be related to their structure and stability.

7.2 Future directive:

Plan-1: Design and synthesis of extended linkers to realize highly porous MOFs with *unh* topology.

The aim of this future plan is to synthesize elongated linkers based on amino acid backbone. The design will involve use of 4-pyridylphenylcarboxaldehyde, quinoline carboxaldehyde and quinoline carboxylic acid instead of 4-pyridinecarboxaldehyde. The reaction should involve both reductive Schiff base coupling as well as amide bond formation reaction (Figure 7.1). This will impart two effects a) The new links will have longer length compared to the earlier one which will provoke added porosity within the systems. b) The optical property of such linker will be useful for designing sensory device. The designs will open up new possibilities for amino acid based MOFs in industrially relevant applications.

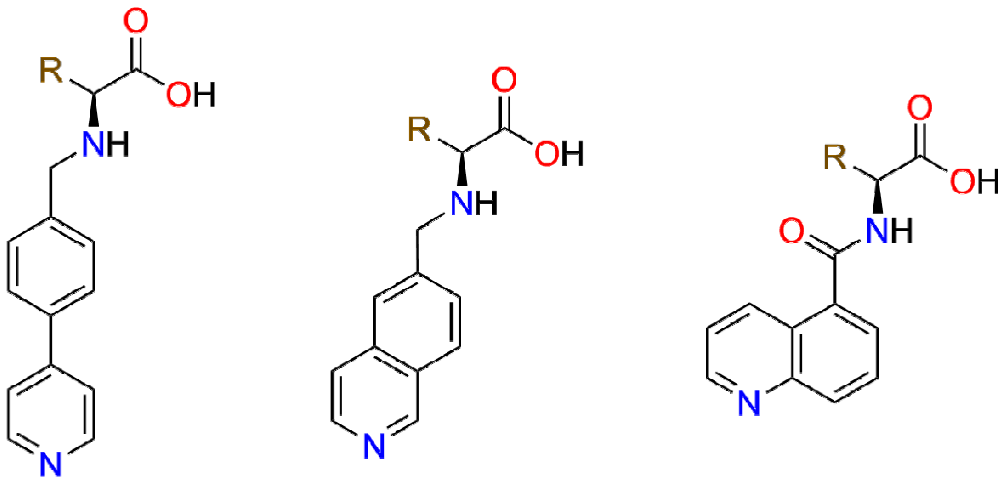

Figure 7.1: Scheme of linkers proposed to get extended metal-organic frameworks for higher porosity.

Plan-2: Phosphoric acid doped benzimidazole based covalent organic frameworks (COFs) for proton conduction.

The objective of this plan is to design and synthesis of new benzimidazole based COFs which can show very high proton conductivity at anhydrous condition. Phosphoric acid (H_3PO_4) doped benzimidazole COFs can have high proton conductivity at high temperature (> 100 °C) without humidification. The proton conduction of the COFs have been initiated by doped H_3PO_4 molecules which form a salt by protonation of the imine N group of imidazole ring (Figure 7.1c) and creates proton hopping channel through the COF backbone. Keep these things in perspective; our approach focuses on the synthesis of stable COFs which will have repeating benzimidazole units (Figure 7.1a) in the framework backbones as such units have proton anchoring sites. The long range periodicity, tailor-made porosity, regular arrangement of voids and dynamic behaviour of COFs are especially beneficial for their use as proton conductors compare to conventional PBI based polymers.

We have designed both *C*2 as well as *C*3 symmetric linkers to form porous COFs with desired characteristics (Figure 7.1b).

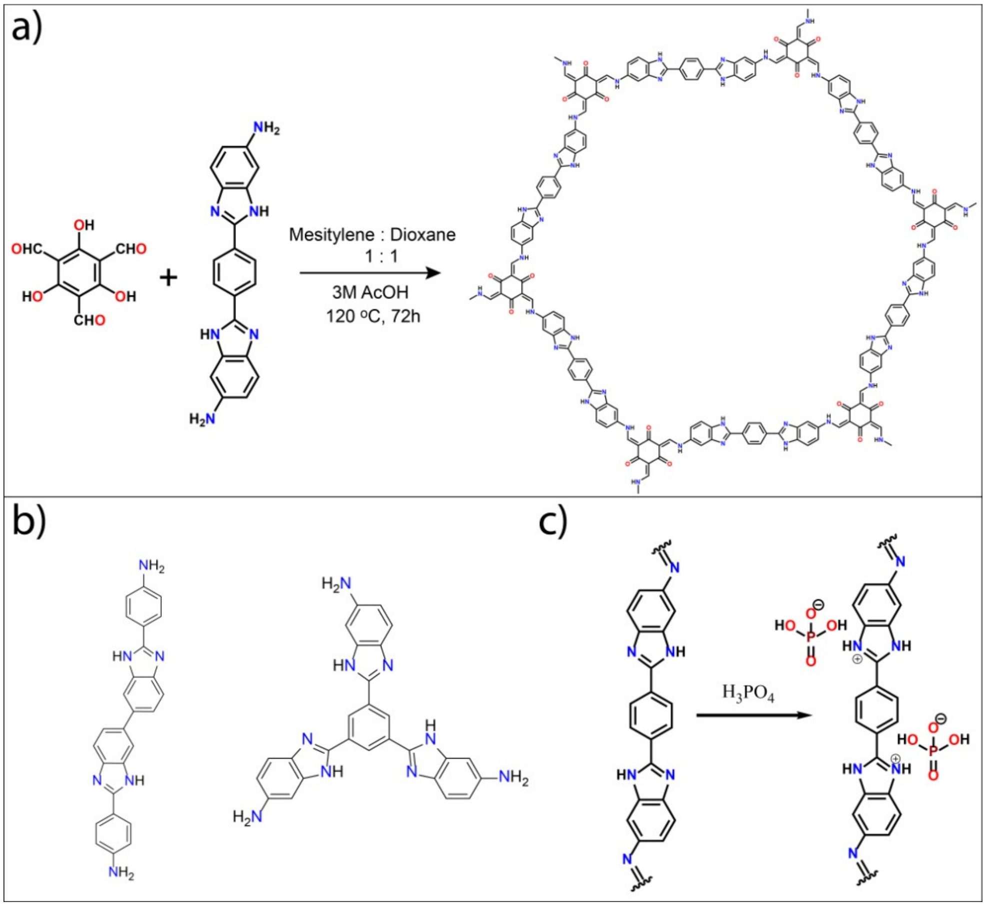

Figure 7.2: Scheme of synthesis and proposed proton conduction mechanism in phosphoric acid loaded benzimidazole based covalent organic frameworks.

REFERANCES

CHAPTER 1

[1.1] (a) J. Lee, J. Kim, T. Hyeon, *Adv. Mater.,* 2006, **18**, 2073. (b) A. Stein, Z. Wang, M. A. Fierke, *Adv. Mater.*, 2009, **21**, 265.

[1.2] (a) M. E. Davis, *Nature*, 2002, **417**, 813. (b) Y. Ma, W. Tong, H. Zhou, S. L. Suib, *Micropor Mesopor Mat*, 2000, **37**, 243.

[1.3] (a) N. Mizoshita, T. Tani, S. Inagaki, *Chem. Soc. Rev.*, 2011, **40**, 789. (b) B. Hatton, K. L,skron, W. Whitnall, D. Perovic, G. A. Ozin, *Acc. Chem. Res.*, 2005, **38** (4), 305. (c) P. V. D. Voort, D. Esquivel, E. D. Canck, F. Goethals, I. V. Driesscheb, F. J. Romero-Salgueroc, *Chem. Soc. Rev.*, 2013, **42**, 3913.

[1.4] H. Li, M. Eddaoudi, M. O'Keeffe, O. M. Yaghi. *Nature,* 1999, **402**, 276.

[1.5] (a) H. K. Chae, D. Y. Siberio-Perez, J. Kim, Y. Go, M. Eddaoudi, A. J. Matzger, M. O'Keeffe, O. M. Yaghi, *Nature*, 2004, **427**, 523. (b) O. M. Yaghi, M. O'Keeffe, N. W. Ockwig, H. K. Chae, M. Eddaoudi, J. Kim, *Nature*, 2003, **423**, 705.

[1.6] (a) N. L. Rosi, J. Eckert, M. Eddaoudi, D. T. Vodak, J. Kim, M. O'Keeffe, O.M. Yaghi, *Science*, 2003, **300**, 1127. (b) Y. Yan, X. Lin, S. Yang, A. J. Blake, A. Dailly, N. R. Champness, P. Hubberstey, M. Schröder, *Chem. Commun.*, 2009, 1025. (c) O. K. Farha, A. O. Yazaydin, I. Eryazici, C. D. Malliakas, B. G. Hauser, M. G. Kanatzidis, S. T. Nguyen, R. Q. Snurr, J. T. Hupp, *Nat. Chem.*, 2010, **2**, 944. (d) H. Furukawa, N. Ko, Y. B. Go, N. Aratani, S. B. Choi, E. Choi, A. O. Yazaydin, R. Q. Snurr, M. O'Keeffe, J. Kim, O. M. Yaghi, *Science*, 2010, **329**, 424.

[1.7] I. Senkovska, S. Kaskel, *Chem. Commun.*, 2014, **50**, 7089.

[1.8] (a) H. Furukawa, K. E. Cordova, M. O'Keeffe, O. M. Yaghi, *Science*, 2013, **341**, 6149. (b) R. J. Kuppler, D. J. Timmons, Q. -R. Fang, J. -R. Li, T. A. Makal, M. D. Young, D. Yuan, D. Zhao, W. Zhuang, H. -C. Zhou. *Coord. Chem. Rev.*, 2009, **253**, 3042. (c) A. Morozan, F. Jaouen, *Energy Environ. Sci.,* 2012, **5**, 9269. (d) A. U. Czaja, N. Trukhan, U. Müller, *Chem. Soc. Rev.*, 2009, **38**, 1284. (e) U. Mueller, M. Schubert, F. Teich, H. Puetter, K. Schierle-Arndt, J. Pastré, *J. Mater. Chem.*, 2006, **16**, 626.

[1.9] (a) J. -R. Li, R. J. Kuppler, H. -C. Zhou, *Chem. Soc. Rev.*, 2009, **38**, 1477. (b) Y. Tao, H. Kanoh, L. Abrams, K. Kaneko, *Chem. Rev.,* 2006, **106**, 896. (c) D. Farrusseng, S. Aguado, C. Pinel, *Angew. Chem. Int. Ed.*, 2009, **48**, 41, 7502. (d) C. Y. Lee , O. K. Farha, B. J. Hong, A. A. Sarjeant, S. T. Nguyen, J. T. Hupp, *J. Am. Chem. Soc.,* 2011, **133**, 15858.

[1.10] C. -P. Li, M. Du *Chem. Commun.*, 2011,**47**, 5958.

[1.11] Y. -X Sun, W. -Y Sun, *Chin. Chem. Lett.*, 2014, 25, 6, 823.

[1.12] M. R. Martinez, M. P. Batten, A. Polyzos, K. –C. Carey, J. I. Mardel, K. –S. Lim, M. R. Hill, *Sci. Rep.,* 2014, 5443.

[1.13] N. Stock, S. Biswas, *Chem. Rev*., 2012, **112**, 933.

[1.14] T. Friščić, *J. Mater. Chem.*, 2010, **20**, 7599.

[1.15] D. Wu, F. Xu, B. Sun, R. Fu, H. He, K. Matyjaszewski, *Chem. Rev.*, 2012, **112**, 3959.

[1.16] (a) Y. Ma, W. Tong, H. Zhou, S. L. Sui, *Micropor Mesopor Mat*, 2000, **37**, 243. (b) N. R. E. N. Impens, P. V. D. Voort, E. F Vansant, *Micropor Mesopor Mat*, 1999, **28**, 217. (c) J. Pérez-Ramírez, C. H. Christensen, K. Egeblad, C. H. Christensen, J. C. Groen, *Chem. Soc. Rev.*, 2008, **37**, 2530.

[1.17] (a) M. O'Keeffe, M. A. Peskov, S. J. Ramsden, O. M. Yaghi, *Acc. Chem. Res.,* 2008, **41**, 1782. (b) M. O'Keeffe, O. M. Yaghi, *Chem. Rev.,* 2012, **112**, 675. (c) N. W. Ockwig, O. D.-Friedrichs, M. O'Keeffe, O. M. Yaghi, *Acc. Chem. Res.,* 2005, **38**, 176. (d) D. J. Tranchemontagne, Z. Ni, M. O'Keeffe, O. M. Yaghi, *Angew. Chem. Int. Ed.,* 2008, **47**, 5136.

[1.18] G. Férey, C. Mellot-Draznieks, C. Serre1, F. Millange, J. Dutour, S. Surblé, I. Margiolaki, *Science*, 2005, **309**, 2040.

[1.19] J. H. Cavka, S. Jakobsen, U. Olsbye, N. Guillou, C. Lamberti, S. Bordiga, K. P. Lillerud, *J. Am. Chem. Soc.,* 2008, **130**, 13850.

[1.20] W. J. Lough, I. W. Wainer, *Chirality in Natural and Applied Science*, CRC, Oxford, 2002. (b) S. Mason, *Trends in Pharmacological Sciences*, 1986, **7**, 20.

[1.21] J. D. Lear, Z. R. Wasserman, W. F. DeGrado, *Science*, 1988, **240**, 1177.

[1.22] E. L. Eliel, S. H. Wilen, *The Stereochemistry of Organic Compounds*, Wiley-Interscience, Weinheim, 1994.

[1.23] C. S. Stinson, *Fine chemicals*, *Chem. Eng. News*, 2001, **79**, 65.

[1.24] (a) J. Yu, R. Xu, *J. Mater. Chem.*, 2008, **18**, 4021. (b) M. W. Anderson, O. Terasaki, T. Ohsuna, A. Philippou, S. P. MacKay, A. Ferreira, J. Rocha , S. Lidin, *Nature*, 1994, **367**, 347. (c) J. M. Newsam, M. M. J. Treacy, W. T. Koetsier, C. B. de Gruyter, *Proc. R. Soc. London Ser. A*, 1988, **420**, 375.

[1.25] L. B. McCusker, C. Baerlocher, E. Jahn, M. Bülow, *Zeolites*, 1991, **11**, 308.

[1.26] C.S. Cundy, P.A. Cox, *Chem. Rev.*, 2003, **103**, 663.

[1.27] T. Ezuhara, K. Endo, Y. Aoyama, *J. Am. Chem. Soc.*, 1999, **121**, 3279.

[1.28] S. H. Cho, B. Q. Ma, S. T. Nguyen, J. T. Hupp, T. E. Albrecht-Schmitt, *Chem Commun.*, 2006, 2563.

[1.29] D. N. Dybtsev, A. L. Nuzhdin, H. Chun, K. P. Bryliakov, E. P. Talsi, V. P. Fedin , K. Kim, *Angew. Chem. Int. Ed.*, 2006, **45**, 916.

[1.30] J. S. Seo, D. Whang, H. Lee, S. I. Jun, J. Oh, Y. J. Jeon, K. Kim, *Nature*, 2000, **404**, 982.

[1.31] (a) C. D. Wu, W. Lin, *Angew Chem Int Ed.*, 2005, **44**, 1958. (b) L. Ma, J. M. Falkowski, C. Abney, W. Lin, *Nat. chem.*, 2010, **2**, 838.

[1.32] (a) G. Li , W. Yu , J. Ni , T. Liu , Y. Liu , E. Sheng , Y. Cui , *Angew. Chem. Int. Ed.*, 2008, **47**, 1245. (b) G. Li, W. Yu, Y. Cui, *J. Am. Chem. Soc.*, 2008, **130**, 4582 .

[1.33] (a) R. Katsarava, V. Beridze, N. Arabuli, D. Kharadze, C. C. Chu, C. Y. Won, *J. Polym. Sci., Part A: Polym. Chem.*, 1999, **37**, 391. (b) T. C. Holmes, *Trends Biotechnol.*, 2002, **20**, 16. (c) R. J. Mart, R. D. Osborne, M. M. Stevens, R. V. Ulijn, *Soft Matter*, 2006, **2**, 822. (d) S. Kiyonaka, K. Sugiyasu, S. Shinkai, I. Hamachi, *J. Am. Chem. Soc.*, 2002, **124**, 10954. (e) M. D. Brown, A. Schätzlein, A. Brownlie, V. Jack, W. Wang, L. Tetley, I. F. Uchegbu, *Bioconjugate chem.*, 2000, **11**, 880. (f) F. Sanda, T. Endo, *Macromol. Chem. Phys.*, 1999, **200**, 2651. (g) L. Andersson, B. Sellergren, K. Mosbach, *Tetrahedron Lett.*, 1984, **25**, 5211.

[1.34] (a) H. Y. An, E. B. Wang, D. R. Xiao, Y. G. Li, Z. M. Su, L. Xu, *Angew. Chem.*, 2006, **118**, 918. (b) C. L. Gatlin, F. Turecek, T. Vaisar, *J. Am. Chem. Soc.*, 1995, **117**, 3637. (c) D. A. Hill, E. R. Peo. Jr., A. J. Lewis, J. D. Crenshaw, *J. Anim. Sci.* 1986, **63**, 121. (d) R. G. Denning, T. S. Piper, *Inorg. Chem.*, 1966, **5**, 1056. (e) D. D. Perrin, *J. Chem. Soc.*, 1958, **633**, 3125. (f) C. Djordjevic, N. Vuletic, B. A.

Jacobs, M. Lee-Renslo, E. Sinn, *Inorg. Chem.*, 1997, **36**, 1798. (g) F. E. Smith, R. C. Hynes, T. T. Ang, L. E. Khoo, G. Eng, *Can. J. Chem.*, 1992, **70**, 1114. (h) B. A. Goodman, D. B. McPhail, H. K. J. Powell, *J. Chem. Soc., Dalton Trans.*, 1981, **3**, 822. (i) J. -J. Zhang, T. -L. Sheng, S. -M. Hu, S. -Q. Xia, G. Leibeling, F. Meyer, Z. -Y. Fu, L. Chen, R. -B. Fu, X. -T. Wu, *Chem. Eur. J.*, 2004, **10**, 3963. (j) P. K. Sasmal, A. K. Patra, M. Nethaji, A. R. Chakravarty, *Inorg. Chem.*, 2007, **46**, 11113. (k) A. T. Tovar, L. R. Ramrez, A. Campero, A. R. Romerosa, M. Esparza, M. J. R. Hoz, *J. Inorg. Biochem.*, 2004, **98**, 1045.

[1.35] R. Vaidhyanathan, D. Bradshaw, J. -N. Rebilly, J. P. Barrio, J. A. Gould, N. G. Berry, M. J. Rosseinsky, *Angew. Chem. Int. Ed.*, 2006, **45**, 6495.

[1.36] J. Perez Barrio, J. -N. Rebilly, B. Carter, D. Bradshaw, J. Bacsa, A. Y. Ganin, H. Park, A. Trewin, R. Vaidhyanathan, A. I. Cooper, J. E. Warren, M. J. Rosseinsky, *Chem. Eur. J.*, 2008, **14**, 4521.

[1.37] J. Rabone, Y. F. Yue, S. Y. Chong, K. C. Stylianou, J. Bacsa, D. Bradshaw, M. J. Rosseinsky, *Science*, 2010, **329**, 1053.

[1.38] A. P. Katsoulidis, K. S. Park, D. Antypov, C. Martí-Gastaldo, G. J. Miller, J. E. Warren, C. M. Robertson, F. Blanc, G. R. Darling, N. G. Berry, J. A. Purton, D. J. Adams, M. J. Rosseinsky, *Angew. Chem. Int. Ed.*, 2014, **53**, 193.

[1.39] M. Wang, M. H. Xie, C. D. Wu, Y. G. Wang, *Chem. Commun.*, 2009, 2396.

[1.40] T. T. Ong, P. Kavuru, T. Nguyen, R. Cantwell, Y. Wojtas, M. J. Zaworotko, *J. Am. Chem. Soc.*, 2011, **133**, 9224.

[1.41] S. R. Miller, D. Heurtaux, T. Baati, P. Horcajada, J. M. Greneche, C. Serre, *Chem. Commun.*, 2010, **46**, 4526.

[1.42] J. Canivet, A. Fateeva, Y. Guo, B. Coasnecd, D. Farrusseng, *Chem. Soc. Rev.*, 2014, **43**, 5594.

[1.43] (a) L. Guillemot, T. Biben, A. Galarneau, G. Vigier, E. Charlaix, *Proc. Natl. Acad. Sci. U. S. A.*, 2012, **109**, 19557. (b) F. Cailliez, M. Trzpit, M. Soulard, I. Demachy, A. Boutin, J. Patarin, A. H. Fuchs, *Phys. Chem. Chem. Phys.*, 2008, **10**, 4817.

[1.44] (a) J. Liu, P. K. Thallapally, B. P. McGrail, D. R. Brown, J. Liu, *Chem. Soc. Rev.*, 2012, **41**, 2308. (b) J. Liu, J. Tian, P. K. Thallapally , B. P. McGrail, *J. Phys. Chem. C*, 2012, **116**, 9575. (c) E. Soubeyr-Lenoir, C. Vagner, J. W. Yoon, P. Bazin, F.

Ragon, Y. K. Hwang, C. Serre, J. -S. Chang, P. L. Llewellyn, *J. Am. Chem. Soc.*, 2012, **134**, 10174. (d) A. O. Yazaydin, A. I. Benin, S. A. Faheem, P. Jakubczak, J. J. Low, R. R. Willis, R. Q. Snurr, *Chem. Mater.*, 2009, **21**, 1425. (e) Y. F. Chen, R. Babarao, S. I. Sandler, J. W. Jiang, *Langmuir*, 2010, **26**, 8743. (f) M. Sadakiyo, H. Okawa, A. Shigematsu, M. Ohba, T. Yamada , H. Kitagawa, *J. Am. Chem. Soc.*, 2012, **134**, 5472. (g) A. C. Kizzie, A. G. Wong-Foy, A. J. Matzger, *Langmuir*, 2011, **27**, 6368.

[1.45] a) P. Guo, A. G. Wong-Foy, A. J. Matzger, *Langmuir*, 2014, **30**, 1921. (b) N. A. Khan, B. K. Jung, Z. Hasan, S. H. Jhung, *J. Hazard. Mater.*, 2014, DOI: 10.1016/j.jhazmat.2014.03.047. (c) L. Xie, D. Liu, H. Huang, Q. Yang, C. Zhong, *Chem. Eng. J.*, 2014, **246**, 142. (d) H. Furukawa, F. Gandara, Y. B. Zhang, J. Jiang, W. L. Queen, M. R. Hudson, O. M. Yaghi, *J. Am. Chem. Soc.*, 2014, **136**, 4369.

[1.46] J. J. Low, A. I. Benin, P. Jakubczak, J. F. Abrahamian, S. A. Faheem, R. R. Willis, *J. Am. Chem. Soc.*, 2009, **131**, 15834.

[1.47] K. A. Cychosz, A. J. Matzger, *Langmuir*, 2010, **26**, 17198.

[1.48] (a) D. Feng, Z. Y. Gu, J. R. Li, H. L. Jiang, Z. Wei, H. -C. Zhou, *Angew. Chem. Int. Ed.*, 2012, **51**, 10307. (b) D. Feng, W. C. Chung, Z. Wei, Z. Y. Gu, H. L. Jiang, Y. P. Chen, D. J. Darensbourg, H. -C. Zhou, *J. Am. Chem. Soc.*, 2013, **135**, 17105. (c) H. L. Jiang, D. Feng, K. Wang, Z. Y. Gu, Z. Wei, Y. P. Chen, H. -C. Zhou, *J. Am. Chem. Soc.*, 2013, **135**, 13934.

[1.49] K. S. Park, Z. Ni, A. P. Cote, J. Y. Choi, R. Huang, F. J. Uribe-Romo, H. K. Chae, M. O'Keeffe , O. M. Yaghi, *Proc. Natl. Acad. Sci. U. S. A.*, 2006, **103**, 10186.

[1.50] D. Cunha, M. B. Yahia, S. Hall, S. R. Miller, H. Chevreau, E. Elkaim, G. Maurin, P. Horcajada, C. Serre, *Chem. Mater.*, 2013, **25**, 2767.

[1.51] J. Canivet, J. Bonnefoy, C. Daniel, A. Legr, B. Coasne, D. Farrusseng, *New J. Chem.*, 2014, DOI: 10.1039/C4NJ00076E.

[1.52] (a) J. Liu, Y. Wang, A. I. Benin, P. Jakubczak, R. R. Willis , M. D. LeVan, *Langmuir*, 2010, **26**, 14301. (b) S. K. Henninger, F. Jeremias, H. Kummer, C. Janiak, *Eur. J. Inorg. Chem.*, 2012, **16**, 2625.

[1.53] (a) C. Janiak, S. K. Henninger, *Chimia*, 2013, **67**, 419. (b) G. Akiyama, R. Matsuda, H. Sato, A. Hori, M. Takata , S. Kitagawa, *Micropor Mesopor Mat.*, 2012, **157**, 89.

[1.54] P. Kuesgens, M. Rose, I. Senkovska, H. Froede, A. Henschel, S. Siegle, S. Kaskel, *Micropor Mesopor Mat.*, 2009, **120**, 325.

[1.55] (a) H. Furukawa, F. Gandara, Y. B. Zhang, J. Jiang, W. L. Queen, M. R. Hudson , O. M. Yaghi, *J. Am. Chem. Soc.*, 2014, **136**, 4369. (b) P. M. Schoenecker, C. G. Carson, H. Jasuja, C. J. J. Flemming, K. S. Walton, *Ind. Eng. Chem. Res.*, 2012, **51**, 6513. (c) P. Kuesgens, M. Rose, I. Senkovska, H. Froede, A. Henschel, S. Siegle, S. Kaskel, *Micropor Mesopor Mat.*, 2009, **120**, 325. (d) F. Jeremias, A. Khutia, S. K. Henninger, C. Janiak, *J. Mater. Chem.*, 2012, **22**, 10148. (e) M. Wickenheisser, F. Jeremias, S. K. Henninger, C. Janiak, *Inorg. Chim. Acta*, 2013, **407**, 145. (f) G. Akiyama, R. Matsuda, H. Sato, A. Hori, M. Takata, S. Kitagawa, *Micropor Mesopor Mat*, 2012, **157**, 89. (g) A. Khutia, H. U. Rammelberg, T. Schmidt, S. Henninger, C. Janiak, *Chem. Mater.*, 2013, **25**, 790. (h) F. Jeremias, V. Lozan, S. K. Henninger, C. Janiak, *Dalton Trans.*, 2013, **42**, 15967. (i) G. E. Cmarik, M. Kim, S. M. Cohen, K. S. Walton, *Langmuir*, 2012, **28**, 15606. (j) J. Canivet, J. Bonnefoy, C. Daniel, A. Legrand, B. Coasne, D. Farrusseng, *New J. Chem.*, 2014, DOI: 10.1039/C4NJ00076E. (k) H. Reinsch, M. A. van der Veen, B. Gil, B. Marszalek, T. Verbiest, D. de Vos, N. Stock, *Chem. Mater.*, 2013, **25**, 17. (l) S. Aguado, J. Canivet, D. Farrusseng, *J. Mater. Chem.*, 2011, **21**, 7582. (m) K. Zhang, R. P. Lively, M. E. Dose, A. J. Brown, C. Zhang, J. Chung, S. Nair, W. J. Koros, R. R. Chance, *Chem. Commun.*, 2013, **49**, 3245.

[1.56] U.S. Department of Energy, U.S. Energy Information Administration: International Energy Outlook 2013 (Report: DOE/EIA-0484(2013)), 2013.

[1.57] (a) G. Boyle, *Renewable energy*, OXFORD university press, 2004. (b) T. B. Johansson, B. Laurie, eds. *Renewable energy: sources for fuels, electricity*. Isl, Press, 1993.

[1.58] (a) G. W. Crabtree, M. S. Dresselhaus, *MRSBull*. 2008, **33**, 421. (b) S. Hamrock , M. A. Yandrasits, *Polym. Rev.*, 2006, **46**, 219.

[1.59] (a) K. D. Kreuer, *Chem. Mater.,* 1996, **8**, 610. (b) K. D. Kreuer, *J. Membr. Sci.,* 2001, **185**, 29. (c) K. D. Kreuer, S. J. Paddison, E. Spohr, M. Schuster, *Chem. Rev.,* 2004, **104**, 4637. (c) B. Atilla. *Int. J. Hydrogen Energy,* 2005, **30**, 1181. (d) Y. Shao, G. Yin, Z. Wang, Y. Gao, *J. Power Sources*, 2007, **167**, 235.

[1.60] (a) K. A. Mauritz, R. B. Moore, *Chem. Rev.*, 2004, **104**, 4535. (b) G. Alberti, R. Narducci, M. Sganappa, *J. Power Source*, 2008, **178**, 575. (c) G. Alberti, R. Narducci, *Fuel Cells,* 2009, **9**, 410.

[1.61] (a) C. J. T. de Grotthuss, *Ann. Chim.* 1806, **58**, 54. (b) S. Cukierman, *Biochimica et Biophysica Acta,* 2006, **1757**, 876. (c) O. F. Mohammed, D. Pines, J. Dreyer, E. Pines, E. T. Nibbering, *Science*, 2005, **310**, 83. (d) M. K. Petersen, F. Wang, N. P. Blake, H. Metiu, G. A. Voth, *J. Phys. Chem. B*, 2005, **109**, 3727. (e) G. K. H. Shimizu, J. M. Taylor, S. Kim, *Science*, 2013, **341**, 354. (f) S. Horike, D. Umeyama, S. Kitagawa, *Acc. Chem. Res.,* 2013, **46**, 2376. (g) N. Agmon, *Chem. Phys. Lett.* 1995, **5**, 456. (h) H. Arribart, Y. Piffard, *Solid State Commun*, 1983, **45**, 571. (i) K. D. Kreuer, A. Rabenau, W. Weppner, *Angew. Chem., Int. Ed.,* 1982, **21**, 208.

[1.62] (a) A. Shigematsu, T. Yamada, H. Kitagawa, *J. Am. Chem. Soc.,* 2011, **133**, 2034. (b) J. M. Taylor, R. K. Mah, I. L. Moudrakovski, C. I. Ratcliffe, R. Vaidhyanathan, G. K. H. Shimizu, *J. Am. Chem. Soc.*, 2010, **132**, 14055. (c) T. Yamada, M. Sadakiyo, H. Kitagawa, *J. Am. Chem. Soc.*, 2009, **131**, 3144. (d) M. Yoon, K. Suh, H. Kim, Y. Kim, N. Selvapalam, K. Kim, *Angew. Chem. Int. Ed.,* 2011, **50**, 7870. (e) M. Sadakiyo, T. Yamada, H. Kitagawa, *J. Am. Chem. Soc.,* 2009, **131**, 9906. (f) V. G. Ponomareva, K. A. Kovalenko, A. P. Chupakhin, D. N. Dybtsev, E. S. Shutova, V. P. Fedin, *J. Am. Chem. Soc.*, 2012, **134**, 15640. (g) S. Kanda, K. Yamashita, K. Ohkawa, *Bull. Chem. Soc. Jpn.*, 1979, **52**, 3296. (h) T. Yamada, S. Morikawa, H. Kitagawa, *Bull. Chem. Soc. Jpn.*, 2010, **83**, 42. (i) S. Kim, K. W. Dawson, B. S. Gelf, J. M. Taylor, G. K. H. Shimizu, *J. Am. Chem. Soc.*, 2013, **135**, 963. (j) S. C. Sahoo, T. Kundu, R. Banerjee. *J. Am. Chem. Soc.*, 2011, **133**, 17950. (k) S. Sen, N. N. Nair, T. Yamada, H. Kitagawa, P. K. Bharadwaj, *J. Am. Chem. Soc.,* 2012, **134**, 19432. (l) C. Dey, T. Kundu, R. Banerjee. *Chem. Commun.*, 2012, **48**, 266. (m) H. Okawa, A. Shigematsu, M. Sadakiyo, T. Miyagawa, K. Yoneda, M. Obha, H. Kitagawa, *J. Am. Chem. Soc.*, 2009, **131**, 13516. (n) E. Pardo, C. Train, G. Gontard, K. Boubekeur, O. Fabelo, H. Liu, B. Dkhil, F. Lloret, K. Nakagawa, H. Tokoro, S. Ohkoshi, M. Verdaguer, *J. Am. Chem. Soc.*, 2011, **133**, 15328. (o) B. M. Wiers, M. L. Foo, N. P. Balsara, J. R. Long, *J. Am. Chem. Soc.,* 2011, **133**, 14522. (p) M. Sadakiyo, H. Okawa, A. Shigematsu, M.

Ohba, T. Yamada, H. Kitagawa, *J. Am. Chem. Soc.*, 2012, **134**, 5472. (q) C. Serre, F. Millange, C. Thouvenot, M. Nogus, G. Marsolier, D. Lour, G. Ferey, *J. Am. Chem. Soc.*, 2002, **124**, 13519. (r) A. Shigematsu, T. Yamada, H. Kitagawa, *J. Am. Chem. Soc.*, 2011, **133**, 2034. (s) T. Kundu, S. C. Sahoo, R. Banerjee. *Chem. Commun.*, 2012, **48**, 4998. (t) R. M. P. Colodrero, P. Olivera-Pastor, E. R. Losilla, D. Hernandez-Alonso, M. A. G. Aranda, L. Leon-Reina, J. Rius, K. D. Demadis, B. Moreau, D. Villemin, M. Palomino, F. Rey, A. Cabeza, *Inorg. Chem.*, 2012, **51**, 7689. (u) E. Pardo, C. Train, G. Gontard, K. Boubekeur, O. Fabelo, H. Liu, B. Dkhil, F. Lloret, K. Nakagawa, H. Tokoro, S. I. Ohkoshi , M. Verdaguer, *J. Am. Chem. Soc.*, 2011, **133**, 15328.

[1.63] a) S. Bureekaew, S. Horike, M. Higuchi, M. Mizuno, T. Kawamura, D. Tanaka, N. Yanai, S. Kitagawa, *Nat. Mater.*, 2009, **8**, 831. (b) J. A. Hurd, R. Vaidhyanathan, V. Thangadurai, C. I. Ratcliffe, I. L. Moudrakovski, G. K. Shimizu, *Nat. Chem.*, 2009, **1**, 705. (c) D. Umeyama, S. Horike, M. Inukai, Y. Hijikata, S. Kitagawa, *Angew. Chem. Int. Ed.,* 2011, **50**, 11706. (d) S. Horike, D. Umeyama, M. Inukai, T. Itakura, S. Kitagawa, *J. Am. Chem. Soc.*, 2012, **134**, 7612. (e) D. Umeyama, S. Horike, M. Inukai, T. Itakura, S. Kitagawa, *J. Am. Chem. Soc.*, 2012, **134**, 12780.

CHAPTER 2

[2.1] (a) R. M. Kohli, C. T. Walsh, M. D. Burkart, *Nature*, 2002, **418**, 658. (b) H. Shin, S. Jo, A. G. Mikos, *Biomaterials*, 2003, **24**, 4353. G. N.Tew, D. Liu, B. Chen, R. J. Doerksen, J. Kaplan, P. J. Carroll, W. F. DeGrado, *Proc. Natl. Acad. Sci., USA*, 2002, **99**, 5110.

[2.2] (a) J. Janin, S. Wodak, M. Levitt, B. Maigret, *J. mol. biol.*, 1978, **125**, 357. (b) Y. Cao, R. A. Musah, S. K. Wilcox, D. B. Goodin, D. E. McRee, 1998, **7**, 72. (c) C. Soto, *FEBS Lett*, 2001, **498**, 204. (d) S. J. Teague, *Nat. rev. Drug discov.*, 2003, **2**, 527.

[2.3] (a) A. Meister, *Biochemistry of the amino acids.* Elsevier, 2012. (b) Z. An, Y. Guo, L. Zhao, Z. Li, J. He, *ACS Catal.*, 2014, **4**, 2566. (c) J. Guan, B. Liu, X. Yang, J. Hu,

C. Wang, Q. Kan, *ACS Sustainable Chem. Eng.*, 2014, **2**, 925. (d) Á. Fudala, I. Pálinkó, I. Kiricsi, *Inorg. Chem.*, 1999, **38**, 4653.

[2.4] S. C. Sahoo, M. Ray, *Dalton Trans.*, 2007, 5148.

[2.5] (a) R. Banerjee, G. R. Desiraju, R. Mondal, J. A. K. Howard, *Chem. Eur. J.* 2004, **10**, 3373. (b) G. R. Desiraju, T. Steiner, *The Weak Hydrogen Bond : In Structural Chemistry and Biology,* Oxford University Press, 1999. (c) C. B. Aakeröy, K. R. Seddon, *Chem. Soc. Rev*. 1993, **22**, 397. (d) J. A. van den Berg, K. R. Seddon, *Cryst. Growth Des.* 2003, **4**, 643. (e) C. B. Aakeröy, S. Panikkattu, P. D. Chopade, J. Desper, Advance Article, *CrystEngComm*, 2013, **15**, 3125. (f) G. M. Espallargas, A. J. Florence, J. van de Streek, L. Brammer, *CrystEngComm*, 2011, **13**, 4400. (g) G. R. Desiraju, *Chem. Commun.*, 2005, **24**, 2995. (h) G. R. Desiraju, *Acc. Chem. Res.*, 2002, **35***,* 565.

[2.6] C. Yang, U. Kaipa, Q. Z. Mather, X. Wang, V. Nesterov, A. F. Venero, M. A. Omary, *J. Am. Chem. Soc.*, 2011, **133**, 18094.

[2.7] G. M. Sheldrick, 2004, *CELL_NOW*. University of Göttingen, Germany. T. Steiner, *Acta Cryst*. 1998, **B54**, 456.

[2.8] Bruker, 2004, *SAINT-Plus* (Version 7.03). Bruker AXS Inc., Madison, Wisconsin, USA.

[2.9] G. M. Sheldrick, 2002, *SADABS* (Version 2.03), *TWINABS* (Version 1.02).University of Göttingen, Germany.

[2.10] G. M. Sheldrick, 1997, *SHELXS '97*, *SHELXL '97*. University of Göttingen, Germany.

[2.11] (a) WINGX version 1.80.04. Louis Farrugia, University of Glasgow. (b) A. L. Spek, 2005, PLATON, *A Multipurpose Crystallographic Tool*, Utrecht University, Utrecht, The Netherlands.

[2.12] (a) L. A. Dakin, P. C. Ong, J. S. Panek, R. J. Staples, P. Stavropoulos, *Organometallics*, 2000, **19**, 2896. (b) S. Noro, R. Kitaura, M. Kondo, S. Kitagawa, T. Ishii, H. Matsuzaka, M. Yamashita, *J. Am. Chem. Soc*., 2002, **124**, 2568. (c) M. Eddaoudi, J. Kim, D. Vodak, A. Sudik, J. Wachter, M. O'Keeffe, O. M. Yaghi, *Proc. Natl. Acad. Sci., USA*, 2002, **99**, 4900. (d) R. A. Heintz, H. Zhao, X. Ouyang, G. Gr,inetti, J. Cowen, K. R. Dunbar, *Inorg. Chem*., 1999, **38**, 144. (e) K. Biradha,

Y. Hongo, M. Fujita, *Angew. Chem. Int. Ed.*, 2000, **39**, 3843. (f) P. Grosshans, A. Jouaiti, M. W. Hosseini, , N. Kyritsakas, *New J. Chem.*, 2003, **27**, 793. (g) N. Takeda, K. Umemoto, K. Yamaguchi, M. Fujita, *Nature,* 1999, **398**, 794. (h) M. Eddaoudi, J. Kim, N. Rosi, D. Vodak, J. Wachter, M. O'Keeffe, O. M. Yaghi, *Science*, 2002, **295**, 469. (i) B. Kesanli, Y. Cui, M. R. Smith, E. W. Bittner, B. C. Bockrath, W. Lin, *Angew. Chem. Int. Ed.*, 2005, **44**, 72. (j) F. A. Cotton, C. Lin, C. A. Murillo, *Inorg. Chem.*, 2001, **40**, 478.

[2.13] T. Kundu, S. C. Sahoo, R. Banerjee *CrystEngComm.*, 2013, **15**, 9634.

[2.14] T. Kundu, S. C. Sahoo, R. Banerjee, *Cryst. Growth Des.*, 2012, **12**, 4633.

CHAPTER 3

[3.1] M. O'Keeffe, O. M. Yaghi, *Chem. Rev.,* 2012, **112**, 675.

[3.2] (a) K. Schlosser, Y. Li, *Nat. Chem. Biol.*, 2007, **3**, 753. (b) A. J. Boersma, R. P. Megens, B. L. Feringa , G. Roelfes, *Chem. Soc. Rev.*, 2010, **39**, 2083. (c) G. L. Holliday, D. E. Almonacid, J. B.O. Mitchell, J. M. Thornton *J. Mol. Biol.*, 2007, **372**, 1261.

[3.3] I. A. Baburin, S. Leoni, G. Seifert, *J. Phys. Chem. B*, 2008, **112**, 9437.

[3.4] (a) K. Mitsuoka, K. Murata, T. Walz, T. Hirai, P. Agre, J. B. Heymann, A. Engel, Y. Fujiyoshi, *J. Struct. Biol*. 1999, **128**, 34. (b) D. A. Doyle, J. M. Cabral, R. A. Pfuetzner, A. Kuo, J. M. Gulbis, S. L. Cohen, B. T. Chait, R. MacKinnon, *Science*, 1998, **280**, 69.

[3.5] (a) R. Ludwig, *Angew. Chem*., 2001, **113**, 1856; *Angew. Chem. Int. Ed*. 2001, **40**, 1808. (b) D. Konozo, M. Yasui, L. S. King, P. Agre, *J. Clin. Invest*. 2002, **109**, 1395. (c) B. Roux, R. MacKinnon, *Science*, 1999, **285**, 100. (d) U. Buck, F. Huisken, *J. Am. Chem. Soc*., 2000, **100**, 3863.

[3.6] (a) K. S. Park, N. Zheng, A. P. Cöté, J. Y. Choi, R. Huang, F. J. Uribe-Romo, H. K. Chae, M. O'Keeffe, O. M. Yaghi, *Proc. Natl. Acad. Sci., U.S.A.*, 2006, **103**, 10186. (b) R. Banerjee, A. Phan, B. Wang, C. Knobler, H. Furukawa, M. O'Keeffe, O. M. Yaghi, *Science*, 2008, **319**, 939. (c) R. Banerjee, H. Furukawa, D. Britt, C. Knobler, M. O'Keeffe, O. M. Yaghi, *J. Am. Chem. Soc.*, 2009, **131**, 3875.

[3.7] (a) G. Alberti, M. Casciola, *Solid State Ionics*, 2001, **145**, 3. (b) N. G. Hainovsky, Y. T. Pavlukhin, E. F. Hairetdinov, *Solid State Ionics*, 1986, **20**, 249.

[3.8] L. Bernard, A. Fitch, A. F. Wright, B. E. F. Fender, A. T. Howe, *Solid State Ionics*, 1981, **5**, 459.

[3.9] A. T. Howe, M. G. Shilton, *J. Solid State Chem.* 1979, **28**, 345.

[3.10] (a) M. Eddaoudi, H. Li, O. M. Yaghi, *J. Am. Chem. Soc.*, 2000, **122***,* 1391. (b) K. E. deKrafft, Z. Xie, G. Cao, S. Tran, L. Ma, O. Z. Zhou, W. Lin, *Angew. Chem. Int. Ed.*, 2009, **48**, 9901.

[3.11] (a) F. Nouar, J. F. Eubank, T. Bousquet, L. Wojtas, M. J. Zaworotko, M. Eddaoudi, *J. Am. Chem. Soc.*, 2008, **130**, 1833. (b) S. Xiang, W. Zhou, J. M. Gallegos, Y. Liu, B. Chen, *J. Am. Chem. Soc.*, 2009, **131**, 12415. (c) D. J. Tranchemontagne, J. L. Mendoza-Cortes, M. O'Keefe, O. M. Yaghi, *Chem. Soc. Rev.*, 2009, **38***,* 1257. (d) M. O'Keeffe, M. Eddaoudi, H. Li, T. M. Reineke, O. M. Yaghi, *J. Solid State Chem.*, 2000, **152***,* 3. (e) M. O'Keeffe, B. G. Hyde, *Crystal Structures I. Patterns, Symmetry*; Mineralogical Society of America: Washington, DC, 1996.

[3.12] A. W. Addison, T. N. Rao, J. Reedijk, J. V. Rijn, G. C. Verschoor, *J. Chem. Soc., Dalton Trans.*, 1984, 1349.

[3.13] S. C. Sahoo, T. Kundu, R. Banerjee, *J. Am. Chem. Soc.*, 2011, **133**, 17950.

CHAPTER 4

[4.1] J. Yang, A. Grzech, F. M. Mulder, T. J. Dingemans, *Chem. Commum.*, 2011, **47**, 5244.

[4.2] (a) T. Chen, I. Popov, O. Zenasni, O. Daugulisa, O. Š. Miljanić, *Chem. Commun.*, 2013, **49**, 6846. (b) J. G. Nguyen, S. M. Cohen, *J. Am. Chem. Soc.*, 2010, **132**, 4560.

[4.3] T. Kundu, S. C. Sahoo, S. Saha, R. Banerjee, *Chem. Commun.* 2013, **49**, 5262.

CHAPTER 5

[5.1] a) X. W. Xie, Y. Li, Z. Q. Liu, M. Haruta, W. J. Shen, *Nature,* 2009, **458**, 746. (b) J. M. Perez, *Nat. Nanotech.*, 2007, **2**, 535. (c) N. Zheng, G. D. Stucky*, J. Am. Chem. Soc.*, 2006, **128**, 14278. (d) M. C. Daniel, D. Astruc, *Chem. Rev.*, 2004, **104**, 293.

(e) M. Raula, M. H. Rashid, T. K. Paira, E. Dinda, T. K. Mandal, *Langmuir*, 2010, **26**, 8769. (f) J. A. Rodriguez, M. F. Garcia, *Synthesis, Properties, Applications of Oxide Nanomaterials*, Wiley Interscience 2007. (g) Z. W. Deng, M. Chen, G. X. Gu, L. M. Wu, *J. Phys. Chem. B*, 2008, **112**, 16. (h) Y. Yang, L. Qu, L. Dai, T. S. Kang, M. Durstock, *Adv. Mater.*, 2007, **19**, 1239. (i) V. M. Aroutiounian, V. M. Arakelyan, G. E. Shahnazaryan, *Solar Energy*, 2005, **78**, 581.

[5.2] (a) H. G. El-Shobaky, M. Mokhtar, G. A. El-Shobaky, *Appl.Catal. A*, 1999, **180**, 335. (b) G. Glaspell, G. Fuoco , M. Samp, *J. Phys. Chem. B*, 2005, **109**, 17350.

[5.3] (a) B. Bott, T. A. Jones, B. Mann, *Sensors and Actuators*, 1984, **5**, 65. (b) M. W. Ahn, K. S. Park, J. H. Heo, J. G. Park, D. W. Kim, K. J. Choi, J. H. Lee, S. H. Hong, *Appl. Phys. Lett.*, 2008, **93**, 263103. (c) H. Gullapalli, V. S. M. Vemuru, A. Kumar, A. B. Mendez, R. Vajtai, M. Terrones, S. Nagarajaiah, P. M. Ajayan, *Small,* 2010, **6**, 1641.

[5.4] (a) S. C. Pillai, J. M. Kelly, D. E. McCormack, R. Ramesh, *J. Mater. Chem.,* 2004, **14**, 1572. (b) S. C. Pillai, J. M. Kelly, D. E. McCormack, P. O'Brien, R. Ramesh, *J. Mater. Chem.,* 2003, **13**, 2586. (c) H. Nanto, T. Minami, S. J. Takata, *J. Appl. Phys.*, 1986, **60**, 482.

[5.5] (a) T. Minami, *MRS Bull.*, 2000, **25**, 38. (b) D. C. Look, *Mater. Sci. Eng. B*, 2001, **80**, 383. (c) S. C. Minne, S. R. Manalis, C. F. Quate, *Appl. Phys. Lett.*, 1995, **67**, 3.

[5.6] (a) D. R. Clarke, *J. Am. Ceram. Soc.* 1999, **82**, 485. (b) T. K. Gupta, *J. Am. Ceram. Soc.* 1990, **73**, 1817. (c) M. Law, L. E. Greene, J. C. Johnson, R. Saykally, P. Yang, *Nat. Mater.* 2005, **4**, 455. (d) C. Battaglia, J. Escarré, K. Söderström, M. Charrière, M. Despeisse, F. -J. Haug, C. Ballif, *Nat. Photonics* 2011, **5**, 535.

[5.7] (a) S. Monticone, R. Tufeu, A. V. Kanaev, *J. Phys. Chem. B,* 1998, **102**, 2854. (b) A. V. Dijken, J. Makkinje, A. Meijerink, *J. Lumin*. 2001, **92**, 323.

[5.8] (a) Z. R. Tian, J. A. Voigt, J. Liu, B. Mckenzie, M. J. Mcdermott, M. A. Rodriguez, H. Konishi, H. Xu, *Nat. Mater.* 2003, **2**, 821. (b) C. Xu, P. Shin, L. Cao, D. Gao, *J. Phys. Chem. C,* 2010, **114**, 125. (c) J. Zhang, L. Sun, J. Yin, H. Su, C. Liao, C. Yan, *Chem. Mater.* 2002, **14**, 4172. (d) P. M. Aneesh, K. A. Vanaja, M. K. Jayaraj, *Proc. of SPIE,* 2007, **6639**, 66390J-9. (e) M. -H. Lai, A. Tubtimtae, M. -W. Lee, G. -J. Wang, *Int. J. Photoenergy* 2010, 1.

[5.9] (a) T. Y. Han, M. A. Worsley, T. F. Baumann, J. H. Satcher, *J. Mater. Chem.* 2011, **21**, 330. (b) M. Krumm, C. L. Pueyo, S. Polarz, *Chem. Mater.* 2010, **22**, 5129. (c) P. G. Yanping, N. Charlotte, L. J. Weeks, *Chem. Mater.* 2007, **19**, 6007.

[5.10] (a) L. Madler, W. J. Stark, S. E. Pratsinis, *J. Appl. Phys*. 2002, **92**, 6537. (b) M. J. Height, L. Madler, S. E. Pratsinis, *Chem. Mater*. 2006, **18**, 572. (c) D. Li, H. Haneda, *J. Photochem. Photobiol. A: Chem.* 2003, **155**, 171.

[5.11] (a) B. Liu, S. Han, K. Tanaka, H. Shioyama, Q. Xu, *Bull. Chem. Soc. Jpn.* 2009, **82**, 1052. (b) S. Jung, W. Cho, H. J. Lee, M. Oh, *Angew. Chem. Int. Ed.* 2009, **48**, 1459. (c) L. Zhang, Y. H. Hu, *J. Phys. Chem. C* 2010, **114**, 2566. (d) C. Y. Su, A. M. Goforth, M. D. Smith, P. J. Pellechia, H. C. Loye, *J. Am. Chem. Soc.* 2004, **126**, 3576.

[5.12] (a) S. J. Dalgarno, N. P. Power, J. L. Atwood, *Coord. Chem. Rev.* 2008, **252**, 825. (b) K. T. Holman, A. M. Pivovar, M. D. Ward, *Science* 2001, **294**, 1907. (c) J. J. Perry, V. C. Kravtsov, G. J. McManus, M. J. Zaworotko, *J. Am. Chem. Soc.,* 2007, **129**, 1076. (d) Y. Cui, Y. Yue, G. Qian, B. Chen, *Chem. Rev.* 2012, **112**, 1126. (e) C. B. Aakeröy, A. M. Beatty, B. A. Helfrich, *Angew. Chem. Int. Ed.* 2001, **40**, 3240. (f) T. Lasanta, O. M. Elena, L. Laguna, D. Antonio, M. Jóse, P. Naumov, *J. Am. Chem. Soc.,* 2011, **133**, 16358. (g) J. L. Atwood, L. J. Barbour, A. Jerga, *Science* 2002, **296**, 2367. (h) J. L. Rowsell, E. Spencer, C. J. Eckert, A. K. Howard, O. M. Yaghi, *Science* 2005, **309**, 1351. (i) O. M. Yaghi, H. Li, L. T. Groy, *J. Am. Chem. Soc.* 1996, **118**, 9096. (j) S. Wang, H. Xing, Y. Li, J. Bai, M. Scheer, Y. Pan, X. You, *Chem. Commun.* 2007, 2293. (k) J. K. Schnobrich, O. Lebel, K. A. Cychosz, A. Dailly, A. G. Wong-Foy, A. J. Matzger, *J. Am. Chem. Soc.* 2010, **132**,13941. (l) L. R. MacGillivray, G. S. Papaefstathiou, T. Friščić, T. D. Hamilton, D. -K. Bučar, Q. Chu, D. B. Varshney, I. G. Georgiev, *Acc. Chem. Res.* 2008, **41**, 280.

[5.13] S. Jung, W. Cho, H. J. Lee, M. Oh, *Angew. Chem. Int. Ed.* 2009, **48**, 1459.

[5.14] (a) W. Wang, D. Yuan *Sci. Rep.*, 2014, **4**, 5711. (b) J. Yu, X. Yu, *Environ. Sci. Technol.*, 2008, **42**, 4902. (c) J. Mu, C. Shao, Z. Guo, Z. Zhang, M. Zhang, P. Zhang, Y. Liu, *ACS Appl. Mater. Interfaces*, 2011, **3**, 590.

[5.15] C. Y. Su, A. M. Goforth, M. D. Smith, P. J. Pellechia, H. C. zur Loye, *J. Am. Chem. Soc.* 2004, **126**, 3576.

[5.16] Powder Diffraction File PDF#00-036-1451. All the peaks of the ZnO architecture prepared under different conditions can be indexed to the wurtzite ZnO (JCPDS card No. 36–1451, a = 3.249 Å, c = 5.206 Å with high crystallinity.

[5.17] (a) R. Argazzi, N. Murakami, Y. H. Zabri, F. Odobel, C. A. Bignozzi, *Coord. Chem. Rev.* 2004, **248**, 1299. (b) A. B. F. Martinson, J. W. Elam, J. T. Hupp, M. J. Pellin, *Nano Lett.* 2007, **7**, 2183. (c) S. H. Ko, D. Lee, H. W. Kang, K. H. Nam, J. Y. Yeo, S. J. Hong, C. P. Grigoropoulos, H. J. Sung, *Nano Lett.* 2011, **11**, 666. (d) S. A. Agarkar, R. Kulkarni, V. V. Dhas, A. A. Chinchansure, P. Hazra, S. P. Joshi, S. B. Ogale, *ACS Appl. Mater. Interfaces,* 2011, **3**, 2440. (e) J. Qui, M. Guo, X. Wang, *ACS Appl. Mater. Interfaces,* 2011, **3**, 2358.

CHAPTER 6

[6.1] (a) S. S. Han, W. Q. Deng, W. A. Goddard, *Angew. Chem.*, 2007, **119**, 6405. (b) A. Mallick, S. Saha, P. Pachfule, S. Roy, R. Banerjee, *J. Mater. Chem.* 2010, **20**, 9073. (c) S. Gadipelli, J. Ford, W. Zhou, H. Wu, T. J. Udovic, T. Yildirim, *Chem. Eur. J.* 2011, **17**, 6043. (d) A. E. Platero-Prats, V. A. de la Peña-O'Shea, N. Snejko, Á. Monge, E. Gutiérrez-Puebla, *Chem. Eur. J.*, 2010, **16**, 11632. (e) A. E. Platero-Prats, V. A. de la Peña-O'Shea, N. Snejko, Á. Monge, E. Gutiérrez-Puebla, *ChemCatChem*, 2010, **2**, 147. (f) Z. Fei, T. J. Geldbach, R. Scopelliti, P. J. Dyson, *Inorg. Chem.*, 2006, **45**, 6331.

[6.2] (a) A. K. Mohanty, E. A. Mistri, A. Ghosh, S. Banerjee, *Journal of Membrane Science*, 2012, **409**, 145. (b) L. Jin, Z. Li, S. Wang, Z. Wang, F. Dong, X. Yin, *React. Funct. Polym.* 2012, **72**, 549. (c) M. Geormezi, V. Deimede, N. Gourdoupi, N. Triantafyllopoulos, S. Neophytides, J. K. Kallitsis, *Macromolecules* 2008, **41**, 9051. (d) M. A. Hickner, H. Ghassemi, Y. S. Kim, B. R. Einsla, J. E. McGrath, *Chem. Rev.* 2004, **104**, 4587. (e) M. Schuster, C. C. de Araujo, V. Atanasov, H. T. Andersen, K.-D. Kreuer, J. Maier, *Macromolecules* 2009, **42**, 3129.

[6.3] K. Kanaizuka, S. Iwakiri, T. Yamada, H. Kitagawa, *Chem. Lett.* 2010, **39**, 2829.

APPENDIX 1

Table A1. Crystallographic table for chapter 2:

	ThrZnOAc	**LeuCdCl**	**LeuCdBr**	**SerCdCl**	**SerCdBr**	**ThrCdCl**	**ThrCdBr**
Formula	$C_{12}H_{26}N_2O_{10}Zn$	$C_{12}\ H_{17}\ Cl\ N_2\ O_3\ Cd$	$C_{12}\ H_{17}\ Br\ N_2\ O_2\ Cd$	$C_9\ H_{11}\ Cl\ N_2\ O_4\ Cd$	$C_{18}\ H_{21}\ Br_2\ N_4\ O_9Cd_2$	$C_{10}\ H_{13}\ Cl\ N_2\ O_5Cd$	$C_{10}\ H_{13}\ Br\ N_2\ O_5\ Cd$
*M*r	423.66	385.14	413.59	359.06	822.01	389.08	432.53
CCDC No.	943050	851353	851354	851355	851356	851357	851358
Temperature	100(2)K	296(2)K	296(2)K	296(2)K	296(2)K	296(2)K	296(2)K
Crystal system	Hexagonal	Orthorhombic	Orthorhombic	Orthorhombic	Monoclinic	Monoclinic	Monoclinic
Space group	$P6_1$	$P2_12_12_1$	$P2_12_12_1$	$P2_12_12_1$	$P2_1$	$P2_1$	$P2_1$
a (Å)	17.4807(3)	7.123(3)	7.2398(6)	5.8751(17)	9.4628(12)	7.9060(7)	7.9689(12)
b (Å)	17.4807(3)	13.896(5)	13.7041(11)	15.067(4)	15.1900(19)	10.7338(10)	10.7406(15)
c (Å)	10.4350(2)	15.893(6)	16.5286(13)	16.416(5)	10.0319(12)	8.9647(8)	8.9501(13)
β(°)					110.630(2)	110.5280(10)	110.444(13)
V[Å^3]	2761.47(9)	1573.1(11)	1639.9(2)	1453.1(7)	1349.5(3)	712.45(11)	717.80(18)
Z	6	4	4	4	2	2	2
ρ/g cm^{-1}	1.492	1.626	1.675	1.641	2.020	1.814	2.001
μ/mm^{-1}	1.385	1.563	3.779	1.689	4.587	1.736	4.320
F(000)	1272	768	808	704	790	384	418
Flack parameter	0.0(9)	0.01(5)	0.0009(2)	0.0009(1)	0.055(14)	-0.02(2)	0.11(3)
Reflections collected	7339	3677	3871	3420	6139	2583	2245
Independent reflections	3035	3445	3568	3389	5890	2571	2197
GOF	1.05	1.033	1.066	1.097	1.067	1.021	1.081
Final *R*1, $wR2[I > 2\sigma(I)]$	R1 = 0.0513, wR2 = 0.1358	$R_1 = 0.0434$, $wR_2 = 0.1059$	$R_1 = 0.0421$, $wR_2 = 0.1300$	$R_1 = 0.0336$, $wR_2 = 0.0952$	$R_1 = 0.0485$, $wR_2 = 0.1325$	$R_1 = 0.0189$, $wR_2 = 0.0501$	$R_1 = 0.0625$, $wR_2 = 0.1446$
R indices (all data)	R1 = 0.0533, wR2 = 0.1378	$R_1 = 0.0475$, $wR_2 = 0.1079$	$R_1 = 0.0461$, $wR_2 = 0.1342$	$R_1 = 0.0341$, $wR_2 = 0.0956$	$R_1 = 0.0506$, $wR_2 = 0.1344$	$R_1 = 0.0190$, $wR_2 = 0.0501$	$R_1 = 0.0630$, $wR_2 = 0.1450$

Table A2. Crystallographic table for chapter 3:

	***l*-ValZnCl**	***l*-ValZnBr**	***d*-ValZnCl**	***d*-ValZnBr**	***l*-ValZnCl@120**	***l*-ValZnBr@40**
Formula	C_{11} H_{15} Cl N_2 O_4 Zn	C_{11} H_{15} Br N_2 O_4 Zn	C_{11} H_{15} Cl N_2 O_4 Zn	C_{11} H_{15} Br N_2 O_4 Zn	C_{11} H_{15} Cl N_2 O_2 Zn	C_{11} H_{15} Br N_2 O_2 Zn
*M*r	340.09	384.54	340.09	384.54	308.09	352.54
CCDC No.	831054	831055	831056	831057	831058	831059
Temperature	195(2)K	195(2)K	195(2)K	195(2)K	353(2)K	313(2)K
Crystal system	Hexagonal	Hexagonal	Hexagonal	Hexagonal	Hexagonal	Hexagonal
Space group	$P6_1$	$P6_1$	$P6_5$	$P6_5$	$P6_1$	$P6_1$
a (Å)	17.691(2)	17.768(2)	17.703(2)	17.7786(7)	17.661(15)	17.8590(10)
b (Å)	17.691(2)	17.768(2)	17.703(2)	17.7786(7)	17.661(15)	17.8590(10)
c (Å)	10.5617(12)	10.4796(11)	10.585(5)	10.4868(18)	10.5104(16)	10.5031(12)
V[$Å^3$]	2862.76(6)	2865.2(5)	2872.9(14)	2870.6(5)	2873.0(6)	2901.1(4)
Z	6	6	6	6	6	6
ρ_{calcd}[g cm^{-1}]	1.184	1.337	1.179	1.335	1.068	1.211
Absorption coefficient	1.434	3.385	1.423	3.379	1.414	3.330
F(000)	1044	1152	996	1152	948	1056
θ range[°]	2.30- 26.81	2.29- 20.90	2.34 - 27.13	2.29 - 22.66	1.32- 27.46	1.32- 27.46
Reflections collected	4581	4567	4460	4492	4331	4368
Independent reflections	4302	3827	4023	3555	3241	4137
GOF	1.017	1.017	1.053	1.046	1.005	1.071
Final *R*1, *wR*2[$I > 2\sigma(I)$]	$R_1 = 0.0384$, $wR_2 = 0.1154$	$R_1 = 0.0618$, $wR_2 = 0.1928$	$R_1 = 0.0469$, $wR_2 = 0.1325$	$R_1 = 0.0583$, $wR_2 = 0.1731$	$R_1 = 0.0642$, $wR_2 = 0.1470$	$R_1 = 0.0573$, $wR_2 = 0.1512$
R indices (all data)	$R_1 = 0.0430$, $wR_2 = 0.1203$	$R_1 = 0.0803$, $wR_2 = 0.2133$	$R_1 = 0.0532$, $wR_2 = 0.1387$	$R_1 = 0.0750$, $wR_2 = 0.1859$	$R_1 = 0.0915$, $wR_2 = 0.1665$	$R_1 = 0.0600$, $wR_2 = 0.1532$

Table A3. Crystallographic table for chapter 4:

	ValZnFor	**ValZnOAc**	**AlaZnCl**	**AlaZnBr**	**AlaZnFor**	**AlaZnOAc**
Formula	$C_{12}H_{15}N_2O_6Zn$	$C_{13}H_{18}N_2O_6Zn$	$C_9H_{11}ClN_2O_4Zn$	$C_9H_{11}BrN_2O_4Zn$	$C_{10}H_{11}N_2O_6Zn$	$C_{11}H_{13}N_2O_6Zn$
*M*r	348.65	363.68	312.04	356.49	320.60	334.62
Temperature	100(2)K	100(2)K	100(2)K	100(2)K	100(2)K	100(2)K
Crystal system	Hexagonal	Hexagonal	Hexagonal	Hexagonal	Hexagonal	Hexagonal
Space group	$P6_1$	$P6_1$	$P6_1$	$P6_1$	$P6_1$	$P6_1$
a (Å)	17.7336(11)	17.4542(6)	17.4587(2)	17.7440(3)	17.5911(7)	17.5806(7)
b (Å)	17.7336(11)	17.4542(6)	17.4587(2)	17.7440(3)	17.5911(7)	17.5806(7)
c (Å)	10.3433(8)	10.3953(3)	10.24475(14)	10.17155(19)	10.1716(3)	10.1486(2)
V[Å^3]	2817.0(5)	2742.63(16)	2704.31(6)	2773.45(12)	2725.87(17)	2716.5(3)
Z	6	6	6	6	6	6
ρ_{calcd}[g cm^{-1}]	1.233	1.321	1.150	1.281	1.172	1.227
Absorption coefficient	1.329	1.368	1.513	3.492	1.368	1.376
F(000)	1074	1128	948	1056	978	2264
θ range[°]	3.03- 29.24	3.33 – 29.10	3.07- 29.14	3.05 – 29.22	3.06 – 29.11	3.07 – 28.05
Reflections collected	7392	6242	19898	6778	8057	6610
Independent reflections	3718	2991	4382	4042	3676	3289
GOF	1.108	1.102	1.142	1.093	1.090	1.073
Final *R*1, $wR2[I > 2\sigma(I)]$	$R_1 = 0.0711$, $wR_2 = 0.1895$	$R_1 = 0.0546$, $wR_2 = 0.1480$	$R_1 = 0.0420$, $wR_2 = 0.1237$	$R_1 = 0.0482$, $wR_2 = 0.1309$	$R_1 = 0.0645$, $wR_2 = 0.1891$	$R_1 = 0.0732$, $wR_2 = 0.1952$
R indices (all data)	$R_1 = 0.0793$, $wR_2 = 0.2060$	$R_1 = 0.0586$, $wR_2 = 0.1505$	$R_1 = 0.0436$, $wR_2 = 0.1253$	$R_1 = 0.0507$, $wR_2 = 0.1351$	$R_1 = 0.0783$, $wR_2 = 0.2059$	$R_1 = 0.0903$, $wR_2 = 0.2109$

Table A4. Crystallographic table for chapter 6:

	Ca-SBBA	**Ba-SBBA**	**Sr-SBBA**
Empirical formula	$C_{23}H_{29}CaN_3O_9S$	$C_{48}H_{56}Ba_2N_4O_{16}S_2$	$C_{80}H_{76}Sr_5N_8O_{36}S_4$
Formula weight	563.633	1283.77	2291.87
Temperature	296(2)K	296(2)K	293(2)K
Wavelength	1.54184 Å	0.71073 Å	1.54184 Å
Crystal system	Monoclinic	Triclinic	Triclinic
Space group	$P\,2_1/c$	$P\,\bar{1}$	$P\,\bar{1}$
Unit cell dimensions	a = 8.7220(3)Å b = 27.5302(8)Å c = 11.2194(3) Å	a = 13.985(2) Å b = 14.614(3) Å c = 16.700(3) Å	a = 13.9492(9) Å b = 15.6692(13) Å c = 15.9071(13) Å
Volume	2572.31(13) Å^3	2784.1(9) Å^3	2871.2(5) Å^3
Z	4	2	1
Density (calculated)	1.455/m^3	1.531 /m^3	1.326 /m^3
Absorption coefficient	3.361	1.548	4.247
F(000)	1184	1288	1154
Crystal size	0.30 × 0.20 × 0.10 mm^3	0.30 × 0.20 × 0.20 mm^3	0.28 × 0.16 × 0.08 mm^3
Reflections collected	4407	12609	19525
Independent reflections	3315	8752	8511
Completeness (to theta)	95 %(67.70)	98 %(27.56)	94.8 % (73.36)
Absorption correction	Multi-scan	Multi-scan	Multi-scan
Goodness-of-fit on F^2	1.028	1.074	1.116
Final R indices [I>2sigma(I)]	R_1 = 0.0386, wR_2 = 0.0936	R_1 = 0.0557, wR_2 = 0.1273	R_1 = 0.0825, wR_2 = 0.2336
R indices (all data)	R_1 = 0.0591, wR_2 = 0.1045	R_1 = 0.0837, wR_2 = 0.1413	R_1 = 0.0990, wR_2 = 0.2534

ABOUT THE AUTHOR

Tanay Kundu, son of Madhusudan Kundu and Minakshmi Kundu, was born in Krishnagar, Nadia, West Bengal, India, in 1987. He received his secondary and higher secondary education from Saktinagar High School, Krishnagar. He completed his B.Sc. from Ramakrishna Mission Vivekananda Centenary College, Rahara. After the completion of his B.Sc. he joined Department of Chemistry in Scottish Church College, Calcutta University to pursue his M.Sc. He joined Department of Physical and Materials chemistry, CSIR-NCL, Pune to pursue his Ph.D. degree in July 2009. He was awarded research fellowship by Council of Scientific and Industrial Research (JRF and SRF) for 2009-2014.

List of Publications

1. Subash C. Sahoo*, **Tanay Kundu,** and Rahul Banerjee* *"Helical Water Chain Mediated Proton Conductivity in Homochiral Metal–Organic Frameworks with Unprecedented Zeolitic unh-Topology"*

J. Am. Chem. Soc., *2011*, 133, 17950-17958.

2. Tanay Kundu, Subash C. Sahoo, and Rahul Banerjee* *"Alkali earth metal (Ca, Sr, Ba) based thermostable metal–organic frameworks (MOFs) for proton conduction"*

Chem. Commun., *2012*, 48, 4998-5000.

3. Tanay Kundu, Subash C. Sahoo, Subhadeep Saha, and Rahul Banerjee* *"Salt metathesis in three dimensional metal–organic frameworks (MOFs) with unprecedented hydrolytic regenerability"*

Chem. Commun., *2013*, 49, 5262-5264.

4., Tamas Panda, **Tanay Kundu (equal contribution)**, and Rahul Banerjee* *"Self-assembled one dimensional functionalized metal–organic nanotubes (MONTs) for proton conduction"*

Chem. Commun., *2012*, 48, 5464-5466.

5. Chandan Dey, **Tanay Kundu**, and Rahul Banerjee* *"Reversible phase transformation in proton conducting Strandberg-type POM based metal organic material"*

Chem. Commun., *2012*, 48, 266-268.

6. Arijit Mallick, **Tanay Kundu**, and Rahul Banerjee* *"Correlation between coordinated water content and proton conductivity in Ca–BTC-based metal–organic frameworks"*

Chem. Commun., *2012*, 48, 8829-8831.

7. Tamas Panda, **Tanay Kundu**, and Rahul Banerjee* *"Structural isomerism leading to variable proton conductivity in indium (III) isophthalic acid based frameworks"*

Chem. Commun., *2012*, 48, 6197-6199.

8. Tanay Kundu, Subash C. Sahoo*, and Rahul Banerjee* *"Solid-State Thermolysis of Anion Induced Metal–Organic Frameworks to ZnO Microparticles with Predefined Morphologies: Facile Synthesis and Solar Cell Studies"*

Cryst. Growth Des., *2012*, 12, 2572-2578.

9. Tanay Kundu, Subash C. Sahoo, and Rahul Banerjee* *"Variable Water Adsorption in Amino Acid Derivative Based Homochiral Metal Organic Frameworks"*

Cryst. Growth Des., *2012*, 12, 4633-4640.

10. Tanay Kundu, Subash C. Sahoo, and Rahul Banerjee* *"Relating pore hydrophilicity with vapour adsorption capacity in a series of amino acid based metal organic frameworks"*

CrystEngComm, *2012*, 12, 4633-4640.

11. Subhadeep Saha, Juergen Bachl, **Tanay Kundu,** David Díaz Díaz and Rahul Banerjee* *"Amino acid-based multiresponsive low-molecular weight metallohydrogels with load-bearing and rapid self-healing abilities"*

Chem. Commun., *2014*, 50, 3004-3006.

12. Subhadeep Saha, Juergen Bachl, **Tanay Kundu,** David Díaz Díaz and Rahul Banerjee* *"Dissolvable Metallohydrogels for Controlled Release: Evidence of a Kinetic Supramolecular Gel Phase Intermediate"*

Chem. Commun., *2014*, 50, 7032-7035.

13. Chandan Dey, **Tanay Kundu**, Bishnu P. Biswal, Arijit Mallick, Rahul Banerjee* "*Crystalline metal-organic frameworks (MOFs): synthesis, structure and function*"

Acta Crystallographica Section B: Structural Science, Crystal Engineering and Materials, *2014*, 70, 1.

14. Shouvik Mitra, Sourov Chandra, **Tanay Kundu**, Rahul Banerjee, Panchanan Pramanik, Arunava Goswami, "*Rapid microwave synthesis of fluorescent hydrophobic carbon dots"*

RSC Advances*, 2012,* 2, 12129-12131.

15. Suman Chandra, **Tanay Kundu (equal contribution)**, Sharath Kandambeth, Ravichandar BabaRao, Yogesh Marathe, Shrikant M. Kunjir and Rahul Banerjee* *"Phosphoric acid Loaded Azo (-N=N-) based Covalent Organic Framework for Proton Conduction"*

J. Am. Chem. Soc. *2014*, 136, 6570-6573.

16. Tanay Kundu, Shouvik Mitra, Prasun Patra, Arunava Goswami, David Díaz Díaz and Rahul Banerjee* "*Mechanical Downsizing of a Gd(III)-based Metal-Organic Framework for Anticancer Drug Delivery"*

Chem. Eur. J. *2014***,** 20, 10514-10518.

17. Tanay Kundu*, and Rahul Banerjee*

"*Structural diversity in serine derived homochiral metal organic frameworks"*

J. Chem. Sci. *2014***,** (Accepted Article).